UCTEA Turkish Chamber of Civil Engineers

Teknik Dergi

Technical Journal

Volume 33 Issue 1 January 2022

TEKNİK DERGİ PUBLICATION PRINCIPLES

Teknik Dergi is a scientific and technical journal indexed by the Science Citation Index Expanded. Annually six issues are published, three in Turkish in the months of January, May and September, three in English in March, July and November. Its main principles of publication are summarized below:

1. Articles reporting original scientific research and those reflecting interesting engineering applications are accepted for publication. To be classified as original, the work should either produce new scientific knowledge or add a genuinely new dimension to the existing knowledge or develop a totally new method or substantially improve an existing method.
2. Articles reporting preliminary results of scientific studies and those which do not qualify as full articles but provide useful information for the reader can be considered for publication as technical notes.
3. Discussions received from the readers of the published articles within three months from publication are reviewed by the Editorial Board and then published together with the closing remarks of the author.
4. Manuscripts submitted for publication are evaluated by two or three reviewers unknown to the authors. In the light of their reports, final decision to accept or decline is taken by the Editorial Board. General policy of the Board is to get the insufficient manuscripts improved in line with the reviewers' proposals. Articles that fail to reach the desired level are declined. Reasons behind decisions are not declared.
5. A signed statement is taken from the authors, declaring that the article has not been published as a "journal article or book chapter". In case the Editorial Board is in the opinion that the article has already been published elsewhere with minor changes or suspects plagiarism or a similar violation of ethics, then not only that article, but none of the articles of the same authors are published.
6. Papers reporting works presented as conference papers and developed further may be considered for publication. The conference it was presented to is given as a footnote in the first page.
7. Additionally, a document signed by all authors, transferring the copyright to UCTEA Chamber of Civil Engineers is submitted together with the manuscript.

UCTEA Turkish Chamber of Civil Engineers

Teknik Dergi

Technical Journal

Volume 33 Issue 1 January 2022

UCTEA *(TMMOB)*
Turkish Chamber of Civil Engineers *(İnşaat Mühendisleri Odası)*
Necatibey St. No: 57, Kızılay 06440 Ankara, Turkey
Tel: +90.312.294 30 00 - Faks: +90.312.294 30 88
E-mail: imo@imo.org.tr - www.imo.org.tr

Publisher *(Sahibi)*:
Taner YÜZGEÇ
On behalf of UCTEA Turkish Chamber of Civil Engineers

Administrative Officer *(Yazı İşleri Müdürü)*:
Özer AKKUŞ

Volume 33 - Issue 1 - January 2022 *(Cilt 33 - Sayı 1 - Ocak 2022)*
Published bi-monthly. Local periodical. *(İki ayda bir yayınlanır, yerel süreli yayın)*
Date of Print: January 1, 2022 *(Baskı Tarihi: 1 Ocak 2022)*
Number of copies: 1.000 *(1.000 adet basılmıştır)*

ISSN: 1300-3453

Teknik Dergi is indexed by
- Science Citation Index Expanded
- Scopus
- Journal Citation Reports / Science Edition
- Engineering Index
- Concrete Abstracts (American Concrete Institute)
- National Technical Information Service (US NTIS)
- CITIS
- Ulrich's International Periodical's Directory
- TR Index

Teknik Dergi is a peer reviewed open access periodical publishing papers of original research and interesting practice cases. It addresses both the research community and the practicing engineers.

Teknik Dergi ekidir.

UCTEA Turkish Chamber of Civil Engineers
Teknik Dergi

Reviewers:

This list is renewed each year and includes reviewers who served in the last two years of publication.

Şükran AÇIKEL
Merve AÇIKGENÇ ULAŞ
Süleyman ADANUR
Ali Mardani AGHABAGLOU
Perviz AHMEDZADE
Bülent AKBAŞ
Ragıp AKBAŞ
Sami Oğuzhan AKBAŞ
Şeref Doğuşcan AKBAŞ
Rıfat AKBIYIKLI
Özge AKBOĞA KALE
Hüseyin AKBULUT
Sarven AKCELYAN
Burcu AKÇAY ALDANMAZ
Cihan Taylan AKDAĞ
Cem AKGÜNER
Muhammet Vefa AKPINAR
Atakan AKSOY
Hafzullah AKSOY
Hakan AKSU
Tülay AKSU ÖZKUL
Büşra AKTÜRK
Zuhal AKYÜREK
Uğurhan AKYÜZ
Sadık ALASHAN
Cenk ALHAN
Ayşe Burcu ALTAN SAKARYA
Sinan ALTIN
Adlen ALTUNBAŞ
Ahmet Can ALTUNBAŞ
Ahmet Can ALTUNIŞIK
Yalçın ALVER
Bahadır ALYAVUZ
Özgür ANIL
Necati ARAS
Yalın ARICI
Yalçın ARISOY
Musa Hakan ARSLAN
Deniz ARTAN İLTER
Şenay ATABAY
Ali Osman ATAHAN
Hakan Nuri ATAHAN
Hakan Nuri ATAHAN
Bekir Özer AY
Ersin AYDIN
Gökçe AYDIN
Hakan AYGÖREN
Mustafa Tamer AYVAZ
İhsan Engin BAL
Selim BARADAN
Eray BARAN
Türkay BARAN
Bekir Oğuz BARTIN
Eyüp Ensar BAŞAKIN
Özgür BAŞKAN
Niyazi Özgür BEZGİN
Senem BİLİR MAHÇİÇEK
Gökçen BOMBAR
Burak BOYACI
İlknur BOZBEY
Zafer BOZKUŞ
Atıl BULU
Burcu BURAK BAKIR
Halil İbrahim BURGAN
Erdem CANBAY
Zekai CELEP
Cihan CENGİZ
Halim CEYLAN
Hüseyin CEYLAN
Ömer CİVALEK
Ayşe COŞKUN BEYAN
Melih ÇALAMAK
Gülben ÇALIŞ
Süheyla Pelin ÇALIŞKANELLİ
Dilay ÇELEBİ
Tevfik Kutay ÇELEBİOĞLU
Ahmet Ozan ÇELİK
Oğuz Cem ÇELİK
Semet ÇELİK
Hilmi Berk ÇELİKOĞLU
Mahmut ÇETİN
Mecit ÇETİN
Gökhan ÇEVİKBİLEN
Erdal ÇOKÇA
İsa ÇÖMEZ
İsmail DABANLI
Ömer DABANLI
Atilla DAMCI
Yakup DARAMA
Osama M.F. DAWOUD
Tayfun DEDE
Özgür DEĞERTEKİN
Abdullah DEMİR
Cem DEMİR
Emre DEMİR
Munise Didem DEMİRBAŞ
Ender DEMİREL
Mehmet Cüneyd DEMİREL
Fatih DİKBAŞ
Seyyit Ümit DİKMEN
Ali Ersin DİNÇER
İsmail DURANYILDIZ
Selim DÜNDAR
Nurhan ECEMİŞ ZEREN
Volkan Ş. EDİGER
Muhammet Emin EMİROĞLU
Murat Altuğ ERBERİK
Ali ERCAN
Hakan ERDEM
Sinan Turhan ERDOĞAN
Ramazan Cüneyt ERENOĞLU
Esin ERGEN PEHLEVAN
Gökmen ERGÜN
Bülent ERKMEN
Barış ERKUŞ
Tuğba ESKİŞAR TEFÇİ
Burak FELEKOĞLU
Okan FISTIKOĞLU
Abdullah GEDİKLİ
Ergun GEDİZLİOĞLU
Ömer GİRAN
Zehra Canan GİRGİN
Ilgın GÖKAŞAR
Serdar GÖKTEPE
Fazlı Erol GÜLER
Ilgın GÜLER
Hamza GÜLLÜ
Gürkan GÜNAY
Taylan GÜNAY
Murat GÜNAYDIN
Samet GÜNER
Ülker GÜNER BACANLI
Oğuz GÜNEŞ
Mehmet Şükrü GÜNEY
Tuba GÜRBÜZ BÜYÜKKAYIKÇI
Melike GÜREL
İbrahim GÜRER
Aslı Pelin GÜRGÜN
Iman HAJİRASOULİHA
Soner HALDENBİLEN
Mustafa HATİPOĞLU
Bo-Tao HUANG
Zeynep IŞIK
Hande IŞIK ÖZTÜRK
Sabriye Banu İKİZLER
Ragıp İNCE
Recep İYİSAN
Nihat KABAY
Mehmet Sedat KABDAŞLI
Mehmet Rifat KAHYAOĞLU
Özkan KALE
Volkan KALPAKÇI
Murat KARACASU
Halil KARAHAN
Cenk KARAKURT
Mustafa KARAŞAHİN
Zülküf KAYA
Hasan Ahmed KAZMEE
Mustafa Kubilay KELEŞOĞLU
Elçin KENTEL
Havvanur KILIÇ
Young Hoon KIM
Ufuk KIRBAŞ
Veysel Şadan Özgür KIRCA
Cem KIRLANGIÇOĞLU
Güven KIYMAZ
Gökhan KİRKİL
Kasım KOÇAK
Salih KOÇAK
Niyazi Uğur KOÇKAL
Mehmet Melih KOŞUCU
Baha Vural KÖK
Mete KÖKEN
Şerife Yurdagül KUMCU
Murat KURUOĞLU
Akif KUTLU
Abdullah KÜRKÇÜ
Hilmi LUŞ
Kasım MERMERTAŞ
Mehmet Murat MONKUL
Hamid MORTEZAİE
Yetiş Şazi MURAT
Sepanta NAİMİ
Öcal NECMİOĞLU
Sinan Melih NİĞDELİ
Elif OĞUZ
Fuad OKAY
Umut OKKAN
Derviş Volkan OKUR
Mehmet Hakkı OMURTAG
Engin ORAKDÖĞEN
Şeref ORUÇ
Akın ÖNALP
Halil ÖNDER
Jülide ÖNER
Bihrat ÖNÖZ
Ali Hakan ÖREN
Mustafa ÖZAKÇA
Ceyhun ÖZÇELİK
Yiğit ÖZÇELİK
Gökhan ÖZDEMİR
Osman Nuri ÖZDEMİR
Halit ÖZEN
Murat ÖZEN
Pelin ÖZENER
Cem ÖZER
Hasan ÖZER
Serkan ÖZGEN
Eren Arman ÖZGÜVEN
Hakkı Oral ÖZHAN
M. Hulusi ÖZKUL
Zeynep Huri ÖZKUL BİRGÖREN
Gülen ÖZKULA
Ahmet ÖZTOPAL
Sadık ÖZTOPRAK
Turan ÖZTURAN
Hasan Tahsin ÖZTÜRK
Mustafa ÖZUYSAL
Ahmet Onur PEHLİVAN
Onur PEKCAN
Seval PINARBAŞI ÇUHADAROĞLU
Elişan Filiz PİROĞLU
Selim PUL
Selçuk SAATÇİ
Selman SAĞLAM
Mehmet SALTAN
İlyas SARIBAŞ
Metin SARIGÖL
Afşin SARITAŞ
Altuğ SAYGILI
Serdar SELAMET
Senem SEYİS
Alper SEZER
Osman SİVRİKAYA
Behzad SOLTANBEIGI
Celal SOYARSLAN
Serdar SOYÖZ
Rifat SÖNMEZ
Tayfun Altuğ SÖYLEV
Erol ŞADOĞLU
Güvenç ŞAHİN
Olcay ŞAHİN
Ömer Lütfi ŞEN
Burak ŞENGÖZ
Özkan ŞENGÜL
Aynur ŞENSOY ŞORMAN
Karin ŞEŞETYAN
Okan ŞİRİN
Ali Ünal ŞORMAN
Gülüm TANIRCAN
Serhan TANYEL
Yüksel TAŞDEMİR
Kerem TAŞTAN
Gökmen TAYFUR
Beytullah TEMEL
Rasim TEMÜR
Egemen TEOMETE
Serdal TERZİ
Berrak TEYMUR
Hüseyin Onur TEZCAN
Mesut TIĞDEMİR
Şahnaz TİĞREK
Salih TİLEYLİOĞLU
Vedat TOĞAN
Onur Behzat TOKDEMİR
İrem Dikmen Toker TOKER
Cengiz TOKLU
Ali TOPAL
İlker Bekir TOPÇU
Cem TOPKAYA
Kamile TOSUN FELEKOĞLU
Gökçe TÖNÜK
Ülgen Mert TUĞSAL
Gürsoy TURAN
Ö. Tuğrul TURAN
Cüneyt TÜZÜN
Eren UÇKAN
Ergin ULUTAŞ
Berna UNUTMAZ
Tayfun UYGUNOĞLU
Volkan Emre UZ
Nihal UZCAN ERATLI
İbrahim Mert UZUN
Deniz ÜLGEN
Mehmet ÜLKER
Mehmet Barış Can ÜLKER
Yurdanur ÜNAL
Cüneyt VATANSEVER
Syed Tanvir WASTI
Ahmet YAKUT
Mehmet Cem YALÇIN
Aslı YALÇIN DAYIOĞLU
Ahmet Cevdet YALÇINER
İsmail Özgür YAMAN
Arcan YANIK
Mert Yücel YARDIMCI
Ufuk YAZGAN
Anıl YAZICI
Halit YAZICI
Seda YEŞİLMEN
Tahsin Alper YIKICI
İrem Zeynep YILDIRIM
Mehmet YILDIRIMOĞLU
Abdülazim YILDIZ
Koray Kamil YILMAZ
Mehmet YILMAZ
Mustafa Tolga YILMAZ
Mustafa Tuğrul YILMAZ
İsmail YÜCEL
Ömer YÜKSEK
Shaban Isamel Albrka Ali ZANGENA
Abdullah Can ZÜLFİKAR

UCTEA Turkish Chamber of Civil Engineers

Teknik Dergi

Volume: 33 Issue: 1 January 2022

CONTENTS

A New Minimum Delay Model for Multi-Lane Traffic Circles 11429
Serhan TANYEL, Süheyla Pelin ÇALIŞKANELLİ, Mustafa ÖZUYSAL

Application of the Dynamic Compaction Method for Ground Improvement of Collapsible Loess in Qinhai 11455
Jun CAI, Jingtao ZHANG, Guangyin DU, Han XIA

Sediment Incipient Motion in Sewer with a Bed Deposit 11473
Wan Hanna Melini WAN MOHTAR, Charles HIN JOO BONG, Aminuddin AB. GHANI, Mir Jafar Sadegh SAFARI, Aizat Mohd TAIB, Haitham Abdulmohsin AFAN, Ahmed EL-SHAFIE

Teaching-Learning Based Optimization of Nonlinear Isolation Systems under Far Fault Earthquakes 11487
Seda ÖNCÜ-DAVAS, Rasim TEMÜR, Cenk ALHAN

The Strain Sensitivity of Coal Reinforced Smart Concrete by Piezoresistive Effect 11507
Özkan Ayberk KOLATAR, Egemen TEOMETE, Serap KAHRAMAN

Analysis of a Prefabricated Vertical Drain (PVD) Soil Improvement Project 11521
Ahmet Can MERT, Akın ÖNALP, Ersin AREL

Lightweight Cement-Based Composites Incorporating Hollow Glass Microspheres: Fresh and Hardened State Properties 11543
Nihat KABAY, Ahmet B. KIZILKANAT, Büşra AKTÜRK, Yusuf KAHRAMAN

Fundamental Frequencies of Elliptical Plates using Static Deflections 11569
Murat ALTEKIN

Estimation of Intensity-Duration-Frequency (IDF) Curves from Large Scale Atmospheric Dataset by Statistical Downscaling 11591
Khaled ALRAMLAWI, Okan FISTIKOĞLU

TECHNICAL NOTE
Large Scale Direct Shear Box Tests on Gravels 11617
Ali Anıl YUNATCI, Kemal Önder ÇETİN

Teknik Dergi, 2022 11429-11454, Paper 641

A New Minimum Delay Model for Multi-Lane Traffic Circles

Serhan TANYEL[1]
Süheyla Pelin ÇALIŞKANELLİ[2]
Mustafa ÖZUYSAL[3]

ABSTRACT

Minimum delay (or service delay) is one of the most important performance measures for intersection analysis. It can be described as the delay to a vehicle, which is waiting at the stop (or yield) line of an unsignalized intersection. In this study, an appropriate minimum delay equation is derived for multi-lane traffic circles in İzmir, Turkey. For this purpose, observations are made at six approaches of five multi-lane traffic circles. Simple and multiple regression analysis, in which circulating flow and geometric parameters are chosen as independent variables, are used to model minimum delay. Results have shown that geometry of a traffic circle has an important effect on minimum delay and should be considered in analysis but the model may fail to define minimum delay values greater than 22 seconds. Analyses have shown that models which depend on entry capacity are more effective in estimation of minimum delay at multi-lane traffic circles.

Keywords: Minimum delay, traffic circles, unsignalized intersections.

1. INTRODUCTION

Traffic circle is one of the most preferred intersection types in Turkey. However, because of poor design implementations and lack of appropriate capacity and performance analysis procedures, traffic signals are frequently deployed at traffic circles especially in urban areas. Therefore, research on capacity and performance of traffic circles has great importance. Several studies have been presented on capacity of traffic circles like Tanyel et al. [1], Özuysal et al. [2], Çalışkanelli et al. [3], Tanyel and Yayla [4, 5] and Ersoy and

Note:
- This paper was received on April 25, 2019 and accepted for publication by the Editorial Board on August 14, 2020.
- Discussions on this paper will be accepted by March 31, 2022.
- https://doi.org/10.18400/tekderg.557823

1 Dokuz Eylül University, Department of Civil Engineering, İzmir, Turkey - serhan.tanyel@deu.edu.tr https://orcid.org/0000-0001-8549-9442

2 Dokuz Eylül University, Department of Civil Engineering, İzmir, Turkey - pelin.caliskanelli@deu.edu.tr https://orcid.org/0000-0002-0530-3276

3 Dokuz Eylül University, Department of Civil Engineering, İzmir, Turkey - mustafa.ozuysal@deu.edu.tr https://orcid.org/0000-0002-3276-3075

Çelikoğlu [6]. However only a limited number of studies like Tanyel et al. [7] have been conducted on performance of traffic circles.

Delay can be used in designing, operating and comparing the performance of intersections under different control and flow conditions, as it directly reflects side effects of traffic flow like fuel consumption increase, driver dissatisfaction and increased travel time [8]. Akçelik [9] has defined delay as "the difference between interrupted and uninterrupted travel times through the intersection". A general form of the equation for average delay per vehicle (D_{av}) can be expressed as [10]:

$$D_{av} = D_{\min} \cdot \left(1 + \frac{\gamma + \varepsilon \cdot \rho}{1 - \rho}\right) \tag{1}$$

where γ and ε are constants, ρ is the degree of saturation and D_{min} *is* minimum delay (seconds). Troutbeck [11, 12] has defined γ and ε constants according to Cowan's [13] studies. The value of γ depends on the arrival characteristics of minor stream flow: if minor stream vehicles arrive at random, then γ is set to "0"; if the minor stream vehicles arrive in platoons, then γ should be greater than "0". For random stream arrivals, ε can also be calculated by using the following equation:

$$\varepsilon = \frac{e^{q_c T_0} - q_c T_o - 1 + q_c\left(e^{q_c T_0} - 1\right) D_{\min}}{q_c\left(e^{q_c T_0} - 1\right) D_{\min}} \tag{2}$$

where q_c is the major stream flow (veh/sec), T_o is the follow-up time (seconds) and ε is approximately equal to "1.0" [10, 12].

Minimum delay (or service delay) is an important component of average delay. It is the delay a driver will experience while waiting at the entry of minor approach of an unsignalized intersection or roundabout. Minimum delay can also be described as the delay a driver in the minor stream will experience when minor stream demand is nearly zero. Minimum delay starts when a minor stream vehicle reaches to the stop or yield line of an approach, includes the waiting time of the driver for an acceptable headway or gap in the major stream (critical gap) and ends when the vehicle enters and joins the major flow. In other words, minimum delay is the sum of waiting time of a vehicle at the entry of the intersection and follow-up time between entering vehicles in the minor approach [14]. The term minimum delay was first introduced by Adams in 1936 for pedestrians and since then minimum delay is named as Adams delay [15].

In the literature, like capacity of unsignalized intersections and traffic circles, two different methods (or approaches) are widely used for modeling minimum delay [14, 16, 17, 18, 19].

1. theoretical (or behavioural) models which mainly depend on critical gap acceptance method,
2. empirical models which mostly depend on field data and regression analysis.

The first example of theoretical models is Adams' delay function [20]. He stated that traffic flow can be defined statistically as a Poisson process. According to this assumption, if the flow rate is q_c (veh/sec), then headways between vehicles are exponentially distributed with mean $1/q_c$. By using these assumptions, Adams [20] suggested the following equation for average delay for pedestrians:

$$E(D) = \frac{e^{-q_c T} - 1}{q_c} - T \tag{3}$$

where T is the accepted gap in seconds between vehicles by a pedestrian waiting on the sidewalk or at the roadside (if the minimum acceptable major-stream headway "T" is assumed to be equal for all pedestrians or vehicles waiting at the entry of a minor approach, then it is called as critical gap). However, previous studies have shown that, while the upper tail of observed headways can be defined by a negative exponential distribution, the lower tail of the headways are influenced by a safety headway (or following distance), which can be defined as the minimum headway between vehicles in the major flow (Δ) [21, 22, 23, 24]. Thus in another early study on traffic engineering, Tanner [21] assumed that the vehicles in the major stream follow each other with headways, which can be modeled with shifted negative exponential distribution and suggested the following equation for estimating minimum delay at unsignalized intersections:

$$D_{\min} = \frac{e^{q_c \cdot (T-\Delta)}}{q_c \cdot (1 - \Delta \cdot q_c)} - T - \frac{1 - \Delta \cdot q_c + \Delta^2 \cdot q_c^2}{q_c \cdot (1 - \Delta \cdot q_c)} + \frac{\frac{1}{2} \cdot \Delta^2 \cdot q_c}{(1 - \Delta \cdot q_c)^2} \tag{4}$$

where Δ is the minimum headway between major-stream vehicles (seconds) and T is the critical gap (seconds). Tanner [21] derived Equation 4 for the condition that there is only one lane in the major road. For two-lane major stream, he stated that minimum headway between vehicles can be assumed as zero and headways between vehicles can be modeled by using negative exponential distribution.

Drew [25] used Erlang distribution for modeling headways in major flow and he developed an equation for modeling service delay of entering vehicles from minor approach:

$$D_{\min} = \frac{e^{k \cdot q_c \cdot T} - \sum_{i=0}^{k} \frac{(k \cdot q_c \cdot T)^i}{i!}}{q_c \cdot \sum_{i=0}^{k} \frac{(k \cdot q_c \cdot T)^i}{i!}} \tag{5}$$

Here "k" is the Erlang number. If "k=1" then the equation transforms into the following form, which was suggested by Ashworth [26]:

$$D_{\min} = \frac{\left(e^{q_c \cdot T} - 1 - q_c \cdot T\right)}{q_c} \tag{6}$$

Studies have shown that minimum delay (D_{min}) highly depends on the platooning characteristics of major flow [10]. For this reason, mixed distributions like Hyperexpoential, Hyperlang, Cowan M3 (or M/D/1 model) or Cowan M4 (or M/G/1 model) are started to be used in modeling headways in the major flow, and thus delay models started to be developed by using these distributions. One of the most known model is suggested by Troutbeck [11, 27]. He used Cowan M3 distribution instead of shifted negative exponential distribution and suggested the following function which is also used for estimating the performance of roundabouts in Sweden [28]:

$$D_{\min} = \frac{e^{\lambda \cdot (T-\Delta)}}{\alpha \cdot q_c} - T - \frac{1}{\lambda} + \frac{\lambda \cdot \Delta^2 - 2 \cdot \Delta + 2 \cdot \Delta \cdot \alpha}{2 \cdot (\lambda \cdot \Delta + \alpha)} \tag{7}$$

where α is the proportion of free vehicles and λ is a decay constant which can be found by using the following formula:

$$\lambda = \frac{\alpha q_c}{1 - \Delta q_c} \tag{8}$$

For two major streams, Equation 5 is rewritten as:

$$\mathrm{D}_{\min} = \frac{e^{-\Lambda(T-\Delta)}}{(q_1 + q_2)A} - T - \frac{1}{\Lambda} + \frac{\Lambda\Delta^2 + 2\Lambda\Delta + 2\beta\Delta^2 - 4/3\Lambda\Delta^3\beta}{2\Lambda\Delta + 2A - 2\Lambda\beta\Delta^2} \tag{9}$$

where

$$\beta = \frac{q_1 q_2}{q_1 + q_2} \tag{10}$$

$$A = \frac{\alpha_1 q_1 (1 - \Delta q_2) + \alpha_2 q_2 (1 - \Delta q_1)}{q_1 + q_2} \tag{11}$$

$$\Lambda = \lambda_1 + \lambda_2 \tag{12}$$

In the equations, q_1 and q_2 are the traffic flows on lanes 1 and 2, α_1 and α_2 are the proportion of free vehicles on major streams 1 and 2, and λ_1 and λ_2 are the decay constants.

Flannery et al. [29] have developed a general formula for expected value of minimum delay:

$$E(D_{\min}) = \frac{1}{\bar{t}}\left(\frac{1}{2}T^2 - \int_0^T tF(t)dt + (1-F(T))^{-1}\left(T - \int_0^T F(t)dt \int_0^T tdF(t)\right)\right) \quad (13)$$

In Equation 13, *F(T)* is the probability distribution of accepted gaps, *t* is headway between vehicles in the major stream (seconds), $\bar{t}$ is the mean headway (seconds) and *F(t)* is the probability distribution of a general distribution used for modeling headways. If the general distribution is assumed as negative exponential distribution then Equation 13 may reduce to Adams' delay model given in Equation 3.

Besides the models presented above, some empirical minimum delay models have been developed especially for stop controlled intersections. One of the first empirical models is suggested by Kyte et al. [18]:

$$D_{\min} = 17.28Q_c \quad (14)$$

where Q_c is the conflicting flow in front of the minor stream flow (veh/h). This function is valid for conflicting traffic volumes that range between 0.051~0.31 veh/sec.

Al-Omari and Benekhoal [19] suggested different equations of minimum delay calculation for different maneuver types from a minor approach as follows:

$$D_{\min R} = 3.28 + 0.00886Q_R \quad (15)$$

$$D_{\min TH} = 3.59 + 0.00730Q_{TH} \quad (16)$$

$$D_{\min L} = 3.25 + 0.01070Q_L \quad (17)$$

where D_{mini} is the delay for the *i*th maneuver (seconds); Q_i is the conflicting flow in front of the minor stream approach *i*th maneuver (veh/hr) and R, L and TH indices denote right turning, left turning and through passing maneuvers, respectively.

While Kyte et al. [18] and Al-Omari and Benekhoal [19] have suggested linear functions, Chandra et al. [30] have used an exponential function for estimating minimum delay:

$$D_{\min} = 2.1955e^{2.0868Q_c} \quad (18)$$

A similar approach for single lane traffic circles has also been tested by Tanyel et al. [7], where they also showed that a power function can be an adequate alternative for minimum delay estimation. Çelik [31] also suggested an exponential equation, which is derived by using the outputs of a simulation program he developed:

$$D_{\min} = (Tq_c)^2 e^{1+0.23\Delta^2} \quad (19)$$

Ashalata and Chandra [32], by using simulation technique, tried to model minimum delay at unsignalized intersections for different priority movements under varying composition of conflicting traffic. Their results showed that delay, as experienced by a priority movement vehicles, increases with the increase of heterogeneity of conflicting flow.

Several studies have shown that minimum delay and critical gap values are highly affected from each other [33]. It is also known that critical gap acceptance value depends on the conflicting flow (circulating flow at traffic circles) and the geometric properties of the traffic circle. From this point of view, it can be said that minimum delay also highly depends on the geometric properties of an intersection. Thus Tanyel et al. [7] have developed the following empirical function, which defines the effect of geometric parameters on minimum delay at single-lane traffic circles:

$$D_{\min} = -0.042D_i - 0.118w_{ent} + 26.72q_c + 0.009\phi \tag{20}$$

where D_i is the inscribed diameter of traffic circle (m), w_{ent} is the entry lane width of the minor approach (m) and ϕ is the conflict angle.

From the above equation, it is clear that minimum delay (D_{min}) mainly depends on the platooning characteristics in the major stream [10], critical gap and follow-up times of vehicles in the minor stream and geometric characteristics of an intersection [7]. However, the number of entering vehicles from minor approach may also be an important parameter in estimating minimum delay as it depends on the same parameters. In Highway Capacity Manual, it is assumed that minimum delay decreases as the number of entering vehicles from minor approach increases [34, 35]:

$$D_{\min} = \frac{1}{q_e} \tag{21}$$

where q_e is the capacity (entry flow) of minor approach in veh/sec. Adapting a similar approach, Akçelik [9] has suggested the following equation by using signal analogy concept:

$$D_{\min} = \left((1 - T_0 \cdot q_e\right) \cdot \left(\frac{e^{\lambda \cdot (T-\Delta)}}{\alpha \cdot q_c} - \frac{1}{\lambda} - 0.5 \cdot T_0 \right) \tag{22}$$

where T_0 is follow-up time for minor-stream drivers (seconds). Tanyel et al. [7] have also investigated the effect of entering vehicles on minimum delay. They used the function suggested by Horton [36] for infiltration capacity, which can be written in general form for minimum delay as:

$$D_{\min} = D_{\min low} + \left(D_{\min up} - D_{\min low}\right) e^{-Kq_e} \tag{23}$$

where D_{minup} is the upper limit of minimum delay (sec), D_{minlow} is the lower limit of minimum delay (sec) and K is a constant. For single-lane traffic circles, they found the function below:

$$D_{\min} = 0.100 + (83.86 - 0.100)e^{-16.87 q_e} \quad (24)$$

Consequently, it is clear that the studies on minimum delay at unsignalized intersections in Turkey are very limited and there are no studies on minimum delays at multi-lane traffic circles. However, an adequate minimum delay function has a great importance in estimating average delay of an approach.

As mentioned before, both theoretical and empirical approaches can be used for developing a minimum delay function. Several studies proved that theoretical and empirical models, if they are built correctly, give close results with each other [5, 37]. Although theoretical models provide more detailed information about drivers' behavior, which is an important issue in traffic engineering, they have relatively complex structure. On the other hand, empirical models may provide simple and applicable solutions.

In this study, it is aimed to develop a simple model for minimum delays at traffic circles that can be used in practice; hence, several empirical functions are proposed based on different geometric parameters (inscribed diameter, entry lane width, etc.) and/or operational parameters (circulating flow, entry capacity etc.), which can be easily collected from field by practitioners.

The paper is organized as follows: i) First, study areas and data collection procedure are presented. ii) Then, the different approaches that are used to define an adequate empirical minimum delay and drivers' behavior in Turkey are described. iii) Obtained empirical models are compared with existing models, which were suggested by different researchers. iv) A discussion on the effect of geometric design parameters and critical gap acceptance on minimum delay is presented.

2. DATA COLLECTION PROCEDURE

In this study, the data was collected from five multi-lane traffic circles in İzmir, Turkey. Three of the traffic circles are located in Alsancak (Montrö, Lozan and Alsancak Gar), one is located in Bornova (Meydan) and one is located in Buca (Üçkuyular). Some geometric properties of traffic circles are given in Table 1. Observations were made at peak hours by using a video camera, which is located at a higher building near intersection during weekdays under dry and clear weather conditions. From video recordings data such as entry flow rate per approach (veh/hr), circulating flow rate per approach (veh/hr), headways in the circulating stream (sec), accepted and rejected gaps/lags in the circulating streams, follow-up times of entering vehicles (sec) and minimum delay values (sec) are derived.

In the literature, it is generally accepted to collect and use 15 min data sets for analysis [19, 29]. However, this approach may lead to use a limited number of data. To overcome this problem, the data extraction method is preferred instead [7, 18, 30]. This method can be briefly explained as follows:

Table 1 - Geometric parameters of observed traffic circles

	Intersection Parameter	Abbreviation		Alsancak Gar	Buca Üçkuyular	Montrö	Lozan	Bornova
Geometric Parameters	Inscribed diameter	(D_i) (m)		55.00	30.00	65.00	67.00	46.00
	Number of entry lanes	(n_{ent})		2	2	2	2	2
	Entry lane width	(w_{ent}) (m)		3.00	3.80	3.00	3.00	3.50
	Number of exit lanes	(n_{exit})		2	2	-	2	-
	Exit lane width	(w_{exit}) (m)		3.00	3.00	-	3.00	-
	Width of splitter island	(w_{island}) (m)		10.00	10.00	-	9.00	-
	Number of circulating lanes	(n_c)		3	2	3	3	2
	Width of circulating area	(w_c) (m)		15.00	8.00	20.00	20.00	10.00
	Conflict angle	(ϕ) (^{o})		45	45	46	54	61
Observations	Number of observations			78	24	128	165	86
	Circulating flow	(Q_c) (veh/h)		1513	680	1456	558	1028
	Minimum delay	(D_{min}) (sec)	*mean:*	16.52	2.58	10.02	2.01	5.19
			st. dev.:	9.27	1.23	6.51	1.41	1.91
	Critical gap	(T) (sec)	*mean:*	3.16	4.05	3.05	4.00	3.31
			st. dev.:	0.30	0.15	0.35	0.38	0.32

The microscopic analysis requires the definition of the conflicting traffic flow as seen by each subject approaching vehicle. If t_0 is defined as the time of arrival of the subject approaching vehicle at the reference line, t_d is defined as the time of departure of the subject approaching vehicle, n is the number of observed conflicting vehicles for the subject vehicle and t_n is the time of arrival of the nth conflicting vehicle at the reference point [30]. Then conflicting flow rate can be found by using the following equation:

$$\text{Conflict flow rate} = \frac{n}{t_n - t_0} \tag{25}$$

In the equation, the conflicting flow rate, which is experienced by a driver waiting at the entrance of the subject approach, is defined as the number of observed conflicting vehicles divided by the observation time [30]. The service delay then can be computed by using Eq. 26:

$$\text{Minimum delay} = t_d - t_0 \tag{26}$$

Chandra et al. [30] stated that the major advantage of using disaggregate data in microscopic analysis is that, information is not lost by aggregation, and the number of data points are highly increased. Besides, it gives instantaneous conflicting flow rate as observed by a driver waiting for a suitable gap.

All the data, which include heavy vehicles in the major and/or minor flow are excluded due to the limited number of data, and observations which include only passenger cars are used in the analysis. As a result, 481 observed data in total (79 from Alsancak Gar, 24 from Buca Üçkuyular, 86 from Bornova, 128 from Montrö and 165 from Lozan) have been obtained and used in this study.

3. PARAMETERS AFFECTING MINIMUM DELAY

Previous studies have shown that there is a high relation between critical gap and average delay [11, 12, 21]. A similar relation may be expected between critical gap and minimum delay also. In the simplest term, critical gap can be defined as the minimum gap that all drivers in the minor stream are assumed to accept at all similar locations [10]. In Figure 1, relation between observed accepted gaps, circulating flow and minimum delay is shown. It is clear in Figure 1 that, as the accepted gap values increase, minimum delay values decrease. However, a completely opposite trend might have been expected, since vehicles would enter the main flow more easily when they accept smaller gaps. Although this assumption is true in most cases, the results presented in Figure 1 are quite valid, since they reflect drivers' behavior at unsignalized intersections. Studies have shown that under low circulating flow conditions, drivers in the minor stream tend to accept longer gaps, since they may provide safer entering opportunities. However, if they have to wait longer, they may get impatient and accept lower gap values and may also force the main stream to slow down or completely stop. These situations are named as gap forcing or limited priority merge conditions [5].

As mentioned before, critical gap acceptance values depend not only on circulating flow but also on geometric parameters. Collection of critical gap acceptance data from the field may be difficult but geometric parameters of a traffic circle can be measured easily. In Figure 2, geometric parameters of a multi-lane traffic circle are shown. In the figure, D_i is inscribed diameter (m), w_{ent} is entry lane width (m); w_{exit} is exit lane width (m), w_{island} is width of the splitter island (m), w_c is circulating lane width (m) and ϕ is conflict angle (°).

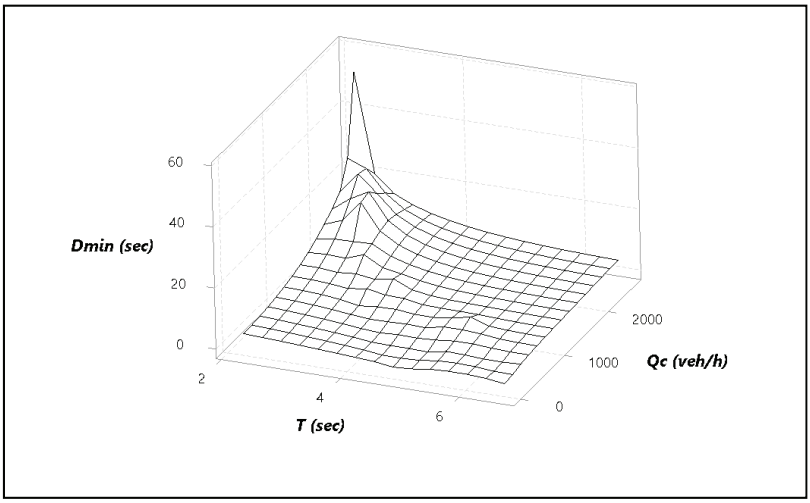

Figure 1 - Relation between accepted gaps and minimum delay values

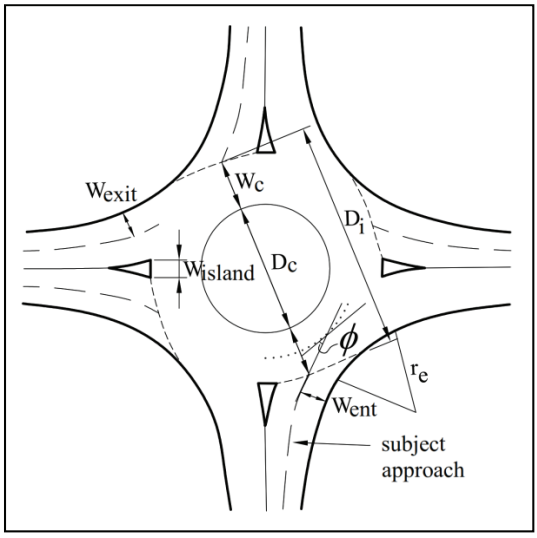

Figure 2 - Geometric parameters of a traffic circle

Tanyel et al. [7] stated that there may be the following expectations for the effect of geometric parameters on minimum delay:

- When inscribed diameter is increased, minimum delay may be decreased.
- When entry width is increased, minimum delay may be decreased.
- When exit lane width is increased, minimum delay is decreased.
- When entry angle is increased, minimum delay is also increased.

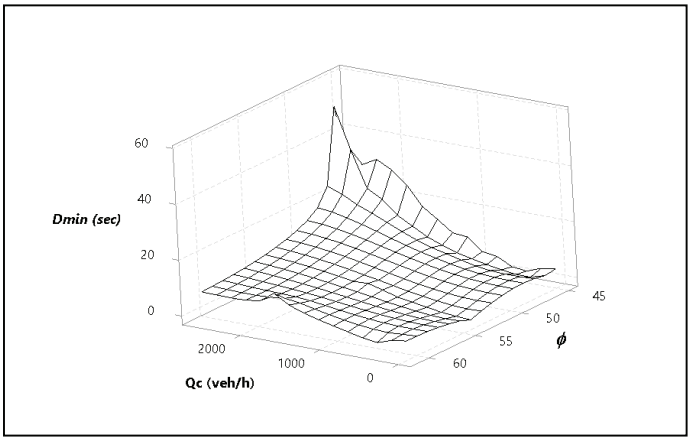

Figure 3 - Effect of entry angle on minimum delay

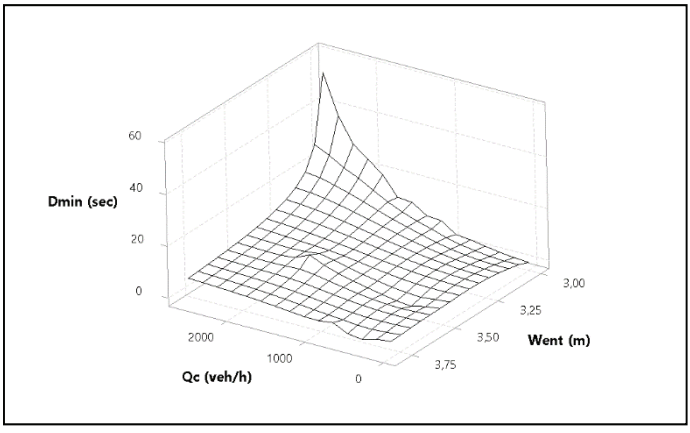

Figure 4 - Effect of entry width on minimum delay

For single-lane traffic circles Tanyel et al. [7] found that as inscribed diameter increases, minimum delay also increases which was just the opposite of the first expectation listed above. In Figures 3~5, the relationship between some of the geometric parameters and minimum delay with respect to circulating flow (Q_c, in veh/h) are shown. From the figures, the following inferences can be made:

- unlike the expectation defined above, as the entry angle increases, minimum delay decreases.
- as the entry width increases, minimum delay decreases.
- for low or moderate circulating flow values, as the inscribed diameter increases minimum delay decreases. However, when circulating flow exceeds 100 veh/h and reaches up to 2000 veh/h, minimum delay increases with increasing inscribed diameter value. This is probably due to the result in drivers' improper lane use in the circulating stream, as the inscribed diameter increases, circulating width also increases (Figure 6). This may increase the difficulty of minor stream drivers entering the intersection.

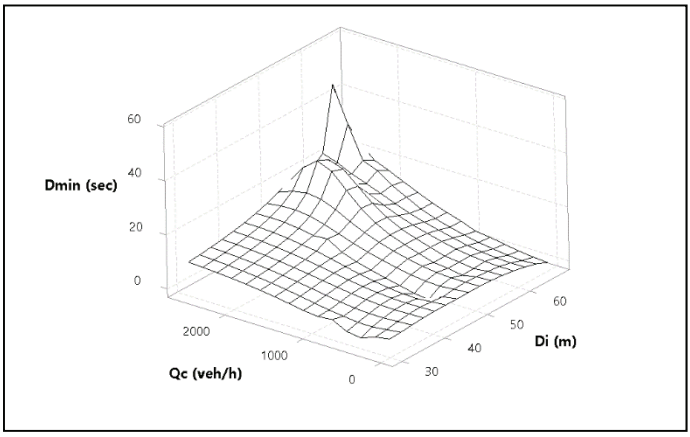

Figure 5 - Effect of inscribed diameter on minimum delay

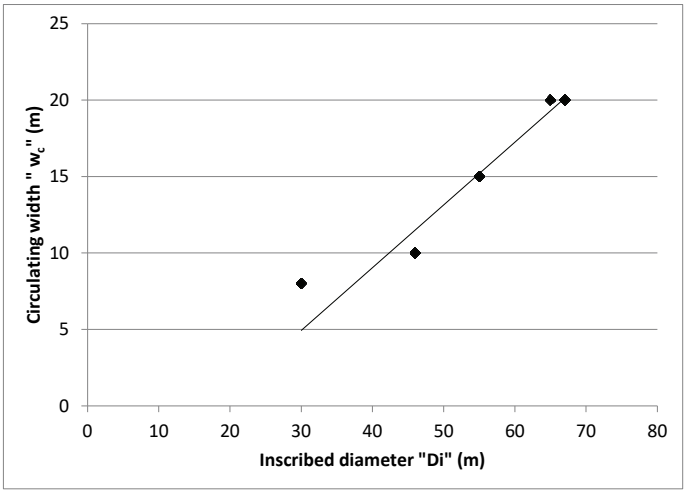

Figure 6 - Relation between inscribed diameter and circulating width

4. MODEL DEVELOPMENT

In the study, models for minimum delay are developed according to three different approaches:

1. models based on circulating (conflicting) flow,
2. models based on geometric parameters and circulating flow,
3. models based on entry flow (or capacity).

4.1. Models Based on Circulating Flow

As explained in the introduction section, most of the empirical models are developed by investigating the relationship between minimum delay (D_{min}) and circulating flow (q_c). By preferring a similar approach, exponential and power functions are applied. The results are shown in Figure 7 and Equations 27and 28.

It is clear from Figure 7 that power function gives better results than exponential function but both functions fail when circulating flow exceeds 0.6 veh/sec.

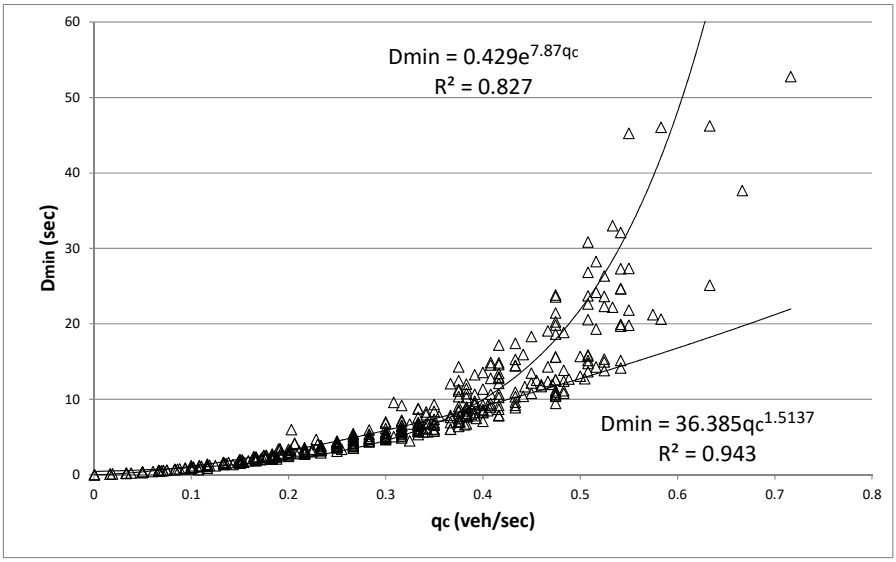

Figure 7 - Regression models developed between minimum delay and circulating flow

$$D_{\min} = 0.429e^{7.87q_c} \tag{27}$$

$$D_{\min} = 36.385q_c^{1.5137} \tag{28}$$

4.2. Models Based on Geometric Parameters and Circulating Flow

As a second step, the effect of geometric parameters on minimum delay is tried to be modeled by using multiple regression analysis. For this purpose, inscribed diameter (D_i), entry lane width (w_{ent}), exit lane width (w_{exit}), width of the splitter island (w_{island}), circulating lane width (w_c) and conflict angle (ϕ) are chosen as independent variables along with circulating flow (q_c, veh/sec).

Previous studies have shown that there can be a significant relationship between geometric parameters. To identify the relation between independent variables, Pearson Correlation values are calculated (Table 2). The Pearson coefficient values greater than 0.5 indicate the multicollinearity between independent variables. Bold values in the table show that, there are significant correlations between the pairs D_i -w_{ent}, D_i-w_c, w_c-w_{entry} and w_{exit}-w_{island}. In the analysis, these parameters are tested separately.

Table 2 - Pearson Correlation Values between geometric parameters

	D_i	w_{ent}	w_{exit}	w_{island}	w_c
w_{ent}	**-0.915**				
w_{exit}	0.135	-0.262			
w_{island}	0.086	-0.240	**0.997**		
w_c	**0.973**	**-0.902**	0.169	0.126	
ϕ	*-0.170*	*0.432*	*-0.123*	*-0.165*	*-0.339*

Table 3 -Multiple Regression Model 1

	β	***Sdt.Error***	***t Stat***	***P-value***
D_i	-0.053	0.013	-4.15	0.000
w_{island}	0.398	0.034	11.51	0.000
ϕ	-0.099	0.014	-7.36	0.000
q_c	46.031	1.054	43.67	0.000

R^2= 0.892; SS=44722.88; MS=11180.72; F-value=987.79; F-prob= 6.64x10-229

Table 4 - Multiple Regression Model 2

	β	***Sdt.Error***	***t Stat***	***P-value***
w_{ent}	-2.731	0.136	-20.010	0.000
w_{island}	0.388	0.034	11.535	0.000
q_c	47.368	1.093	43.344	0.000

R^2= 0.892; SS=44691.26; MS=14897.09; F-value=1311.20; F-prob= 6.80x10-230

Three empirical models, which show the effect of geometry on minimum delay are obtained by using multiple regression analysis. The results of analysis are given in Tables 3, 4, 5 and models are given in Equations 29, 30 and 31 respectively. From the tables, it is clear that R-square values of all three models are very close to each other.

Table 5 - Multiple Regression Model 3

	β	Sdt.Error	t Stat	P-value
w_{exit}	1.113	0.106	10.470	0.000
ϕ	-0.149	0.008	-19.214	0.000
q_c	44.920	1.011	44.425	0.000

R^2= 0.888; SS=44506.39; MS=14835.46; F-value=1262.79; F-prob= 2.00x10-226

Model 1 $$D_{\min} = -0.053D_i + 0.398w_{island} - 0.099\phi + 46.031q_c \quad (29)$$

Model 2 $$D_{\min} = -2.731w_{ent} + 0.388w_{island} + 47.368q_c \quad (30)$$

Model 3 $$D_{\min} = 1.113w_{exit} - 0.149\phi + 44.920q_c \quad (31)$$

4.3. Models Based on Entry Flow

Minimum delay is highly affected by the decision of drivers in the minor stream. Critical gap (T) and follow-up time (T_0) values are two parameters which can be used to define driver characteristics at an unsignalized intersection. Accordingly, a strong relationship between minimum delay and entry flow can be expected.

When D_{min} values are plotted with respect to q_e values, an exponential form is observed for multi-lane traffic circles (Figure 4). When a regression analysis is performed, an exponential function gives acceptable results as shown in Figure 8 and Equation 32:

$$D_{\min} = 71.71e^{-14.7q_e} \quad (32)$$

As stated before, Tanyel et al. [7] used the function suggested by Horton [36] for infiltration capacity for modeling minimum delay. A similar approach is also followed in this study. The parameters of Horton function are found by using the “solver” feature of Excel software. The solver feature uses a nonlinear optimization code called “Generalized Reduced Gradient” which was developed by Waren and Lasdon [38, 39]. The code

minimizes the sum of square errors between the observed and estimated pairs with a nonlinear manner. As a result, the following function is obtained:

$$D_{\min} = 1.21 + (78.44 - 1.21)e^{-17.25 q_e} \quad (33)$$

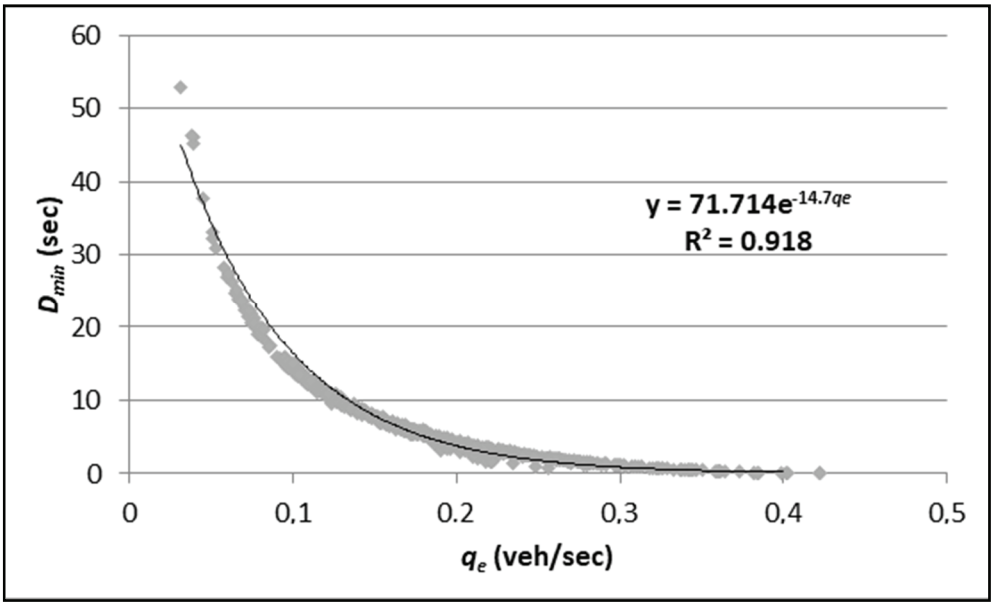

Figure 8 - Observed minimum delay values and proposed exponential function line

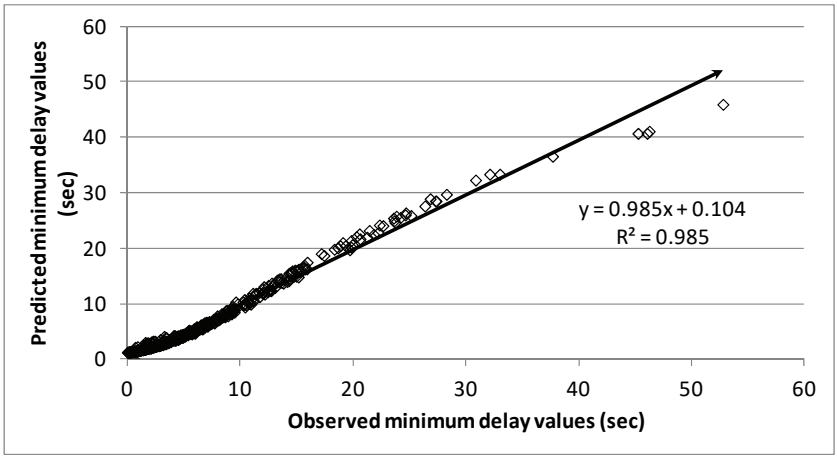

Figure 9 - Comparison of observed and estimated minimum delay values

Estimation of the equation and observed minimum delay values are compared in Figure 9. It is clear from the figure that Horton function approach gives adequate results in estimation of minimum delay at multi-lane traffic circles.

4.4. Comparison of Empirical Models

In previous three sections, different empirical models are developed with different assumptions. By considering the R^2 values, it can be said that the best results are obtained from Equations 17??? and 21???. Thus all models give acceptable R^2 values.

However, in defining the accuracy of a model, making decisions based on only R^2 values is not reliable. To define and compare the accuracy of these models, root mean square error (RMSE) and efficiency factor (EF) values are used.

Efficiency factor (EF), which is commonly known as Nash–Sutcliffe Model Efficiency Coefficient (NSE) [40] accounts for model errors in estimating the mean of the observed data set ranging from minus infinity to 1.0. "EF = 1" corresponds to a perfect match of modeled values to the observed data. "EF = 0" indicates that the model estimations are as accurate as the mean of the observed data and an efficiency less than zero ($-\infty<EF<0$) shows worse estimation than the mean. The general equation for the model is given below:

$$EF = 1 - \left(\frac{\sum_{i=1}^{N} \left(D_{\min obs\,i} - D_{\min est\,i} \right)^2}{\sum_{i=1}^{N} \left(D_{\min obs\,i} - \overline{D}_{\min} \right)^2} \right) \tag{34}$$

Where $D_{minobs\ i}$ indicates observed minimum delay value (sec), $D_{minest\ i}$ is the estimated minimum delay value (sec), "i" is the observation number and $\overline{D}_{min}$ is the mean of observed minimum delay values (sec).

RMSE is a frequently used measure of the differences between the estimated values and the actual (observed) values and serves to aggregate the residuals into a single measure of predictive power [41]:

$$RMSE = \sqrt{\frac{\sum_{i=1}^{N} \left(D_{\min obs\,i} - D_{\min est\,i} \right)^2}{N}} \tag{35}$$

The results of RMSE and EF are given in Table 6. It is clear that Horton function gives the best result when compared with other models. Models which depend on circulating flow give the worst results. This indicates that, models depending only circulating flow may mislead the practitioners. Circulating flow values should be validated with other parameters which have influence on minimum delay.

When circulating flow and geometric parameters are considered together, better results are obtained. Although all three models have close R^2, RMSE and EF values, their accuracy is

not sufficient. An important point is that the models developed are obtained only by using data from five intersections. In Figure 10, $(D_{minobs}-D_{minest})^2$ values are plotted with D_{minobs} values. From the figure, it can be seen that all three models give acceptable results, where D_{min} values are below 22 seconds, but fail after this threshold.

Table 6 - Results of RMSE and EF analysis

Models		**R^2**	**RMSE**	**EF**
Models depend on circulating flow	Eq(27)	0.827	5.239	0.490
	Eq(28)	0.943	4.186	0.675
Models depend on geometric parameters	Eq(29)	0.892	3.170	0.813
	Eq(30)	0.892	3.218	0.808
	Eq(31)	0.888	3.282	0.800
Models depend on entry flow	Eq(32)	0.918	1.222	0.972
	Eq(33)	0.985	0.890	0.985

As stated before, best results are obtained when minimum delay is modeled by using entry flow. However, accuracy of Horton function drops for D_{min} values greater than 38 seconds. In fact, there are only 4 observed minimum delay values greater than 38 seconds. Because of insufficient number of data, Horton function fails to define D_{min} values greater than 38 seconds, but it gives better results than other empirical functions.

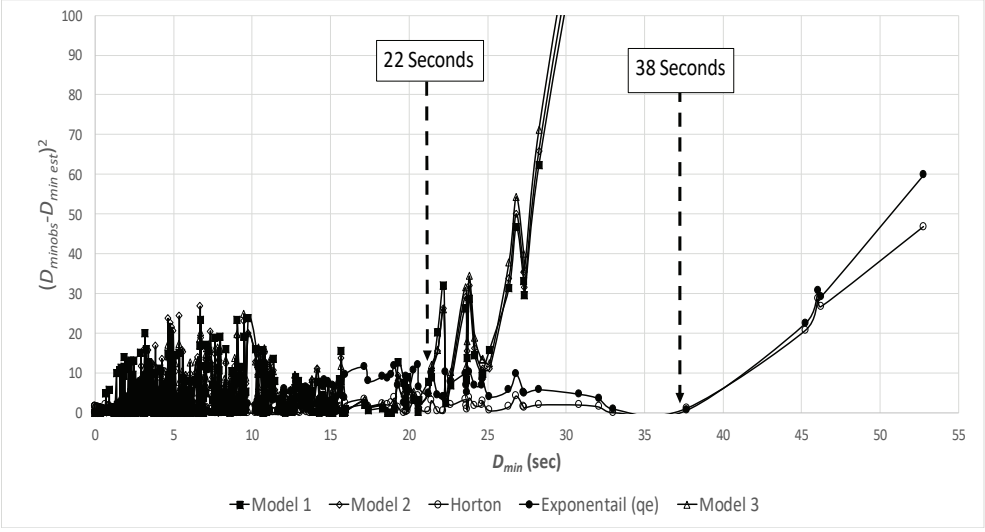

Figure 10 - Discrepancy of observed-estimated D_{min} pairs

5. DISCUSSION

5.1. Applicability of Other Models in the Literature

By this part of the study, only derivations of empirical models are presented. However, theoretical models may give more information about drivers' behavior and interaction between different traffic flows (like circulating and entering traffic flows). Consequently, determining the ability of the theoretical models to represent observation data may also provide a better opinion about the applicability of empirical relations. For this purpose, by using the observed data, minimum headways of minor stream vehicles are calculated by means of Tanner, Troutbeck, Akçelik and Highway Capacity Manual (HCM) models.

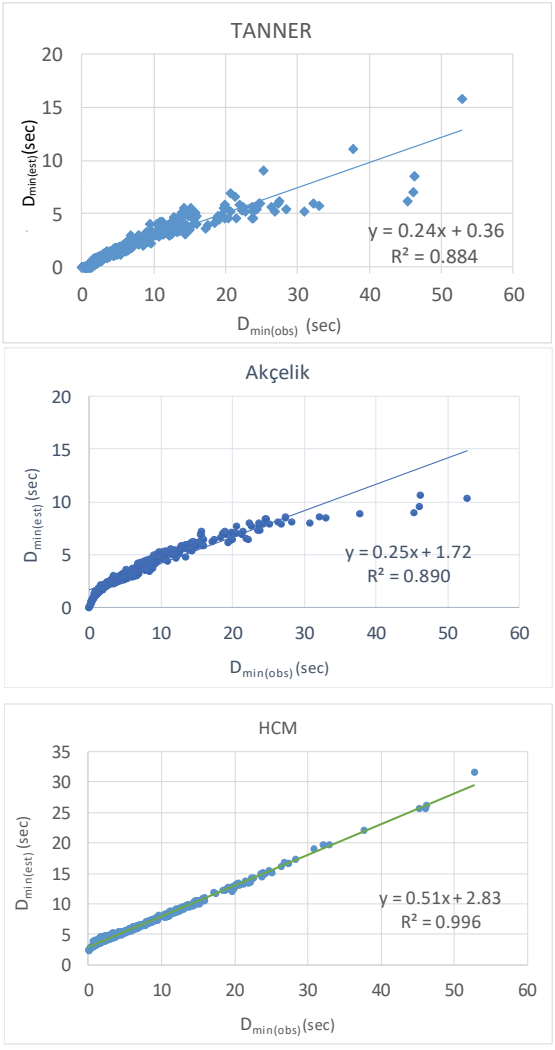

Figure 11 - Observed and estimated minimum delay values

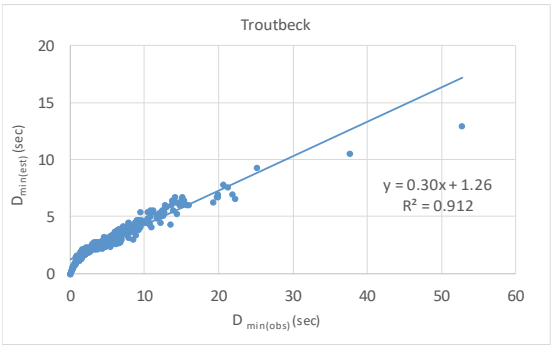

Figure 11 - Observed and estimated minimum delay values (continued)

Observed minimum delay values are compared with estimated values and their correlation are shown in Figure 11. From the figures, the following inferences can be made:

1. For a model to be acceptable, the observed and estimated values are expected to be close to each other. If a linear relationship is sought between these two data groups, the intercept of the linear function is expected to be significantly close to zero, and the slope of the line should converge significantly to one. With respect to this, it is clear from the figures that all the models fail to define the observed minimum delay values.
2. HCM model give the best results (R^2 value is very close to 1) but it cannot estimate D_{min} values smaller than 2.83 seconds.
3. The second-best result is obtained from Troutbeck model but it doesn't show any significant difference from Akçelik and Tanner models.
4. These results lead to the conclusion that, it becomes necessary to conduct a detailed and comprehensive study for the calibration of theoretical models.

5.2. Applicability of the Suggested Model to Other Multi-lane Traffic Circles

A model, whether analytical or empirical, should also be used to determine the performance of different intersections. This can be tested by using data obtained from different intersections other than the ones used for model development. For this purpose, observations from two multi-lane traffic circles in Buca, İzmir are used. Both intersections are located on Yavuz Sultan Selim Street. Yavuz Sultan Selim 1 intersection is a traffic circle with four approaches and located at the intersection point of Yavuz Sultan Selim and Özbekistan Streets. Yavuz Sultan Selim 2 intersection is at the intersection point of Yavuz Sultan Selim and Dede Korkut Streets. Observations are made at only one approach of each intersection by using the methods defined in Section 2 of this paper. Some properties of the test circles of traffic are given in Table 7.

Table 7 - Properties of test traffic circles

	Intersection Parameter	Abbreviation		Yavuz Sultan Selim 1	Yavuz Sultan Selim 2
Geometric Parameters	Inscribed diameter	(D_i) (m)		37.00	31.50
	Number of entry lanes	(n_{ent})		2	2
	Entry lane width	(w_{ent}) (m)		4.15	3.00
	Number of exit lanes	(n_{exit})		2	1
	Exit lane width	(w_{exit}) (m)		4.50	3.25
	Width of splitter island	(w_{island}) (m)		12.50	8.00
	Number of circulating lanes	(n_c)		2	2
	Width of circulating area	(w_c) (m)		9.78	8.75
	Conflict angle	(ϕ) (°)		41	58
Observations	Number of observations			37	45
	Circulating flow	(Q_c) (veh/h)		744	828
	Minimum delay	(D_{min}) (sec)	*mean:*	3.07	4.66
			st. dev.:	1.31	2.06
	Critical gap	(T) (sec)	*mean:*	3.49	4.43
			st. dev.:	0.28	0.35

82 minimum delay values in total (37 from Yavuz Sultan Selim 1, 45 from Yavuz Sultan Selim 2) are obtained from the test intersections. Observed delay values are compared with the values estimated by using Horton's function and the results are shown in Figure 12. Analysis showed that Horton function can be applied to multi-lane traffic circles with different geometries and different traffic characteristics.

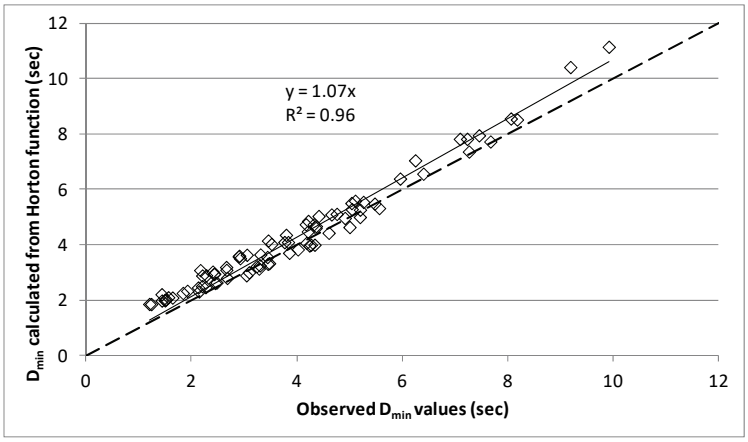

Figure 12 - Comparison of observed and estimated D_{min} values for test traffic circles

5.3. Comparison of Minimum Delay Models for Single- and Multi-lane Traffic Circles

In this study, although the effect of geometric parameters of multi-lane traffic circles on minimum delay values is evaluated, perhaps one of the most important geometric parameters hasn't been discussed: number of circulating lanes.

Analysis up to this point has shown that Horton function can be an important tool in modeling of minimum delays at traffic circles, which is initially suggested by Tanyel et al. [7]. In Figure 13, estimated minimum delay values of single and multi-lane traffic circles for different entry flow values are presented. Both models give very close results, especially for entry flows between 400 and 600 veh/h. Differences between two models can be seen for high or low entry flow values. Thus, RMSE and EF values for single lane model are calculated as 1.24 and 0.972, respectively.

This similarity is a result of the nature of the data. In both cases (for single-lane and multi-lane traffic circles) minimum delay values are obtained for each entry lane separately. Accordingly, these results may indicate that the vehicles entering from two different lanes in an approach of a multi-lane traffic circle are not affected by each other, but other factors like circulating flow rate, critical gap acceptance, etc. are also valid for single-lane traffic circles.

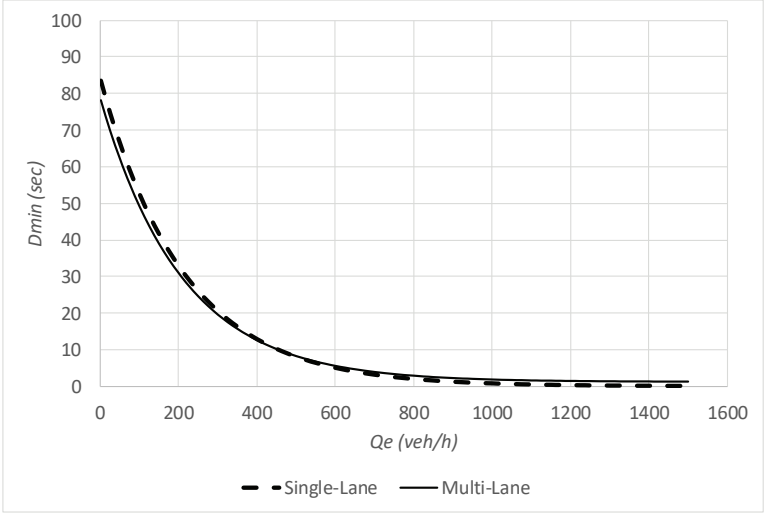

Figure 13 - Comparison of models for single-lane and multi-lane traffic circles

6. CONCLUSIONS

In this study, a new empirical minimum delay function for multi-lane traffic circles in İzmir, Turkey is presented. For this purpose, observations made at five multi-lane roundabouts at the city center of İzmir, Turkey. The obtained results are listed as follows:

- Although the models which depend on only circulating flow are simple and easy to apply, they have a very low accuracy in estimation of minimum delay at multi-

lane traffic circles. This indicates that circulating flow alone cannot be used in modelling minimum delay.

- On the other hand, models which depend on geometric variables and circulating flow give better results, but they all fail to define minimum delay values greater than 22 seconds. At this point we should mention that the data was limited to only five approaches of five multi-lane traffic circles. If the number of observed intersections is increased, better calibrated models can be obtained. This may be a motive for future studies.
- Results have shown that Horton's function gives the best results in estimation of minimum delay at traffic circles. Yet, the number of entering vehicles highly depends on many variables such as circulating flow, gap acceptance characteristics of minor stream drivers, etc. If the entry flow values are desired to be obtained from observations, there should be a constant queue of vehicles at the entrance of the observed approach for at least 30 minutes (which is the case when data was collected for this study). This type of data is collected when empirical capacity function is attempted to be obtained or for calibration of a function, which is derived according to critical gap acceptance method. It can be said that minimum delay models which are based on entry flow should be used in conjunctions with the entry capacity models. This means that an entry capacity model should be developed or calibrated in future studies.

Symbols

D_{av} : average delay per vehicle (seconds)

D_i : inscribed diameter of a traffic circle (m)

D_{min} : minimum delay (seconds)

D_{minlow} : lower limit of minimum delay (sec)

D_{minup} : upper limit of minimum delay (sec)

K : a constant in Horton's function

k : Erlang number

n : the number of observed conflicting vehicles for the subject vehicle

q_c : major stream flow (veh/sec)

q_e : capacity (entry flow) of minor approach (veh/sec)

T : critical gap (seconds)

T_0 : follow-up time (seconds)

t_d : the time of departure of the subject approach vehicle

t_0 : the time of arrival of the subject approach vehicle at the reference line

t_n : the time of arrival of nth conflicting vehicle at the reference point

w_c : circulating lane width (m)

w_{ent} : entry lane width of the minor approach (m)

w_{exit} : exit lane width (m)

w_{island} : width of the splitter island (m)

Δ : minimum headway between major-stream vehicles (seconds)

α : proportion of free vehicles (%)

ε : a delay constant

ϕ : the conflict or entry angle

γ : a delay constant

λ : a decay constant

ρ : the degree of saturation

References

[1] Tanyel, S., Baran, T. and Özuysal, M. (2007). Applicability of various capacity models for single-lane roundabouts in Izmir, Turkey. *Journal of Transportation Engineering*, Vol. 133(2), pp. 647-653.

[2] Özuysal, M., Caliskanelli, S.P., Tanyel, S. and Baran, T. (2009). Capacity estimation for traffic circles. Applicability of ANN. *Proceedings of ICE-Transport*, Vol. 162(4), pp. 195-206.

[3] Çalışkanelli, S.P., Özuysal, M., Tanyel, S. and Yayla, N. (2009). Comparison of different capacity models for traffic circles. *Transport*, Vol. 24(4), pp. 257–264.

[4] Tanyel, S., Yayla, N., (2003). A discussion on the parameters of Cowan M3 distribution for Turkey, *Transportation Research Part A: Policy and Practice*, 37(2), 129-143.

[5] Tanyel, S. and Yayla, N. (2010). Yuvarlakada kavşakların kapasiteleri üzerine bir tartışma. *Teknik Dergi*, Vol. 21(1), pp. 4935–4958.

[6] Ersoy, M. and Çelikoğlu, H. (2014). Çok şeritli dönel kavşaklarda kapasite analizi: Highway Capacity Manual 2010 kapasite modeliyle bir değerlendirme. *Pamukkale Üniversitesi Mühendislik Bilimleri Dergisi*, Vol. 20(6), pp. 225-231.

[7] Tanyel, S., Celik, K., Özuysal, M. and Çalışkanelli S. P. (2013). Different approaches to minimum delay estimation at single-lane traffic circles in İzmir, Turkey. *Canadian Journal of Civil Engineering*, Vol. 40(3), pp. 274-284.

[8] Akgüngör, A.P. (2004). Sinyalize kavşaklarda gecikme tahmininin matematiksel modellemesi-I: Farklı çözümleme süreleri için zamana bağli yeni bir gecikme modeli. *Teknoloji*, Vol. 7(3), pp. 369-379.

[9] Akçelik, R. (1998). Traffic circles: Capacity and performance analysis, ARRB Research report ARR 321, Vermont, Australia.

[10] Troutbeck, R. and Brilon, W. (1995). *Unsignalized intersection theory*. In Traffic Flow Theory: A State of Art Report 8-1, Eds. Gartner, N., Messer, C.J and Rathi, A. K., pp. 8-44.

[11] Troutbeck, R. J. (1990). Traffic interactions at traffic circles. *Conference of the Australian Road Research Board, NPT-5, Traffic Engineering and Planning*, pp. 17-42.

[12] Troutbeck, R. (1991). Unsignalized intersections and traffic circles in Australia: Recent developments. *Intersections Without Traffic Signals II*, pp. 238-257, Bochum, Germany.

[13] Cowan, R. C. (1987). An extension of Tanner's results on uncontrolled intersections. *Queueing Systems*, Vol. 1, pp. 249-263.

[14] Luttinen, R. T. (2004). *Capacity and level of service at Finnish unsignalized intersections.* Finra Reports 1/2004, Finnish Road Administration, Helsinki, Finland.

[15] Gerlough, D. L. and Huber, M. J. (1975). *Traffic flow theory*. Transportation Research Board Special Report 165, Washington D.C., USA.

[16] Surti, V. H. (1970). *Operation efficiency efficiency evaluation of selected at-grade intersectections.* HHR 321, pp. 60-73, Highway Research Board, National Research Council, Washington, D.C.

[17] Teply, S., Abou-Henaidy, M. I., Hunt, J. D. (1997). Gap acceptance behaviour-aggregate and logit perspectives: Part 2. *Traffic Engineering and Control*, Vol. 38(10), pp. 540-544.

[18] Kyte, M., Clemow, C., Mahfood, N., Lall, B. K. and Khisty, C. J. (1991). *Capacity and delay characteristics of two-way stop-controlled intersections*. Transportation Research Record 1320, Transportation Research Board, National Research Council, Washington, D.C. pp. 160–167.

[19] Al-Omari, B. and Benekohal, R. F. (1999). Hybrid delay models for unsaturated two-way stop controlled intersections. *Journal of Transportation Engineering*, Vol. 125(4), pp. 292–293.

[20] Adams, W. F. (1936). Road traffic considered as a random series. *Journal of the Institution of Civil Engineers*, Vol. 4(1), pp. 121-130.

[21] Tanner, J.C. (1962). A theoretical analysis of delays at an uncontrolled intersection. *Biometrika*, Vol. 49(1-2), pp. 163-170.

[22] Cowan R. J. (1975). Useful headway models. *Transportation Research*, Vol. 9, pp. 371-375.

[23] Cowan, R. J. (1984). Adam's formula revised. *Traffic Engineering and Control*, Vol. 25 (5), pp. 272-274.

[24] Luttinen R. T. (1996). *Statistical analysis of vehicle time headways.* Teknillien Korkeakoulu, Julkaisu, , Liikennetekniikka, Otaniemi, Finland.

[25] Drew, D. R. (1968). *Traffic flow theory and control*. McGraw-Hill, New York.

[26] Gedizlioğlu, E. (1979). *Denetimsiz kavşaklarda yan yol sürücülerinin davranışlarına göre pratik kapasite saptanması için bir yöntem*. Doktora Tezi, İ.T.Ü. Mühendislik-Mimarlık Fakültesi, İstanbul.

[27] Troutbeck, R. J. (1986). Average delay at an unsignalized intersction with two major streams each having a dichotomized headway. *Transportation Science*, Vol. 20(4), pp. 272-286.

[28] Hagring, O. (2003). *Capacity model for traffic circles*. Trivector Report 2003:7, Lund, Sweden.

[29] Flannery, A., Kharoufeh, J. P., Gautam, N. and Elefteriadou, L. (2005). Queuing delay models for single-lane traffic circles. *Civil Engineering and Environmental Science*, Vol. 22(3), pp. 133-150.

[30] Chandra, S., Agrawal, A. and Rajamma, A. (2009). Microscopic analysis of service delay at uncontrolled intersections in mixed traffic conditions. *Journal of Transportation Engineering*, Vol. 135(6), pp. 323–329.

[31] Çelik, F. (1987). *Denetimsiz eşdüzey kavşak sisteminin simülasyonu ve taşıt gecikmelerinin formüle edilmesi*. Doktora Tezi, İ.T.Ü. Fen Bilimleri Enstitüsü, İstanbul.

[32] Ashalatha R. and Chandra, S. (2011). Service delay analysis at TWSC intersections through simulation. *KSCE J. of Civ. Eng.*, Vol. 15(2), pp. 413–425.

[33] Kittelson, W.K. and Vandehey, M.A. (1991). *Delay effects on driver gap acceptance characteristics at two-way stop-controlled intersections*. Transportation Research Record 1320, pp. 154-159.

[34] Transportation Research Board (TRB). (2000) *Highway Capacity Manual*. National Research Council, Washington D.C., U.S.A.

[35] Transportation Research Board (TRB). (2010) *Highway Capacity Manual*. National Research Council, Washington D.C., U.S.A.

[36] Horton, R.E. (1940). An approach toward a physical interpretation of infiltration capacity. *Soil Science Society of America Journal*, Vol. 5, pp. 399–417.

[37] Kimber R. M. (1980). *The traffic capacity of roundabouts.* Transport and Road Research Laboratory, Report 942, Crowthorne, England.

[38] Waren, A. D. and Lasdon, L. S. (1979). The status of nonlinear programming software. *Operations Research*, Vol. 27 (3), pp. 431–456.

[39] Lasdon, L. S. and Waren, A.D. (1983). Large scale nonlinear programming. *Computers and Chemical Engineering*, Vol. 7(5), pp. 595–604.

[40] Nash, J. E., Sutcliffe, J. V. (1970). River flow forecasting through conceptual models part I - A discussion of principles. *Journal of Hydrology*, Vol. 10 (3), pp. 282–290.

[41] Barnston, A. G. (1992). Correspondence among the correlation RMSE (root mean square error) and Heidke forecast verification measures; refinement of the Heidke score. *Notes and Correspondence,* Vol. 7(4), pp. 699-709.

Teknik Dergi, 2022 11455-11472, Paper 642

Application of the Dynamic Compaction Method for Ground Improvement of Collapsible Loess in Qinhai

Jun CAI[1]
Jingtao ZHANG[2]
Guangyin DU[3]
Han XIA[4]

ABSTRACT

The collapsibility of loess has a great influence on subgrade construction in Qinghai, China, so laboratory tests are utilized to evaluate the collapsibility influencing factors, which illustrates that the collapsibility of this region is not dominated by soluble salts but an alkaline environment, high porosity and a low water content. The in situ self-weight submerging test reveals the settlement regularities, with a maximum settlement of 22.4 cm, which suggests that the soil in the test region is self-weight collapsible loess. In consideration of the economy and applicability, dynamic compaction was chosen as the ground improvement method. The optimal number of drops (N) for an energy level of 1000 kN·m is 6, and for the energy levels of 1500 kN·m and 2000 kN·m, N is 8. Besides the maximum effective depth for 1000 kN·m is 5 – 6 m, and it is 6 – 7 m for 1500 kN·m and 2000 kN·m.

Keywords: Loess, collapsibility, ground treatment, dynamic compaction.

1. INTRODUCTION

Loess accounts for 9.3% of the land area in the world and 3% in Asia. In China, loess is also widely distributed in Qinghai, Ningxia, Shaanxi and Inner Mongolia [1]. Loess is a yellow powdery soil formed during the quaternary period, with a high porosity, its structure is sensitive to water. When loess is eroded by water, the structure of the soil will rapidly be damaged, and the bearing capacity of the foundation will decrease quickly with settlement.

Note:
- This paper was received on May 30, 2019 and accepted for publication by the Editorial Board on June 26, 2020.
- Discussions on this paper will be accepted by March 31, 2022.
- https://doi.org/10.18400/tekderg.571877

1 Southeast University, Institute of Geotechnical Engineering, Nanjing, China - caijun129@seu.edu.cn https://orcid.org/0000-0001-9569-7418

2 CCCC First Highway Consultants Co, Ltd., Xi'an, China - 646772644@qq.com https://orcid.org/0000-0002-3102-6751

3 Southeast University, Institute of Geotechnical Engineering, Nanjing, China - guangyin@seu.edu.cn https://orcid.org/0000-0002-1253-5761

4 Southeast University, Institute of Geotechnical Engineering, Nanjing, China - imxiahan@hotmail.com https://orcid.org/0000-0001-7575-1392

The collapsible settlement of loess is a kind of hazard, resulting in large settlement or differential settlement, cracking, inclination and damage. If it is not treated properly, engineering problems may occur.

The main features of loess are its structural properties and collapsibility, and these two characteristics are closely related [2]. The influencing factors of loess collapsibility can be complicated, and some laboratory tests [3-9] on the relationship between collapsibility and soil physical-mechanical parameters have been studied, among which the soluble salt, water content, void ratio and dry density are the high relative factors. As the performance of the in situ soaking test can be closer to that of the actual situation, valuable settlement regularity and collapsibility evaluations can be acquired, so the tests were conducted on different scales [10-14], and prominent loess collapsible features were found.

Because of the poor properties of collapsible loess, reasonable and effective treatments are needed for construction in loess regions. The most common methods are dynamic compaction, compaction pile and pre-soaking methods, among which dynamic compaction is most widely used and economical. Lyu [15] and Xing [16] provided suggestions about the dynamic compaction parameters for collapsible loess treatment. Zhan [17] presented an empirical formula for the treating depth of dynamic compaction in Gansu, China. For different collapsible loess layer thicknesses, Huang [18] proposed the foundation treatment depth and remaining collapsible settlement standards. Hu [19] acquired the optimum centre distance of dynamic compaction in Lishi, China.

These achievements have made great contributions to infrastructure construction in loess regions; as for the particularity of loess in different regions, more loess parameters and dynamic compaction parameters are still needed. Therefore, for the construction of a high-grade highway subgrade in Qinghai Province, a series of tests on collapsible loess properties and dynamic compaction parameters have been conducted, which can be valuable for the treatment of loess.

2. LOESS PROPERTIES

2.1. Geological Conditions

The test site is located in Huangyuan County of Xining city (Fig. 1a). The geological investigation report reveals that the main constituents of the loess are silt and clay, (Fig. 1b), and it contains developed pores; the collapsible loess depth exceeds 10 m. The groundwater level is over 20 m below the surface, so the influence of underground water does not need to be considered.

The main property of loess is its collapsibility, with the influence of gravity stress or additional stress from overlaying soil. When natural loess is eroded by water, the soil structure is rapidly damaged, and significant settlement occurs. According to the Chinese Technical Code [20], the collapsibility coefficient is defined by (1):

$$\delta_{\mathrm{s}} = \frac{h_{\mathrm{p}} - h_{\mathrm{p}}^{'}}{h_0} \tag{1}$$

where h_p is the height of the soil sample (cm) when the soil settlement is stable under a certain pressure condition (p) with a natural soil water content and structure; h_p' is the height of the soil sample (cm) when it is immersed in water and the settlement is stable; and h_0 is the original height of the soil (cm). For the pressure condition (p) of formula (1) in the collapsibility coefficient test, when the soil sampling depth is 0 - 10 m under the bottom of the base, p is 200 kPa; when the soil sampling depth is beyond 10 m, p is the saturated self-weight pressure of the overlying soil (if p is over 300 kPa, p is 300 kPa). When $\delta_s < 0.015$, the soil sample is non-collapsible loess, and when $\delta_s \geq 0.015$, the soil is collapsible loess.

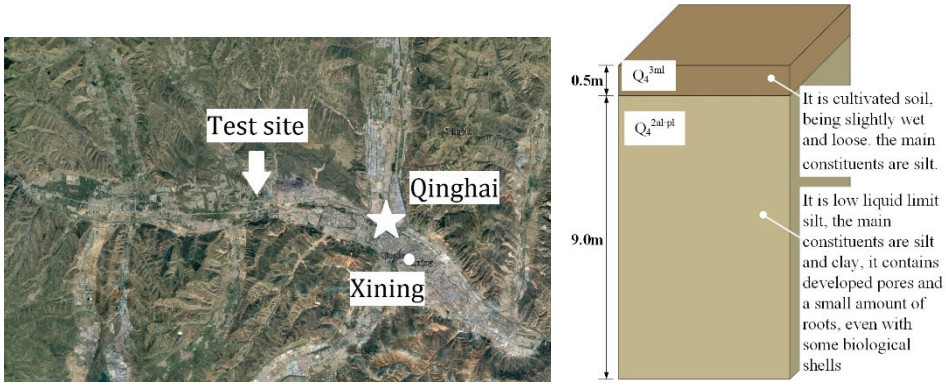

(a) Satellite Map (http//:map.bing.com) *(b) Soil Profile*

Figure 1 - Geological Condition of the Test Site

Table 1 shows the physical parameters of the loess and that the loess contains developed pores. Particle size analysis shows that the loess in this region is mainly composed of silt particles (0.05 ~ 0.005 mm), accounting for 62 – 63% of the total content.

Table 1 - Physical Parameters of the Loess

Unit weight /γ (kN/m^3)	*Dry unit weight* /γ_d (kN/m^3)	*Water content* /w (%)	*Void ratio* /e	*Liquid limit* /w_L (%)	*Plasticity index* /I_P (%)
17.2	15.1	16.4	0.81	25.1	6.9

2.2. Soluble Salt

Table 2 shows the analysis of soluble salt in soil. The pH of collapsible loess in Qinghai is between 7.3 and 7.5, and it is slightly alkaline. As organic matter in soil is acidic, flocculent organic matter can be easily dissolved in alkaline environments [21], which causes the porosity to increase and the loess in Qinghai to easily collapses.

Table 2 - Soluble salt in loess (unit: mg/kg)

Depth/m	1	2.5	4
pH	7.5	7.3	7.5
HCO^{3-}	348.7	320.8	432.3
Cl^{-}	64.46	119.71	119.71
SO_4^{2-}	137.8	137.8	275.5
K^{+}	5.35	6.30	10.35
Na^{+}	21.90	16.65	21.90
Ca^{2+}	137.9	126.49	137.99
Mg^{2+}	48.84	34.89	69.77
Salinity	710.0	730.0	990.0

Aeolian deposition is the dominant factor for loess deposition in Western China. Wind causes silt particles to accumulate loosely on the ground, and less rainfall infiltration causes soluble salt to dissolve and recrystallize; thus, the soil particle connections are not dominated by mechanical friction but rather soluble salt chemical links. Soluble salt plays an important role in the loess structure [22]. Research shows that when the content of soluble salt in soil is less than 0.50%, the soluble salt has little effect on the compactness and shape of loess [22]; the content of soluble salt in Qinghai is 0.052% - 0.15%, which is far less than 0.5%, so the collapsibility of this region is not dominated by soluble salts.

2.3. Water Content

In Fig. 2, for the laboratory test results, a curve with a high fitting coefficient cannot be obtained, so an obvious relationship between the collapsibility and water content is not

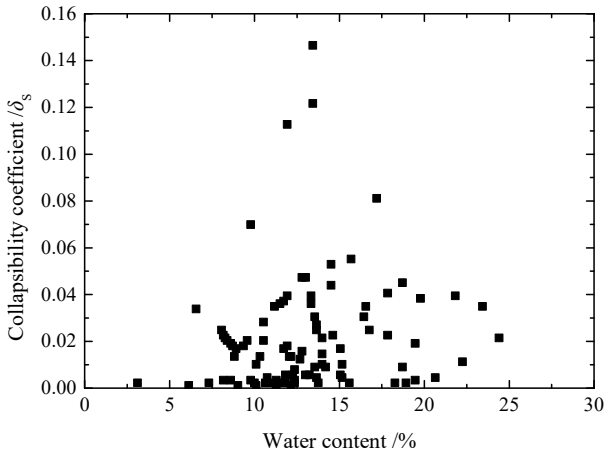

Figure 2 - Relationship between the Collapsibility Coefficient and Water Content

available. But considering the collapsibility mechanism of loess, when loess is immersed in water under stress, collapsible failure occurs, so the influence of water content on loess collapsibility exists. It may be that the collapsibility coefficient not only related to water content, Liu [23] believes that the motivations of loess collapsibility are stress and water, there is no linear correlation between water content and collapsibility. With different sampling depth, the stress and sedimentary state of samples are different, which results in different collapsibility, besides the water content is affected by environmental precipitation. So loess collapsibility coefficient may not have a certain correlation with water content, it is also found by Lin [24] and Wang [25].

2.4. Void Ratio

The void ratio of loess soil reflects its density, and the void ratio is defined as (2):

$$e = \frac{V_v}{V_s} = \frac{d_s(1+w)\rho_w}{\rho} - 1 \tag{2}$$

Where V_v is the volume of the voids in the soil, V_s is the volume of the soil particles, d_s is the relative density of the soil particles, w is the water content, ρ_w is the density of water, ρ is the density of the soil, and e is the void ratio, which can be calculated by these parameters.. In Fig. 3, after eliminating some discrete points, it shows that the collapsibility coefficient of collapsible loess increases exponentially with the void ratio. When collapse occurs, the porous granular structure is destroyed. The larger the void ratio is, the greater the coefficient of collapsibility becomes.

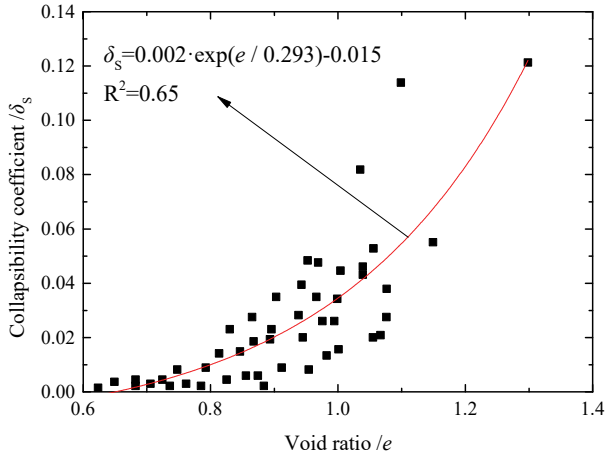

Figure 3 - Relationship between the Collapsibility Coefficient and Void Ratio

2.5. Dry Unit Weight

In Fig. 4, by eliminating some discrete results, the curve was fitted, with the increase in the dry unit weight (γ_d), the collapsible loess shows an exponentially decreasing trend. The larger

the dry unit weight is, the denser the loess structure becomes, and the collapsibility becomes weaker.

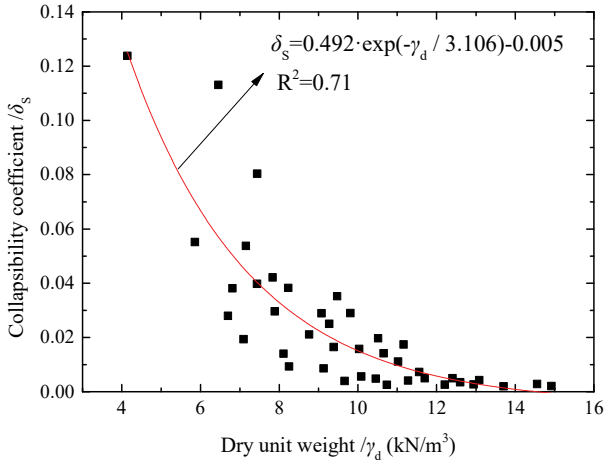

Figure 4 - Relationship between the Collapsibility Coefficient and Dry Unit Weight

3. LOESS COLLAPSIBILITY IN SITU TESTS

At present, there are two main methods for acquiring the collapsibility of loess: one is sampling the undisturbed soil and conducting the uniaxial immersion compression test to obtain the collapsibility coefficient, while the other is performing the in situ submerging test, with either the self-weight submerging test (SWST) or load submerging test (LST).

3.1. Self-Weight Submerging Test (SWST)

A square or circle test pit is needed for the self-weight submerging test, and the length of the pit must be longer than the depth of the collapsible loess soil thickness and be no less than 10 m. The geologic report shows that the collapsible loess depth is 9.5 m, so the width of the testing pit is 10 m, and the depth is 0.5 m. For the convenience and accuracy of the observations, the bottom elevation difference does not exceed 2 cm, and coarse sand was paved as the bottom levelling layer, with the thickness of the layer being 10 cm.

For the settlement observation at different depths, observation rods were arranged on the surface of the pit and inserted into the soil at depths of 0.5 m, 1.5 m and 2.5 m. For the stability of the rods on the surface, concrete pedestals (15 cm × 15 cm × 15 cm) were fixed at the bottom. In the test, water level indicators were used around the test pit to maintain a water depth of 40 cm. To avoid the influence of water erosion, a water injection hole was set and filled with pebbles, while the water inflow velocity was controlled during the process. Fig. 5 shows the monitoring point distribution in the SWST.

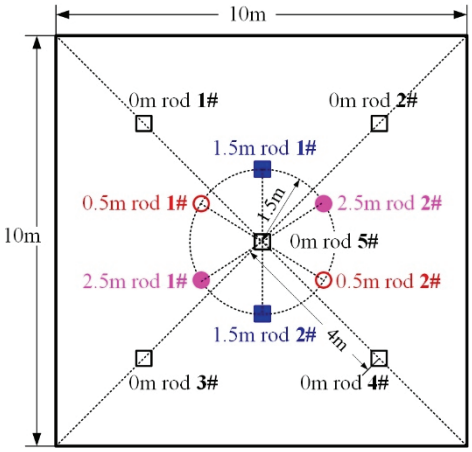

(a) Rod Arrangement *(b) Test Site*

Figure 5 - Self-weight Submerging Test

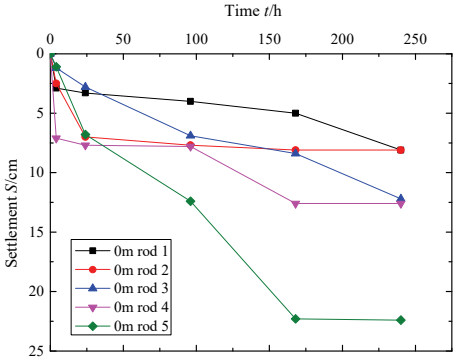

(a) 0 m

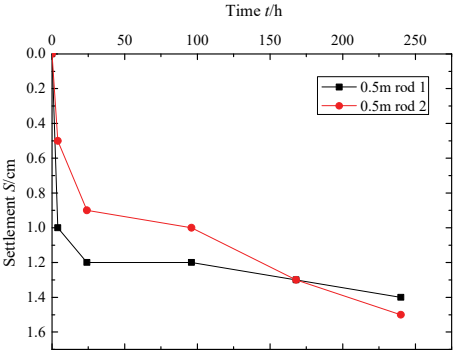

(b) 0.5 m

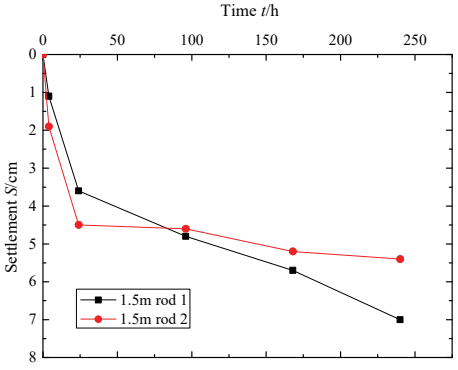

(c) 1.5 m

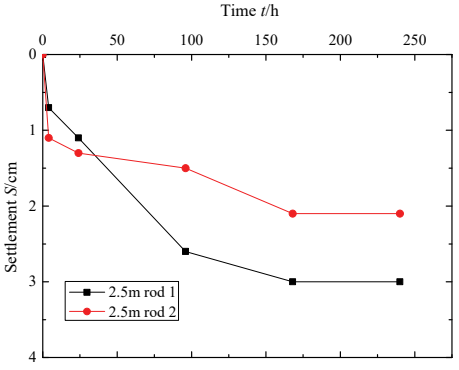

(d) 2.5 m

Figure 6 - Rod Settlement at Different Depths for the SWST

In the initial phase of the test, the settlement was obvious. After 4 h, 2 cracks appeared around the pit; after 24 h, large annular cracks formed around the testing pit, the average length was 27 cm, and water infiltrated into the pit wall at approximately 31 cm. After 96 h, for the majority of the monitoring points, the settlement was over 50% of the total settlement, and some points reached 70%. At 240 h, the settlement of all the points became stable, and many cracks appeared around the test pit.

Fig. 6 indicates that the settlement of each place in the pit is different. In Fig. 6(a), for shallow rods, the maximum settlement is 22.4 cm, which is at the centre of the pit (0 m rod 5 in Fig. 5), and the minimum settlement is 8.1 cm, which is close to the edge of the test pit. According to the Chinese Technical Code [20], the total self-weight collapsible settlement exceeds 70 mm, so the soil is self-weight collapsible loess. Comparing the settlement of the rods at different depths (Fig. 5), with increasing depth, the self-weight collapsibility increases to a maximum at 1.5 m and then gradually decreases.

3.2. Load Submerging Test (LST)

The load submerging test was performed in a pit with a size of 3 m × 4 m × 0.5 m (Fig. 7), and rods were arranged in the same way as the SWST (Fig. 5). The loading plate was a square steel plate (70.7 cm × 70.7 cm × 1.2 cm) on the bearing platform with loading sandbags (Fig. 7). Before the loading procedure, the soil in the test pit was soaked in water for 10 days to make it saturated. The loading weight should not exceed 25 kPa in each step, and the settlement was measured for each 100 kPa, producing a final loading weight of 300 kPa. Then, the settlement was measured 6 h and 24 h later. During the loading process, when the settlement was no more than 0.2 mm in 2 h, an additional load was added. Throughout the test, the water depth was kept at 40 cm.

During the test, at day 2, annular cracks and soil settlement occurred around the test pit, the average width of the cracks was 40 - 50 cm, and the depth of water infiltration into the pit wall was approximately 50 cm. After 10 days, the annular collapse around the test pit nearly stopped. After loading to 300 kPa, and after 24 h, the settlement was stabilized, and the test was finished.

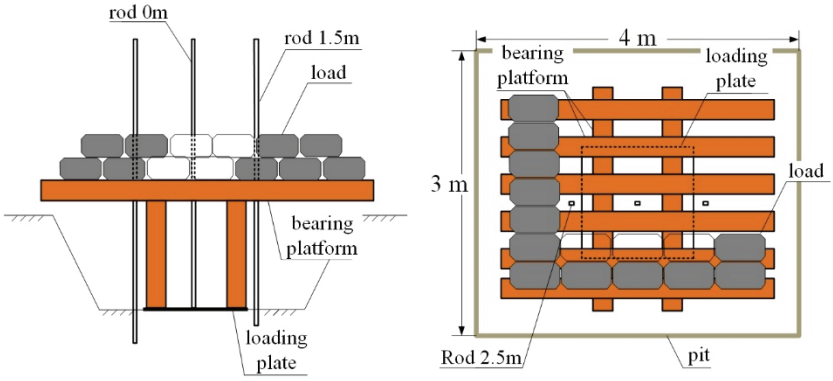

(a) Sketch of the Test

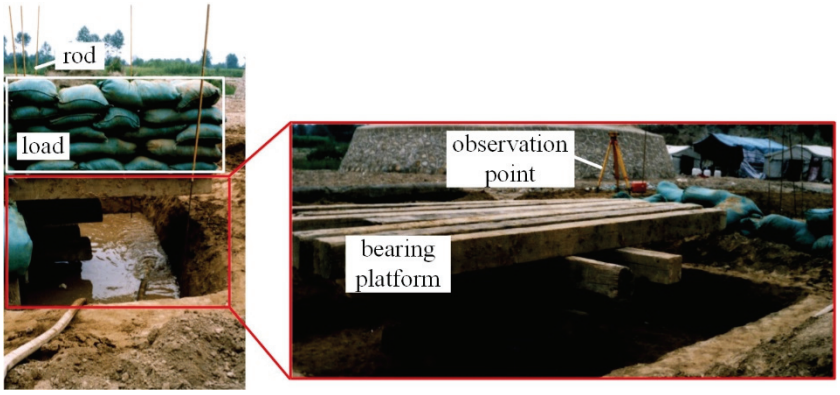

(b) Scene of the Site

Figure 7 - Load Submerging Test

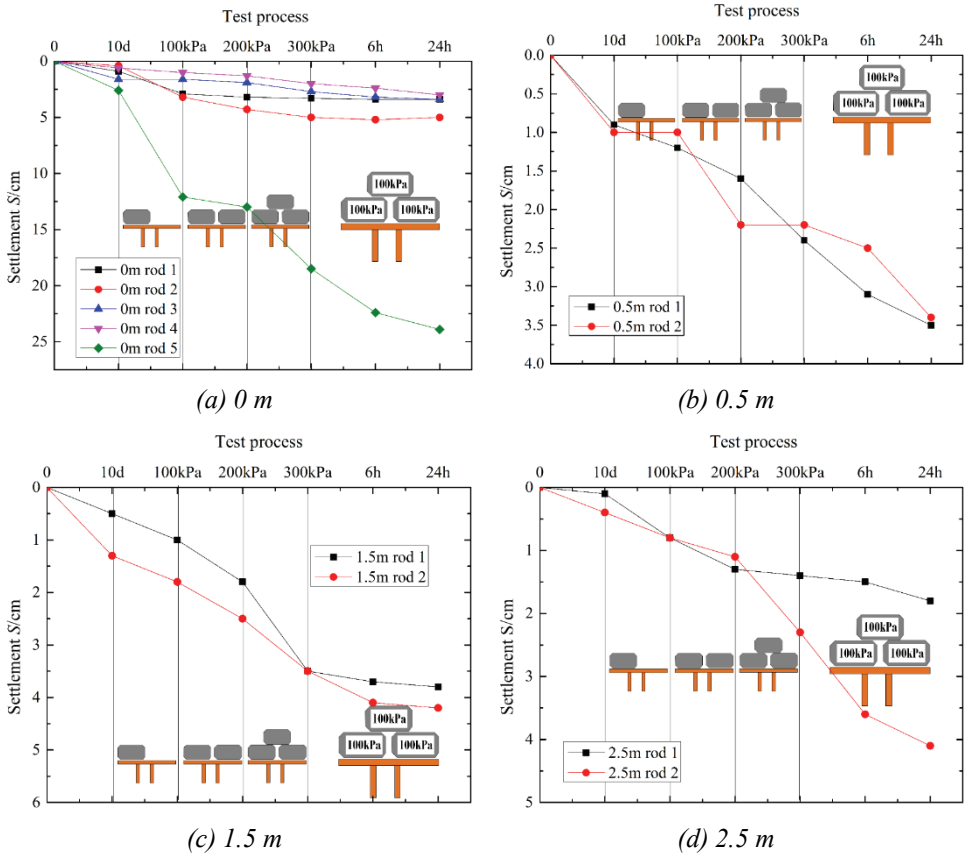

(a) 0 m *(b) 0.5 m*

(c) 1.5 m *(d) 2.5 m*

Figure 8 - Rod Settlement at Different Depths for the LST

Fig. 8 illustrates that the maximum settlement is in the centre of the loading plate with a depth of 0 m, which is 23.9 cm. After loading, the soil continues to collapse, so the settlement grows slowly. Compared with the SWST, the collapsible settlement is related to the area of the test pit; the larger the pit area is, the larger the settlement, which is also illustrated by Huang [26]. The collapsible settlement is also related to the additional stress, and the collapsible deformation is the total settlement of two factors: compressive deformation and collapsible deformation. The collapsible deformation can be divided into two stages: first, during the collapsible deformation stage, the loess structure is destroyed, and collapsibility occurs; second, during the reconsolidation stage, the pressure is constant, the soil particles rearrange, and the strength gradually increases as the collapsibility becomes stable.

4. DYNAMIC COMPACTION METHOD AND APPLICATION

The dynamic compaction method is illustrated in Fig. 9, and the compaction procedure is shown in Table 3. The hammer is cylindrical and made from cast iron with a diameter of 2.5 m and a weight of 13.5 t. The hoisting equipment is a crawler crane (Fig. 9). During compaction, compressional wave energy can be generated in the soil, which will squeeze the voids between soil particles. Therefore, the air in the soil particles is eliminated first, the particles are rearranged, and then the volume and plastic deformation of the soil reach a new stable state [27].

According to the Chinese Technical Code [28], the energy level division is based on the energy of each drop, so the compaction energy is calculated by (3) and divided into three levels: 1000 kN·m, 1500 kN·m and 2000 kN·m. The number of drops (N) is set as 8, 10 and 12, so the test can be categorized into 9 conditions (Fig. 10).

$$E = M \cdot H \tag{3}$$

where E is the energy level of each drop (kN·m), M is the weight of the hammer (kN), and H is the height of the falling hammer.

Table 3 - Dynamic Compaction Procedure

Procedure	
Step 1	Mark the grid point location on the levelling ground and measure the elevation
Step 2	Position the crane to ensure that the hammer is aligned with the point
Step 3	Lift the hammer to the designed height, free the hammer, and measure the height of the hammer
Step 4	According to the designed number of drops and control standards, repeat step 3 to complete the compaction
Step 5	Fill the compaction point with the bulldozer and measure the ground elevation

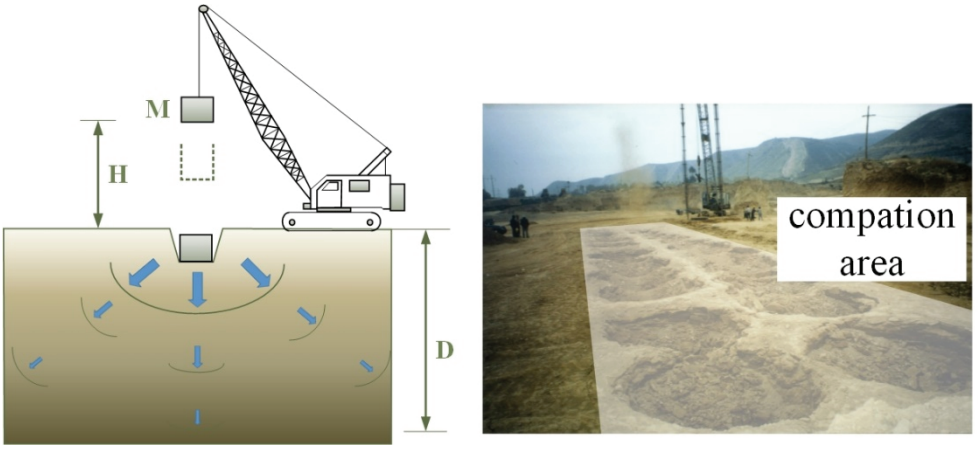

Figure 9 - Dynamic Compaction Test Hoisting Equipment and Hammer [29]

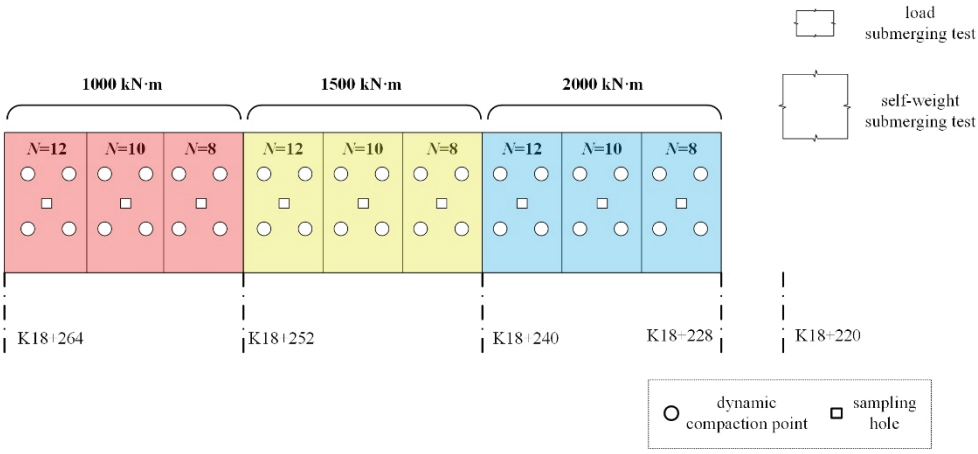

Figure 10 - Test Design

4.1. Compaction Settlement

Fig. 11 is the mean value and standard deviation results of relative settlement for the 3 energy levels, and the curves were fitted from the mean value. It can be seen that the compaction settlement of the first drop increases with the energy levels, for 1000 kN·m it is 20 cm, and for 1500 kN·m it is 30 cm, for 2000 kN·m it is 45 cm. And when the number of drops (*N*) increases, the relative settlement decreases as a power function. So according to the function, the relative settlement of each drop can be calculated. According to the Chinese Technical Code [28], it has noted that for energy levels lower than 4000 kN·m, when the average settlement for the last two drops is less than 5 cm, compaction can be finished. As the dark

dotted line shows, for the 1000 kN·m level, N is 5, and for the 1500 and 2000 kN·m levels, N is 8.

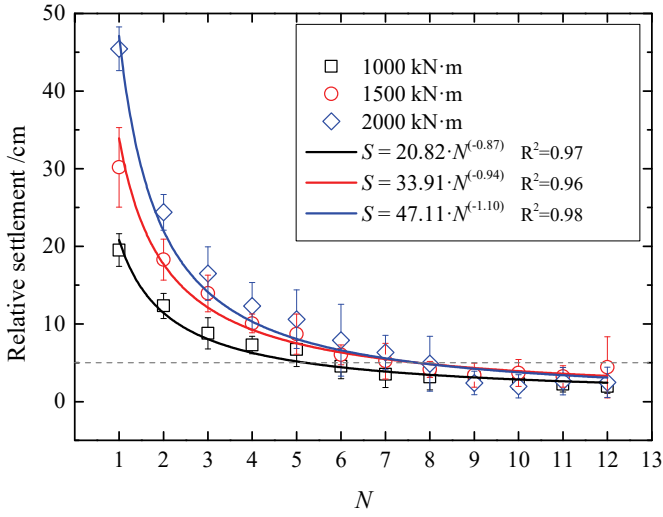

Figure 11. Relationship between the Relative Settlement and Number of Drops (N) for the three Energy Levels: 1000 kN·m, 1500 kN·m and 2000 kN·m

4.2. Comparison of Collapsibility Elimination

Samples of different depths were taken by drilling and tested indoors to acquire the collapsibility coefficient as defined in formula (1). Fig. 12 illustrates that after compaction, the collapsibility of the loess has been mainly eliminated, except for some abnormal data points, which may be from the influence of the sampling error. The sampling hole is in the

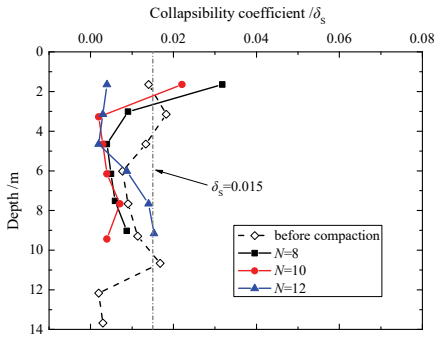

(a) 1000 kN·m

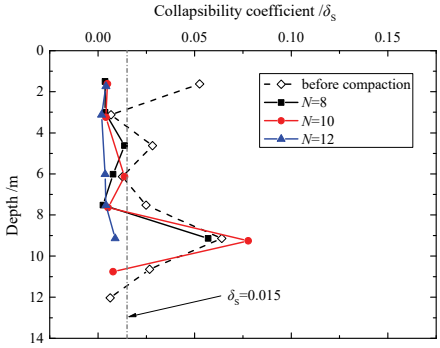

(b) 1500 kN·m

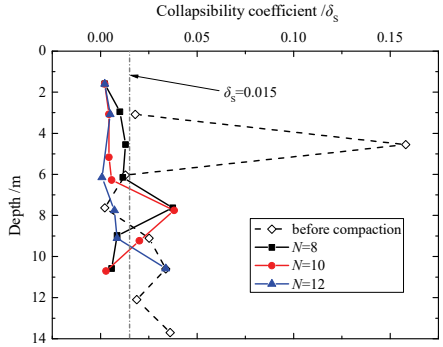

(c) 2000 kN·m

Figure 12 - Relationship between the Collapsibility Coefficient and N for the three Energy Levels: 1000 kN·m, 1500 kN·m and 2000 kN·m

middle of the 4 compaction points (Fig. 10), and it may be disturbed by the compaction vibration, which leads to the discrepancy of the soil in the middle. For the higher energy level, with the increase in the number of drops (N), the effect of eliminating collapsibility becomes more obvious. For 1000 kN·m, the difference between 8, 10 and 12 drops is not obvious, and the maximum effective depth is approximately 5 m. For 1500 kN·m, the maximum effective depth for 8, 10 and 12 drops is 6 m. For 2000 kN·m, the maximum effective depth for 8 and 10 drops is approximately 6 m, and it is 7 m for 12 drops.

4.3. Comparison of the CPT

For the CPT results, the dotted line is the result before compaction, and the solid line is the result after compaction, and P_s is the specific penetration resistance. Fig. 13 shows that, for 1000 kN·m, the specific penetration resistance has been improved in 0 – 6 m, and beyond 6 m, the effect of the improvement is not obvious. For N = 10, the maximum effective depth is approximately 5 m, and for N = 12, it is approximately 6 m. Therefore, for the 1000 kN·m energy level, the maximum effective depth is approximately 5 – 6 m, and increasing the N from 8 to 12 is not obvious for the effect of improvement.

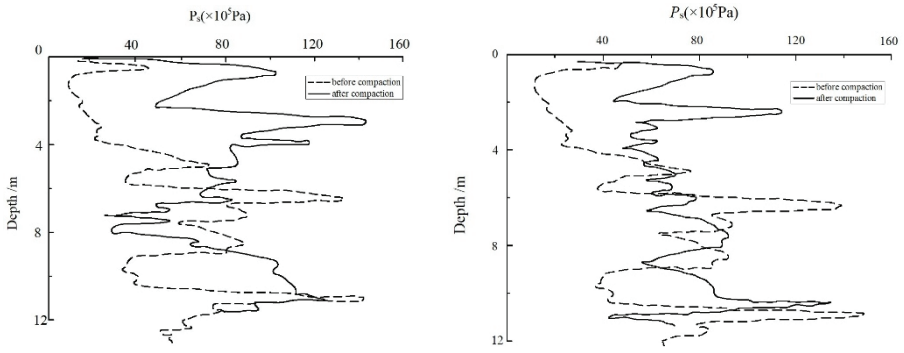

(a) N = 8 *(b) N = 10*

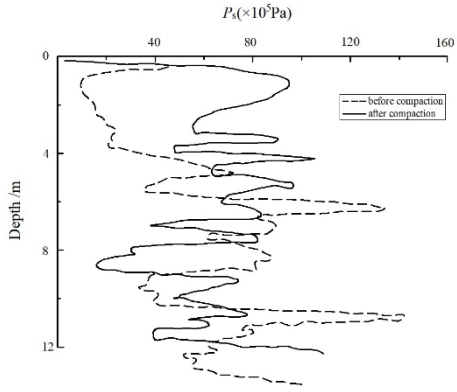

(c) N = 12

Figure 13 - CPT Curves for Different N at an Energy Level of 1000 kN·m

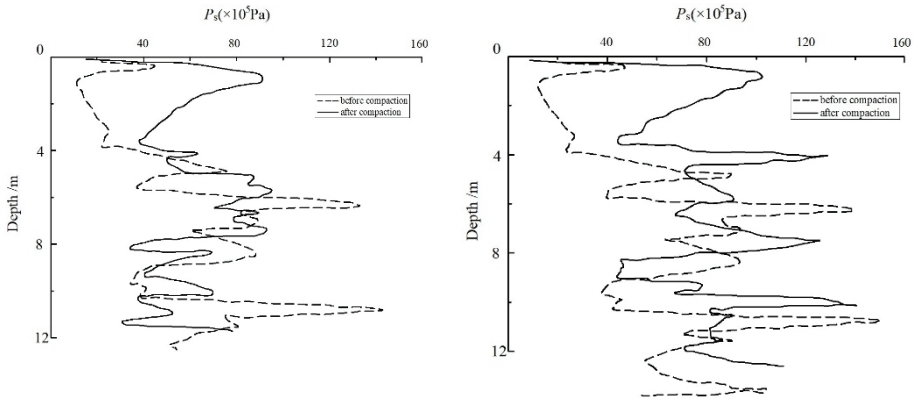

(a) N = 8 *(b) N = 10*

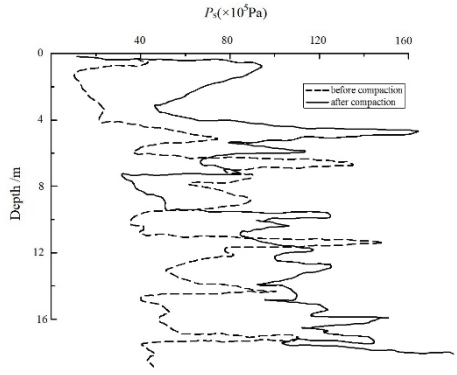

(c) N = 12

Figure 14 - CPT Curves for Different N at an Energy Level of 1500 kN·m

Fig. 14 illustrates the CPT results for 1500 kN·m. According to the shape of the curves, for the sharp points, it is possible that the probe cone tip touched a hard object. Therefore, the maximum effective depth is approximately 6 m.

Fig. 15 illustrates that for 8 drops, the maximum effective depth is 6 m. For 10 and 12 drops, the specific penetration resistance at 0-7 m increases significantly, so the maximum effective depth for 12 drops is 7 m.

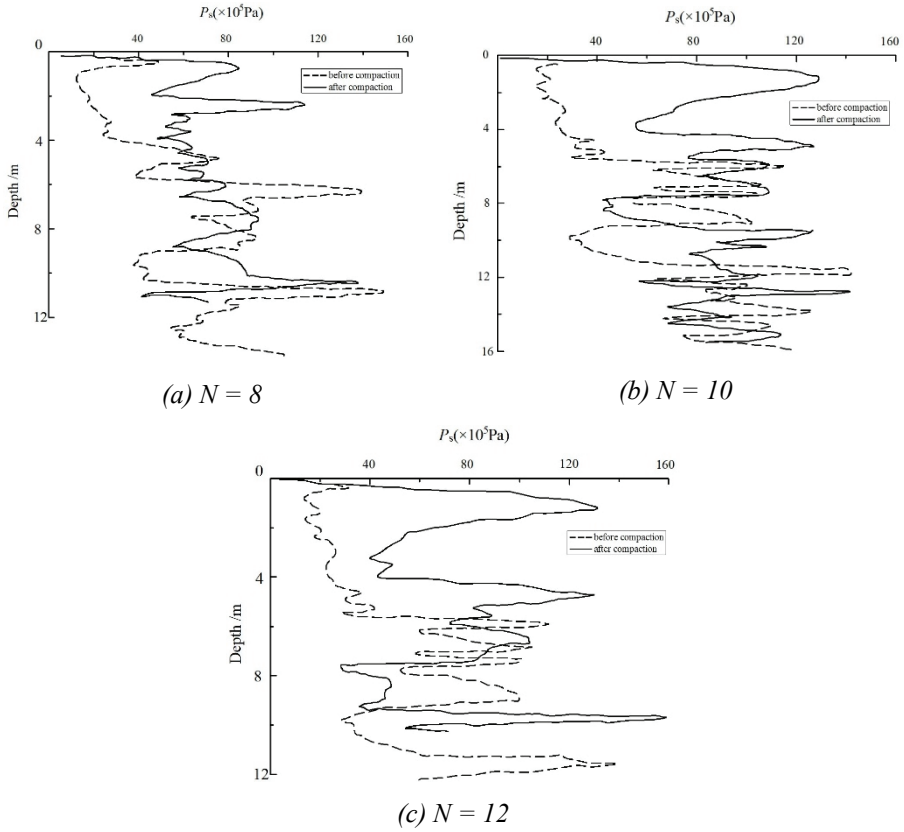

(a) N = 8

(b) N = 10

(c) N = 12

Figure 15 - CPT Curves for Different N at an Energy Level of 2000 kN·m

The indoor collapsibility tests and CPT tests indicate that the two results are consistent. For the energy levels of 1000 kN·m and 1500 kN·m, the effect of improvement is not significant as the number of drops (N) increases. The maximum effective depth for 1000 kN·m is about 5 – 6 m, and for 1500 kN·m, it is 6 m. For 2000 kN·m, the maximum effective depth increases with the number of drops where it is 6 m for N = 8, 6 – 7 m for N = 10, and 7 m for N = 12.

5. CONCLUSION

For the construction of high-grade highway subgrades in collapsible loess regions in Qinghai, China, where differential settlement of collapsibility always occurs, a series of loess property tests were conducted, and various collapsibility influencing factors and in situ collapsible settlement regularities were systematically discussed. Accordingly, the dynamic compaction method was chosen to improve the foundation, and the effect of the treatment was evaluated. The results can be concluded as follows:

(1) The loess collapsibility in situ tests indicate that the soil in the test region is self-weight collapsible loess. The maximum settlement in the self-weight submerging test is 22.4 cm and that in the load submerging test is 23.9 cm; they are all in the centre of the test pit. For deep collapsible settlement, with increasing depth, the collapsibility increases to a maximum at 1.5 m and then gradually decreases. In addition, the collapsible deformation can be divided into two stages: the collapsible deformation stage and the reconsolidation stage.

(2) For economy and applicability, the dynamic compaction method was applied for collapsible loess treatment. By fitting, the relationship between relative settlement and number of drops (N) at different energy levels is obtained. The optimization of N is also conducted at different energy levels, according to the quality control standards of the Chinese Technical Code (JGJ 79-2012), N is 5 for 1000 kN·m and N is 8 for 1500 kN·m and 2000 kN·m.

(3) Loess collapsibility laboratory tests and in situ CPT tests were utilized for the evaluation of the compaction effect; for energy levels of 1000 kN·m and 1500 kN·m, increasing the number of drops (N) from 8 to 12 is ineffective. The maximum effective depth for 1000 kN·m is about 5 – 6 m, and for 1500 kN·m, it is 6 m. For 2000 kN·m, the maximum effective depth increases with the number of drops (N), where the depth is 6 m for $N = 8$, 6 – 7 m for $N = 10$, and 7 m for $N = 12$.

Acknowledgments

The work in this paper was substantially supported by the Qinghai provincial authority of high-grade highway construction management and Chang'an University.

References

[1] Qian H. X, Luo Y. S. Collapsible loess subsoil. Beijing: China Architecture & Building Press, 1985.

[2] Yao Z. H., Huang X. F., Chen Z. H., Zhang J. H., Comprehensive submerging tests on self-weight collapse loess with heavy section in Lanzhou region. Chinese Journal of Geotechnical Engineering, 1(34):65 – 74, 2012.

[3] Liu Z. D, Mechanics and engineering of loess. Xi'an: Shanxi Sciences and Technology Press, 1996.

[4] Chen Z. H., Xu Z. H., Liu Z. D., Some problems of collapsed loess. Chinese Journal of civil Engineering, 19(3):62 – 69, 1986.

[5] Shao S. J., Yang C. M., Ma X. T. et al, Correlation analysis of collapsible parameters and independent physical indices of loess. Rock and Soil Mechanics, 34 Supp(2): 27 - 34, 2013.

[6] Gao G. R., A structure theory for collapsing deformation of loess soils. Chinese Journal of Geotechnical Engineering, 12(4): 1 – 10, 1990.

[7] Kovacs, J; Raucsik, B, Varga, A., et al, Clay mineralogy of red clay deposits from the central Carpathian Basin (Hungary): implications for Plio-Pleistocene chemical weathering and palaeoclimate. Turkish Journal of Earth Sciences, (22): 414 – 426, 2013.

[8] Walsh K., Houston W., Houston S. L., Evaluation of in-place witting using soil suction measurement. Geotechnical Engineering, 119(5):862 – 873, 1993.

[9] Miao T. D., Liu Z. Y., Ren J. S., Deformation mechanism and constitutive relation of collapsed loess. Chinese Journal of Geotechnical Engineering, 21(4):383 – 387, 1999.

[10] Liao S. X., Study on pre-submerging of collapsible loess. Nonferrous Metallurgy Construction, 3(2): 1 – 13, 1983.

[11] Qian H. J., Zhu M., Xie S., Experimental study on the regularities of collapsible deformation of loess foundation in Hejin, Shanxi. Chinese Journal of Geotechnical Engineering, 14(6): 1 – 9, 1992.

[12] Li D. Z., He Y. H., Sui G. X., Study and test on immersion of Q2 loess in large area. Chinese Journal of Geotechnical Engineering, 15(2): 1 – 11, 1993.

[13] Houston S. L., Foundations and pavements on unsaturated soils. Proceeding 1st International Conference on Unsaturated Soils, Paris, France, 1995.

[14] Huang X. F., Chen Z. H., Ha S., Xue S. G., Sun S. X., Xu Y. M., Jin X. J., Zhu Y. Q., Large area field immersion test on characteristics of deformation of self-weight collapse loess under overburden pressure. Chinese Journal of Geotechnical Engineering, 28(3): 382 – 389, 2006.

[15] Lyu X. J., Gong X. N., Li J. G., Research on parameters of construction with dynamic compaction method. Rock and Soil Mechanics, 27(9): 1628 – 1633, 2006.

[16] Xing Y. D., Wang C. M., Zhang L. X., Effect analysis of dynamic ramming for collapsible loess roadbed in west of Liaoning. Journal of Liaoning Technical University (Natural Science), 27(3): 371 – 373, 2008.

[17] Zhan J. L., Shui W. H., Application of high energy level dynamic compaction to ground improvement of collapsible loess for petrochemical project. Rock and Soil Mechanics, 30(S2): 469 – 472, 2009.

[18] Huang X. F., Chen Z. H., Fang X. W., Zhu Y. Q., Guo J. F., Wei X. F., Study on foundation treatment thickness and treatment method for collapse loess with large thickness. Chinese Journal of Rock Mechanics and Engineering, 26(S2): 4332 – 4338, 2007.

[19] Hu C. M., Mei Y., Wang X. Y., Experimental research on dynamic compaction parameters of collapsible loess foundation in Lishi region. Rock and Soil Mechanics, 33(10):2903 – 2909, 2012.

[20] Code for building construction in collapsible loess regions, GB/ 50025-2004, China Architecture and Building Press

[21] Mitchell J. J., Kenichi S., Fundamentals of soil behavior. John Wiley & Sons Inc, Hoboken, New Jersey, 2005.

[22] Xie D. Y., Xing Y. C., Soil Mechanics for Loess Soils. Beijing: Higher Education Press, 2016.

[23] Liu Z. D., Li J., Guo Z. Y., Rao W. Y., Deformation behaviours and deformation parameter of loess in Shanxi district. Chinese Journal of Geotechnical Engineering, 6(3): 24 – 34, 1984.

[24] Lin Y., Study on engineering characteristics of deep layer collapsible loess in Pengjiaping area of Lanzhou City, Lanzhou University, 2019

[25] Wang J. Q., Lei S. Y., Li X. L., Wang Y. M., Liu Z., Wang X. G., Correlation of wet collapsibility coefficient and physical property parameters of loess. Coal Geology and Exploration, 41(3): 42 – 50, 2013.

[26] Huang X. F., Yang X. H., A study progress on in-situ soaking test on collapsible loess. Rock and Soil Mechanics, 34(S2): 222 – 228, 2013.

[27] Xu Z. J., Zhang Y. N., Dynamic compaction and dynamic compaction replacement methods for reinforcing foundation. Beijing: China Machine Press, 2004.

[28] Technical code for ground treatment of buildings. Ministry of Housing and Urban-Rural Development of the People's Republic of China. 2012, (JGJ 79-2012).

[29] Lukas R. G., Delayed soil improvement after dynamic compaction. Ground Improvement, Ground Reinforcement, Ground Treatment. Published by the ASCE, 1997: 409 – 420, 1997.

Teknik Dergi, 2022 11473-11486, Paper 643

Sediment Incipient Motion in Sewer with a Bed Deposit

Wan Hanna Melini WAN MOHTAR[1]
Charles HIN JOO BONG[2]
Aminuddin AB. GHANI[3]
Mir Jafar Sadegh SAFARI[4]
Aizat Mohd TAIB[5]
Haitham Abdulmohsin AFAN[6]
Ahmed EL-SHAFIE[7]

ABSTRACT

This paper analyses experimental data on sediment incipient motion with varying sediment bed thickness (of d_{50}, 5, 10 and 24 mm). Sediment particles (with sizes ranging from 0.5 mm to 4.78 mm) were used to evaluate the effect of deposited bed. Variation of shear velocity estimation was investigated where the critical Shields parameter was expressed using bed-slope product u_{*cb}, log-law u_{*cl} and was extended in terms of critical mean velocity. The critical Shields parameters obtained were significantly lower than the traditional Shields curve when u_{*cl} was used compared to u_{*cb}. Higher critical mean velocity is needed for shallower deposits.

Keywords: Threshold criteria of sediment motion, shields parameter, sediment bed thickness.

Note:
- This paper was received on May 31, 2019 and accepted for publication by the Editorial Board on September 28, 2020.
- Discussions on this paper will be accepted by March 31, 2022.
- https://doi.org/10.18400/tekderg.572529

1 Universiti of Kebangsaan Malaysia, Department of Civil Engineering, Bandar Baru Bangi, Malaysia
hanna@ukm.edu.my - https://orcid.org/0000-0002-5684-5577

2 Universiti of Malaysia Sarawak, Department of Civil Engineering, Sarawak, Malaysia
bhjcharles@unimas.my - https://orcid.org/0000-0001-5447-0786

3 Universiti of Sains Malaysia, River Engineering and Urban Drainage Research Centre, Penang, Malaysia
redac02@usm.my - https://orcid.org/0000-0002-8921-9569

4 Yasar University, Department of Civil Engineering, Izmir, Turkey
jafar.safari@yasar.edu.tr - https://orcid.org/0000-0003-0559-5261

5 Universiti of Kebangsaan Malaysia, Department of Civil Engineering, Bandar Baru Bangi, Malaysia
amohdtaib@ukm.edu.my - https://orcid.org/0000-0002-0307-3016

6 Department of Civil Engineering, Al-Maarif University College, Ramadi, Iraq
haitham.afan@gmail.com - https://orcid.org/0000-0002-4957-756X

7 Universiti of Malaya, Department of Civil Engineering, Kuala Lumpur, Malaysia
elshafie@um.edu.my - https://orcid.org/0000-0001-5018-8505

1. INTRODUCTION

The work on incipient sediment motion have been exhaustively conducted since the pioneer work of Shields (1936). Since then, abundant research studies have looked into the phenomenon and studied it in terms of sediment characteristics and flow behaviour, including varying definitions of incipient sediment motion (Buffington and Montgomery, 1997). The accuracy of incipient sediment motion is important in determining the bedload transport (Toriman et al., 2009, Wan Mohtar et al., 2016), sediment resuspension (Wan Mohtar, 2017) and river bank erosion (Toriman et al., 2013). The most commonly used approach to obtain the threshold value for sediment motion is the Shields diagram based on sediment flux, which is an extrapolation of bed load transport rates to zero or low value. This well-established curve was developed based on homogeneous particles on a loose boundary condition. The threshold value of sediment motion can be obtained through the particle Reynolds number, often presented as $Re_* = u_{*c}d/\nu$, where u_{*c} is the critical shear velocity and d is the sediment size. However, with the parameter u_{*c} is in both abscissa and ordinate (from the critical bed shear stress) makes it implicit, hence, the shear velocity has been eliminated from the sediment characteristics and is presented as dimensionless grain size parameter defined by $D_* = \sqrt{g(s-1)d^3/\nu}$ (Yalin, 1972). This parameter presents only the sediment and flow characteristics, eliminating the shear velocity u_{*c} from abscissa which made the interpretation of threshold criteria more straightforward to be solved explicitly.

The presence of sediment has been established to be found even in sewerage pipes, commonly described as 'in-sewer sediment' (Crabtree, 1989; Tait et al., 1998; Seco et al., 2018). When the flow velocity is considerably lower than the critical velocity, the sediment tends to be deposited and, overtime, accumulated to a certain depth. In particular, during dry seasons with low flow, the condition promotes long-term deposition, whereby the deposited sediment changes the surface roughness, affects the velocity distribution, reduces the flow capacity and increases hydraulic resistance (Banasiak et. al., 2005). In European countries, where the sewerage is often combined with storm water sewers, 90 % of the pollution load during storm events is from the accumulated in-sewer sediment (Crabtree, 1989; Schertzinger et al., 2019).

In-sewer sediments carry high loads of both organic and inorganic particles. The fraction of organic and inorganic materials in the sewer sediment mixture depends on catchment characteristics, sewer type, geometry, the type of wastewater and sanitary habits of the population (Banasiak et al., 2005; Regueiro-Picallo et al., 2018). High organic content in the wastewater has high microbial community, which promotes the formation of biofilm on the accumulated sediment, particularly on a stable sediment bed surface (Vollertsen, 2000; Ahyerre et al., 2001; McLellan and Roguet, 2019). The cementing process obviously reduced the effective area of pipes, which consequently resulted in undesirable environmental complications such overflow wastewater spill particularly during storm events.

In sewer pipes, the sediment bed is better presented as rigid boundary condition and the threshold criteria might be different (Novak & Nalluri, 1975; Ashley et al., 2004; Safari et al., 2017). The deposited sediment in pipes may have thickness t_s less than 10 mm and can go up to 100 mm (Ashley et al., 1992), and can be as high as 330 mm in storm water drains (Bong et al., 2014). Even so, due to limited studies on the threshold criteria on rigid boundary conditions, in particular with bed deposits, the established Shields method is still applied in

sewerage and storm networks (Verbanck et al., 1994). Shields described the threshold movement (of a loose-boundary channel) based on shear stress approach, characterising the near bed influence through the critical shear velocity u_{*c}. However, the effect of sediment deposit thickness was not considered, and the characterisation of incipient sediment motion is rendered inaccurate, particularly with increasing deposition thickness. Furthermore, we investigate the variation of u_{*c} on threshold criteria based on two definitions, i.e. bed slope product and the logarithmic law of the wall. Despite estimation of shear stress based criteria being hydraulically correct, presenting as simple mean velocity is more useful and straightforward, particularly concerning the self-cleansing design (Novak and Nalluri, 1975; Bong et al., 2013). Thus, analysis is extended to evaluate the incipient sediment motion on various bed thicknesses, based on the mean flow velocity. This study also incorporates the results from previous work of Salem (1998) which permits a more exhaustive analysis of the influence of sediment deposits in the threshold criteria of sediment movement in a rigid boundary.

2. METHODOLOGY

The experimental works were conducted in a glass walled, tilting flume with dimensions of 0.6 m × 0.4 m × 6.3 m, located at the hydraulic laboratory of Universiti Sains Malaysia. The velocity and discharge values were obtained through readings from an electronic current meter, placed at the inlet of flume. The detailed experimental parameters are described in Table 1. Note that the range of slope S_0, sediment size d_{50} and sediment thickness presented here followed the site characteristics observation by Ab. Ghani et al. (2000).

Table 1 - The experimental parameters conducted, and associated parameters related to the work of Salem (1998).

Parameter	this study	Salem (1998)
Flume width, B(m)	0.6	0.3
Slope, S_0	1/200, 1/350, 1/500, 1/1000	1/500, 1/600, 1/750, 1/1000, 1/1200, 1/1700
Median grain size, d_{50} (mm)	0.81, 1.53, 4.78	0.55, 0.97, 1.80, 3.09, 4.78
Dimensionless grain number D_*	89.6, 232.6, 1297.0	50.6, 116.0, 289.0, 636.6, 180.6
Thickness of sediment deposit, t_s(mm)	d_{50}, 5, 10, 24	d_{50}, 5, 10, 24

The observation section was placed about 3.5 m from the inlet, where the flow was ensured to be uniform and steady by placing a corrugated sheet stack at the front. Sediment with varying bed thickness (as described in Table 1) was filled in the observation section (with the total length up to 2.1 m) and levelled with a trowel.

The flume was slowly filled with water to minimise disturbances to the levelled sediment bed, before reaching the desired water depth. The discharge (i.e. the velocity too) was systematically increased until incipient sediment motion was observed. The definition of incipient sediment motion employed was general intermittent movement, as described by Kramer (1935). The critical mean velocity U_c that is, the velocity when the incipient sediment motion was observed, is defined as the mean (depth) averaged flow velocity.

The fundamental quantity to describe the incipient sediment motion is the dimensionless critical Shields parameter θ_c, described as,

$$\theta_c = \frac{\tau_c}{(\rho_s - \rho)gd}, \tag{1}$$

where $\tau_c = \rho u_{*c}^2$ is the critical bed shear stress, u_{*c} is the critical shear velocity, i.e. a characteristic velocity defined at the near-bed region, $d = d_{50}$ is the mean grain diameter and ρ_s and ρ are the sediment and fluid densities, respectively.

In this study, the critical shear velocity u_{*c} is presented in two forms. One is calculated through the bed-slope product, denoted as the critical shear velocity u_{*cb} was obtained using

$$u_{*cb} = \sqrt{gRS_0}. \tag{2}$$

As the mean critical velocity U_c for each set of experiments were obtained, the critical shear velocity was also calculated using the log-law layer,

$$\frac{U_c}{u_{*cl}} = \frac{1}{\kappa} ln \frac{z}{z_0}, \tag{3}$$

whereby the critical shear velocity calculated using Equation (3) was denoted as u_{*cl}. The symbol κ is denoted as the Von Karman coefficient, taken as 0.4, z_0 is the roughness layer, calculated as $z_0 = d_{50}/30$ and $z = 0.2h$.

Novak and Nalluri (1975) (as cited in Novak and Nalluri, 1984), proposed the representation of incipient sediment motion (in terms of relative particle size (d/R)) as particle critical Froude Number F_d

$$F_d = \frac{U_c}{\sqrt{gd(s-1)}} = a\left(\frac{d}{R}\right)^b, \tag{4}$$

where U_c is the critical mean velocity (obtained at the incipient sediment motion) and R is the hydraulic radius. The coefficients a and b were found as 0.5 and -0.4, respectively. The work of El-Zaemey (1991) incorporated wider sediment sizes, and the coefficients of a and b were found as 0.75 and -0.34, respectively.

Equation (4), also known as densimetric Froude number was found to be better correlated with sediment pickup rate compared to the Shields parameter (Cheng and Emadzadeh, 2015). Taking into account past research, this study investigates the relation of $\theta_c \sim D_*$ and revisits the Equation (4) in a more robust manner. To assess the effect of thickness in a more comprehensive approach, the results obtained from this study are combined with the data

obtained from Salem (1998). The details of Salem's experimental parameters are presented in Table 1. Note that the sediment thickness employed in both studies are similar, which permits a combination of evaluation and analysis, in particular in terms of sediment size.

3. RESULTS AND DISCUSSION

3.1. Representation of the Shields Curve

Fig. 1 shows θ_c against particle Reynolds number D_* for varying slope S_0. The modified Shields curve is also included which was calculated using the empirical function developed by Brownlie (1981), $\theta_c = 0.22D_*^{0.6} + 0.06\exp(-17.77D_*^{0.6})$. The discussion starts with Fig. 1, recalling that θ_{cb} was obtained using u_{*cb}.

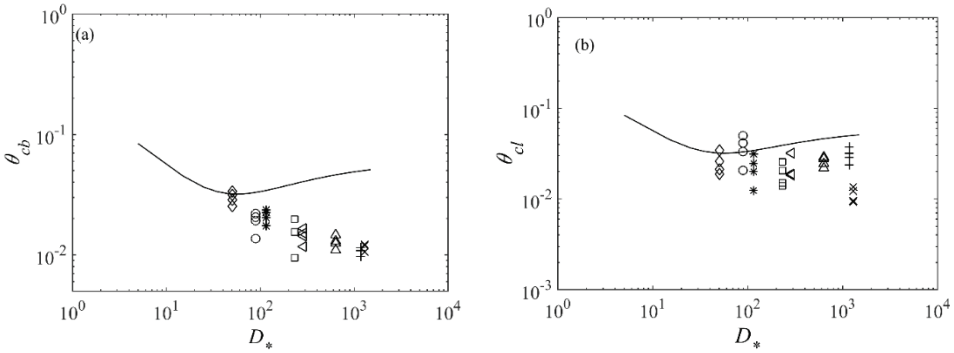

Fig. 1 - Parameter θ_c calculated using (a) bed slope product and (b) log-law. The Shields curve calculated using Brownlie (1981) is also presented, marked here as the solid line. The symbols present particle Reynolds number D_* of 50.6 (◊), 89.6 (○), 116.0 (*), 232.0 (□), 289.0 (<), 636.6 (△), 1180.6 (+) and 1297.0 (×).

In general, the sediment thickness plays an important role for low, dimensionless grain size, i.e. D_*<200 region. A huge gap of $\theta_c$was observed, corresponding to the sediment thickness, where higher sediment thickness requires more forces to observe the incipient sediment motion. As the particle size gets bigger, that is for D_*>200, the effect of sediment thickness became insignificant where the range of θ_c became narrower. As the bed slope S_0 gets higher, the horizontal weight forces $W_x = WgS_0$ becomes more evident and contributes to the movement due to self-weight. The symbol Wrepresents the submerged weight particle; assuming the sediment grain is spherical, W is calculated as $W = \pi(s-1)\rho g d^3/6$. Therefore, the fluid forces needed to initiate sediment movement are less, even with the thicker sediment depth.

Most, if not the majority of the data fall well below the Shields curve. The obtained θ_{cl} are about two orders of magnitude smaller than the traditional Shields curve. The θ_{cl} obtained using the log law provides better representation compared to the ones in Fig. 1a, when the critical Shields parameter was calculated using u_{*cb}. Although the profile is rather similar, where both critical Shields parameter are low as D_* increases, the θ_{cl} consistently has a higher

value than θ_{cb}. Moreover, the θ_{cl} falls closer to the Shields line compared to θ_{cb}. This difference in the magnitude is only within the order of [10^{-1}]. This indicates that, for better incipient sediment motion, the shear velocity using log-law has a better approximation.

For $t_s = d_{50}$, the θ_c obtained by both methods were similar, particularly for $D_* \leq 200$ and significantly deviates for a larger particle size. However, increasing $t_s$to 5 mm shows that the $\theta_c$value obtained by both methods started to depart even for $D_* \leq 200$. The difference became more apparent as the sediment thickness was increased to 10 mm and 24 mm. The deposited sediment evidently influences the value of the bottom friction factor *f* and increased the surface roughness of the pipe. The often-adopted depth-slope based shear stress $\tau = \rho g H S_0$ does not take into account the influence of bottom friction factor *f*. The mean wall shear stress calculated based on the Darcy's $\tau = \frac{1}{8} f \rho (U_c^2)$ can be more than five times compared to the (basic) type based pipe roughness when t_s= 24 mm.

3.2. Representation of Particle Critical Froude Number

The data of F_d against d_{50}/y_0 was plotted for each sediment size D_*. Fig. 2 shows the representation of a typical F_d-d_{50}/y_0 plot, where the effect of thickness is evident. F_d was consistently higher for the lowest t_s and steadily decreased as $t_s$was increased. Based on the data, the influence of t_s (as denominator) in Equation 4 proved to be more salient in the determination of the F_d parameter.

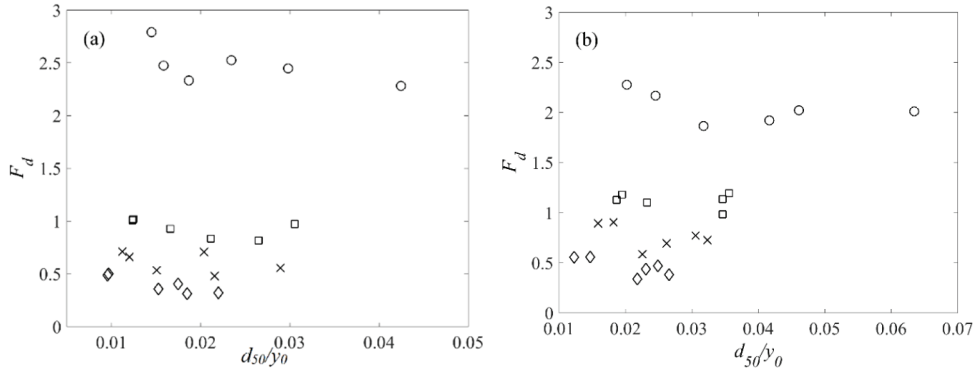

Fig. 2 - Representative plots of F_d against d_{50}/y_0 for sediment sizes d_{50} of (a) 0.55 mm and (b) 0.97 mm. Symbols represent sediment thickness D_* at d_{50} (○), 5 mm (□), 10 mm (×) and 24 mm(◇).

The coefficients of a and power law b were individually obtained through the power law relationship for each sediment thickness t_s and sediment size D_* using Equation (4). In this analysis, the evaluation is extended to the sediment thickness of 50 mm, where the data was taken from the work of Schvidchenko (2000). Figures 3 and 4 show the plots for $a \sim D_*$ and $b \sim D_*$, respectively.

The profile for a will be discussed first. In general, the values of a were found to be relatively constant and independent of D_*. Values of a were found around $1 < a < 2.1$, with an averaged value $a \approx 1.5$ at $t_s = d_{50}$ As the sediment thickness increases to 5 mm, a was found to be less than 1 and falls between the range of 0.5 to 1 (except for D_*= 636). It is acknowledged that this data may be an outlier but was included anyway in the plot to show the variation.

Increasing sediment thickness decreases the coefficient a to a lower value, where $a \approx 0.37$ for t_s= 10 mm. Coefficient a was found at about ≈ 0.2 when the sediment thickness is 24 mm. The sediment bed thickness of 50 mm (taken from the Schvidchenko data) was seen to have a similar trend of decreasing a (with value ≈0.17), but only for D_*<500, whereas, above this value, a was obtained at about ≈ 0.8.

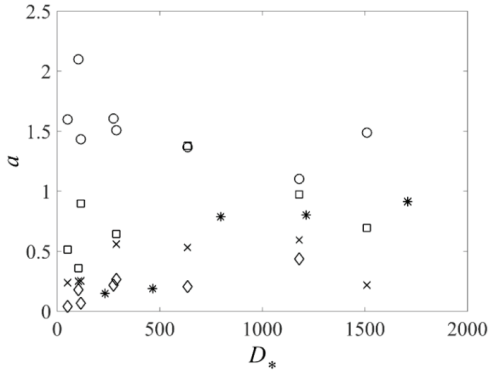

Fig. 3 - The determined coefficient a against D_* for varying sediment thickness t_s; d_{50} (○), 5 mm (□), 10 mm (×), 24 mm (⋄) and 50 mm (∗).

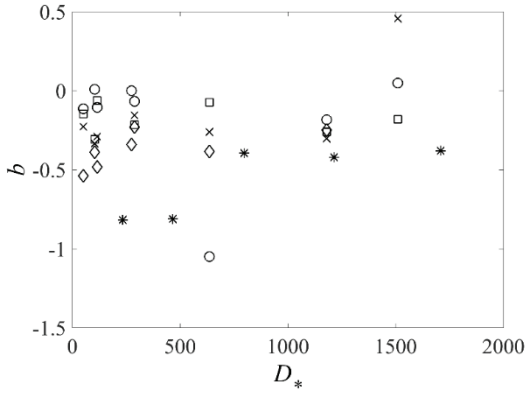

Fig. 4 - The determined coefficient b against D_* for varying sediment thickness t_s; d_{50} (○), 5 mm (□), 10 mm (×), 24 mm (⋄) and 50 mm(∗).

A decreasing trend of coefficient a as sediment thickness t_s is increased, was observed. This indicates that for a fixed sediment size, the critical velocity U_c decreased as the sediment thickness increased. Thicker sediment resulted in an increase of the surface roughness on the rigid boundary, simultaneously decreasing U_c.

Next, the relationship of $b \sim D_*$ is analysed on. The profile of power law b shows a similar trend where, as t_s increases, coefficient b was found to be consistently decreased (except for t_s= 50 mm at high D_*), which shows an adverse pattern with coefficient a. Interestingly, the power law b was about ≈ 0.4 for D_*> 500 but has significantly decreased to about 0.8 for lower D_*. The summary of coefficients a and b are presented in Table 2 along with the values obtained from previous studies of Novak & Nalluri (1984) and El-Zaemey (1991). Note that the values a and b for t_s= 50 mm from the Schvidchenko data was omitted due to unexplainable disparities of both coefficients a and b between low and high D_*.

Table 2 - Summary of coefficients a and b for different sediment thickness t_s and comparison with values obtained from Novak & Nalluri (1984) and El-Zaemey (1991).

Study	t_s (mm)	a	b
Novak & Nalluri (1984)	1	0.5	-0.4
El-Zaemey (1991)	1.5	0.75	-0.34
this study	d_{50}	1.53	-0.18
	10	0.78	-0.18
	5	0.38	-0.26
	24	0.20	-0.38

The values of coefficient a and power law b obtained in this study were within the similar range as the values reported in the works of Novak & Nalluri (1984) and El-Zaemey (1991). Even so, it is worth highlighting that the same range of 0.3 <b<0.4 were obtained despite the higher t_s used in this study.

Obviously higher threshold criteria are needed for $t_s \approx d_{50}$, believed due to the hydraulically smooth behaviour at near bed. The finer sediment size, in particular, lies well within the laminar sub-viscous layer and higher fluid forces are needed to initiate movement and sediment entrainment. Within this layer, the viscous stresses are dominant and reduced the local fluid velocity. It is noted that the smaller size discussed here is D_* = 89.6 (i.e. 0.55 mm), which is considered medium sand and usually not associated with a hydraulically smooth region. But it is anticipated that for smaller sediment size, in particular for d_{50}<0.2 mm, it will be the case.

On the other hand, increasing t_s subsequently increased the surface roughness where a hydraulically rough region is highly likely. The bed roughness inhibits the formation of the viscous sublayer, exposing the sediment particles to the near-bed turbulence, causing them to be more easily entrained (Wan Mohtar & Munro, 2013).

Fig. 3 shows that the deposit thickness is an important parameter, where the constant coefficient a value as given in Equation (4) might provide an inaccurate representation of F_d. To assess the influence of grain-bed ratio d_{50}/t_s in coefficients a and b, Fig.5 depicts plots of both coefficients with d_{50}/t_s.

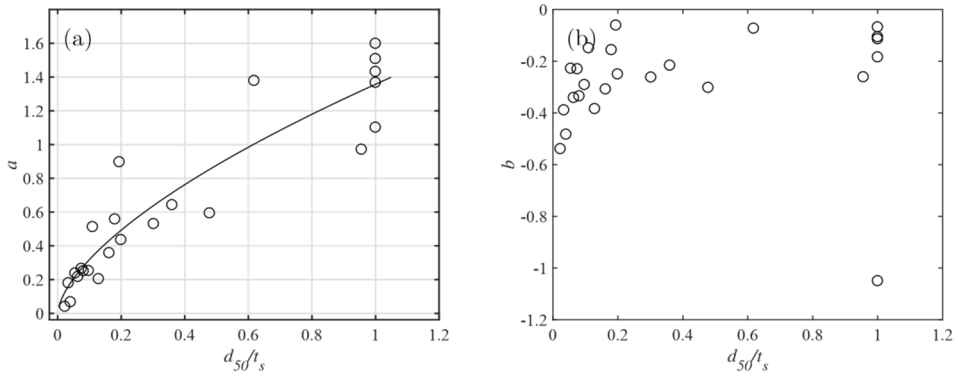

Fig. 5 - The relation of d_{50}/t_s against coefficients (a) a and (b) b.

The coefficient a increases as grain-bed ratio increases and lies within the range 1 ~ 1.6 for d_{50}/t_s= 1. As d_{50}/t_s<1, the value of a gradually decreases and becomes close to ~ 0 when $d_{50}/t_s \ll 1$. Based on the data, a dependency of coefficient a on the ratio of sediment size to deposit thickness is obvious. A regression analysis on the data was performed and shows a power law relationship as $a = 1.46(d_{50}/t_s)^{0.74}$. On the contrary, the power law b is independent on the d_{50}/t_s ratio, and it can be said (by averaging the b values for all set of data except for $t_s = d_{50}$) that $b \approx -0.29$. In comparison, the averaged coefficient b obtained in this study is much lower than the values obtained in the works of Novak & Nalluri (1975) and El-Zaemey (1991).

Substituting the relation of a into Equation (4), a better accuracy to find the critical velocity for sediment deposit in a rigid pipe is presented as

$$F_{d,c} = \frac{U_c}{\sqrt{gd(s-1)}} = 1.46\left(\frac{d_{50}}{t_s}\right)^{0.74}\left(\frac{d_{50}}{y_0}\right)^{-0.25} . \quad (5)$$

3.3. Comparison of Empirical Equations

The performance of predicted F_d, obtained from Equation (5) is assessed by comparing with calculated F_d through the Novak & Nalluri (1984) and El-Zaemey (1991) equations. Fig. 6 shows that the developed equation managed to well incorporate the effect of sediment bed thickness. Despite overestimation, at larger F_d (that is at lower thickness), the equation is able to provide an accurate F_d (hence, critical velocity) value at higher sediment thickness. Most of the data falls close to the line of agreement. This is useful as the thickness of the sediment deposit in rigid pipes (or open channels) is often much larger than the median grain size d_{50}.

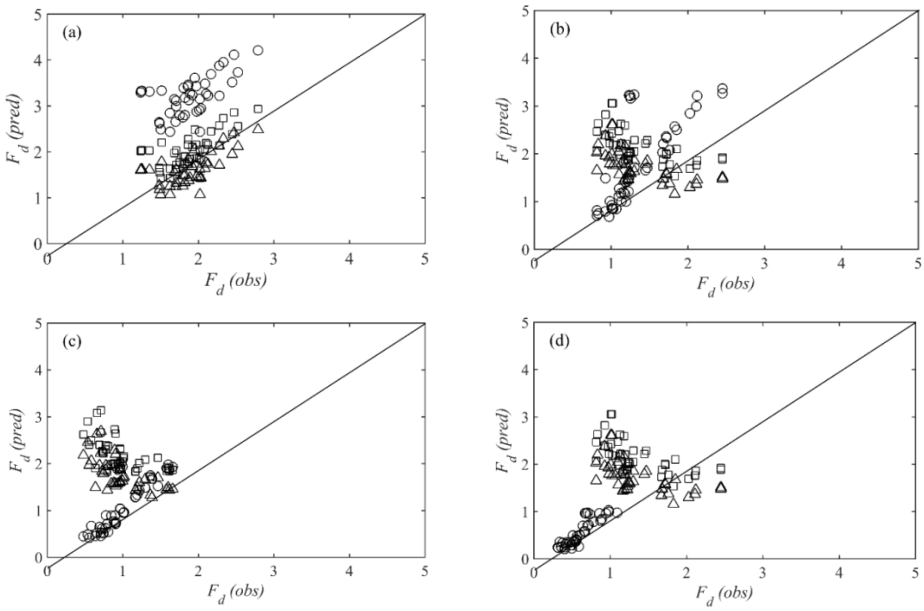

Fig. 6 - The performance of predicted F_d based on El-Zaemey's (□), Novak's (△) and proposed equations (i.e. Eq. 5) (○) for bed thicknesses of (a) d_{50}, (b) 5 mm, (c) 10 mm and (d) 24 mm.

Interestingly, Fig. 6 (a) shows that the prediction of F_d through both Novak and Nalluri (1984) and El-Zaemey (1991) equations work well for higher F_d, where the data points coincide well with the line of agreement. On the contrary, calculated F_d for $t_s = d_{50}$ is consistently overestimated, and deviates from the line of agreement. Therefore, to analyse the influence of bed depth, the data is revisited and individually plotted according to the sediment thickness to determine the feasibility of both El-Zaemey and Equation (5), shown in Fig. 6 (b), (c) and (d) for t_s= 5, 10 and 24 mm, respectively.

Data in Fig. 6 shows that the prediction of F_d is good when using both Novak and Nalluri's and El-Zaemey's equations for $t_s = d_{50}$. It is worthwhile to highlight that although both equations provide similar efficiency (based on the concentrated values close to the line of agreement), the El-Zaemey based F_d are slightly overestimated whilst the Novak and Nalluri equation on the other hand underestimated the F_d.

However, as thickness increases and the ratio $\frac{d_{50}}{t_s} < 1$, the suitability of Novak and Nalluri's and El-Zaemey's equations diminishes where calculated F_d by Equation (5) proved to have better prediction. In Fig. 6(c), where thickness is 10 mm, the critical Froude number calculated using Equation (5) lies well on the line of agreement. The validity of developed Froude number equation becomes more evident at higher bed thickness (or low grain-bed ratio), where the prediction values are concentrated on the line of agreement. Values calculated using both Novak and Nalluri's and El-Zaemey's equations, on the contrary, deviated from the line of agreement. It is interesting to observe that F_d using both Novak and

Nalluri's and El-Zaemey's equations are mostly overestimated up to three times more, in particular for thicker deposition at $t_s \geq 5$ mm.

Based on the analysis, this study proposed the calculation of critical velocity (through Froude number) for rigid pipes as

$$F_d = 0.75\left(\frac{d_{50}}{R}\right)^{-0.34} \quad \text{for} \quad t_s = d_{50} \text{ and,}$$

$$F_d = 1.46\left(\frac{d_{50}}{t_s}\right)^{0.74}\left(\frac{d_{50}}{y_0}\right)^{-0.25}, \quad \text{for } t_s > d_{50}. \tag{6}$$

The subjectivity of the definition of sediment incipient motion that is based on the interpretation of a researcher is believed to be one of the elements in the deviation of available equations. This study described the parameter F_d based on the incipient sediment motion as adopted by Novak and Nalluri (1984), whereas El-Zaemey (1991) presented the limitation of movement is based on the threshold of sediment deposition in sewer pipes. The Shields entrainment curve (which furnishes the value of θ_c) for a range of sediment when described based on initial deposition criteria, lies above the trend obtained based on incipient motion (Safari et al., 2014).

4. CONCLUSIONS

In this paper, the threshold criteria of sediment motion with varying sediment thickness t_s ranging from d_{50} to 50 mm is reported. Using a set of homogeneous sediment with diameters from 0.55 mm to 4.75 mm, a series of experiments were conducted to obtain the critical mean velocity U_c for sediment movement. Attention was also focused on evaluating the Shields curve, whereby the shear critical velocity $u_{*c}$was expressed using the bed-slope product and log law. Both sets of data displayed underestimation of critical Shields parameter θ_c, which is well below the traditional Shields curve. Increasing sediment thickness was found to subsequently increase the θ_c, particularly for lower Reynolds particle number D_*, whereas for higher sediment size, a relatively constant $\theta_c$was observed and can be said to be independent of t_s.

We also expressed the threshold criteria based on the increasingly received attention parameter of particle critical Froude number F_d to obtain the mean critical fluid velocity U_c. A higher value of U_c is needed for smaller sediment thickness and decreased as the thickness gets bigger. For smaller t_s, U_c exponentially increased as the sediment size got bigger but the big variation of U_c lessen as the sediment bed gets thicker. The effect of sediment bed thickness is rather evident and should be taken into account in the engineering design, particularly in the determination of self-cleansing velocity in rigid pipes.

Acknowledgments

The first author thanks the Ministry of Higher Education for the Fundamental Research Grant Scheme FRGS/1/2018/TK01/UKM/02/4 and the second author expresses gratitude to Universiti Malaysia Sarawak for financial support under the MyRA Special Grant Scheme (Grant No.: F02/SpGS/1542/2017).

References

[1] Ab. Ghani, A., Zakaria, N. A., Kassim, M. and Nasir, B. A. Sediment size characteristics of urban drains in Malaysian cities. Urban Water Journal. 2(4):335341, 2000.

[2] Ahyerre, M., Chebbo, G., and Saad, M. Nature and dynamics of the water sediment interface in combined sewers. J. Environ. Eng. ASCE. 127(3):233239, 2001.

[3] Ashley,R. M., Wotherspoon, D. J. J., Coghlan, B. P. and McGregor, I. The erosion and movement of sediments and associated pollutants in combined sewers. Water Science and Technology. 25:101-114, 1992.

[4] Ashley, R. M., Bertrand-Krajewski, J.-L., Hvitved-Jacobsen, T. and Verbanck, M. Solids in Sewers Characteristics, Effects and Control of Sewer Solids and Associated Pollutants. IWA Publishing, London, 2004.

[5] Banasiak, R., Verhoeven, R., De Sutter, R. and Tait, S. The erosion behaviour of biologically active sewer sediment deposits: Observations from a laboratory study. Water Research. 39:5221-5231, 2005.

[6] Bong, C. H. J., Lau, T. L., and Ab. Ghani, A. Verification of Equations for Incipient Motion Studies for a Rigid Rectangular Channel. Water Science and Technology. 67(2):395-403, 2013.

[7] Bong, C. H. J., Lau, T. L. and Ab. Ghani, A. Sediment size and deposition characteristics in Malaysian urban concrete drains-a case study of Kuching city. Urban Water Journal. 11(1):74-89, 2014.

[8] Bong, C. H. J., Lau, T. L., Ab. Ghani, A. and Chan, N.W. Sediment deposit thickness and its effect on critical velocity for incipient motion. Water Science and Technology. 74(8):1876-1884, 2016.

[9] Brownlie, W. Prediction of flow depth and sediment discharge in open channels. Tech. Rep. No. Report No. KH-R-43A. Pasadena, California: California.Inst. Tech., 1981.

[10] Buffington, J. M. and Montgomery, D. A systematic analysis of eight decades of incipient motion studies, with special reference to gravel-bedded rivers. Water Res. Res. 33:19932029, 1997.

[11] Cheng, N. and Emadzadeh, A. Estimate of sediment pickup rate with the densimetric Froude number. Journal of Hydraulic Engineering. 06015024, 2015.

[12] Crabtree, R.W. Sediments in sewers. J. Inst. Water Environ. Manage. 3:569578, 1989.

[13] El-Zaemey, A. K. S. Sediment Transport Over Deposited Bed Sewers. PhD Thesis, University of Newcastle upon Tyne, 1991.

[14] Kramer, H. Sand mixtures and sand movement in fluvial models. Transaction, ASCE. 100:798-878, 1935.

[15] McLellan, S.L., Roguet, A. The unexpected habitat in sewer pipes for the propagation of microbial communities and their imprint on urban waters. Current Opinion in Biotechnology, 57, 34-41, 2019.

[16] Novak, P. and Nalluri, C. Sediment transport in smooth fixed bed channels. Journal of the Hydraulics Division. 101:1139-1154, 1975.

[17] Novak, P. and Nalluri, C. Incipient motion of sediment particles over fixed beds. Journal of Hydraulic Research. 22(3):181-197, 1984.

[18] Regueiro-Picallo, M., Anta, J., Suarez, J., Jeronimo, P., Jacome, A., Naves, J. Characterization of sediments during transport of solids in circular sewer pipes. Water Science Technology, 2017(1), 8-15, 2018.

[19] Safari, M.J.S., Mohammadi, M., Gilanizadehdizaj, G. On the effect of cross sectional shape on incipient motion and deposition of sediments in fixed bed channels. J. Hydrol. Hydromech., 62(1), 7581, 2017.

[20] Safari, M. J. S., Aksoy, H., Unal, N. E., Mohammadi, M. Experimental analysis of sediment incipient motion in rigid boundary open channels. Environmental Fluid Mechanics, 17(6), 1281-1298, 2017.

[21] Salem, A. M. Incipient motion over loose deposited beds in a rigid rectangular channel, MSc. thesis, Universiti Sains Malaysia, 1998.

[22] Shields, A. Anwendung der ahnlichkeitsmechanik und der turbulentzforschung auf die geshiebebewegung. PhD, Mitt. Preuss. Versuchsanst. Wasserbau Schiffbau, 1936.

[23] Schertzinger, G., Zimmermann, S., Sures, B. Predicted sediment toxicity downstream of combined sewer overflows corresponds with effects measured in two sediment contact bioassays. Environmental Pollution, 258, 782-791, 2019.

[24] Seco, I., Schellart, A., Gomez-Valentin, M., Tait, S. Prediction of Organic Combined Sewer Sediment Release and Transport. Journal of Hydraulic Engineering, 144(3), 1-14, 2018.

[25] Shvidchenko, A. B. Incipient Motion of Streambeds. PhD tesis, University of Glasgow, Glasgow, UK, 2000.

[26] Tait, S.J., Rushforth, P.J., Saul, A.J. A laboratory study of the erosion and transport of cohesive-like sediment mixtures in sewers. Water Sci. Technol. 37 (1):163170, 1998.

[27] Toriman, M.E., Kamarudin, M.K.A., Idris, M., Jamil, N.R., Gazim, M.B., Abd Aziz, N.A. Sediment concentration and load analyses at Chini River, Pekan, Pahang, Malaysia. Research Journal of Earth Sciences, 1:43-50, 2009.

[28] Toriman, M.E., Ata, F.M., Mohd, K., Idris, M. Bedload sediment profile and effect of river bank erosion on river cross-section. American Journal of Environmental Sciences, 9(4):292-300, 2013.

[29] Verbanck, M. A., Ashley, R. M., Bachoc, A. International workshop on origin, occurrence and behaviour of sediments in sewer systems: summary of conclusions. Water Research. 28(1):187-194, 1994.

[30] Vollertsen, J. and Hvitved-Jacobsen, T. Resuspension and oxygen uptake of sediments in combined sewers. Urban Water. 2:21-27, 2000.

[31] Yalin, M.S. Mechanics of Sediment Transport. Pergamon, New York, 1972.

[32] Wan Mohtar, W.H.M. Junaidi, Sharil, S., Mukhlisin, M. Representative sediment sizes in predicting the bed-material load for non-uniform sediments. International Journal of Sediment Research. 31:79-86, 2016.

[33] Wan Mohtar, W.H.M. Enhanced understanding on incipient sediment motion and sediment suspension through oscillating-grid turbulence experiments. J Zhejiang Univ-Sci A (Appl Phys & Eng). 18(11):882-894, 2017.

[34] Wan Mohtar, W.H.M. and R.J. Munro. Threshold criteria for incipient sediment motion on an inclined bedform in the presence of oscillating-grid turbulence. Phys. Fluids. 25:015103, 2013.

Teknik Dergi, 2022 11487-11505, Paper 644

Teaching-Learning Based Optimization of Nonlinear Isolation Systems under Far-Fault Earthquakes

Seda ÖNCÜ-DAVAS[1]
Rasim TEMÜR[2]
Cenk ALHAN[3]

ABSTRACT

Seismic isolation systems exposed to far-fault earthquakes can reduce floor accelerations and story drift ratios to acceptable levels. However, they exhibit different structural performances in each earthquake due to different excitation frequency contents. By optimizing the isolation system parameters, their performance may be maintained at the best level under different far-fault earthquakes. In this study, the optimization of the parameters of the nonlinear isolation system of a 5-story benchmark building is performed by Teaching-Learning Based Optimization (TLBO) algorithm to minimize peak floor accelerations under historical far-fault earthquakes with and without exceeding a specified base displacement limit. According to the results of the analyses, it can be said that TLBO algorithm is a robust algorithm with low standard deviations for determining optimum nonlinear isolation system parameters.

Keywords: Seismic isolation, nonlinear isolation system, optimization, far-fault earthquake.

1. INTRODUCTION

Seismic isolation is one of the structural control techniques used to protect buildings against severe earthquake effects and improve their structural performance. The main principle of seismic isolation is based on lengthening the fundamental period of the structure via the use of laterally flexible isolation elements placed between the foundation and the structure. As the structure period is moved away from the dominant earthquake period, effective earthquake forces acting on the structure are reduced. In addition, earthquake energy can be dissipated due to the hysteretic damping during the earthquake; thus, the energy transmitted from the foundation to the structure can be limited. Also, the superstructure moves like a

Note:
- This paper was received on October 16, 2019 and accepted for publication by the Editorial Board on June 26, 2020.
- Discussions on this paper will be accepted by March 31, 2022.
- https://doi.org/10.18400/tekderg.633636

1 İstanbul University - Cerrahpaşa, Department of Civil Engineering, İstanbul, Turkey - seda.oncu@istanbul.edu.tr - https://orcid.org/0000-0001-5023-1980

2 İstanbul University - Cerrahpaşa, Department of Civil Engineering, İstanbul, Turkey - temur@istanbul.edu.tr - https://orcid.org/0000-0001-7154-2286

3 İstanbul University - Cerrahpaşa, Department of Civil Engineering, İstanbul, Turkey - cenkalhan@istanbul.edu.tr -https://orcid.org/0000-0002-6649-8409

rigid block on the isolation system, which helps to reduce the inter-story drifts further. This way, inter-story drifts and floor accelerations can be reduced simultaneously [1]. Thus, structural and/or non-structural damages that may occur in the superstructure can be avoided.

Seismic isolation technique is used for both improving seismic performance of existing structures and earthquake-resistant design of new structures. This method is mostly preferred in hospitals, financial centers, telecommunication centers, etc. where serviceability is essential during and after earthquakes. Seismic isolation has attracted significant attention from researchers during the last forty years and is practically applied especially in the US, Japan, China, New Zealand, Italy, and Turkey [2]. The isolators used in the seismic isolation systems can be categorized into two main groups as rubber-based and friction-based. Rubber-based seismic isolators are also divided into three main types as low damping rubber bearings (LDRB), high damping rubber bearings (HDRB), and lead-rubber bearings (LRB). Among them, high damping rubber bearings (HDRB) and lead-core rubber bearings (LRB) exhibit nonlinear hysteretic behavior. The behavior is typically close to bi-linear, which is clearly observed in the force-displacement relationships of such isolators [3].

Properly designed seismic isolation systems can be very successful by effectively reducing floor accelerations and inter-story drift ratios to acceptable levels without causing excessive base displacement demands when they are especially subjected to typical far-fault earthquakes. The observed performances of seismically isolated buildings under historical earthquakes support this finding. For example, the peak top floor acceleration of the seismically isolated USC hospital building under the 1994 Northridge earthquake was reduced to 50% of the maximum ground acceleration. Peak inter-story drifts were also found to be less than 30% of the value specified in the design code [4]. Likewise, seismically isolated West Japan Computer Center Building performed well in the 1995 Kobe earthquake [1]. On the other hand, seismically isolated buildings can be exposed to far-fault earthquakes with different frequency contents which would lead to different base displacement and floor acceleration demands. In this case, by optimizing the isolation system parameters, it can be ensured that optimum seismic performance is attained under different far-fault earthquakes.

Optimum isolation system parameters can be obtained by using metaheuristic optimization algorithms that provide successful results in many engineering problems. Metaheuristic optimization algorithms employ processes in which one or more objective functions that are determined explicitly specific to the problem and are maximized or minimized within the allowed number of cycles. Examples of metaheuristic algorithms, most of which are inspired by nature, are given as Genetic Algorithm (GA) [5], Ant Colony Optimization (ACO) [6], Particle Swarm Optimization (PSO) [7], Artificial Bee Colony Optimization (ABC) [8] and Teaching-Learning Based Optimization (TLBO) [9].

Optimum isolation system parameters can also be determined by systematically changing these parameters and monitoring the seismic performance. In such studies [10-12], isolation system parameters that yield the best seismic performance are selected and labeled as the optimum. However, true optimization can only be reached by using optimization methods. There exist a very limited number of studies in the literature in which the optimum values of the isolation system parameters are determined using optimization methods. In a study conducted in this context [13], the parameters of the *linear* isolation system of seismically isolated buildings exposed to historical earthquakes were optimized by the Harmony Search (HS) method. In the study conducted by Çerçevik and Avşar [14], Crow Search algorithm

was used to determine the optimum *linear* isolation system parameters of the same benchmark seismically isolated building. For optimizing *nonlinear* isolation systems, the Genetic Algorithm (GA), which is another old optimization algorithm, was applied by Pourzeynali and Zarif [15] to high rise shear-type seismically isolated building under strong ground motions. Unlike these studies, in this study, optimization of nonlinear isolation system parameters via Teaching-Learning Based Optimization (TLBO) algorithm is presented in the context of a medium-rise prototype building exposed to historical far-fault earthquakes. The optimization process has been realized using TLBO because this algorithm typically gives more consistent results compared to many other meta-heuristic algorithms. Furthermore, unlike many other meta-heuristic algorithms, TLBO does not require any algorithm-specific parameters [16-19]. The objective function in determining the optimum values of the isolation system parameters in this study is set as minimizing peak top floor acceleration with and without exceeding a specified base displacement limit. Thus, the robustness of TLBO is evaluated for obtaining optimum values of the non-linear isolation system parameters.

In this context, primarily the formulation of nonlinear seismic isolation system is introduced in Section 2. The properties of the TLBO algorithm used in the study are briefly given in the next section. Then, the implementation of TLBO algorithm to the optimization of nonlinear isolation systems is described in Section 4. Finally, optimization process is performed for a numerical example and the results are presented.

2. STRUCTURAL MODEL

The structural model of the seismically isolated building used in this study consists of a superstructure and a non-linear base isolation system containing rubber bearings with non-linear behavior (Figure 1 (b)) [10]. A stick model with floor stiffnesses $k_1=k_2=k_3=k_4=k_5$ and floor masses $m_1=m_2=m_3=m_4=m_5=m_{izo}$ is used for which the superstructure floor stiffness and floor mass values are adjusted so that the first-mode fixed-base fundamental period of the superstructure is 0.5 s. The modal damping ratio of the superstructure is taken as 3% for all modes. Besides, it is assumed that the displacements in the superstructure stay within elastic limits during the earthquake simulations.

The nonlinear behavior of isolation systems can be defined mathematically by the Bouc-Wen model [20] shown in Figure 1 (a). The main mechanical parameters of the rubber isolators are the pre-yield stiffness (K_1), the post-yield stiffness (K_2), the characteristic force (Q), the yield force (F_y) and the yield displacement (D_y). Here, the maximum strength (F_{max}) corresponds to maximum base displacement (D). The total post-yield stiffness (K_{2t}) can be calculated using Equation 1, depending on the target isolation system period (T_0) and the total mass of the building (m_t) [10].

$$T_0 = 2\pi \left(m_t / K_{2t} \right)^{1/2} \tag{1}$$

In determining the total characteristic force (Q_t) of the isolation system, the target total characteristic force ratio (Q_t/W) is taken into account. By considering the total characteristic force (Q_t) and the yield displacement (D_y), the total pre-yield stiffness is calculated as [1]:

$$K_{1t} = Q_t / D_y + K_{2t} \tag{2}$$

The post-yield to pre-yield stiffness ratio is obtained by Equation (3).

$$\alpha = K_{2t} / K_{1t} \tag{3}$$

Depending on the total pre-yield stiffness (K_{1t}) and the yield displacement (D_y), the total yield force (F_{yt}) is calculated as in Equation (4)

$$F_{yt} = D_y K_{1t} \tag{4}$$

Then, by dividing K_{1t}, K_{2t}, Q_t/W, and F_{yt} by the total number of isolators, the pre-yield stiffness K_1, the post-yield stiffness K_2, the characteristic force (Q) and the yield strength F_y are obtained for each individual rubber bearing.

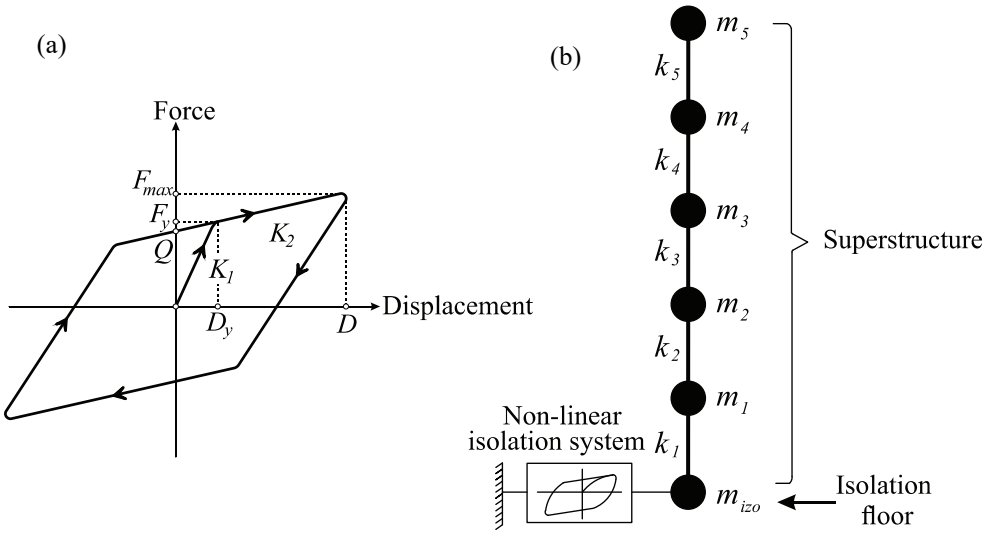

Figure 1 - (a) Bi-linear hysteretic model that represents nonlinear isolation system behavior, (b) Schematic representation of the structural model

3. TEACHING-LEARNING BASED OPTIMIZATION (TLBO) ALGORITHM

Optimization algorithms are processed in a way where one or more objective functions determined in a problem-specific manner are maximized and/or minimized within the allowed number of cycles. One of the metaheuristic algorithms is "Teaching-Learning Based Optimization" (TLBO) algorithm presented by Rao et al. [9] who were inspired by the learning process. According to TLBO, the learning process is divided into 'teacher phase' and 'learner phase'. The first stage represents the learners' learning process from the teacher.

At this stage, a teacher attempts to increase the average success of the class in the subject taught by her/him and new solutions are generated using Equation (5)

$$X_{new} = X_{old} + rnd \cdot \left(X_{teacher} - T_F \cdot X_{mean} \right) \tag{5}$$

where X_{new} is a new value, X_{old} is the former value, *rnd* is the random number generated between 0 and 1, $X_{teacher}$ is the value of the best solution, T_F is the teaching factor, and X_{mean} is the mean value of all candidate solutions. Teaching factor takes a value of either 1 or 2 and is formulated as:

$$T_F = round\left[1 + rnd\right] \tag{6}$$

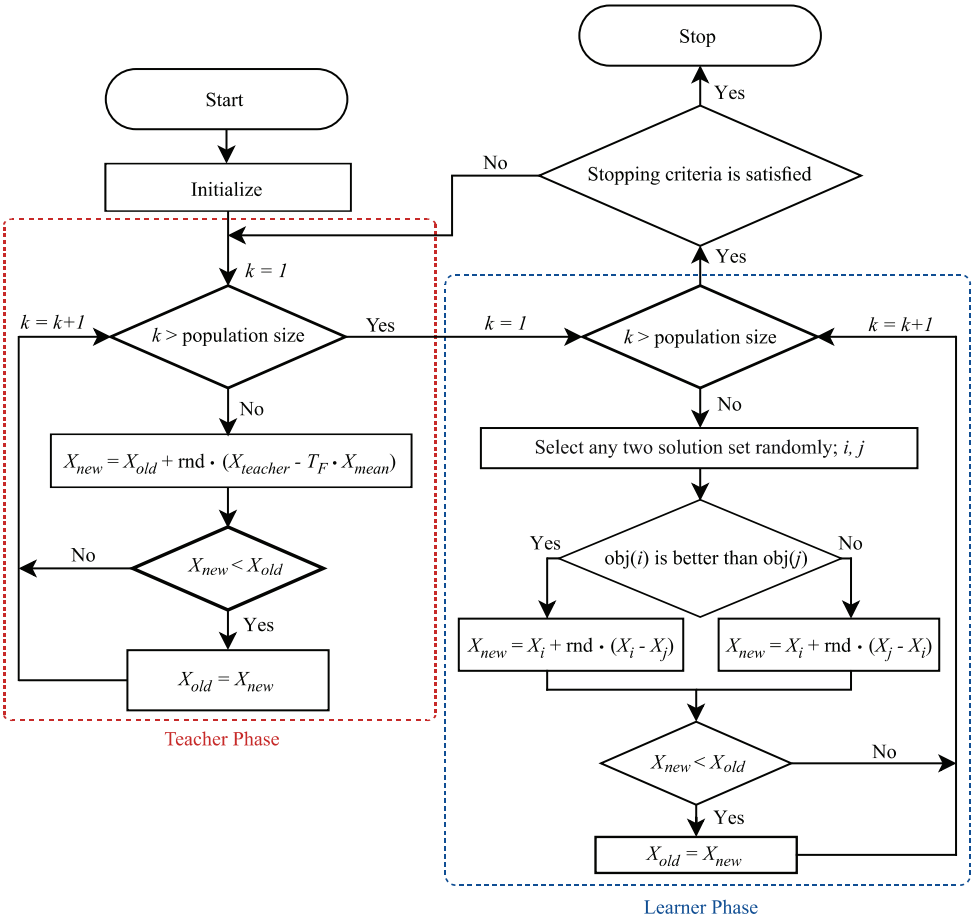

Figure 2 - The flowchart of the TLBO algorithm

The second stage represents the learners' learning experience through out-of-class and group work. In other words, a learner develops his/her knowledge by randomly interacting with other learners. The population determined within the algorithm consists of learners and teachers. New solutions are generated as below at the learner phase:

$$X_{new} = \begin{cases} X_{old} + rnd \cdot \left(X_i - X_j \right) & if \quad f(X_i) > f(X_j) \\ X_{old} + rnd \cdot \left(X_j - X_i \right) & if \quad f(X_j) > f(X_i) \end{cases} \tag{7}$$

where X_i and X_j are randomly selected solutions that are different from each other. If the new solutions are better than the previous related solutions, they are replaced with each other. The flowchart for the teaching-learning based optimization (TLBO) algorithm is depicted in Figure 2.

4. IMPLEMENTATION OF TLBO FOR THE NON-LINEAR ISOLATION SYSTEM OPTIMIZATION

The scope of the optimization problem examined in this study is to determine the optimum value of the non-linear seismic isolation system parameters of a seismically isolated building via the use of TLBO algorithm. For this scope, three independent design variables (X_1, X_2, X_3) are used to describe the mechanical parameters of the non-linear isolation system, as given in Section 2. Among these mechanical parameters, the isolation system period ($X_1 = T_0$), the yield displacement ($X_2 = Q_t/W$), and the total characteristic force ratio ($X_3 = D_y$) are optimized by selecting them as design variables. Once the design variables are optimized, the dependent variables K_{1t}, K_{2t}, F_{yt}, and α are obtained via Equations (1)-(4).

4.1. Constraints

During the solution of the optimization problem, there may also be parameters set as constraints. A set of constraints to which the solution is subjected to can generally be expressed as follows:

$$lower\ bound \le g_j(X) \le upper\ bound, \qquad j = 1, m \tag{8}$$

in which m is the number of constraints, where m is equal to 2 in this study.

While optimizing the independent design variables, the post-yield to pre-yield stiffness ratio (α) is determined as a constraint ($g_1(X)$) to avoid values beyond reasonable limits representing rubber bearings. In this study, the upper and lower limits of $g_1(X)$ are determined as:

$$0.025 \le g_1(X) \le 0.40 \tag{9}$$

The other constraint of the optimization problem ($g_2(X)$) is considered as the peak base displacement limit (D_{limit}). In this study, $g_2(X)$ is determined as 15 cm, which may be considered as an economical design displacement value for far-fault regions.

$$g_2(X) \leq 15\ cm \tag{10}$$

Further information on the constraints used the in optimization problem is given in the Numerical Example Section.

4.2. Objective Function

In this study, the objective function $f(X)$ is determined under the above-mentioned constraints ($g_1(X)$, $g_2(X)$) during the optimization of the nonlinear isolation system as follows:

$$f(X) = \min(ptfa(X)) + \sum penalty \tag{11}$$

where X is the design variable vector. The design variable vector comprises of total independent design variables. The information about the design variables of this study is given in the Numerical Example Section.

$$X = \{X_1, X_2, X_3\} \tag{12}$$

In the optimization process, if the specified constraints are violated, penalties having a considerable value are assigned to the objective function. Penalty values are calculated separately for the base displacement constraint and the post-yield to pre-yield stiffness ratio (α) constraint as follows:

$$penalty(D) = \begin{cases} \left((pbd - D_{\text{limit}}) \cdot 1000 + 1 \right)^2 - 1 & if \quad pbd > D_{\text{limit}} \\ 0 & if \quad pbd \leq D_{\text{limit}} \end{cases} \tag{13}$$

Here, $penalty(D)$ is the displacement penalty function, pbd is the peak base displacement, D_{limit} is the base displacement limit.

$$penalty(\alpha) = \begin{cases} \left((\alpha - \alpha_{\max}) \cdot 1000 + 1 \right)^2 - 1 & if \quad \alpha > \alpha_{\max} \\ \left((\alpha_{\min} - \alpha) \cdot 1000 + 1 \right)^2 - 1 & if \quad \alpha < \alpha_{\min} \\ 0 & if \quad \alpha_{\min} < \alpha < \alpha_{\max} \end{cases} \tag{14}$$

Where, $penalty(\alpha)$ is the penalty function for post-yield to pre-yield stiffness ratio, α_{max} is the upper limit for α and α_{min} is the lower limit for α. At the end of the optimization process, the final result is reached when the penalty value is equal to 0. In other words, reaching a penalty value of 0 means that the specified constraints are met.

5. NUMERICAL EXAMPLE

In order to obtain the optimum values of non-linear seismic isolation system parameters of the 5-story benchmark seismically isolated building (Figure 1) exposed to historical far-fault earthquakes, the non-linear time-history analyses are performed in 3D-BASIS software [21]. As seen in Figure 3, the optimization process is carried out by recursively running 3D-BASIS software simultaneously with the optimization program generated in MATLAB in the context of this study that employs TLBO algorithm. In the TLBO algorithm, whose flowchart is shown in Figure 2, parameters are determined with design constants and lower and upper limits of design variables. Design constants consist of the mathematical model of the superstructure and the number of isolators, while the design variables consist of the main mechanical parameters of the seismic isolation system.

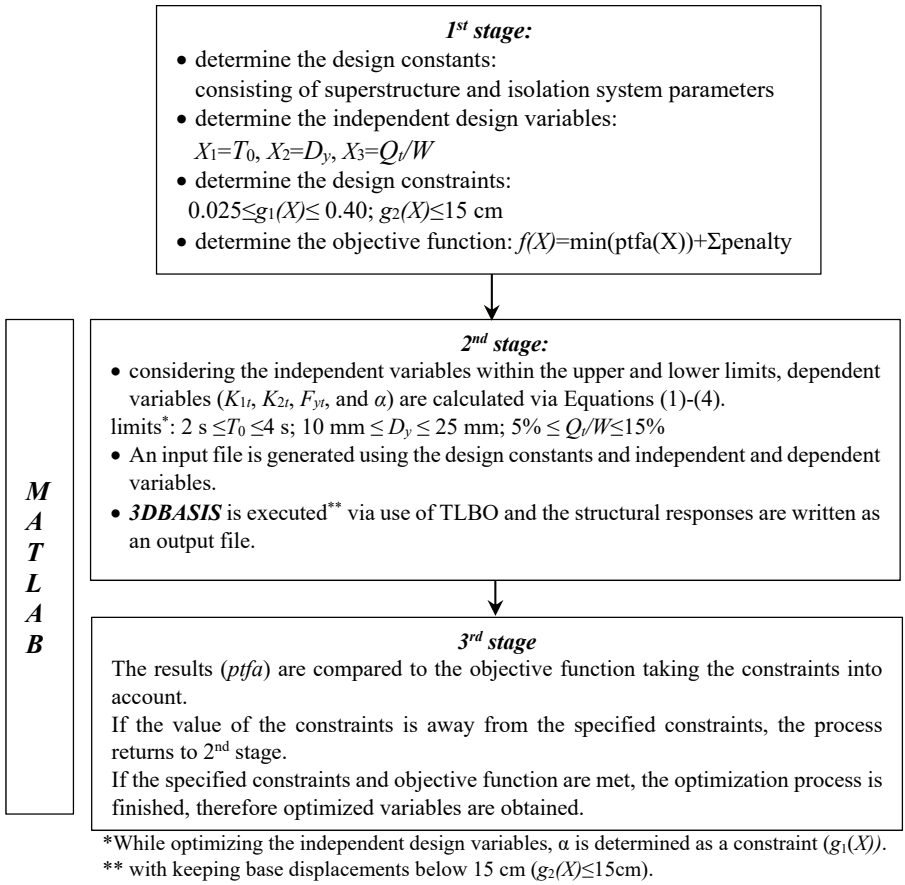

Figure 3 - Schematic illustration of optimization process via use of 3DBASIS and MATLAB software

A range of values is to be specified for each design variable that indicate the upper and lower limit values for the independent design variables. Among the design variables, the isolation

system period ($X_1=T_0$) is specified to remain in the range of 2 s to 4 s, which is a typical range for practical applications [22]. Similarly, the yield displacement ($X_2=D_y$) is selected to be optimized within the range of 10 mm to 25 mm which is a suitable range for rubber isolators ([10], [23]), while the characteristic force ratio ($X_3=Q_t/W$) is taken in the range of 5% to 15% which are typically the smallest and largest values in practical applications ([24], [25]).

While optimizing the independent design variables, the post-yield to pre-yield stiffness ratio (α) is determined as a constraint since otherwise it may attain values beyond reasonable limits representing rubber bearings. According to a study presented by Dicleli and Buddaram [24], the post-yield stiffness to pre-yield stiffness ratio values of 0.025 to 0.10 are attributed to lead-rubber bearings, and the values of 0.133 to 0.40 are attributed to high-damping rubber bearings. Thus, the assumed range of post-yield stiffness to pre-yield stiffness ratio values in this study encompasses a range that represents rubber-based isolators (i.e. both lead-rubber and high-damping rubber bearings). In this study, α is bound by a lower limit of 0.025 and an upper limit of 0.40 ($0.025 \leq g_1(X) \leq 0.40$).

Since the goal of seismic isolation is set as reducing floor accelerations while keeping base displacements below practical and economic limits, the other constraint of this optimization problem ($g_2(X)$) is considered as the peak base displacement (*pbd*). In the literature (e.g. [26]-[28]), it has been observed that the base displacements of the buildings with seismic isolation systems under far-fault earthquakes vary between 10 and 20 cm. Thus, the peak base displacement constraint is determined as 15 cm for far-fault earthquakes which may be considered as an economical design displacement value for far-fault regions. It should be noted that this limit may vary on a project basis. In this study, the optimization process is carried out by minimizing the peak top floor accelerations (ptfa) while keeping base displacements below 15 cm ($g_2(X) \leq 15$cm). The optimization is also carried out without considering the peak base displacement constraint (only for $0.025 \leq g_1(X) \leq 0.40$).

5.1. Earthquake Records

Five different far-fault earthquakes given in Table 1 are used in the optimization process. They are suggested by FEMA P695 [29] and retrieved from the PEER database [30]. In Table 1, information such as recording station, ground motion component name, and peak ground acceleration (PGA), peak ground velocity (PGV), earthquake magnitude (M_w), and closest distances to the fault (r) values are presented. In the time-history analyses, the determined components are applied uni-directionally.

Table 1 - Properties of historical earthquake records

Earthquake	Date	Station	Component	PGA (g)	PGV (m/s)	M_w	r (km)
Imperial Valley-06	10/15/1979	Delta	H-DLT262	0.35	0.33	6.53	22
Kocaeli	8/17/1999	Düzce	DZC270	0.36	0.56	7.51	15.4
Landers	6/28/1992	Coolwater	CLW-TR	0.42	0.43	7.28	19.7
Northridge	1/17/1994	Canyon Country	LOS270	0.47	0.41	6.69	12.4
Northridge-01	1/17/1994	Beverly Hills	MUL279	0.49	0.67	6.69	17.2

5.2. Optimum Population Size

Unlike many other algorithms, TLBO does not need any algorithm-specific parameters. The population size, which is the common control parameter of all heuristic algorithms, is adequate for TLBO to run. Population size affects algorithm performance and the appropriate population size for the type of problem should be determined. Therefore, eight different population sizes are investigated as 5, 10, 15 20, 25, 30, 35, and 40. Results of meta-heuristic optimization algorithms need to be statistically evaluated because they work with randomly generated numbers. For this reason, one hundred independent optimization processes are performed for each population size under five different far-fault earthquake records given in Table 1. The statistical results of the optimization processes, which include the maximum, the minimum, and the mean values and the standard deviations of the peak top floor acceleration (ptfa), are presented in Table 2.

Table 2 - The peak top floor acceleration (ptfa)[1] results obtained from 100 independent optimization process considering different population size without the peak base displacement constraint.

Earthquake Record		***Population Size***							
		5	***10***	***15***	***20***	***25***	***30***	***35***	***40***
CLW-LN	*Min. (m/s^2)*	1.22	1.22	1.22	1.22	1.22	1.22	1.22	1.22
	Max. (m/s^2)	**2.06**	1.22	1.22	1.22	1.22	1.22	1.22	1.22
	Mean (m/s^2)	**1.26**	1.22	1.22	1.22	1.22	1.22	1.22	1.22
	St. Dev.	**0.17**	0.00	0.00	0.00	0.00	0.00	0.00	0.00
DZC270	*Min. (m/s^2)*	1.44	1.44	1.44	1.44	1.44	1.44	1.44	1.44
	Max. (m/s^2)	**1.86**	**1.55**	**1.69**	**1.61**	1.44	1.44	1.44	1.44
	Mean (m/s^2)	**1.51**	**1.44**	**1.45**	**1.45**	1.44	1.44	1.44	1.44
	St. Dev.	**0.09**	**0.02**	**0.03**	**0.02**	0.00	0.00	0.00	0.00
H-DLT362	*Min. (m/s^2)*	0.97	0.97	0.97	0.97	0.97	0.97	0.97	0.97
	Max. (m/s^2)	**1.50**	0.97	0.97	0.97	0.97	0.97	0.97	0.97
	Mean (m/s^2)	**0.99**	0.97	0.97	0.97	0.97	0.97	0.97	0.97
	St. Dev.	**0.09**	0.00	0.00	0.00	0.00	0.00	0.00	0.00
LOS270	*Min. (m/s^2)*	0.99	0.99	0.99	0.99	0.99	0.99	0.99	0.99
	Max. (m/s^2)	**1.75**	**1.32**	0.99	0.99	0.99	0.99	**1.00**	**1.00**
	Mean (m/s^2)	**1.02**	**1.00**	0.99	0.99	0.99	0.99	0.99	0.99
	St. Dev.	**0.11**	**0.05**	0.00	0.00	0.00	0.00	0.00	0.00
MUL279	*Min. (m/s^2)*	1.66	1.66	1.66	1.66	1.66	1.66	1.66	1.66
	Max. (m/s^2)	**1.99**	1.66	1.66	1.66	1.66	1.66	1.66	1.66
	Mean (m/s^2)	**1.67**	1.66	1.66	1.66	1.66	1.66	1.66	1.66
	St. Dev.	**0.04**	0.00	0.00	0.00	0.00	0.00	0.00	0.00

[1]*ptfa values higher than the minimum value and standard deviations greater than 0 are shown in bold.*

It is seen that the minimum values of ptfa under CLW-LN, DZC270, H-DLT362, LOS270, and MUL279 records are obtained as 1.22 m/s^2, 1.44 m/s^2, 0.97 m/s^2, 0.99 m/s^2, and 1.66 m/s^2, respectively. While minimum ptfa values do not change for different population sizes, the maximum values depend on the size of the population. For example, if the population size of 5 is used under CLW-LN record, the minimum ptfa value is 1.22 m/s^2 while the maximum ptfa value is 2.06 m/s^2. In this case, the maximum error ratio is calculated as 69%. Considering the population size of 10 and above, the minimum and maximum ptfa values equalize and thus, the standard deviation value is equal to 0. In case of DZC-270 record, when 5, 10, 15, and 20 populations are considered, the maximum values of ptfa are 29%, 8%, 17%, and 12% higher than those of minimum ptfa values. If the population size is taken as 25 and above, the maximum ptfa value is equal to the minimum ptfa value, and the standard deviation value is 0. Optimization analyses performed with a population size of 5 under H-DLT362 and MUL279 records, the error ratios are obtained as 51% and 20% while the standard deviation values are calculated as 0.09 and 0.04, respectively. When the population size of 10 and above is taken into consideration, the standard deviation is obtained as 0. It has been observed that there is an error ratio of up to 77% for the population size of 5 and 10 under LOS270 record. The minimum and maximum ptfa values are equal for all population sizes between 15 and 30. For the population size of 35 and 40, the maximum values of ptfa are 1% greater than those of minimum values, but the ptfa value is equal to the minimum value, accordingly the standard deviation is 0. Consequently, it is concluded that the population size of 25 and above would be reliable for all cases.

The convergence rate of the optimization process can also be considered as a parameter to determine the performance of population sizes. The mean convergence curves are shown in Figure 4 to examine the effects of different population sizes on convergence rates. The figure depicts the variation of ptfa with respect to the number of analyses for the case where the base displacement limit is not taken into consideration. As seen from the convergence curves, the results obtained using a population size of 5 are significantly different from the other results. When the convergence rates are examined, it can be said that there is no significant difference in the population sizes of 10 or more.

Table 3 - ptfa results obtained from 100 independent optimization process considering the base displacement limit of 15 cm.

Statistical results	Earthquake records				
	CLW-LN	DZC270	H-DLT362	LOS270	MUL279
Min. (m/s^2)	1.22	3.22	1.53	0.99	5.88
Max. (m/s^2)	1.22	3.22	1.70	0.99	5.88
Mean (m/s^2)	1.22	3.22	1.53	0.99	5.88
St. Dev.	0.00	0.00	0.02	0.00	0.00

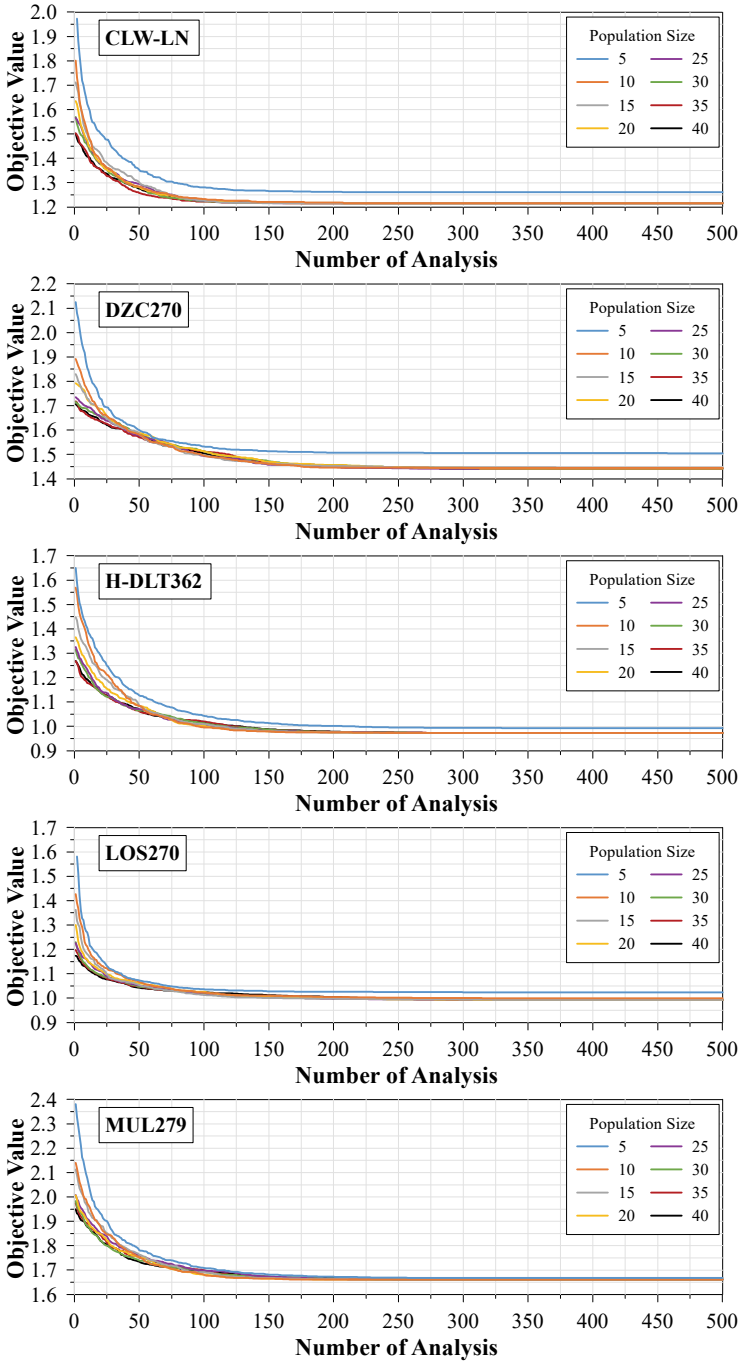

Figure 4 - Convergence curves obtained for different population sizes

As the population size of 25 and above gives reliable results, the 100 independent optimization process with a population size of 25 is performed for each of the five different far-fault earthquake records. The variation of ptfa with respect to the number of analysis is depicted in Figure 5 for the case where the displacement limit of 15 cm is taken into consideration. Each figure shows 100 different optimization processes. Since the base displacements obtained from the analyses under DZC270 and MUL279 records are well above the base displacement limit of 15 cm, penalty values are assigned to the objective function. Therefore, the objective values under DZC270 and MUL279 records are very high in the initial analysis. The statistical results in terms of ptfa obtained by the different optimization processes are presented in Table 3. Accordingly, since the standard deviation is 0 in most cases (exception: H-DLT362 where the standard deviation is 0 .02), it is clear that the results are reliable under all earthquake records.

5.3. Optimum Nonlinear Isolation System

The 100 independent optimization processes with the population size of 25 aiming to minimize the peak top floor accelerations are performed under five different far-fault earthquakes with and without exceeding the base displacement constraint. The optimization process consists of iterative analyses continued until the objective function is reached. When the objective function is satisfied, the optimum nonlinear isolation system parameters including isolation period (T_0), characteristic force ratio (Q_t/W), and yield displacement (D_y) are obtained. Then, the structural response in terms of peak top floor accelerations (*ptfa*) and peak base displacements (*pbd*) are calculated for the corresponding optimum nonlinear isolation system. The optimum nonlinear isolation system parameters and the peak structural responses of the buildings equipped with optimum nonlinear isolation systems are reported in Table 4 and 5 under all earthquake records for cases with and without exceeding the base displacement limits, respectively. It should be noted here that the mechanical parameters of the optimum nonlinear isolation system are within the typical range for practical applications.

Table 4 - Optimum nonlinear isolation system parameters and seismic performance of the buildings equipped with optimum nonlinear isolation system not considering the base displacement limit of 15 cm.

Earthquake records	Peak structural response		Optimum nonlinear isolation parameters		
	pbd (cm)	*ptfa* (m/s^2)	T_0 (s)	Q_t/W	D_y (mm)
CLW-LN	10.35	1.22	3.7	0.05	25
DZC270	**21.89**	1.44	4.0	0.05	25
H-DLT262	**15.91**	0.97	4.0	0.05	25
LOS270	9.36	0.99	3.5	0.05	24
MUL279	**24.62**	**1.66**	**4.0**	**0.05**	**25**

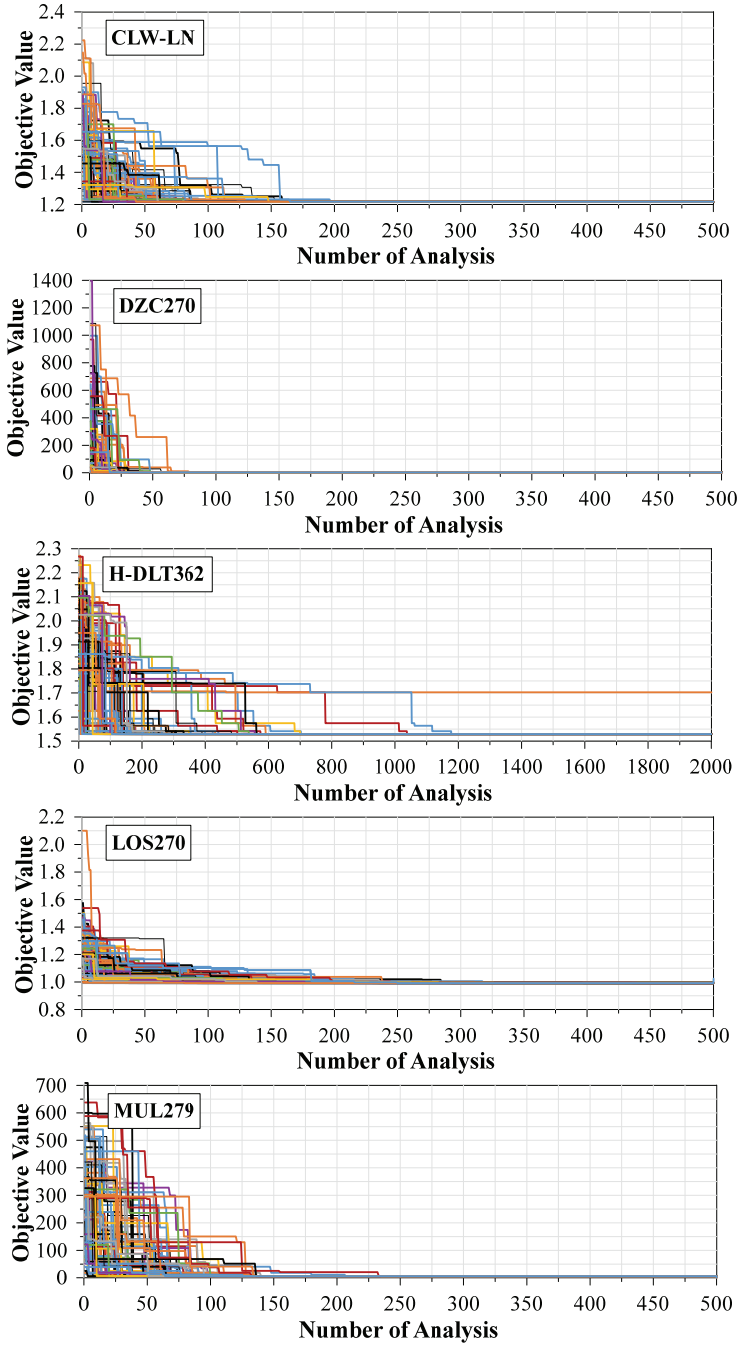

Figure 5 - The variation of ptfa with respect to analysis number under far-fault earthquake records with exceeding the base displacement limit of 15 cm (different lines correspond to 100 independent optimization process)

Table 5 - Optimum nonlinear isolation system parameters and seismic performance of the buildings equipped with optimum nonlinear isolation system considering the base displacement limit of 15 cm.

Earthquake records	Peak structural response		Optimum nonlinear isolation parameters		
	pbd (cm)	*ptfa* (m/s^2)	T_0 (s)	Q_t/W	D_y (mm)
CLW-LN	10.35	1.22	3.7	0.05	25
DZC270	14.78	**3.22**	2.0	0.15	19
H-DLT262	14.95	**1.53**	3.4	0.05	10
LOS270	9.36	0.99	3.5	0.05	24
MUL279	**14.99**	**5.88**	**3.1**	**0.15**	**10**

As seen from Table 4, among the optimum nonlinear isolation system parameters that would perform best under all earthquakes (here the dominant earthquake record is MUL279), isolation period (T_0), characteristic force ratio (Q_t/W) and yield displacement (D_y) are found as 4.0 s, 5%, and 25 mm, respectively. The *pbd* and the ptfa are obtained under MUL279 via nonlinear time-history analyses of the building employing the optimum nonlinear isolation system, and they are calculated as 24.6 cm and 1.66 m/s^2, respectively. When the optimization analyses are conducted under different far-fault earthquakes without exceeding the base displacement limit of 15 cm (see Table 5), T_0, Q_t/W, and D_y are determined as 3.1 s, 15 %, and 10 mm, respectively. In this case, ptfa is obtained as 5.88 m/s^2. Note that, considering the optimum independent variable values, dependent variable values (K_{1t}, K_{2t}, F_{yt}, and α) are calculated via Equations (1)-(4). Then, if desired, the isolation system elements can be dimensioned geometrically using these optimum isolation system parameters.

It can also be seen from Table 4 that *pbd* values under DZC270, H-DLT262, and MUL279 exceed the base displacement limit of 15 cm where the optimum characteristic force ratio (Q_t/W) is 5 %. Considering base displacement limit (Table 5), the peak base displacements obtained under all earthquake records remain below 15 cm while the optimum characteristic force ratio (Q_t/W) is calculated as 15 %. Due to the high damping obtained by increasing the characteristic force ratio (from 5 % to 15 %), ptfa values of the seismically isolated buildings under the earthquake records of DZC270, H-DLT262, MUL279 given in Table 5 are increased compared to the results obtained by not considering the base displacement limit given in Table 4.

The performance of the optimum nonlinear isolation system parameters considering the base displacement limit of 15 cm is also tested under other historical earthquake records and the results are given in the Table 6. As expected, when the seismically isolated buildings with optimum parameters obtained under the most challenging earthquake record (MUL279) ae subjected to other earthquakes, they perform better than the MUL279 record.

Finally, for verifying the optimization process via TLBO, time-history analyses of non-linear isolation systems created by using parameters that deviate ±10% and ±20% from optimum isolation system parameters are performed under the governing earthquake record, MUL279. The results obtained from TLBO optimized cases are compared to those with non-optimum isolation system parameters and presented in Table 7. The results show that the parameters

of the non-linear isolation system larger or smaller than the optimum values cause either higher peak base displacement (pbd) or higher peak top floor accelerations (ptfa) than optimum analysis results.

Table 6 - Analysis result of nonlinear isolation systems with optimum parameters under MUL279 (T_0=3.1 s, Q_t/W=0.15, D_y=10 mm)

Earthquake records	Peak structural response	
	pbd (cm)	*ptfa* (m/s^2)
CLW-LN	10	5.46
DZC270	14.4	4.75
H-DLT262	7.4	4.78
LOS270	12.2	4.86
MUL279	14.99	5.88

Table 7 - Analysis result of nonlinear isolation system parameters deviating from optimum under MUL279.

Deviation of isolation system parameters from optimum	Non-linear isolation system parameters			Peak structural response	
	T_0 (s)	Q_t/W	D_y (mm)	*pbd* (cm)	*ptfa* (m/s^2)
optimum	3.1	0.15	10	14.99	5.88
−10%	2.79	0.14	9	15.46	5.63
+10%	3.41	0.17	11	14.55	6.20
−20%	2.48	0.12	8	16.55	5.45
+20%	3.72	0.18	12	14.28	6.54

6. CONCLUSIONS

In this study, optimization of nonlinear isolation system parameters via Teaching-Learning Based Optimization (TLBO) algorithm is presented in the context of a medium-rise prototype building exposed to historical far-fault earthquakes. The objective function in determining the optimum values of the isolation system parameters is set as minimizing peak top floor acceleration with and without exceeding a specified base displacement. Main accomplishments and findings can be listed as follows:

- A methodology is developed where the optimization process is carried out by recursively running 3D-BASIS software, which performs non-linear time-history

analyses, with an in-house optimization program, which is constructed in MATLAB, that employs TLBO algorithm.

- Population size affects algorithm performance and the appropriate population size for the problem at hand should be determined individually. For the problem evaluated in this study, a population size of 25 was found to be the minimum size required for obtaining a reliable solution.
- As an alternative, the convergence rate of the optimization process can also be considered as a parameter to determine the performance of population sizes.
- The standard deviation of the objective function is obtained as almost 0 for even very small population sizes (i.e 10), indicating that the metaheuristic optimization algorithm TLBO is robust in determining optimum nonlinear isolation system parameters.
- It is shown that using an appropriate population size, TLBO is a robust optimization method that yields optimum values of the non-linear isolation system parameters for achieving minimum peak floor accelerations without exceeding a specified peak base displacement limit under a set of far-fault earthquakes.
- For the benchmark building evaluated here, specifying a base displacement limit resulted in increased characteristic force ratios which indirectly caused increases in peak floor accelerations compared to the case where no limit was specified for the base displacement.

References

[1] Naeim, F., Kelly, J., Design of Seismic Isolated Structures: from Theory to Practice, Newyork. Wiley, 1999.

[2] Martelli, A., Seismic Isolation and Energy Dissipation: Worldwide Application and Perspectives, Earthquake Resistant Engineering Structures VI, Boston, WIT Press, 2007.

[3] Cheng, F.Y., Jiang, H., Lou, K., Smart Structures: Innovative Systems for Seismic Response Control, New York, CRC press, 2008.

[4] Nagarajaiah, S., Xiahong, S., Response of Base-isolated USC Hospital Building in Northridge Earthquake, J. Struct. Eng., 126-10, 1177–1186, 2000.

[5] Goldberg, D.E., Genetic Algorithms in Search, Optimization, and Machine Learning, Machine Learning, 3:2, 95-99,1988.

[6] Dorigo, M., Maniezzo, V., Colorni, A., Ant system: Optimization by a Colony of Cooperation Agents, IEEE Transactions on Systems, Man, and Cybernetics, Part B: Cybernetics, 26:1, 29-41, 1996.

[7] Kennedy, J., Eberhart, R., Particle Swarm Optimization, IEEE International Conference on Neural Networks, Perth, WA, Australia, 1995.

[8] Karaboga, D., Basturk, B.. A Powerful and Efficient Algorithm for Numerical Function Optimization: Artificial Bee Colony (ABC) Algorithm, Journal of Global Optimization, 39(3), 459-471, 2007.

[9] Rao, R.V., Savsani, V.J., Vakharia, D.P., Teaching-learning-based Optimization: A novel Method for Constrained Mechanical Design Optimization Problems, Computer-Aided Design, 43:3, 303-315, 2011.

[10] Matsagar, V.A., Jangid, R.S., Influence of Isolator Characteristic on the Response of Base-isolated Structures, Engineering Structures, 26, 1735-1749, 2004.

[11] Dicleli, M., Buddaram, S., Effect of Isolator and Ground Motion Characteristics on the Performance of Seismic- Isolated Bridges, Earthquake Engineering & Structural Dynamics 35, 233–250, 2006.

[12] Alhan, C., Öncü-Davas, S., Performance Limits of Seismically Isolated Buildings under Near-field Earthquakes, Engineering Structures, 116, 83-94, 2016.

[13] Nigdeli, S.M., Bekdaş, G., Alhan, C., Optimization of Seismic Isolation Systems via Harmony Search, Engineering Optimization, 46:11, 1553-1569, 2014.

[14] Çerçevik, A.E., Avşar, Ö., Doğrusal Sismik İzolasyon Parametrelerinin Karga Arama Algoritması ile Optimizasyonu. Pamukkale Üniversitesi Mühendislik Bilimleri Dergisi, DOI: 10.5505/pajes.2019.93636.

[15] Pourzeynali, S., Zarif, M. Multi-objective Optimization of Seismically Isolated High-rise Building Structures using Genetic Algorithms, Journal of Sound and Vibration, 311(3-5), 1141-1160, 2008.

[16] Rao, R.V., Waghmare, G., Design Optimization of Robot Grippers using Teaching-Learning-Based Optimization Algorithm, Advanced Robotics, 29(6), 431-447, 2015.

[17] Camp, C.V., Farshchin, M., Design of Space Trusses Using Modified Teaching-Learning-Based Optimization, Engineering Structures, 62, 87-97, 2014.

[18] Degertekin, S. O., Hayalioglu, M.S., Sizing Truss Structures using Teaching-Learning-Based Optimization, Computers & Structures, 119, 177-188, 2013.

[19] Temur, R., Bekdaş, G., Teaching Learning-Based Optimization for Design of Cantilever Retaining Walls, Structural Engineering and Mechanics, 57(4), 763-783, 2016.

[20] Nagarajaiah, S., Reinhorn, A.M., Constantinou, M.C., Nonlinear Dynamic Analysis of 3D Base-isolated Structures, J Struct Eng, 117:2035–54, 1991.

[21] Nagarajaiah, S., Reinhorn, A.M., Constantinou, M.C., 3D-Basis: Nonlinear Dynamic Analysis of Three-dimensional Base Isolated Structures: Part II. Technical Report NCEER-91-0005. National Center for Earthquake Engineering, State University of New York at Buffalo; 1991.

[22] Pan, P., Zamfirescu, D., Nakashima, M., Nakayasu, N., Kashiwa, H., Base-isolation Design Practice in Japan: Introduction to the Post-Kobe Approach, J Earthq Eng, 9:1, 147-171, 2005.

[23] Makris, N., Chang, S., Effect of Viscous, Viscoplastic and Friction Damping on the Response of Seismic Isolated Structures, Earthq Eng Struct Dyn, 29, 85-107, 2000.

[24] Dicleli, M., Buddaram, S., Equivalent Linear Analysis of Seismic-isolated Bridges Subjected to Near-field Ground Motions with Forward Rupture Directivity Effect, Engineering Structures, 29, 21-32, 2007.

[25] Providakis, C.P., Effect of Supplemental Damping on LRB and FPS Seismic Isolators under Near-field Excitations, Soil Dyn Earthq Eng, 29, 80-90, 2009.

[26] Tavakoli, H.R., Naghavi, F., Goltabar, A.R., Dynamic Responses of the Base-fixed and Isolated Building Frames under Far-and Near-fault Earthquakes, Arabian Journal for Science and Engineering, 39(4), 2573-2585, 2014.

[27] Bhandari, M., Bharti, S.D., Shrimali, M.K., Datta, T.K., The Numerical Study of Base-isolated Buildings under Near-field and Far-field Earthquakes, Journal of Earthquake Engineering, 22(6), 989-1007, 2018.

[28] Fathi, M., Makhdoumi, A., Parvizi, M., Effect of Supplemental Damping on Seismic Response of Base Isolated Frames under Near & Far Field Accelerations, KSCE Journal of Civil Engineering, 19(5), 1359-1365, 2015.

[29] FEMA Quantification of Building Seismic Performance Factors, Report FEMA P695 Federal Emergency Management Agency, 2009.

[30] PEER, Pacific Earthquake Engineering Resource Center: NGA Database https://ngawest2.berkeley.edu/, [access: February 2019].

Teknik Dergi, 2022 11507-11519, Paper 645

The Strain Sensitivity of Coal Reinforced Smart Concrete by Piezoresistive Effect

Özkan Ayberk KOLATAR[1]
Egemen TEOMETE[2]
Serap KAHRAMAN[3]

ABSTRACT

The structures are challenged by earthquakes, material degradations and other environmental factors. In order to protect the lives, assets, and for maintenance planning, structural health monitoring (SHM) is important. In SHM applications, strain gages are widely used which have low durability, low sensitivity while they have high cost. To monitor a structure, large number of strain gages have to be used that increases the cost. In this study, seven coal reinforced concrete mixtures with 0, 0.35, 0.5, 0.8, 1, 1.5 and 2 volume % of coal were designed; three cubic samples for each mixture were fabricated. Simultaneous strain and electrical resistance measurements of the samples during the compression test were conducted. A strong linear relationship between strain and electrical resistance change with a correlation coefficient of 0.99 was determined. The concrete mixture having 0.8% coal volume had the highest strain sensitivity of K=44, which was 22 times the strain sensitivity of commercial metal strain gages while it had a linearity error of LE=6.9% that was low. This mixture with 0.8% coal volume is a candidate to be smart concrete which can sense its strain. As a contribution to the literature, a phenomenological model for the relationship between gage factor and coal volume percentage was explained in details. The multifunctional smart concrete will be used as a smart material, which can sense its strain in SHM applications while acting as a load bearing material.

Keywords: Smart concrete, strain, electrical resistance, smart materials, piezoresistivity.

Note:
- This paper was received on October 18, 2019 and accepted for publication by the Editorial Board on June 26, 2020.
- Discussions on this paper will be accepted by March 31, 2022.
- https://doi.org/10.18400/tekderg.634659

1 Dokuz Eylul University, Graduate School of Natural and Applied Sciences, Izmir, Turkey - o.a.kolatar@gmail.com - https://orcid.org/0000-0002-5432-2879

2 Dokuz Eylul University, Civil Engineering Department, Izmir, Turkey - egemen.teomete@deu.edu.tr https://orcid.org/0000-0002-7330-7367

3 Dokuz Eylul University, Civil Engineering Department, Izmir, Turkey - serap.kahraman@deu.edu.tr https://orcid.org/0000-0002-7898-050X

1. INTRODUCTION

Concrete is widely used for almost all civil engineering constructions. Concrete structures are challenged by earthquakes, material deteriorations and other environmental factors. Structural health monitoring is vital for the safety of life and assets while it is also important for asset management. Metal strain gages used for structural health monitoring have short life time, small sensitivity and can get point wise measurement. In order to monitor a structure, large number of strain gages are needed; increasing the number of channels in data acquisition system increases monitoring costs considerably [1]. Self-sensing smart concrete can be solution for these problems.

Different researchers worked on self-sensing cement composites reinforced with micro-nano fillers [1-4]. Carbon based materials were widely used due to their high electrical conductivity; among them carbon nanotubes were also widely tested within cement composites for strain sensing [5-9]. Carbon fiber, carbon nanofiber (CNF) and carbon black (CB) reinforced cement composites were used in cement composites for self-sensing [10-18]. Self-sensing cement composites were also tested with graphene and graphene nano-platelets [19-20].

Crack length sensitivity and strain gage factor of cement mortar composites reinforced with 13 mm carbon fibers were tested by Teomete [21]. Direct tensile test was applied to cement composites with 6 mm carbon fibers for strain sensing by Azhari et al. [22]. Effect of carbon fiber aspect ratio on self-sensing characteristics of cement pastes was investigated by Baeza et al. [23].

Studies on self-sensing smart concrete with large aggregates were very few. CNF filled concrete was investigated for strain sensing by Gao et al [24]. Wang et al [25] correlated the damage with electrical resistance of carbon fiber reinforced concrete under flexural loading. Relation between the damage and the resistivity of the carbon fiber reinforced concrete was investigated under cyclic loading by Chu and Chen [26].

Wen and Chung [27] compared the carbon fiber (15 μm diameter) reinforced cement paste and steel fiber reinforced (8 μm diameter) cement paste for strain sensitivity. Teomete and Kocyigit [28] applied split tensile test to determine tensile strain sensitivity of steel fiber reinforced cement mortar. Dong et al. [29] tested reactive powder cement composite that had short-cut super-fine stainless wire and quartz sand for strain sensitivity under compression and flexure. Steel fibers and CNTs were used together in hybrid cement mortars under compression and direct tension test for strain sensing [30-31]. Steel fiber reinforced clay bricks under compressive load were tested for strain sensing [32].

Untreated coal waste increased the compressive strength by 5% and flexural strength by 6% when replaced 5% by weight of aggregate [33]. When cement was replaced by fly ash and coal gangue by 20%, (fly ash / coal gangue ratio was 40/60 in this 20% replacement), 4.5% increase in compressive strength was observed [34]. The tensile strength/cost ratio of concrete was optimized by coal waste considering the cost, the optimal coal waste percent was reported [35]. Splitting tensile, compressive and flexural strengths decreased by addition of ceramic and coal wastes [36]. Coal waste powder when used 5% of binder increased compressive strength and toughness in bending at 28 days [37].

In literature, there is no study on strain sensitivity of coal reinforced cement composite (cement paste, mortar or concrete). In this study, strain sensitivity of low cost coal reinforced industrial concrete with 15 mm aggregate size was studied. Seven concrete mixtures with coal volume ratio of 0, 0.35, 0.5, 0.8, 1, 1.5, 2 % were designed; three 75 mm cubes were cast and cured for each mixture; 21 cubes were prepared. Simultaneous strain and electrical resistance measurements were conducted during the compressions tests. For each mixture, strain sensitivity and linearity were determined as performance measures. There was strong linear relationship between strain and electrical resistance change of coal reinforced concrete.

2. MATERIALS AND METHOD

In this study, seven different concrete mixtures were designed. Reference mixture M0 had no coal while mixtures K035, K05, K08, K10, K15, K20 had coal at 0.35, 0.5, 0.8, 1, 1.5 and 2 % by volume. In all mixes, cement CEM II B-M (L-W) 42.5R, water/binder ratio of 0.37; silica fume/binder ratio of 10%, super-plasticizer/binder ratio of 1% were utilized. The coal had a particle size of 0-10 mm, as seen in Fig.1. The density of coal was 1295 kg/m^3.

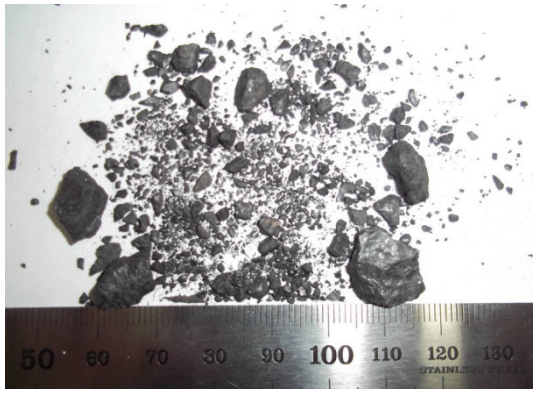

Figure 1 - The coal used in the study.

Modified polycarboxylates based polymer super plasticizer was used. Crushed lime stone fine and coarse aggregates of 0-5 mm and 5-15 mm were used, respectively. Silica fume that has spherical shape with average diameter of 250 μm was used. The concrete mixtures were designed according to TS 802 "Design of Concrete Mixes" standard. The amount of materials in 1 m^3 of concrete is presented in Table 1.

Electrical resistance of cement composites was measured using either two or four probe measurement method. In two-probe method, sample cross section, distance between electrodes and contact resistance affects the measurements while in four-probe method, these do not affect the measurements [38, 39]. In this study, for electrical measurements of the smart concrete, different electrode pairs were used in four-probe method for current supply and voltage measurement. There was 35 mm between inner electrodes and 55 mm between outer electrodes.

Table 1 - Amount of materials in 1 m^3 of concrete (kg/m^3).

Materials	M0	K035	K05	K08	K10	K15	K20
Fiber % in total volume:	0	0.35	0.5	0.8	1	1.5	2
Coal	0	5	6	10	13	19	26
Cement	499	499	499	499	499	499	499
Gravel 5-15mm	547	544	542	539	537	531	526
Sand 0-5 mm	821	815	813	808	805	797	789
Silica fume	55	55	55	55	55	55	55
Water	205	205	205	205	205	205	205
Super-plasticizer	6	6	6	6	6	6	6

A conductive wire or paint is applied on the sample in perimetral (external) electrode method while a conductive plate or mesh is inserted in the sample in embedded electrode method [17,18,40] . In this study, copper wire mesh with square hole of 5 mm and wire diameter of 0.6 mm was used as electrodes. A special cube mold with 75 mm size and electrode slots on either side were designed and manufactured for this study as seen in Fig. 2a. When mixture was cast in the mold, some portions of the electrodes stay outside the mold as in Fig. 2b. Three of 75 mm cubic samples for each 7 mixture were cast. The samples were taken out of the molds 24 hours after casting and cured for 28 days in 20°C water.

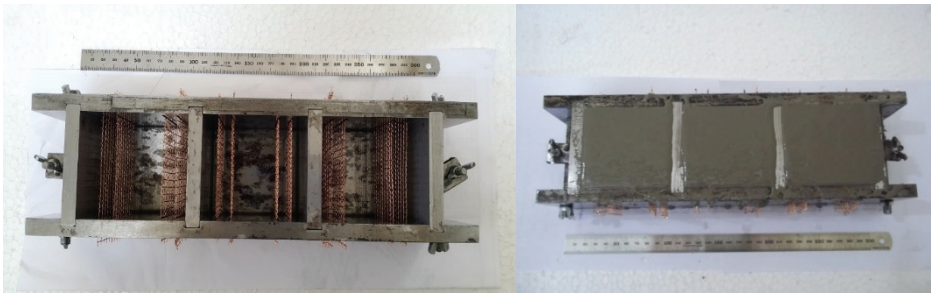

Figure 2 - a) Special mold and electrodes b) After casting concrete

Before compression test, in order to eliminate the effects of polarization, 20 V DC was applied on the samples for 15 minutes. Compression test was applied on the samples, with simultaneous measurement of strain and electrical resistance change. Strain was measured with strain gages. 300 kN capacity electromechanical test machine was used with the loading rate of 0.5 mm/min. In order to insulate the samples, glass fiber epoxy plates were used as in Fig.3a. During compression test, 20 V DC was supplied using the outer two electrodes (E_c), potential difference of the sample Vs was measured using the inner two electrodes (E_v) as seen in Fig.3. Also, during the test, the potential difference (V_r) of the reference resistance (Rr=1000 Ohms) and the current on the circuit I_c were measured as presented in Fig.3b.

Force, strain, potential differences (V_s, V_r), and current were recorded at a rate of 10 Hz (10 sample/sec).

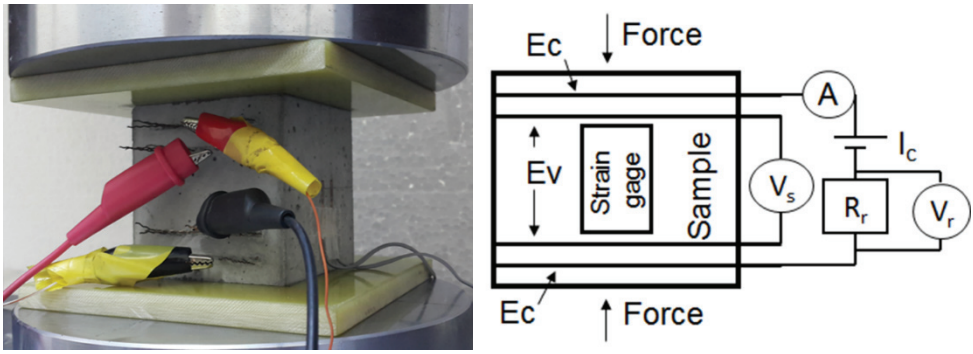

Figure 3 - a) The concrete sample at compression test b) Test circuit

Measured circuit current I_c and the electrical potential of the sample V_s were used to determine the electrical resistance of the sample (R_s) by Eq. 1. The percent change of electrical resistance of the sample (%R) was calculated by Eq. 2. R_{so} is the electrical resistance of the sample without any applied load.

$$R_s = \frac{V_s}{I_c} \tag{1}$$

$$\%R = \left(\frac{R_s}{R_{so}} - 1 \right) \times 100 \tag{2}$$

Strain sensing performance was assessed using gage factor (K) and linearity (LE). Gage factor (K) is the change in electrical resistance per unit strain and determined by Equation 3. Commercial metal foil strain gages have gage factors around 2. The higher the gage factor the more sensitive to strain the sensor is. Linearity (LE) is the percent of maximum difference (Δ_{max}) between the input-output curve (%R versus strain curve) and fitted linear regression line, to full-scale output ($\%R_{fs}$) as in Equation 4. As the linearity decreases, the error in strain measurement decreases.

$$K = \frac{\left(R_s - R_{so}\right) / R_{so}}{\Delta\varepsilon} \tag{3}$$

$$\%LE = \left(\frac{\Delta_{max}}{\%R_{fs}} \right) \times 100 \tag{4}$$

3. RESULTS AND DISCUSSIONS

In this study, seven different concrete mixtures having different coal volume fractions were designed; three cube samples of 75 mm were tested with compression test for each mixture.

Electrical resistance – strain relationship was investigated. The stress- strain – electrical resistance change relationship for all mixtures are presented in Figs. 4-5. The compressive strain closed micro voids, leading to an increase in contacts of fiber-fiber and fiber-matrix, resulting in better electron and ion transfer; decreasing electrical resistance. Thus, piezoresistive effect is observed for all mixtures with or without coal.

The M0 mixture (without any coal) had an average gage factor of K=18.9 and average linearity of LE=20.8% with a correlation coefficient of R^2=0.93 as seen in Fig.4. The K035 mixture which had 0.35 volume % coal was more sensitive to strain with respect to M0, with an average gage factor of 23.5, average linearity of LE=9.8% and a correlation coefficient of R^2=0.99, presented in Fig.5a.

The mixture K05 with 0.5 volume % of coal, had a higher gage factor (sensitivity) with respect to K035 and M0, with a gage factor of K=37. It had an average linearity of LE=6.5%, and correlation coefficient of R^2=0.99, as in seen Fig.5b. Increasing the coal amount to 0.8% volume fraction (for K08 mixture) further increased the gage factor to K=44, with a low linearity of LE=6.9% and a correlation coefficient of R^2=0.99 between strain and %R, presented in Fig.5c. Further increase of volume percent to 1% coal led to a decrease of gage factor to K=37.7 for mixture K10, increased linearity to LE=10.6% and a correlation coefficient of R^2=0.99 (Fig.5d). When the coal volume % was increased to 1.5 % (K15) and 2 % (K20), the gage factor was decreased to K=26 and K=30; the linearity increased to LE=14% and LE=9%, with correlation coefficients of R^2=0.99 and R^2=0.98, respectively (Figs. 5e-f). For most mixtures with coal, the correlation coefficient between strain and %R was 0.99% which testified strong linear relationship.

The variations of average gage factor and LE% with coal volume percent was presented in Fig.6a-b, respectively. The error bars represent ±1 standard deviation from average. As seen in Fig.6a, the gage factor increased up to 0.8% volume ratio, than decreased with increasing volume ratio over 0.8%. At low volume ratios (below 0.8%), there was not enough fiber for new contact formation with strain which led to an increase of gage factor with coal volume %. On the other hand, at higher volume ratios than 0.8%, there are already some direct fiber contacts and development of new fiber contacts with strain did not affect the electrical resistance much, decreasing the gage factor K. Thus, the optimal coal volume percentage was 0.8% for gage factor.

Fig.6b showed that the optimal volume percentage of 0.8 had one of the smallest linearity error. The mixture M08 with 0.8% volume ratio of coal, had the highest gage factor K=44, which was 22 times the gage factor of commercial metal strain gages. It had the lowest linearity LE%=6.9% which can be accepted for a multifunctional material. Thus, the M08 mixture was the most sensitive to strain with least error and a candidate to be smart concrete which can sense its strain.

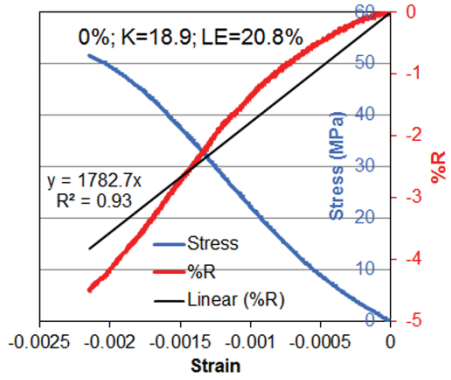

Figure 4 - Stress- strain- electrical resistance change (%R) relationship for concrete mixture M0 (0%; K=18.9; LE=20.8%)

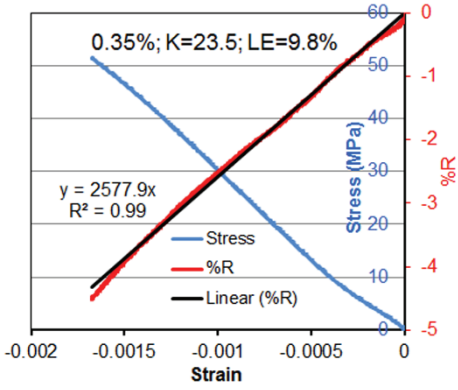

(a)

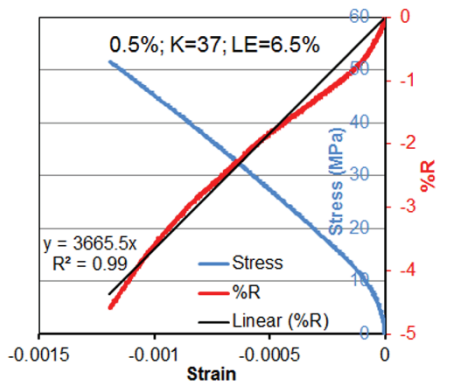

(b)

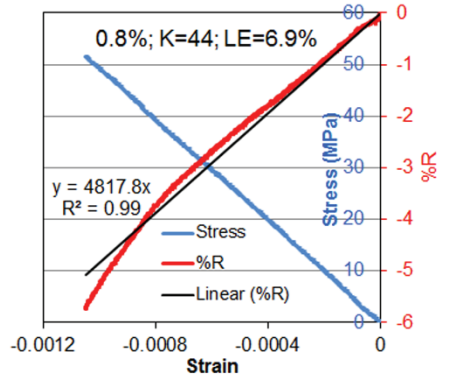

(c)

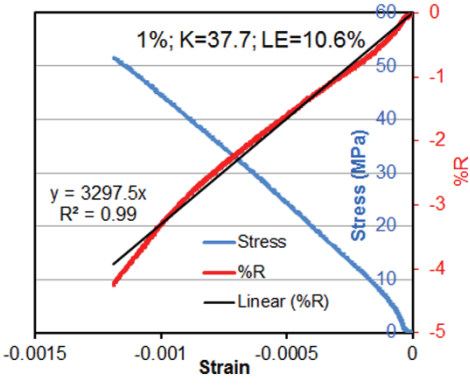

(d)

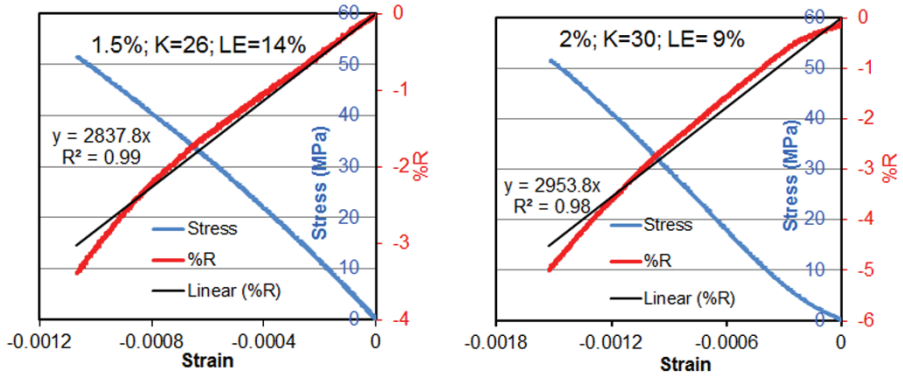

(e) (f)

Figure 5 - Stress- strain- electrical resistance change (%R) relationship for concrete mixtures (a) K035; (b) K05; (c) K08; (d) K10; (e) K15; (f) K20.

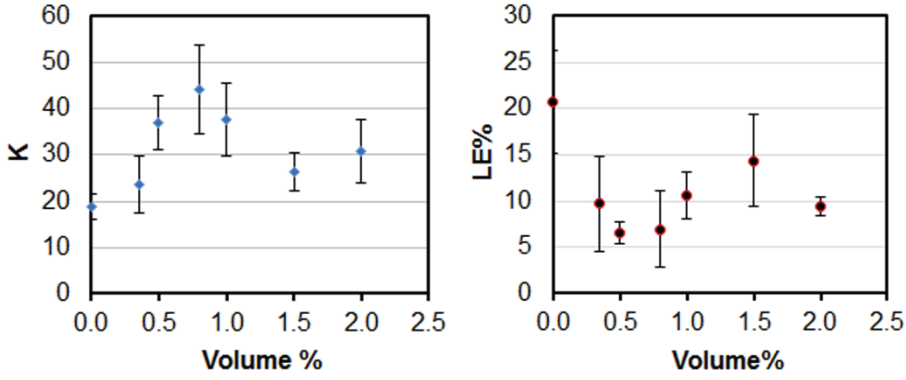

Figure 6 - Relationship between coal volume % and a) Gage factor K b) Linearity LE%

The phenomenological variation of gage factor with coal volume percentage was explained in details in Fig.7. The existing contacts were shown with brown coal particles (in Fig. 7e-f) while all new contacts occurred due to loading were shown with red coal particles. At coal volume percentage lower than 0.8 %, there were small number of coal particles, which did not contact each other before loading while there was only one partial contact after loading as seen in Fig.7a-b. As the coal volume increased to 0.8 %, there were more coal particles which did not contact before loading but developed some contacts after loading as seen in Fig. 7c-d. These new contacts decreased the electrical resistance considerably and maximized the gage factor as seen in Fig. 6a. As the coal volume increased beyond 0.8 %, some contacts already existed before loading shown with brown (in Fig.7e), and application of load only developed some more new contacts (shown in red in Fig.7f) which did not alter the resistivity much, resulting in a decrease in gage factor in Fig.6a.

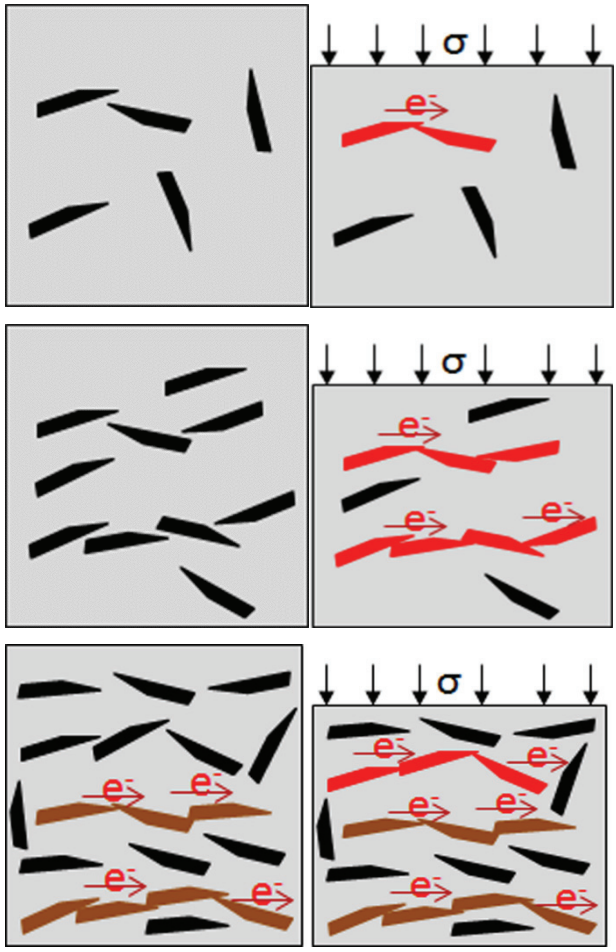

Figure 7 - Compression test of coal reinforced concrete at volume % of a-b) Lower than 0.8% c-d) At 0.8% and e-f) Higher than 0.8%. Existing contacts are brown and new contacts are red.

4. CONCLUSIONS

In this study, strain sensitivity of coal reinforced concrete was determined for seven different volume percentages of coal. Three 75 mm cube samples were cast and tested with compression test for each mixture. Strain and electrical resistance measurements were conducted simultaneously. The results presented in this work are only valid for the sample size of 75 mm due to size effect phenomenon of concrete and only under monotonic uniaxial compression loading. Other sample sizes and loading conditions (tensile, shear, bending, cyclic etc.) can be studied as future study. The results of this study are presented below:

1. The electrical resistance of coal reinforced concrete decreased with compressive strain due to closing of micro voids which led to an increase in fiber - fiber and fiber-matrix contact. Piezoresistive effect was observed.
2. All the coal reinforced concrete mixtures had a strong linear relationship between strain and %R with a correlation coefficient of R^2=0.99.
3. At coal volume percentages lower than 0.8 as there was a small amount of fibers, resistance change was less due to strain because of low amount of new fiber contacts by strain, which ended up with low gage factors. As the coal volume percentage increased, strain could develop more fiber contacts which changed electrical resistance more and gage factor increased. At coal volume percentages higher than 0.8, there were already fiber contacts existed prior to loading and new contacts due to strain did not affect the electrical resistance much, gage factor decreased. The optimal coal volume % was 0.8 at which the change in electrical resistance and gage factor were maximum.
4. The M08 mixture with 0.8% coal had the lowest linearity error of LE=6.9% which was acceptable for a multifunctional smart concrete. It had the highest gage factor of K=44, which was 22 times the gage factor of commercial metal strain gages. Thus, M08 mixture, with highest gage factor and lowest linearity, is a candidate to be multifunctional self-sensing smart concrete.

Smart concrete can be used in important structures (hospitals, nuclear power plants etc.) and only at critical structural elements (Columns of 1st floor etc.) to monitor the structural health. Wireless data transfer and real time monitoring can be applied while discrete measurements can also be obtained after a major event (seismic load, impact) for damage assessment. Commercial metal strain gages can get point wise measurements while smart concrete can monitor entire structure. The coal dust used had a lower price than steel fibers, carbon fibers, carbon nanotubes and graphite, which makes implementation of smart concrete economical for the industry.

Acknowledgements

This work was supported by The Scientific and Technological Research Council of Turkey (TUBITAK) through project “Smart Concrete Production”, Grant no: 213M452. The authors would like to thank to Batıbeton Batıçim West Anatolia Cement Industry Inc. for supplying cement and aggregate; Sika Construction Chemicals Co. for supplying super plasticizer; BASF Chemical Co. for supplying silica fume, Turkish Coal Institution for supplying coal.

References

[1] Chung, D.D.L., Review functional properties of cement –matrix composites. Journal of Material Science, 36, 1315-1324, 2001.

[2] Chung, D.D.L., Piezoresistive cement-based materials for strain sensing. Journal of Intelligent Material Systems and Structures, 13(9), 599-609, 2002.

[3] Chung, D.D.L., Carbon materials for structural self-sensing, electromagnetic shielding and thermal interfacing. Carbon, 50(9), 3342-3353, 2012.

[4] Lu, S.N., Xie, N., Feng, L.C., Zhong, J., Applications of nanostructured carbon materials in constructions: the state of the art. Journal of Nanomaterials, ID: 807416, 2015.

[5] Han, B., Yu, X., Kwon, E., A self-sensing carbon nanotube/cement composite for traffic monitoring. Nanotechnology, 20(44), 1-5, 2009.

[6] Han, B., Zhang, K., Burnham, T., Kwon, E., Yu, X., Integration and road tests of a self-sensing CNT concrete pavement system for traffic detection. Smart Materials and Structures, 22(1), ID: 015020, 2013.

[7] Al-Dahawi, A., Sarwary, M. H., Öztürk, O., Yıldırım, G., Akın, A., Şahmaran, M., Lachemi, M., Electrical percolation threshold of cementitious composites possessing self-sensing functionality incorporating different carbon-based materials. Smart Materials and Structures, 25(10), ID: 105005, 2016.

[8] Jianlin, L., Kwok, L.C., Qiuyi, L., Shunjian, C., Lu, L., Dongshuai, H., Chunwei, Z., Piezoresistive properties of cement composites reinforced by functionalized carbon nanotubes using photo-assisted fenton. Smart Materials and Structures, 26(3), ID: 035025, 2017.

[9] Luo, J., Zhang, C., Duan, Z., Wang, B., Li, Q., Chung, K.L., Zhang, J., Chen, S., Influences of multi-walled carbon nanotube (MCNT) fraction, moisture, stress/strain level on the electrical properties of MCNT cement-based composites. Sensors and Actuators A: Physical, 280, 413–421, 2018.

[10] Meehan, D.G., Wang, S., Chung, D.D.L., Electrical-resistance-based sensing of impact damage in carbon fiber reinforced cement-based materials, Journal of Intelligent Material Systems and Structures, 21(1), 83-105, 2010.

[11] Han, B., Wang, Y., Dong, S., Zhang, L., Ding, S., Yu, X., Ou, J., Smart concretes and structures: A review. Journal of Intelligent Material Systems and Structures, 26(11), 1303-1345, 2015.

[12] Goldfeld, Y., Rabinovitch, O., Fishbain, B., Quadflieg, T., Gries, T., Sensory carbon fiber based textile-reinforced concrete for smart structures. Journal of Intelligent Material Systems and Structures, 27(4), 469-489, 2016.

[13] Han, B., Wang, Y., Ding, S., Yu, X., Zhang, L., Li, Z., Ou, J., Self-sensing cementitious composites incorporated with botryoid hybrid nano-carbon materials for smart infrastructures. Journal of Intelligent Material Systems and Structures. 28(6), 699-727, 2017.

[14] Wang, H., Gao, X., Liu, J., Coupling effect of salt freeze-thaw cycles and cyclic loading on performance degradation of carbon nanofiber mortar. Cold Regions Science and Technology, 154, 95–102, 2018.

[15] Wang, Y., Wang, Y., Wan, B., Han, B., Cai, G., Chang, R., Strain and damage self-sensing of basalt fiber reinforced polymer laminates fabricated with carbon nanofibers/epoxy composites under tension. Composites Part A, 113, 40–52, 2018b.

[16] Wang, Y., Wang, Y., Wan, B., Han, B., Cai, G., Li, Z., Properties and mechanisms of self-sensing carbon nanofibers/epoxy composites for structural health monitoring. Composite Structures, 200, 669–678, 2018.

[17] Li, H., Xiao, H., Ou, J., Effect of compressive strain on electrical resistivity of carbon black-filled cement –based composites. Cement and Concrete Composites, 28, 824-828, 2006.

[18] Li, H., Xiao, H., Ou, J., Electrical property of cement-based composites filled with carbon black under long-term wet and loading condition. Composites Science and Technology, 68, 2114-2119, 2008.

[19] Ozbulut, O. E., Jiang, Z., Harris, D. K., Exploring scalable fabrication of self-sensing cementitious composites with graphene nanoplatelets. Smart Materials and Structures, 27(11), ID: 115029, 2018.

[20] Rehman, S. K., Ibrahim, Z., Jameel, M., Memon, S. A., Javed, M. F., Aslam, M., Mehmood, K., Nazar, S., Assessment of rheological and piezoresistive properties of graphene based cement composites. International Journal of Concrete Structures and Materials, 12(1), UNSP 64, 2018.

[21] Teomete, E., Measurement of crack length sensitivity and strain gage factor of carbon fiber reinforced cement matrix composites. Measurement, 74, 21-30, 2015.

[22] Azhari, F., Banthia, N., Carbon fiber-reinforced cementitious composites for tensile strain sensing. ACI Materials Journal, 114(1), 129-136, 2017.

[23] Baeza, F. J., Galao, O., Zornoza, E., Garcés, P., Effect of aspect ratio on strain sensing capacity of carbon fiber reinforced cement composites. Materials & Design, 51, 1085-1094, 2013.

[24] Gao, D., Sturm, M., Mo, Y. L., Electrical resistance of carbon-nanofiber concrete, Smart Materials and Structures, 18(9), ID:095039, 2009.

[25] Wang, W., Wu, S., Dai, H., Fatigue behavior and life prediction of carbon fiber reinforced concrete under cyclic flexural loading. Materials Science and Engineering, 434(1-2), 347-351, 2006.

[26] Chu, H. Y., Chen, J. K., The experimental study on the correlation of resistivity and damage for conductive concrete. Cement and Concrete Composites, 67, 12-19, 2016.

[27] Wen, S., Chung, D. D. L., A comparative study of steel- and carbon–fibre cement as piezoresistive strain sensors. Advances in Cement Research, 15(3), 119–128, 2003.

[28] Teomete, E., Kocyigit, O. I., Tensile strain sensitivity of steel fiber reinforced cement matrix composites tested by split tensile test. Construction and Building Materials, 47, 962-968, 2013.

[29] Dong, S., Han, B., Ou, J., Li, Z., Han, L., Yu, X., Electrically conductive behaviors and mechanisms of short-cut super-fine stainless wire reinforced reactive powder concrete. Cement & Concrete Composites, 72, 48-65, 2016.

[30] Lee, S. H., Kim, S., Yoo, D. Y., Hybrid effects of steel fiber and carbon nanotube on self-sensing capability of ultra-high-performance concrete. Construction and Building Materials. 185, 530 -544, 2018.

[31] Yoo, D. Y., Kim, S., Lee, S. H., Self-sensing capability of ultra-high-performance concrete containing steel fibers and carbon nanotubes under tension. Sensors and Actuators A-Physical, 276, 125-136, 2018.

[32] D'Alessandro, A., Meoni, A., Ubertini, F., Stainless steel microfibers for strain-sensing smart clay bricks. Journal of Sensors, ID:7431823, 2018.

[33] Karimaei, M., Dabbaghi, F., Sadeghi-Nik, A., Dehestani, M., Mechanical performance of green concrete produced with untreated coal waste aggregates. Construction and Building Materials, 233, Article Number: UNSP 117264, 2020.

[34] Wang, Y., Tan, Y., Wang, Y., Liu, C., Mechanical properties and chloride permeability of green concrete mixed with fly ash and coal gangue. Construction and Building Materials, 233, Article Number: 117166, 2020.

[35] Khataei, B., Nasrollahi, M., Optimizing the tensile strength of concrete containing coal waste considering the cost. Sn Applied Sciences, 2 (1) Article Number: 103, 2020.

[36] Shamsaei, M., Khafajeh, R., Aghayan, I., Laboratory evaluation of the mechanical properties of roller compacted concrete pavement containing ceramic and coal waste powders. Clean Technologies and Environmental Policy, 21(3), 707-716, 2019.

[37] Modarresa, A., Hesamia, S., Soltaninejada, M., Madanib, H., Application of coal waste in sustainable roller compacted concrete pavement-environmental and technical assessment. International Journal of Pavement Engineering, 19(8), 748-761, 2018.

[38] Chiarello, M., Zinno, R., Electrical conductivity of self-monitoring CFRC. Cement and Concrete Composites, 27, 463-469, 2005.

[39] Han, B., Guan, X., Ou, J., Electrode design, measuring method and data acquisition system of carbon fiber cement paste piezoresistive sensors. Sensors and Actuators A, 135, 360-369, 2007.

[40] Chen, B., Liu, J., Damage in carbon fiber –reinforced concrete, monitored by both electrical resistance measurement and acoustic emission analysis. Construction and Building Materials, 22, 2196-2201, 2008.

Teknik Dergi, 2022 11521-11541, Paper 646

Analysis of a Prefabricated Vertical Drain (PVD) Soil Improvement Project

Ahmet Can MERT[1]
Akın ÖNALP[2]
Ersin AREL[3]

ABSTRACT

A settlement analysis has been carried out for several sectors of a rail station yard improved with prefabricated vertical drains (PVD) in Istanbul, that exhibited prolonged consolidation beyond the predicted values in certain sectors of the treated zone. Final settlement and End of Primary (EOP) settlement times have been estimated theoretically as well as using the Asaoka graphical procedure. The compliance of settlement-time curves with in-situ measurements and Asaoka solution has been investigated. A geotechnical model was developed for finite element and three-dimensional consolidation analyses. The settlement curves obtained by varying horizontal-vertical permeability coefficient ratio (k_h/k_v) and in-situ measurements have been compared, and k_h/k_v values corresponding to 90% degree of consolidation has been computed for all sectors. The effect of drain spacing (s_{drain}) as well as drain length (L_{drain}) on the rate of consolidation have been evaluated for each sector, keeping the specified ratios constant. The times corresponding to 95% degree of consolidation (t_{95}) have been calculated using the theoretical solution and compared to in-situ measurements. Calculated t_{95}'s has also been compared to their estimated values by varying the spacing (s_{drain}) and the length (L_{drain}). Additionally, the required intervals of s_{drain} and L_{drain} have been obtained corresponding to the calculated t_{95} times. The analyses suggest that the main reason for prolonged consolidation was the horizontal to vertical permeability coefficient ratio. According to the analysis results, PVD implementation was not efficient in clays having k_h/k_v of approximately unity. The main conclusion of this study was to discover the necessity for optimizing the variables in any such project. The efficacy of the works can be significantly enhanced if simultaneous evaluation of the parameters s_{drain} and L_{drain} and the permeability

Note:
- This paper was received on November 1, 2019 and accepted for publication by the Editorial Board on August 17, 2020.
- Discussions on this paper will be accepted by March 31, 2022.
- https://doi.org/10.18400/tekderg.641218

1 Istanbul Kultur University, Department of Civil Engineering, Istanbul, Turkey - a.mert@iku.edu.tr https://orcid.org/0000-0002-2483-1330

2 Istanbul Okan University, Department of Civil Engineering, Istanbul, Turkey - akin.onalp@okan.edu.tr https://orcid.org/0000-0003-1906-0153

3 Istanbul Okan University, Department of Civil Engineering, Istanbul, Turkey, ersin.arel@okan.edu.tr https://orcid.org/0000-0001-9424-2198

ratio k_h/k_v is carried out prior to field work. Otherwise, "accidents" may emerge as found out in this project.

Keywords: Prefabricated Vertical Drain (PVD), radial consolidation, 3D consolidation, acceleration of consolidation, consolidation settlement, coefficient of permeability, degree of consolidation, consolidation rate, asaoka procedure, numerical analysis.

1. INTRODUCTION

Consolidation of soils has been one of the frequently investigated topics, perhaps because full success in estimating the rate of settlement still avoids the geotechnician. The process of consolidation may be long in clays, since there is a considerable time lag between the application of load and full dissipation of the excess pore water pressures generated.

Improvement may be necessary for clays which require a time longer than the acceptable for the completion of the primary consolidation (EOP) before construction activity starts. One of the commonly used methods for shortening the process is the use of sand drains, or more recently, prefabricated vertical drains (PVD) which provide horizontal drainage in addition to vertical, to dissipate excess pore pressures rapidly. PVD accelerates the process in accordance with the radial consolidation theory. The most influential soil property thus becomes the horizontal coefficient of permeability (k_h). Other essential parameters are drain horizontal spacing (s) and drain installation length (L). Drain spacing should be optimized in order that an efficient remediation is secured. In connection with the installation length, drains should fully penetrate the layer to be consolidated, to secure efficient horizontal drainage. Contrary to Terzaghi one dimensional consolidation theory [1], radial consolidation considers the movement of water through a soil both vertically and laterally. Indeed, Terzaghi emphasized that his assumptions made in the 1D theory should be used with caution by considering the real behavior of soil [2]. The earliest study regarding three-dimensional consolidation has been made by using the elasticity theory with the assumption that water flows through vertical and random planes in a clay medium [3]. It has been discovered through field practice over the years that application of vacuum to the system may be necessary to enhance the efficiency of the system where the ratio (k_h/k_v) is not found to be sufficiently high.

The total degree of consolidation for an undisturbed and PVD-improved soil layer is expressed by both radial (U_r) and vertical (U_z) degrees of consolidation [4]:

$$(1-U_{zr}) = (1-U_r)(1-U_z) \tag{1}$$

Extensive research has been carried out to estimate the radial degree of consolidation U_r [5, 6, 7]. One of the commonly used expressions was proposed by Rendulic [5]. In his study, it was shown that U_r is a function of the coefficient of radial consolidation (c_{vr}) and radial time factor (T_r). Radial degree of consolidation for equal strain condition may be written by using the PVD parameters [6]:

$$U_r = 1-\exp\left(\frac{-8T_r}{\alpha}\right) \tag{2}$$

The coefficient α in Equation (2) depends on drain spacing s. Although the equations developed have been primarily intended for sand drains, they are also applicable for PVD use. The difference emerges in coefficient α, since wick drains are not cyclindrical. Barron's solution for U_r can be rearranged considering equivalent effective PVD diameter D, and the end of consolidation time t for PVD-improved soil is written as [8]:

$$t = \frac{D^2}{8c_{vr}}\left[\ln\frac{D}{d} - \frac{3}{4}\right]\ln\frac{1}{1-U_r} \tag{3}$$

where D can be taken as $1.05s$ for triangular pattern and $1.128s$ for rectangular grid applications. Equivalent drain diameter d can be taken as half of the drain width $d=b/2$. The main parameter for radial consolidation is the coefficient of consolidation ($c_h \equiv c_{vr}$) or permeability (k_h) in lateral direction. Vertical and horizontal permeability of soils, hence the corresponding coefficients of consolidation (c_v, c_h), may differ considerably and it has been determined that horizontal to vertical permeability ratio k_h/k_v may vary from 2 to 10 [9].

A recent study presented a 2D and 3D numerical simulation of vacuum assited PVD application and the results were compared with two previously investigated studies (Suvarnabhumi Airport, Thailand and Tianjin Port, China). A design chart for drain spacing was provided based on the results obtained from the two case histories [10]. Another recently published research emphasized the influence of soil permeability on the use of PVD application with vacuum preloading [11]. The research revealed that the change in permeability especially for large strain can affect the flow characteristics through the soil and vertical drain. Large-strain case was also investigated by another group for vertical drain with preloading where the use of non-linear solutions was emphasized [12].

In the present study, consolidation analyses were carried out for the sectors of a PVD-improved project in Halkali region of Istanbul, which exhibited prolonged consolidation beyond the predicted EOP values, contrary to the case histories presented in the literature [13, 14, 15].

Different horizontal to vertical permeability coefficient ratios (k_h/k_v) were specified for calculations in all sectors of ongoing consolidation to understand the process. In addition to varying the ratios, effect of drain spacing as well as that of drain length on the rate of consolidation time were investigated using conventional 3D consolidation approach, numerical analysis and the empirical Asaoka procedure.

2. FEATURES OF THE REMEDIATION AREA

Normally consolidated (NL) lacustrine clays have been improved by PVD application accompanied by preloading at a rail station yard, which is known to have exhibited excessive settlements under traffic and the ancillary structures, throughout the last century. Although the tracks can tolerate settlements of up to 50mm, the critical issue at the new station was the limiting differential settlements of the passenger platforms and the tracks, which should not exceed 25mm.

To mitigate this by PVD application, the designer calculated that a period of up to 180 days would be sufficient to achieve the foreseen settlements and subsequently complete the construction of the station platforms and the tracks leading to them. This would have enabled the contractor to prevent future settlements and meet the deadlines. This paper gives an account of the events and calculations that led to the failure of meeting the date foreseen for EOP's.

2.1. Soil Profile and Soil Properties at the Improvement Site

The investigated site contains young alluvial and lacustrine deposits overlying limestone-marl bedrock. The segment of this layer above the ground water level (GWL) at 1.5-2.0 m. is lightly over-consolidated by desiccation. Another identified layer is a dark-gray, greenish-gray and green Quaternary (Holocene) aged normally consolidated (NL) clay of Kusdili Formation which extends under the alluvial layer at varying thicknesses of up to 35m. The borehole locations for the studied sectors Sector 1A, 1B and 5B are shown in Figure 1. Figure 2 depicts two characteristic soil profiles from the site.

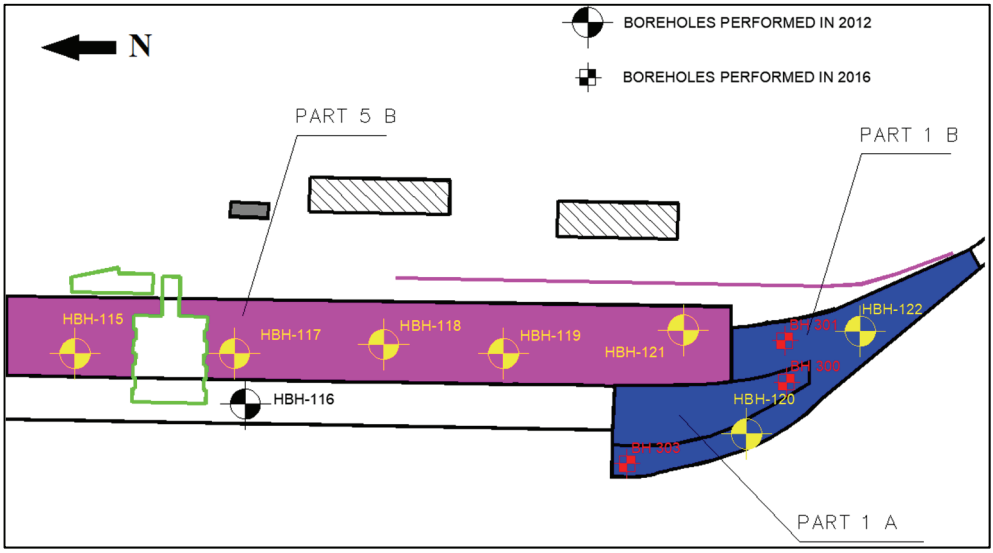

Figure 1 - Borehole locations of Sectors 1A, 1B and 5B (Scale 1:5000)

Samples from the boreholes drilled in 2012 and 2016 were classified by the Unified Soil Classification System USCS [16]. According to the test results, alluvial samples from 3-6m depths classify as ML, CL and SW-SM and Kusdili NL clays under the alluvium classified as CL and CH. The layers have natural moisture contents (w_n) mostly at around the liquid limit (w_L) or slightly below (Figure3a). Liquidity indices (I_L) are typically 0.55-0.93 rising to unity with increasing depth (Figure 3b). Quick triaxial tests (UU) performed on Kusdili clays indicated undrained shearing resistances (S_u) as low as 10-21 kPa (Figure 3c).

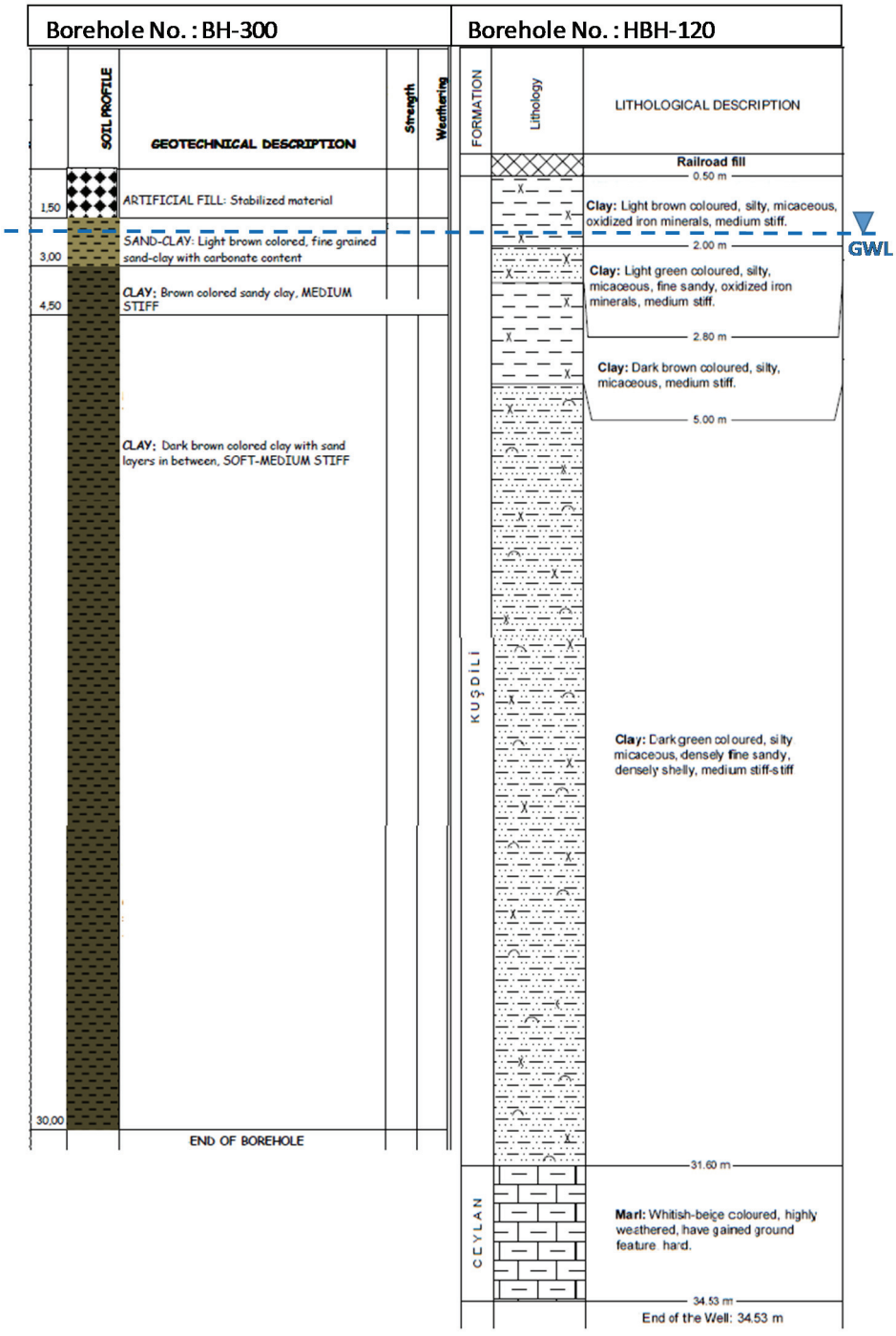

Figure 2 - Representative soil profiles from the boreholes at the study area

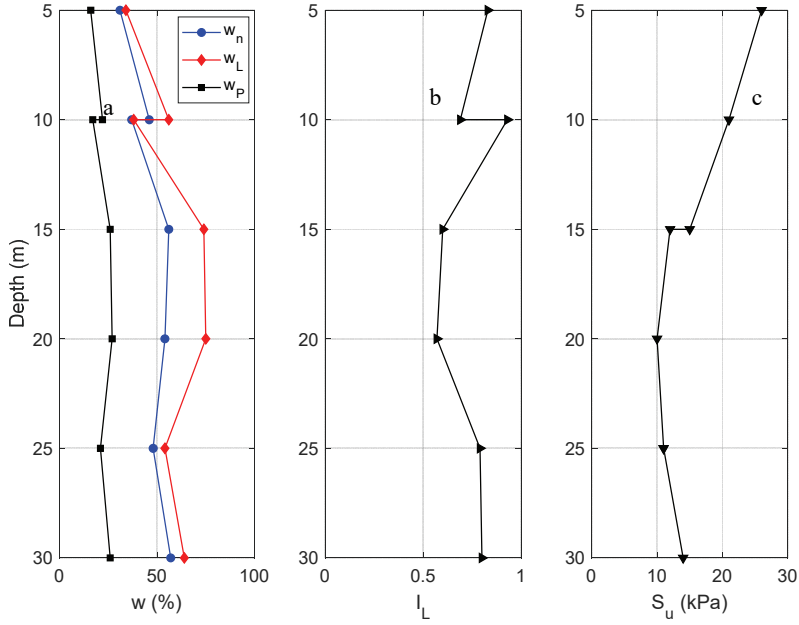

Figure 3 - Depth (z) versus a) consistency limits, b) liquidity index and c) undrained strength

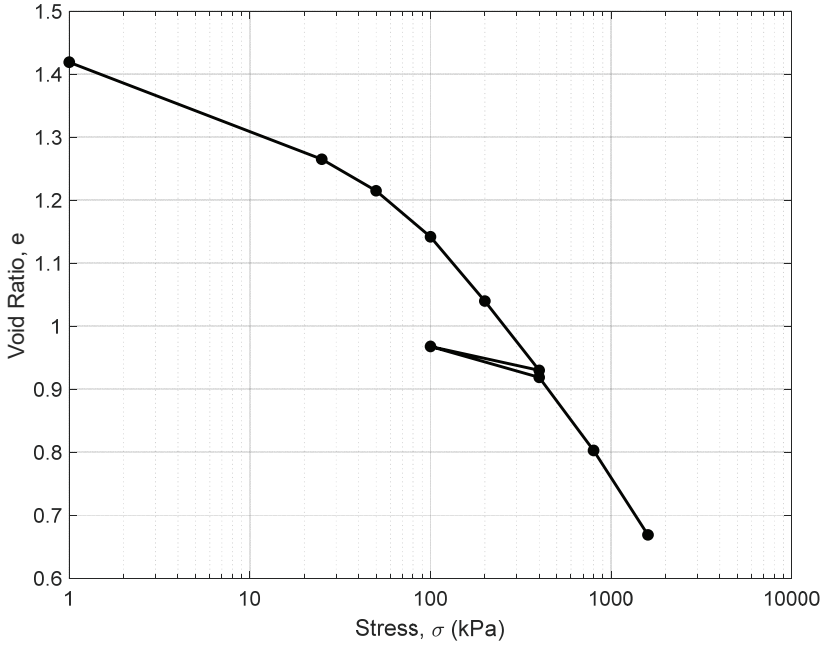

Figure 4 - Characteristic oedometer test result for NL Kusdili Clay

The laboratory test results confirmed that the Kusdili layer consists of soft normally consolidated and lightly overconsolidated clays (Figure 4) with poorly defined boundaries.

In addition to classification and triaxial testing (TX-UU), oedometer tests have been performed to carry out consolidation analyses for the clays to be improved. Oedometer test results illustrated in Figure 5 show that Kusdili clay layer has overconsolidation ratios of OCR=1~1.5, and the clay has a vertical permeability of k_v=10^{-6} m/day. The compression index for the layer was found to rise as high as C_c=0.673.

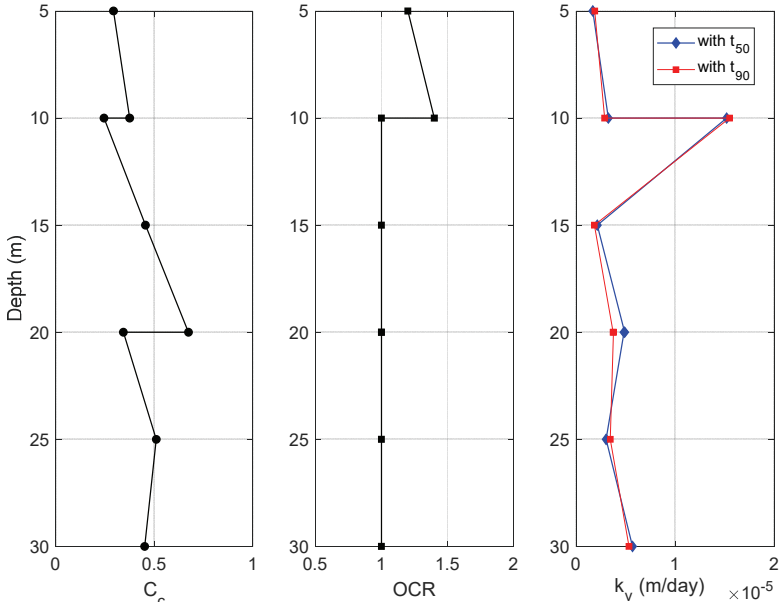

Figure 5 - Oedometer test results by depth

2.2. Implemented PVD Patterns

The designer had selected preloading with PVD as the improvement method to reach the excessive consolidation settlements anticipated at the project site. This was proved to be a feasible solution to achieve the final settlements at the preloaded sectors Sector 3A, 4; and PVD-improved sectors 2A, 2C, 3B, 5A, 5C rapidly. However, the settlements recorded at Sectors 1A, 1B and 5B after treatment not only exceeded the predicted values, but they continued to increase well beyond the estimated EOP times. Table 1 lists the stated details of treatment applied by the contractor at those "problem" sectors.

Figure 6 illustrates settlement-time (Δ-t) curves for the sectors monitored. These curves were plotted using the data from among the settlement plate readings at which the highest values for that specific sector was recorded. The time estimated for EOP by the designer was 6 to 10 months following the PVD application. However, the curves indicated ongoing settlement well beyond 1000 days. Measurements indicated that settlements reached 600-800mm, up to 45% above the predicted values, in 1201 to 1906 days elapsed. More significantly, the durations for EOP were extended unacceptably, obliging the owner of the facility to resort to

the use of piling down to the bedrock about 25-35m below, to catch up with the deadline. Table 2 summarises this paradoxical situation.

Table 1 - PVD Protocol

SECTOR	SPACING, s_{drain} (m)	LENGTH, L_{drain} (m)	PRELOAD	AREA (m^2)
1A	1x1	20	3.0m	5134
1B	2x2	26	2.5m	10629
5B	2x2	24	2.0m	16307

Table 2 - Estimated settlements and in situ measurement results

SECTOR	Designer Predicted Settlement (mm)	InSitu Final Measurement (mm)	Error in estimation	Estimated EOP time (Days)	Time Elapsed (Days)
1A	650	793	22%	180	1906
1B	450	627	39%	180	1201
5B	410	597	46%	180	1271

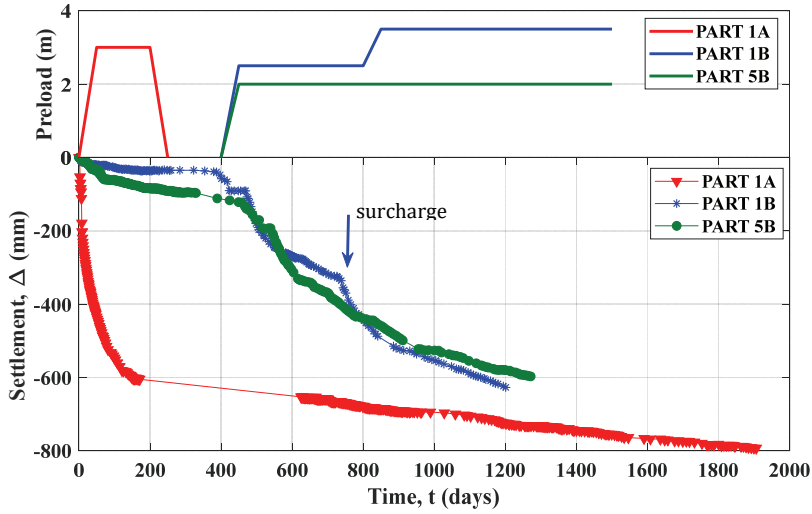

Figure 6 - Settlement-time (Δ-t) measurements for Sector 1A, 1B and 5B

The height of the embankment at Sector 1B was increased by 1m at 738 days, in order to be able to interpret the development of the process. The settlements responded almost proportionally, showing the effects of the surcharge in the implemented area, along with the neighbouring sectors (Figure 6).

3. EVALUATION OF SETTLEMENT AND PVD DESIGN

3.1. Analysis for Estimated and Measured Settlements

Evaluation of PVD performance requires regular in-situ monitoring. The objective of PVD application is to reach the completion of consolidation settlement (EOP) within the estimated time. Site measurements are made as either settlements or porewater pressures. The study by Hansbo et al. on vertical drains revealed that shearing resistance of the improved layer increased at constant porewater pressure, and they recommended the use of settlement measurements to evaluate the rate of consolidation [17]. Accordingly, frequent settlement measurements were carried out to evaluate the effect of PVD application on consolidation, intended for use to apply the Asaoka graphical procedure [18].

Asaoka diagram is constructed by plotting n number of settlement measurements (s_n) taken at equal time intervals (Δt) against the previous value (s_{n-1}) for each reading. He showed that the plotted points fit a straight line with the intercept β_0 and slope β_1 as given in Eq.6, and the intersection of this line with $y=x$ line is assumed to indicate the final settlement (s_f):

$$s_n = \beta_0 + \beta_1 s_{n-1} \tag{4}$$

From the slope β_1 and c_v from oedometer results, the coefficient of radial consolidation c_h can be calculated by,

$$-\frac{\ln \beta_1}{\Delta t} = \frac{8c_h}{D^2 \alpha} + \frac{\pi^2 c_v}{4H^2} \tag{5}$$

where D and α are the terms defined in Eqs.2 and3. H is the drainage path length from one-dimensional consolidation theory. c_h is the controlling parameter and the term containing c_v has less weight compared to the first term in the equation [19]. The expression for j-th settlement value (s_j) and time corresponding to that value $t_j=\Delta t.j$ can be written as in Eq. 6, provided that s_0 is the first settlement value employed. Equation (6) can also be used to calculate the time required to reach the final settlement s_f,

$$s_j = \frac{\beta_0}{1-\beta_1} - \left(\frac{\beta_0}{1-\beta_1} - s_0 \right) (\beta_1)^j \tag{6}$$

Asaoka diagrams were plotted for Sectors 1A, 1B and 5B using the readings of the settlement plate that indicated the highest values in that sector. Figure 7 elucidates the measurements taken at the problematic sectors. The initial readings were omitted to avoid errors that may occur in the calculation. The final settlement s_f for Sector 1A was computed by using the measurements taken after placement of surcharge on the neighbouring sectors. The total final settlement for Sector 1A is the sum of the last measurement taken before unloading and s_f value obtained. The placement of surcharge at Sector 1B resulted in 'jumps' in the diagram. Final settlement for this sector was calculated using the measurements taken after surcharging.

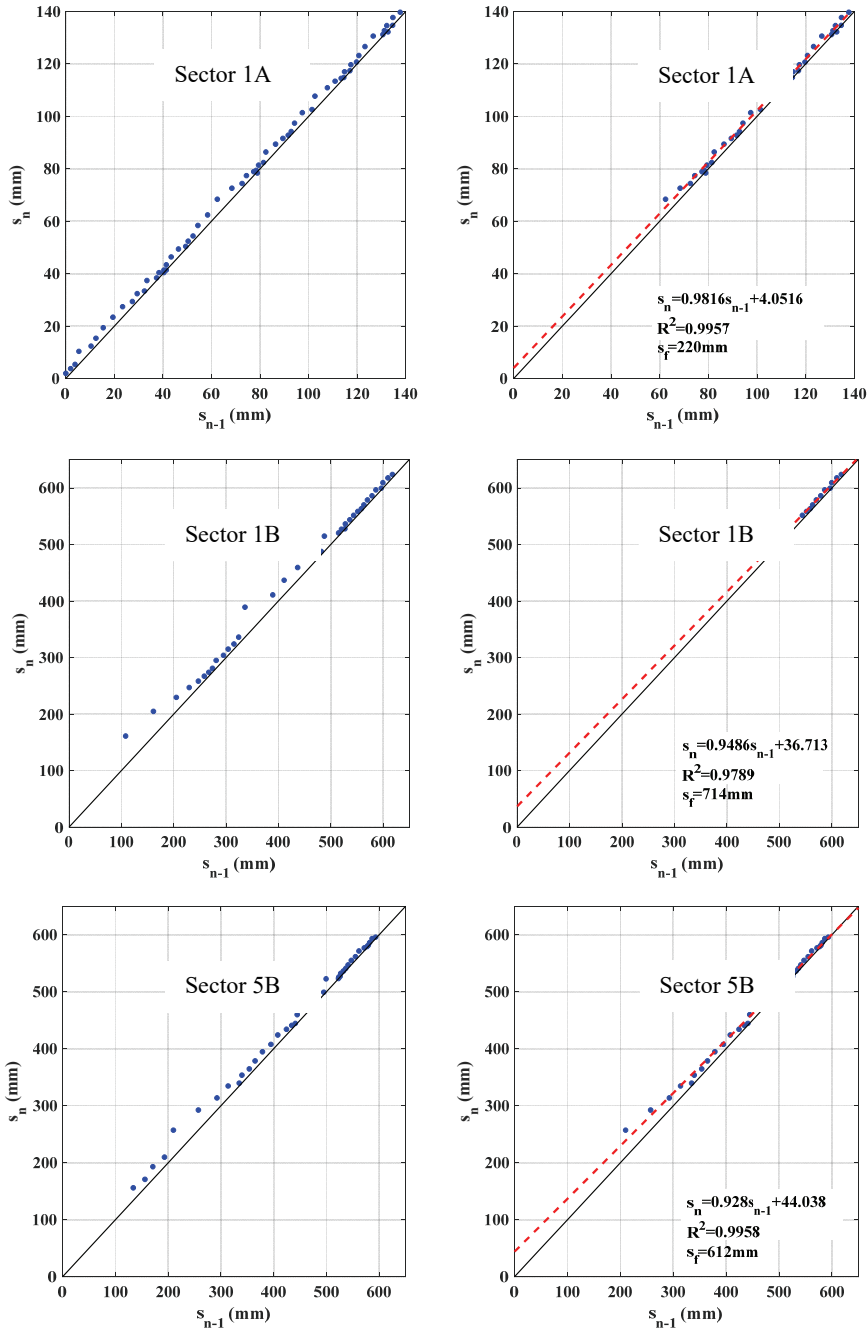

Figure 7 - Asaoka diagrams for Sector 1A, 1B, 5B

The effect of 1m surcharge applied at Sector 1B has also been observed in Sector 5B since this sector is in the settlement dish of Sector 1B. The final settlement for Sector 5B was obtained using readings taken after surcharging, using the same procedure followed for Sector 1B (Figure 7). Δ-t curves for each sector were plotted with the calculated final settlement and EOP by means of Eq. 8. These curves from Asaoka procedure were combined with the available in-situ measurements (Figure 8). In this way, the Asaoka solution and field measurements could be compared, and it was found that there is good agreement, providing a determination coefficient of R^2>0.95. In other words, the final settlements and EOP times from theoretical solution agreed with the in-situ measurements. Settlement readings showed increasing values when the preload was removed after 180 days at Sector 1A, and the measurements started to be taken after the surcharge took effect in Sector 1B, 454 days later. Figure 8 illustrates the combined Δ-t curve for all the sections with Asaoka solution and in-situ measurements following the removal of the preload. In situ data is in agreement with the theoretical solution. Preloading started at 397 and 467 days after the mesurements were initiated in Sector 1B and 5B, respectively. The effect of loading can be inferred from the site measurements (Figure 6). When the curves from Asaoka solution and in-situ measurements were combined for Sector 1B and 5B, it was found that there is a strong tendency for the curves to coincide. The calculated final settlements were found to be significantly greater than the latest readings recorded in situ for all the sectors investigated. Additionally, the elapsed time for the last measurements were shorter than the computed EOP time from the Asaoka solution. This finding verified that consolidation settlement had not ceased at the sectors Sector 1A, 1B and 5B. Table 3 summarizes the results of evaluation of consolidation with Asaoka at the studied sectors.

Table 3 - Measured and estimated settlements and EOP

	SECTOR 1A	**SECTOR 1B**	**SECTOR 5B**
Final settlement measured (mm)	793	627	597
Time (Days)	1906	1201	1271
Final Settlement estimated with Asaoka (mm) [Figure 8]	873*	714	612
Estimated Time to EOP from Asaoka Solution (Days) [Eq.8]	8376	3406	2396
Coefficient of determination for the prediction [Figure 7]	0.996	0.979	0.996

*Sum of s_f by Asakoa (220mm) and final reading before neighbouring preloads (653mm)

It has been determined that the three sectors of the site have exhibited prolonged consolidation, despite the use of PVD. Besides, the calculated final settlements were found to require extended periods well beyond the estimated durations foreseen at the design stage.

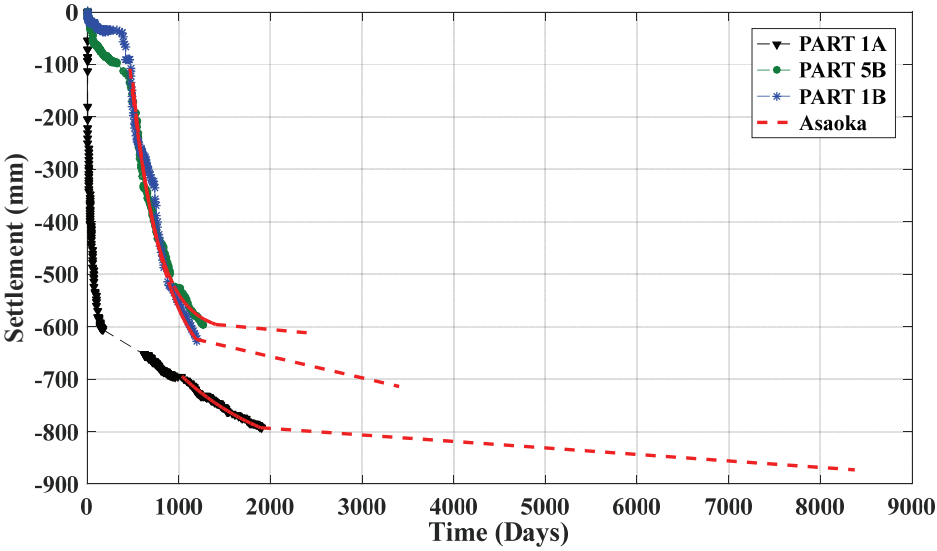

Figure 8 - Δ-t curves extrapolated with Asaoka projection

3.2. Numerical Analysis Models of PVD Design

The effect of main PVD design parameters in the remediation area, namely the coefficients of consolidation c_h or k_h, drain horizontal spacing (s_{drain}), and drain length (L_{drain}), were investigated with three-dimensional consolidation analysis (abbreviated as 3DCONS) as well as the finite element method (FEM). Consolidation analyses were performed using the Settle3D software, and finite element code Plaxis2D. FEM models the soil with constitutive material equations for hardening and softening behaviour. PVDs were modelled as drain elements which consider zero excess porewater pressure along the drain in order that the pressure difference between drains and the surrounding soil provides simulation of radial drainage. 3DCONS models on the other hand, were solved with the conventional radial drainage equations whereby unlike FEM models, constitutive models are not required. The only soil parameter employed was the permeability coefficient, while other values such as the drain length and spacing were adopted from PVD design. The results from 3DCONS and FEM models for each sector were compared with Asaoka predictions and in-situ measurements. The soil profile and properties were assigned to the models from borehole information and laboratory test results. PVD's were modelled by employing the information in Table 1. The assigned soil layers and their properties for each sector are given in Table 4. The Ground Water Table was 1.5~2.0m below the surface. The vertical coefficients of permeability employed in the models are listed in Table 5.

The final settlements calculated with the numerical models and Asaoka solution have been found to be higher than the latest in-situ measurements recorded, suggesting that consolidation was to continue in all the sectors investigated, had further monitoring been implemented.

Table 4 - Assigned soil profile and properties used in 3DCONS and FEM models

SECTOR 1A

	BALLAST	**ALLUVIUM**	**KUSDILI CLAY**	
	+3.00~0.00	**0.00 ~ -4.00**	**>-4.00**	
Model	**Hardening Soil**	**Soft Soil**	**Soft Soil**	**Unit**
ρ_n	22	18	17	**kN/m^3**
ρ_d	23	19	18	**kN/m^3**
c'	2	5	2	**kPa**
ϕ'	40	25	30	**º**
C_c	-	0.250	0.500	
C_r	-	0.070	0.080	
E_{50}^{ref}	50000	-	-	**kPa**
E_{oed}^{ref}	50000	-	-	**kPa**
E_{ur}^{ref}	150000	-	-	**kPa**
OCR	2	2.5	1	

SECTOR 1B

	BALLAST	**ALLUVIUM**	**KUSDILI CLAY**	**WEATHERED MARL**	**LIMESTONE**	
	+2.50~0.00	**0.00 ~ -5.00**	**-4.00 ~ -30.00**	**-30.00 ~ -35.00**	**>-35.00**	
Model	**Hardening Soil**	**Softening Soil**	**Softening Soil**	**Hardening Soil**	**Hardening Soil**	**Unit**
ρ_n	22	18	17	19	22	kN/m^3
ρ_d	23	19	18	20	23	kN/m^3
c'	2	5	2	25	150	kPa
ϕ'	40	25	30	25	25	º
C_c		0.250	0.450			
C_r		0.070	0.080			
E_{50}^{ref}	50000			30000	75000	kPa
E_{oed}^{ref}	50000			30000	75000	kPa
E_{ur}^{ref}	150000			90000	225000	kPa
OCR	2	2.5	1	4	8.0	

SECTOR 5B

	BALLAST	**ALLUVIUM**	**KUSDILI CLAY**	**WEATHERED MARL**	**MARL/ LIMESTONE**	
	+2.00~0.00	**0.00 ~ -4.00**	**-4.00 ~ -26.00**	**-26.00 ~ -30.00**	**>-30.00**	
Model	**Hardening Soil**	**Soft Soil**	**Soft Soil**	**Hardening Soil**	**Hardening Soil**	**Unit**
ρ_n	22	18	17	19	22	kN/m^3
ρ_d	23	19	18	20	23	kN/m^3
c'	2	5	2	25	150	kPa
ϕ'	40	25	30	25	25	º
C_c		0.250	0.500			
C_r		0.070	0.080			
E_{50}^{ref}	50000			30000	75000	kPa
E_{oed}^{ref}	50000			30000	75000	kPa
E_{ur}^{ref}	150000			90000	225000	kPa
OCR	2	2.5	1	4	8.0	

Table 5 - Vertical permeability coefficients employed in the geotechnical models

SECTOR	k_v (m/day)	
	ALLUVIUM	KUSDILI CLAY
1A	2.0×10^{-6}	1.0×10^{-6}
1B	2.0×10^{-6}	3.0×10^{-6}
5B	2.0×10^{-6}	5.0×10^{-6}

Final settlements obtained from the FEM analysis have been found to be close to the Asaoka solution whereas 3DCONS computations gave values noticeably higher than both the FEM and Asaoka solutions. Comparison of in-situ measurements and Asaoka solution with the computed final settlements from 3DCONS and FEM models are summarized in Table 6. The two analysis methods were compared by using percent error of the results with the Asaoka solution taken as reference. Negative percent error represents the case where calculated value is less than the reference settlement.

Table 6 - Comparison of results from 3DCONS, FEM and Asaoka

SECTOR	1A	1B	5B
Final measurement (mm)	793	627	597
Time (days)	1906	1201	1271
Estimated s_f with Asaoka (mm)	873	714	612
Estimated time to reach the s_f, t (Days)	8376	3406	2396
Computed s_f from FEM corresponding to t (mm)	864	706	628
Computed s_f from 3DCONS corresponding to t (mm)	919	797	763
Percent error for FEM results	-1.0%	-1.1%	2.6%
Percent error for 3DCONS results	5.3%	11.6%	24.7%

The error in the FEM analysis remained below 5%. However, the results from 3DCONS models deviated by 5-20% from the Asaoka solution. Thus, further analyses were carried out by FEM because the final settlements computed by FEM gave more consistent values than 3DCONS with respect to the site measurements.

3.3. Effect of Horizontal-Vertical Permeability Ratio in Consolidation

It is known that for a clay treated with PVD, the process is most efficient if the horizontal to vertical permeability coefficient k_h/k_v is higher than unity. Accordingly, *U-t* curves were generated for different k_h/k_v values to estimate the in-situ ratio by FEM. The *U-t* curves derived from numerical analyses were then compared to the curves obtained from in situ

measurements to reach the current k_h/k_v ratios. Finally, a comparison of the FEM results with the Asaoka results was carried out.

The percent consolidation value in the derived *U-t* curves were calculated by taking the ratio of the settlement value *s* to the final settlement s_f obtained in the Asaoka solution.

The *U-t* curves derived from the FEM model and the insitu measurements were plotted in the same diagram, and a horizontal line is drawn from 90% consolidation until it intersects the *U-t* curves. The k_h/k_v value intersecting the field measurement curve was adopted as the actual ratio.

The results arrived at by using this approach is given in Figure 9 for Sector 1A. It was found that the horizontal from *U*=%90 intersected the field measurement line at $k_h/k_v=1$ and this was accepted to be the actual value in situ.

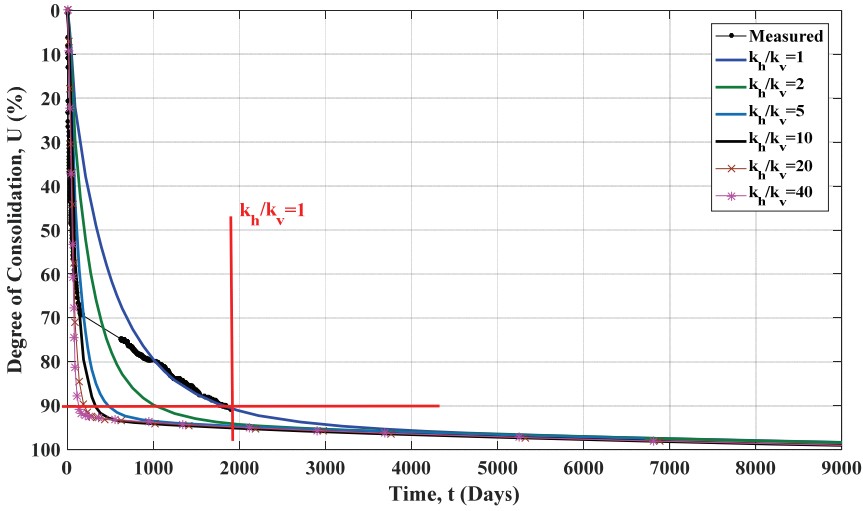

Figure 9 - Determination of k_h/k_v for Sector 1A

Table 7 summarises the k_h/k_v values calculated for all sectors, using the c_h value inferred from Asaoka and the method illustrated in Figure 9.

Table 7 - Comparison of k_h/k_v from FEM with Asaoka solution

SECTOR	c_v (m²/day)	k_v (m/day)	Asaoka c_h (m²/day)	Asaoka k_h/k_v	FEM k_h/k_v
1A	3.5×10^{-4}	1.0×10^{-6}	3.5×10^{-4}	1	1
1B	1.0×10^{-3}	3.0×10^{-6}	5.1×10^{-3}	5	3
5B	2.0×10^{-3}	5.0×10^{-6}	7.2×10^{-4}	4	5

The results show that the Asaoka and FEM solutions indicated almost identical permeability ratios. The Δ-t curves from field monitoring, Asaoka and FEM are depicted in Figure 10.

Sector 1A constitutes a special case in this study. Δ-t curves from Asaoka and FEM for this sector indicated that the time required to reach the final settlement of s_f= 873mm is more than 8000 days. This is a clear indication of the influence of the $k_h/k_v = 1$ ratio slowing down the process despite the presence of PVD.

The time required to reach the final settlement of s_f= 714mm at Sector 1B was calculated to be around 3000 days. Similarly, time required to reach the final settlement of s_f= 612mm at Sector 5B was predicted to be within 2000 days, with almost identical Asaoka and FEM results. It is confirmed from foregoing findings that k_h/k_v is the controlling factor in the process of preloading with PVD.

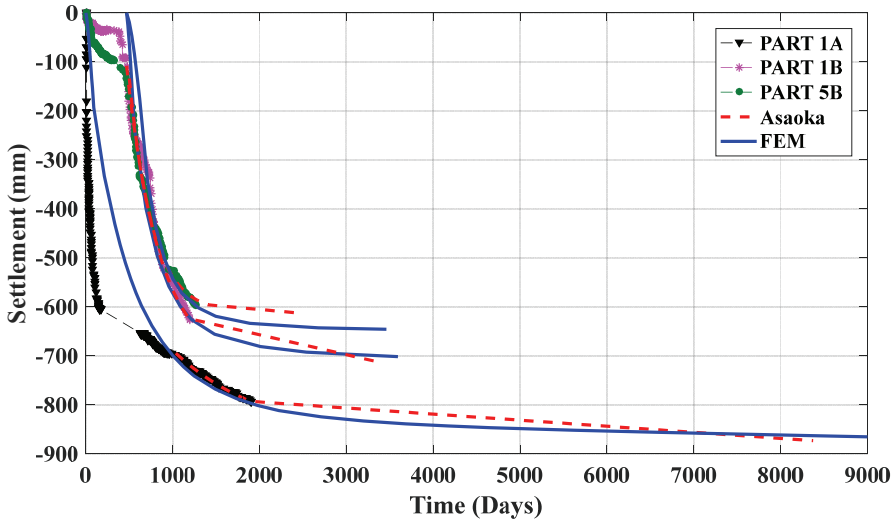

Figure 10 - Measured and FEM settlement-time curves

3.4. The Effect of Drain Spacing

This part of the study was carried out by keeping the k_h/k_v ratios and the lengths of the PVD constant, while the effect of varying the drain spacing s_{drain} on consolidation rates. Field measurements and estimation of Δ-t curves by Asaoka were compared to the FEM solutions for different drain spacings, s_{drain} being increased from 0.5m to 3.0m by steps of 0.5m. Figure 11 illustrates the effect of changing drain spacing on the Δ-t curves. Settlement corresponding to 95% of the total was calculated and the Δ-t curves were intersected with the horizontal drawn from this ordinate(U_{95}). The position of t_{95} on the curve determines the interval of the required drain spacing. It can be seen from the curve that for Sector A the drain spacing to reach 95% of the total settlement in 4856 days must be 1 to 1.5m.

The t_{95} values and the corresponding s_{drain} were calculated for sectors 1A, 1B, 5B in the same fashion and are compared to the values provided by the Asaoka solution in Table 8.

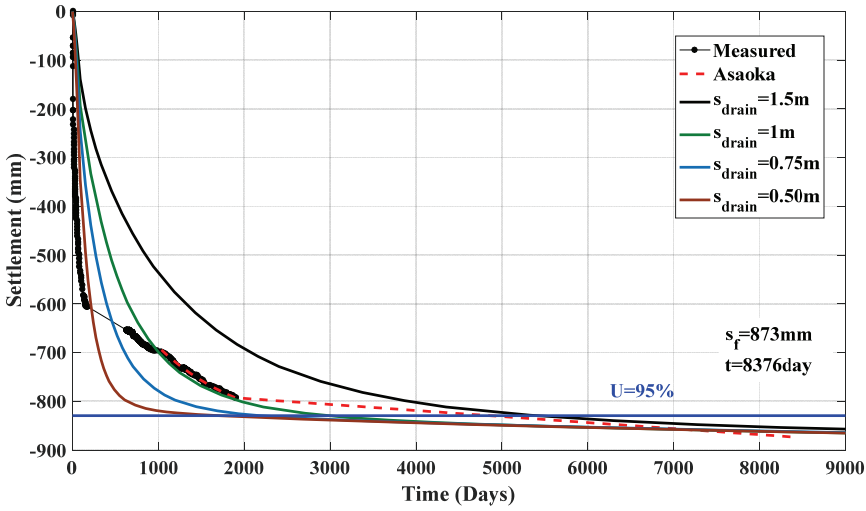

Figure 11 - The effect of variable drain spacing (s_{drain}) on settlement

Table 8 - t_{95} values for different s_{drain} values and Asaoka solution

	SECTOR 1A	**SECTOR 1B**	**SECTOR 5B**
Last in-situ measurement recorded (mm)	793	627	597
Time (Days)	1906	1201	1271
	***t_{95}* (Days)**		
Asaoka Solution	4856	2519	1236
s_{drain}=0.5m	1775	-	-
s_{drain}=0.75m	2261	-	-
s_{drain}=1m	3012	933	799
s_{drain}=1.5m	5414	1305	-
s_{drain}=2m	-	1683	1045
s_{drain}=2.5m	-	2268	1221
s_{drain}=3m	-	2699	1423

3.5. The Effect of Drain Length on Consolidation Settlement

The length of PVD on the rate of consolidation carries equal weight to spacing in the process of preconsolidation, especially if they do not reach a permeable layer at the bottom. Accordingly, the influence of drain length on consolidation was evaluated by increasing L_{drain}

from 15 to 30m using FEM. Δ-t curves for this case were developed keeping s_{drain} and k_h/k_v constant.

The t_{95} projected by Asaoka was compared to those obtained by the FEM. s_{drain} values were calculated using the procedure described above. The result of the analysis for Sector 1A is given in Figure 12, indicating the band $15<L_{drain}<20$m to reach t_{95} in 2519 days. The interval changed to $20<L_{drain}<25$m at Sector 1B and Sector 5B.

The findings of this section suggest that drain lengths used were insufficient to reach the EOP within the specified periods. The influence of changing drain lengths on EOP times are summarized in Table 9.

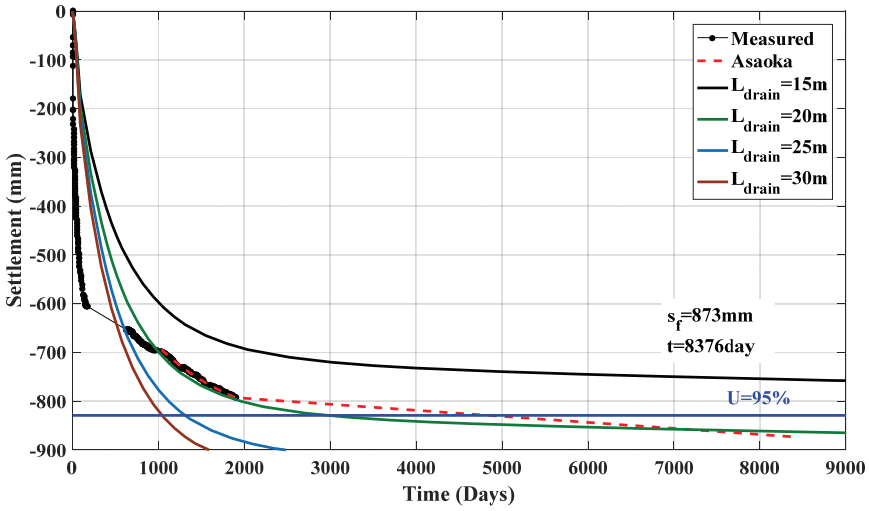

Figure 12 - The influence of L_{drain} variation

Table 9 - t_{95} values for varying L_{drain} and the Asaoka solution

	SECTOR 1A	**SECTOR 1B**	**SECTOR 5B**
Last Measurement (mm)	793	627	597
Elapsed Time (Days)	1906	1201	1271
	***t*95 (Days)**		
Asaoka Solution	4856	2519	1236
L_{drain}=15m	>9000	-	>2500
L_{drain}=20m	3012	>3500	1508
L_{drain}=25m	1316	1690	1055
L_{drain}=30m	1047	1213	1012

Calculations suggest that the EOP was significantly delayed in the case where L_{drain} was shorter than 20m with the result that the time to reach the foreseen s_f would be reached beyond acceptable limits.

4. DISCUSSION

Numerical analyses with finite element method and three-dimensional consolidation software 3DCONS were carried out for three sectors of a PVD-improved area which exhibited delayed consolidation periods. The percent error for FEM results with Asaoka taken as reference, remained below 5%, whereas 3DCONS models showed higher errors up to 5-20%. Furhermore, k_h/k_v from FEM models were found to be close or equal to the ratio obtained by Asaoka solution.

For Sector 1A, it was predicted by Asaoka procedure that the EOP duration would extend beyond 8000 days to reach the total settlement of s_f=873mm. While 714mm settlement predicted by Asaoka solution would be completed beyond 3000 days at Sector 1B. k_h/k_v values were calculated as 1 and 3 and the estimated final settlements and periods by the analyses gave higher values than the site measurements. Consequently, it was deduced that radial drainage which is the main purpose of PVD improvement was not been achieved extending the consolidation process.

For Sector 5B, where the permeability ratio was calculated as 5, PVD application was found to be more efficient than the other two problematic sectors. The preload for this sector was started after 467 days and the last measured settlement was 597mm. Compared to the final settlement of 612mm predicted by Asaoka, 95% of the final settlement had already been reached in the field. However, the EOP in Sector 5B was extended beyond 1200 days possibly due to the impact of surcharge placed on the adjacent sector Sector 1B, as expected.

Conflicting results were reached in studying the effect of drain spacing and length. For all the sectors, numerical analyses were carried out along with the insitu measurements to determine the required drain spacing and length. The analyses disclosed that implemented PVD design as described in Table 1 was unsatisfactory. Drain spacings were found to be larger than required by the analyses. Similarly, it has been demonstrated that PVD should have penetrated to sufficient depth in order that the actual EOPs would match the estimated limits.

A question may be posed here as to whether the low draining capacity detected may have been due to PVD creasing. However, because the settlements in the order of 70cms are relatively low (i.e. smaller than 15% of the original clay depth) to activate significant creasing in lengths of 20m or more, the probability of creasing was considered to be negligible [20, 21].

The reason for low permability ratio k_h/k_v especially in Sector 1A, is believed to be emanating either from inherent property of the marine/lacustrine clays studied, or due to possible smear effect which might have arisen during installation [22, 23].

5. CONCLUSIONS

A consolidation settlement analysis has been performed for the sectors a PVD-improved project area in Istanbul which exhibited prolonged consolidation beyond the expected period. The effect of changing the PVD parameters (k_h, s_{drain} and L_{drain}) on consolidation has been investigated to provide answers to this surprising behavior.

1. FEM models gave results in agreement with the site measurements. Finite element method re-calculates the porewater pressures for stress level at every stage of the analysis; hence, the soil behavior can be reflected realistically.

2. It was confirmed through the analyses that the consolidation process was extended beyond the expected durations. The main reason is believed to be the horizontal and vertical permeability ratios of the soils being quite close at this site. It is not clear whether this is due to the unique property of the clays at the site, or the effect of smearing. According to the analysis results, PVD implementation was not efficient in clays having k_h/k_v of approximately unity.

3. The main conclusion of this study was to discover the necessity for optimizing the variables in similar projects. The efficacy of the works can be significantly enhanced if simultaneous evaluation of the parameters s_{drain} and L_{drain} and the permeability ratio k_h/k_v is carried out prior to field work. Otherwise, "accidents" may emerge as found out in this project.

In addition to the standard analyses, the effect of secondary consolidation must also be investigated which may emerge as a critical issue in Recent clay deposits. One of the reasons of extended settlements can be attributed to secondary compression or creep effect, although no evidence of secondary consolidation was detected in the laboratory test results carried out for this project.

References

[1] Terzaghi K (1925) Erdbaumechanik. Franz Deuticke, Leipzig and Vienna.

[2] Terzaghi K (1943) Theoretical Soil Mechanics. Wiley, New York.

[3] Biot MA (1941) General Theory of Three-Dimensional Consolidation. Journal of Applied Physics 12: 155-164.

[4] Carillo N (1942) Simple two- and three-dimensional cases in the theory of consolidation of soils. Journal of Mathematics and Physics 21: 1-5.

[5] Rendulic L (1935) Der hydrodynamische Spannungsausgleich in zentral entwasserten Tonzylindern. Wasserwirtschaft und Technik 2: 250-253, 269-273.

[6] Barron RA (1948) Consolidation of fine-grained soils by drain wells. Transactions of ASCE 113: 718-754.

[7] Richart FE (1959) Review of the theories for sand drains. Transactions of ASCE 124: 709-736.

[8] Kjellman W (1948) Consolidation of fine-grained soils by drain wells. Transactions of ASCE 113, Contribution to the discussion.

[9] Budhu B (2010) Soil Mechanics and Foundations.3rd Ed. John Wiley and Sons, New York.

[10] Indraratna B, Rujikiatkamjorn C, Balasubramaniam AS, McIntosh G (2012) Soft ground improvement via vertical drains and vacuum assisted preloading. Geotextiles and Geomembranes 30:16-23

[11] Indraratna B, Zhong R, Fox PJ, Rujikiatkamjorn C (2017) Large-strain vacuum-assisted consolidation with non-Darcian radial flow incorporating varying permeability and compressibility. Journal of Geotechnical and Geoenvironmental Engineering 143(1): 04016088

[12] Hu YY, Zhou WH, Cai YQ (2014) Large-strain elastic viscoplastic consolidation analysis of very soft clay layers with vertical drains under preloading. Canadian Geotechnical Journal 51(2): 125-126

[13] Bergado DT, Balasubramaniam AS, Fannin RJ, Holtz RD (2002) Prefabricated vertical drains (PVDs) in soft Bangkok clay: a case study of the new Bangkok International Airport project. Canadian Geotechnical Journal 39: 304-315

[14] Chu J, Yan SW, Yang H (2000) Soil improvement by the vacuum preloading method for an oil storage station. Géotechnique 2000 50(6): 625-632

[15] Zhuang Y, Cui XY (2016) Evaluation of Vacuum Preloading with Vertical Drains as a Soft Soil Improvement Measure. Soil Mechanics and Foundation Engineering 53: 210-217.

[16] ASTM D2487 (2017) Standard Practice for Classification of Soils for Engineering Purposes (Unified Soil Classification System), ASTM International, West Conshohocken, PA, www.astm.org.

[17] Hansbo S, Jamiolkowski M, Kok L (1981) Consolidation by vertical drains. Géotechnique 31: 45-66.

[18] Asaoka A (1978) Observational Procedure of Settlement Prediction. Soils and Foundations 18: 87-101.

[19] Hausmann MR (1990) Engineering Principles of Ground Modification. McGraw-Hill, Singapore.

[20] Hansbo S (1983) How to evaluate the properties of prefabricated drains. Proc. 8th European Conference on Soil Mechanics and Foundation Engineering, Helsinki, pp. 621-626.

[21] Miura N, Chai JC, Toyota K (1998) Investigation on some factors affecting discharge capacity of prefabricated vertical drains. Proc. 6th International Conference on Geosynthetics, Atlanta, Georgia, pp. 845-850.

[22] Hansbo S (1987) Design aspects of vertical drains and lime column installation. Proc. 9th Southeast Asian Geotechnical Conference, Bangkok, Thailand, pp. 8-12.

[23] Bergado DT, Asakami H, Alfaro MC, Balasubramaniam AS (1991) Smear effects of vertical drains on soft Bangkok clay. Journal of Geotechnical Engineering 117: 1509-1530.

Teknik Dergi, 2022 11543-11567, Paper 647

Lightweight Cement-Based Composites Incorporating Hollow Glass Microspheres: Fresh and Hardened State Properties

Nihat KABAY[1]
Ahmet B. KIZILKANAT[2]
Büşra AKTÜRK[3]
Yusuf KAHRAMAN[4]

ABSTRACT

This research aims to develop a lightweight cementitious composite with satisfying mechanical and good thermal insulating properties. Two different types of hollow glass microspheres (HGM) were used as lightweight aggregates and were substituted with fine aggregate by 10, 20, and 40% by volume. The rheological, physical, mechanical, and microstructural properties of the resulting HGM-incorporated composites were investigated and correlations were established between physical and mechanical test results. The results showed that the physical and mechanical properties of individual HGM particles play a dominant role in the properties of lightweight mortars. HGM addition provided reductions up to 20% in the density and 45% in the thermal conductivity values of mortars compared to the reference. The best HGM ratio in the tested range was found as 20%, which provides benefits such as reduced density and enhanced thermal insulation capability without causing a significant reduction in compressive strength. It was concluded that HGMs can be used in the lightweight cementitious mortar production which has great potential in building applications to reduce the heating energy consumption.

Keywords: Hollow glass microspheres, rheology, mechanical properties, thermal conductivity, microstructure.

Note:
- This paper was received on January 24, 2020 and accepted for publication by the Editorial Board on August 17, 2020.
- Discussions on this paper will be accepted by March 31, 2022.
- https://doi.org/10.18400/tekderg.677447

1 Yildiz Technical University, Civil Engineering Department, Istanbul, Turkey - nkabay@yildiz.edu.tr https://orcid.org/0000-0003-4587-7095

2 Yildiz Technical University, Civil Engineering Department, Istanbul, Turkey - bkkanat@yildiz.edu.tr https://orcid.org/0000-0002-4507-704X

3 Istanbul Bilgi University, Civil Engineering Department, Istanbul, Turkey - busra.akturk@bilgi.edu.tr https://orcid.org/0000-0003-1484-7758

4 Yildiz Technical University, Civil Engineering Department, Istanbul, Turkey - yus_kah@hotmail.com https://orcid.org/0000-0002-3561-7348

1. INTRODUCTION

The advantages acquired by using lightweight materials in buildings are the reduced weight and the dead load acting on the structures which result in reduced size of structural elements [1], and lower thermal conductivity which accordingly increases energy savings and improves fire resistance. Reducing the greenhouse gas emissions related to energy consumed during operational issues of a building is crucial considering sustainability issues [2]. Therefore, any material related strategy that can help develop thermally efficient materials with reduced weight and that are structurally sound can also help with optimal building design from multiple performance points of view.

Lightweight concrete (LWC) is usually manufactured by adding lightweight aggregates (LWA) into the cementitious matrix. The most widely used LWA are pumice [3], expanded perlite [4–6], shale [7–9], expanded clay [10], and diatomite [11]. While the incorporation of lightweight materials in cementitious matrix achieves reduced density, traditional LWC and other cementitious composites possess lower mechanical properties. Recently, lightweight fillers (LWF) such as polystyrene beads, thermoplastic microspheres [12], hollow glass microspheres (HGMs) [13–15] and fly-ash [16–18] have been used to manufacture high performance lightweight cementitious composites for structural applications in buildings to compensate the disadvantages of conventional lightweight aggregate concrete.

The HGMs, also known as glass bubbles, can be defined as a glass material filled with air encapsulated by a thin spherical glass enclosure. HGMs are made from soda-lime borosilicate glass, and depending on their characteristic properties they possess different strength and density. They are nonporous, chemically inert, and resist against water and oil [19]. HGMs are commercially available with a variety of particle size and density and are compatible with cementitious materials [20].

HGMs are generally utilized as fillers [14] owing to their unique performance such as chemical, corrosion and fire resistance, light quality, and superior mechanical and physical properties [19,21,22]. Moreover, the spherical shape and the smooth surface of HGM has yielded to their use in oil well cement slurry [23]. It has been reported that HGM particles may cause an alkali-silica reaction in cement mortar [24], therefore before using HGMs in cementitious materials their chemical reactivity with cement compounds should be researched. In addition, the smooth surface, as well as poor bonding interface between matrix phase and HGM, may lead to lower strength and brittle failures [15].

The literature presents only a few studies on the use of HGMs in cementitious composites. Perfilov et al. [25] showed the potential use of HGM to cement oil and gas wells up to 4000 m deep. Al-Gemeel et al. [20] researched the effect of HGM on the mechanical and fracture properties of hybrid fiber reinforced engineered cementitious composite. They found reduced mechanical properties with increasing HGM content, but enhancements in mechanical properties, as well as reductions in density, could be provided with reducing the water to cement ratio. The authors concluded that it was possible to manufacture viable lightweight engineered cementitious composite products using HGM and suggested the need for further study on the feasibility of incorporating a higher amount of HGM in cementitious composites. Brooks et al. [2] performed extensive experimental research to comparatively study the effect of various types of LWF including the HGM on the several physical and mechanical properties of lightweight composites. They found that the thermal properties are significantly

affected by the volumetric ratio of the LWF and the mechanical properties are greatly dependant on the LWF particle properties including the bond between the particles and the cement matrix. Their research also showed that the HGM particles with lower shell thickness to diameter ratio tend to break when subjected to mechanical loads which should also be considered when using such materials in cementitious composites. Yun et al. [13] incorporated HGM at varying ratios up to about 30% by volume of total aggregates in lightweight aggregate concrete and found that HGM helped to reduce the thermal conductivity of concrete and they noted that to satisfy the mechanical soundness, the optimum HGM addition should be no more than 20%.

Limited information exists in the literature regarding the effect of LWA on the rheological properties of cementitious materials. Senff et al. [26] studied the effects of LWAs such as perlite and vermiculite on the rheological and mechanical properties of cement-based mortars. They reported that both types of aggregates improved the rheological properties substantially. On the other hand, the use of LWA degraded the mechanical resistance of mortars. Assaad [27] investigated the effect of styrene-butadiene rubber (SBR) latexes on the rheology of lightweight self-consolidating concrete mixes and found that SBR addition leads to reduced concrete flow rate and passing ability. The author attributed that to the increased cohesiveness resulting from the coalescence of water-soluble latexes and binding of the cementitious matrix. Gogoi et al. [28] researched the synergistic effect of HGM fillers and short bamboo fibers (SBF) on rheological and mechanical properties of light-weight composite materials. The authors found that HGM addition caused a significant improvement in hardness while a marginal decrease on impact strength was observed. They also concluded that both HGM and SBF improved the rheological properties.

The papers reviewed above focus on the potential use of LWAs, LWFs, and HGMs in cementitious materials and their effects on the rheological, mechanical, physical, and thermal properties of cementitious composites. However, the effects of HGM inclusion on the rheological, physical, and thermal properties of cement-based composites have not been revealed in detail yet. Considering the lack of studies on the rheological and thermal properties of HGM-modified cement composites, this experimental study aims to give a contribution to the improvement of thermal and physical properties of HGM-modified lightweight mortar without causing a significant reduction in the compressive strength. Therefore, the effect of two different types of HGMs (differing with their particle size, density, thermal conductivity, and crushing strength) on the fresh and hardened state properties of cement paste and mortar were investigated. Moreover, the best ratio for the HGM incorporation was proposed to give a satisfactory mechanical performance with reduced density and thermal conductivity. It was anticipated that the results obtained from this study will provide as yet unknown details on these lightweight cementitious systems and will contribute to the literature.

2. EXPERIMENTAL DETAILS

2.1. Materials and Mixtures

CEM I 42.5R type Portland cement was used as a binder throughout this study. The physical and chemical properties of cement are listed in Table 1.

CEN Standard sand with a maximum particle size of 2 mm and particle density of 2.68 kg/dm^3 was used as fine aggregate. The particle size distribution of HGMs (coded as HGM-I and HGM-II), cement, and sand were determined with Malvern Mastersizer 2000 instrument and the results are presented in Fig. 1. Fig. 2 shows the SEM micrographs of the HGMs used in this research. It can be seen that both HGMs have a spherical shape, HGM-I has finer diameter compared to HGM-II, and HGM-II presents a few amounts of damaged particles in its natural state.

Table 1 - Chemical composition and physical properties of cement

Compound (%)	SiO_2	18.9
	Al_2O_3	4.8
	Fe_2O_3	3.3
	MgO	1.5
	SO_3	3.3
	Na_2O	0.4
	CaO	63.7
	K_2O	0.7
	TiO_2	-
	Mn_2O_3	-
	S	-
	Cl (ppm)	600
LOI (%)		2.9
Specific surface area (cm^2/g)		3854
Specific gravity		3.1

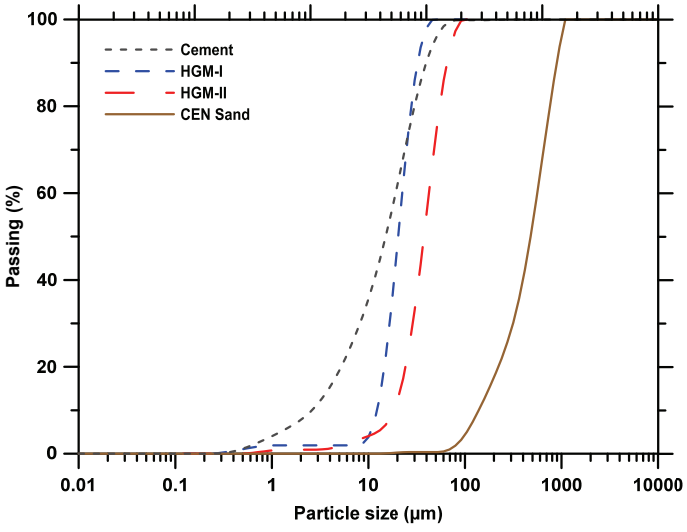

Fig. 1 - Particle size distribution of solid materials

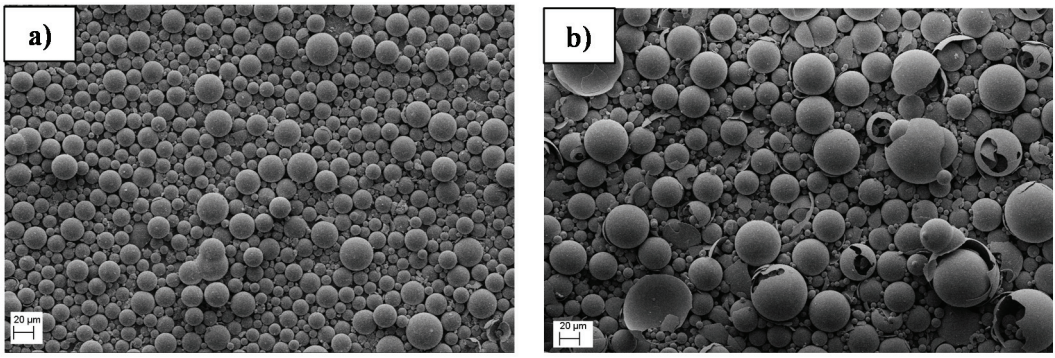

Fig. 2 - SEM images of (a) HGM-I and (b) HGM-II

The physical and mechanical properties of HGMs obtained from the manufacturer are summarized in Table 2. HGM-I can be distinguished from HGM-II with its finer particle size, higher isostatic crush strength, higher density, and higher thermal conductivity coefficient. The median particle size (d_{50}) of sand, cement, HGM-I, and HGM-II was determined by laser diffraction as 479.0 µm, 15.1µm, 20.3 µm and 37.5 µm, respectively.

Table 2 - Physical and mechanical properties of HGMs

HGM code	Isostatic crush strength (MPa)	Density (g/cm^3)	Specific surface area (cm^2/g)	Thermal conductivity (W/mK)
HGM-I	110.3	0.46	5630	0.153
HGM-II	2.8	0.22	2730	0.076

HGMs were introduced into the mortars substituting the sand by 10, 20, and 40% by volume by following a similar methodology from previous studies to maintain the compressive strength [2, 25]. It is well known that the cement replacement method might cause high reductions in strength [30] and therefore aggregate replacement method might be a better way of utilizing inert inclusions in cement composites to avoid significant reductions in mechanical properties [31–33].

A total of seven mortar and paste mixes were obtained and coded as Ref (reference mortar without HGM), HGM-I-10, HGM-I-20, HGM-I-40, HGM-II-10, HGM-II-20 and HGM-II-40, where the numbers represent the volume ratio of HGM. The mortar samples were prepared with a constant paste and aggregate volume of 50% and the HGMs replaced the fine aggregate at three different volumetric ratios as mentioned before. The water to cement ratio was considered as 0.5 in all mixtures.

The mixing started with a dry mix of solid materials (cement, sand, and HGM) for about one minute, then the water was added and the mixing was continued for about another three minutes until a uniform mix was obtained. Paste samples incorporating HGM were also manufactured to analyse the rheological properties and the microstructure. The paste samples were stored in sealed conditions at room temperature until being tested at 28 days for the microstructural analysis. Mix proportions of mortar and paste mixtures are shown in Table 3. The alkali-silica reactivity of the HGMs used in the experimental study was researched as per ASTM C1260 before starting the tests and the volume expansion was found to be below 0.09%.

Table 3 - Mixture proportions (kg) of mortar and paste samples

Mixture code	Cement		Water		Sand		HGM			
							Mortar		Paste	
	Mortar	Paste	Mortar	Paste	Mortar	Paste	HGM-I	HGM-II	HGM-I	HGM-II
Ref	607.8	1215.7	303.9	607.8	1340	0	0	0	0	0
HGM-I-10	607.8	1215.7	303.9	607.8	1206	0	23	0	41.8	0
HGM-I-20	607.8	1215.7	303.9	607.8	1072	0	46	0	76.7	0
HGM-I-40	607.8	1215.7	303.9	607.8	804	0	92	0	131.4	0
HGM-II-10	607.8	1215.7	303.9	607.8	1206	0	0	11	0	20
HGM-II-20	607.8	1215.7	303.9	607.8	1072	0	0	22	0	36.7
HGM-II-40	607.8	1215.7	303.9	607.8	804	0	0	44	0	62.9

2.2. Experimental Procedures

The effect of HGM inclusion on the rheological properties of cement paste was determined at room temperature (20 ± 0.5 °C) by using a rheometer with a strain-controlled mechanism. A four-blade vane configuration was used in this study. Approximately 35 ml of paste was introduced into the rheometer cup and precautions were taken to do the measurements immediately after the mixing. The test procedure consisted of three main stages; (*i*) constant pre-shear at 100/s for 30 s to homogenize the paste, (*ii*) 30 s resting, followed by a (*iii*) stepped ramp up from 0.05-to-100/s, and a stepped ramp down from 100-to-0.05/s (Fig. 3). At each step, steady-state shear stress was achieved after 10 sec. Each shear rate was maintained for 20 sec, data were acquired every second and the average of last 10 consecutive data was used to extract the yield stress (YS) and plastic viscosity (PV) in the down ramp. To obtain a reasonable portion of the stress plateau, a wide range of shear rate was applied as generally considered in the ordinary Portland cement pastes as well [34–40].

The plateau region of the ramp down was considered to be the YS in logarithmical mode. PV was calculated as the slope of the linear proportion of shear rate between 25/s and 100/s.

The workability of mortars was assessed by flow test as per EN 1015-3. Fresh mortar samples were placed into a conical mould with bottom and top diameter of 100 mm and 70 mm, respectively, and with a height of 60 mm. The excess mortar at the top of the cone was

removed and the mould was raised. The flow diameter was measured in two directions to determine the average flow diameter of the mortar. The compressive strength of mortar samples was determined on 50 mm cube specimens as per ASTM C109 at 3, 7, and 28 days and the flexural strength was determined at 28 days on $40 \times 40 \times 160$ mm prismatic specimens as per EN 196-1.

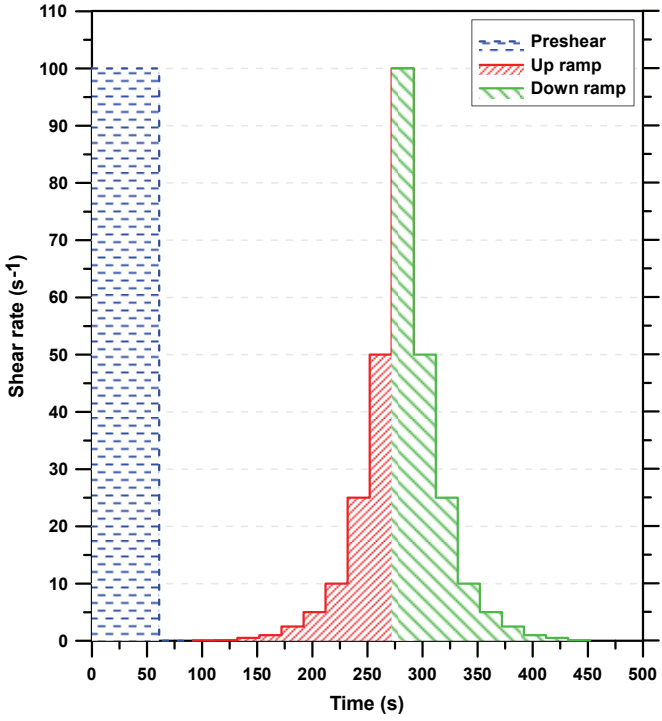

Fig. 3 - Rheological test procedure

The thermal conductivity measurements were performed on oven-dried disc specimens with a nominal diameter of 50 mm and thickness of 25 mm using the *Lasercomp Fox* series heat flowmeter instrument following the ASTM C518, EN 12664, EN 12667 and ISO 8301 standards. The thermal conductivity was determined by the following Eq. (2.1):

$$q = -kA\frac{\Delta T}{\Delta x} \tag{2.1}$$

where $q\ (W/m^2)$ is the heat flow, $k\ (W/mK)$ is the thermal conductivity, $A\ (m^2)$ is the area, $\Delta T\ (K)$ is the temperature difference and $\Delta x\ (m)$ is the sample thickness.

The microstructure of the pastes incorporating HGM was analysed using a scanning electron microscope (SEM). The paste samples were crushed and small pieces taken from the core were used in the SEM analysis to illustrate the distribution of HGMs in the matrix and to analyse the microstructure.

3. RESULTS AND DISCUSSION

3.1. Rheological Properties and Workability

Rheological properties such as YS and PV were determined on fresh paste samples and the workability was determined on fresh mortar samples by flow test. Figs. 4-6 show the variation of the rheological properties and the flow diameter of the paste and the mortar samples according to the ratios of HGM.

Fig. 4 presents the typical flow curves of the HGM modified cement pastes. Shear-thinning behaviour was observed in all mixes. It can be seen that both HGM-I and HGM-II mixes consistently showed higher shear stress values at each shear rate compared to the reference mixes.

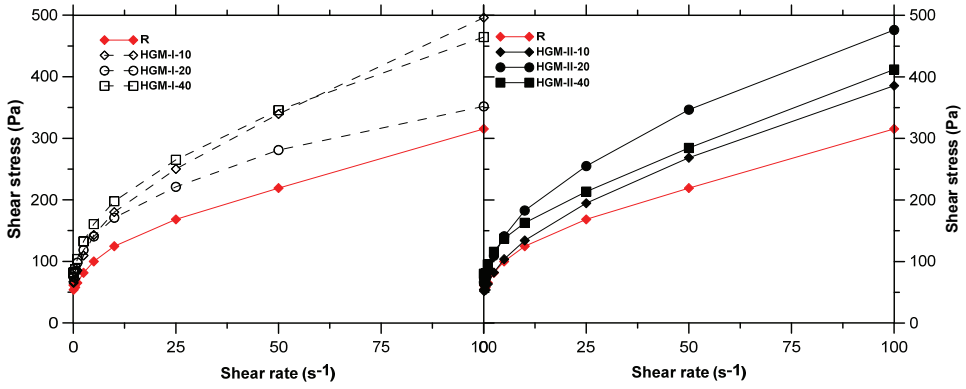

Fig. 4 - Typical flow curve of mixes

The YS values varied between 48.6 - 95.2 Pa and 44.3 - 63.3 Pa for HGM-I and HGM-II mixes, respectively. The YS and PV of the pastes consistently increased with increasing the HGM ratio; the reference mix (Ref) had the minimum YS and PV values, while HGM-I-40 and HGM-II-40 had the maximum values (Fig. 5). In addition, HGM-I mixes presented higher YS values than the HGM-II mixes, possibly due to the several characteristics of HGMs explained below. The PV results followed a similar trend as YS. HGM-I-40 mixes had the maximum PV value of 3.9 Pa.s, while the PV of the reference mix was only 0.3 Pa.s. The inclusion of HGM into the cement paste resulted in an increase in PV and this increase was significant when the HGM ratio increased from 20% to 40%. The increase in PV, with the increase in HGM volume from 20% to 40%, was 215% and 89% for HGM-I and HGM-II mixes, respectively.

It is generally known that an increase in particle concentration results in higher shear viscosity. One of the main reasons for the increase in YS and PV can be explained with the inter-particle forces between the HGM particles and the cement and HGMs. Inter-particle forces increase with the higher surface area of the components [41], therefore higher PV and YS can be expected in HGM-I mixes compared to HGM-II since HGM-I has a higher specific surface area (Table 2). Bentz et al. [42] reported that the rheological response is significantly influenced by both the particle densities and particle surface areas. Particle size distribution

(PSD) of the components of the blended mixes might be another parameter affecting the rheology. Lee et al. [43] noted that as the PSD of a cement/fly ash paste becomes wider, paste fluidity increases, which in turn reduces the apparent viscosity. Similarly, in this study, the PSD curves become narrower with HGM inclusion and consequently increases PV and YS. Since the YS values of the pastes were altered in the presence of HGM and the volume of the HGM was the same in HGM-I and HGM-II mixes, it can be concluded that the YS was mainly controlled by the fineness of the HGMs. Considering both the YS and the PV values of the mixes, it can be deduced that the rheological properties are greatly affected by HGM-I type HGM inclusion.

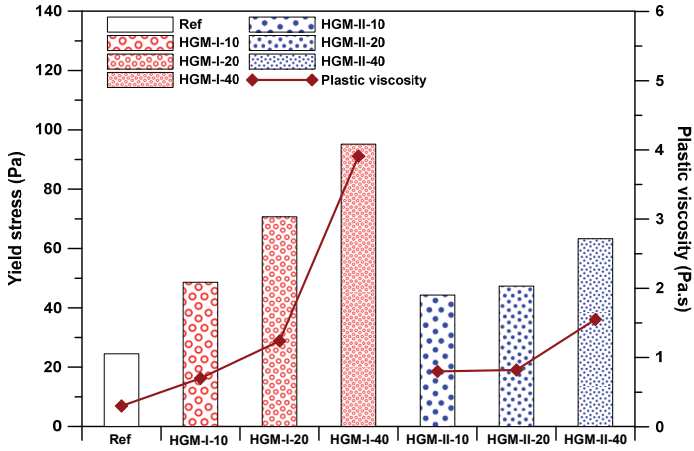

Fig. 5 - Yield stress and plastic viscosity of paste samples

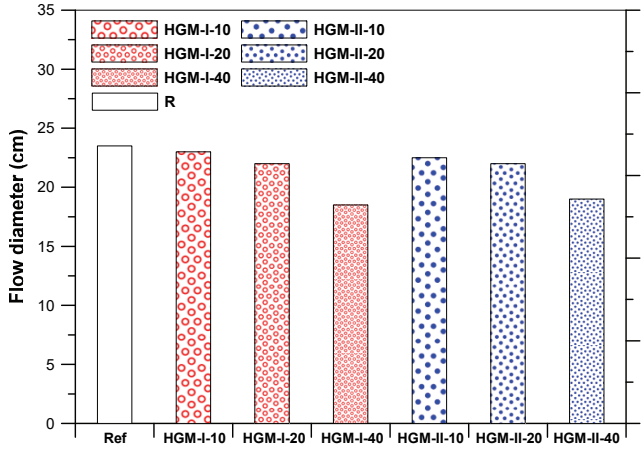

Fig. 6 - Flow diameter of mortar mixes

The workability test results are presented in Fig. 6. The flow diameter of mortars incorporating HGM reduced due to HGM inclusion. It could be thought that the incorporation of HGM may contribute to the flowability owing to its spherical shape. However, a significant reduction of about 20% (compared with the reference mortar) in flow diameter was noticed at 40% HGM ratio in HGM-I-40 and HGM-II-40 mixes. The reason for this behaviour was attributed to the fact that high amount of very small particles of HGMs negatively affects the workability and increases the water demand of mortar. On the other hand, lower HGM inclusion caused only slight reductions in workability (Fig.6).

Flow test results can be used to predict the rheological properties, such as YS, of the fresh cementitious materials [44–47]. Therefore, the results obtained in this research were used to establish a correlation between the rheological properties and flow diameter of HGM incorporated cement paste and mortars. The relationship between the determined rheological properties is presented in Fig. 7, where it can be noticed that they are correlated with each other, i.e. the higher the PV yields higher YS, and the higher the YS results in a lower flow diameter.

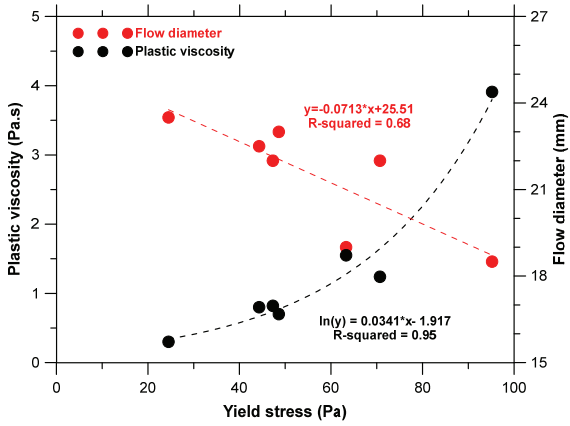

Fig. 7 - Correlations between plastic viscosity - yield stress and flow diameter - yield stress

3.2. Physical Properties

The physical properties of mortars are plotted in Figs. 8 and 9. Oven-dry density and thermal conductivity of the mortars proportionally reduced with the incorporation of both HGMs due to their low density and thermal conductivity. The reduction in the oven-dry density was relatively small for the ratios of 10 and 20%, but substantial reductions were recorded at higher ratios. The highest reduction (about 15% in HGM-I-40 and 20% in HGM-II-40) in the oven-dry density was observed at 40% incorporation ratio of both HGMs compared to the reference. The reduction in the thermal conductivity was found to be higher and the thermal conductivity consistently reduced by increasing the ratio of both HGMs. Thermal conductivity reduced by about 20% even at the lowest substitution ratio for each HGM, and the highest reduction was observed in the HGM-II-40 mix as 45%, compared to the reference. Comparing the effect of two HGMs on the thermal conductivity of mortars, it can be noticed

that the HGM-II mixes consistently possessed a lower thermal conductivity coefficient than the HGM-I mixes. The improvement in thermal conductivity is attributed to the lower thermal conductivity coefficient of the HGM-II particles.

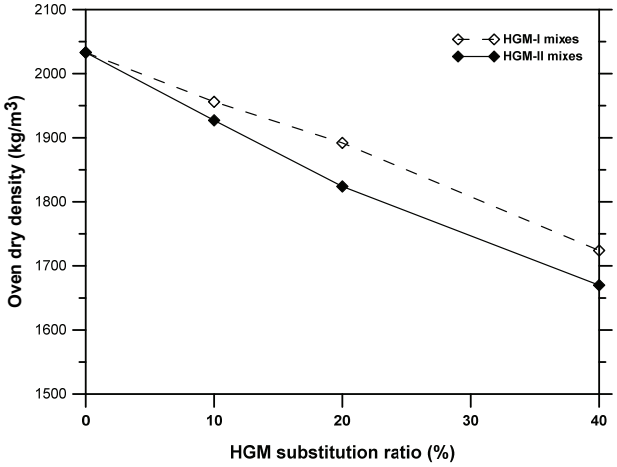

Fig. 8 - Oven dry density as a function of HGM ratio

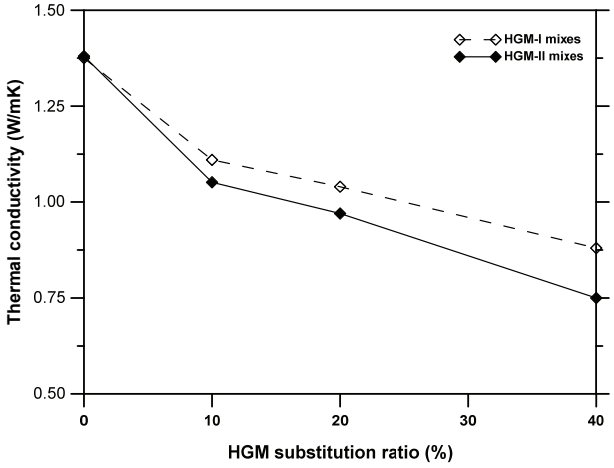

Fig. 9 - Thermal conductivity as a function of HGM ratio

3.3. Mechanical Properties

Compressive strength development of the mortars as a function of age is presented in Figs. 10 and 11, where a consistent increase in compressive strength of mortars by hydration time was noted. HGM inclusion created significant strength reductions at 40% ratio. The reduction was 25% in HGM-II-40 and 16% in HGM-I-40 mixtures at 28 days compared to the reference (Table 4), nevertheless, the lowest compressive strength at 28 days was 43 MPa (HGM-II-40 mix). The literature presents similar reductions in compressive strength with HGM

incorporation. Al-Gemeel et al. [20] studied the effect of HGM addition on fiber-reinforced cementitious composites. Their research showed reduced compressive strength which was attributed to the increased voids in the cementitious matrix due to the hollow sphere structure of HGM. Zhang et al. [48] reported strength reductions when using excessive amounts of HGM in geopolymer matrix, but higher strengths with lower HGM dosage. Brooks et al. [2] analyzed the effect of several LWAs including HGMs on the physical and mechanical properties of mortars. Their research showed that the compressive strength of mortars depends highly on the particle size and the shell property of the LWA and that the mortars having smaller size HGM and thicker shells yield higher compressive strength. In addition, it is also reported that the smooth surface and poor bonding between HGMs and the cement matrix might be another reason for lower strength performance [15].

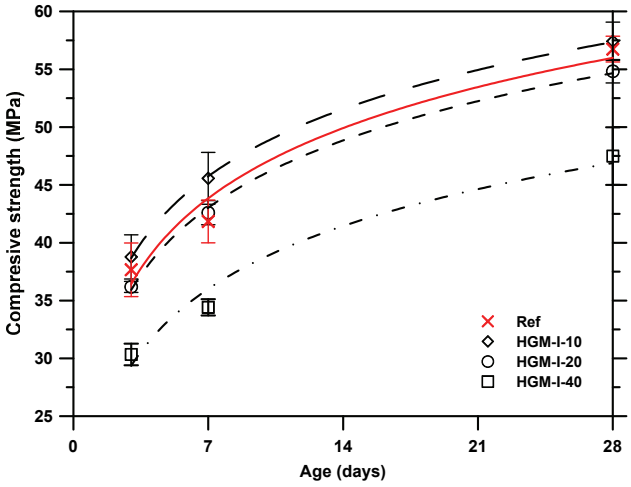

Fig. 10 - Compressive strength values of HGM-I mixes

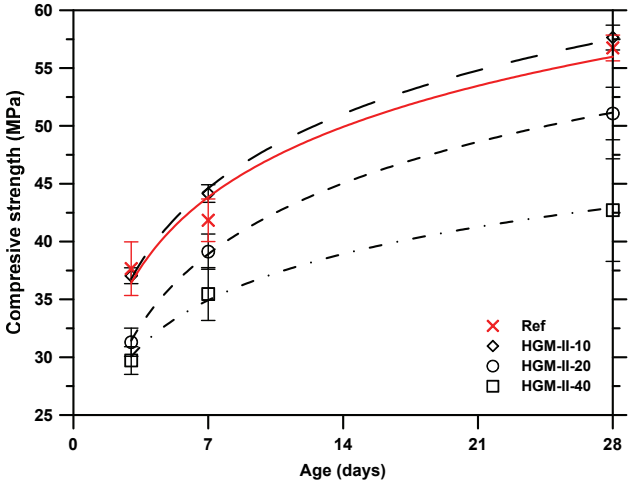

Fig. 11 - Compressive strength values of HGM-II mixes

The results of the present study show that at lower ratios (HGM-I-10 and HGM-II-10 mixtures) the compressive strength of mortars slightly increases compared to the reference (Table 4). The reduction in compressive strength was noted to be 3-10% at 28 days when the HGM ratio was 20%, which suggests a maximum substitution ratio with sand without sacrificing the compressive strength of cement mortar. It is also noteworthy to mention that the inclusion of HGM also reduces the density and the thermal conductivity of the mortar which also shows the probability of designing lightweight cementitious materials with lower density and higher thermal insulation properties without significant reduction in compressive strength. The effect of HGM type on the compressive strength results clearly shows that the mixtures incorporating HGM-I yields higher compressive strength compared to HGM-II. The main reason for this is possibly due to the higher strength property of HGM-I (about 40 times of HGM-II) particles and also its finer size distribution. It has been reported that the stress distribution of cementitious materials is related to both the sizes of inclusions and the difference in Young modulus of matrix and the inclusions and that the compressive strength increases with a decrease in LWA size [49]. Therefore, the finer particle size of the HGMs compared to the sand they substitute might have modified the stress distribution under compressive loads and improved the strength at especially lower substitution ratios. However, at higher ratios, the mechanical properties of HGM particles govern the compressive strength of the cement composites, and the achieved strength values of HGM incorporated mixes fail to surpass the reference mix where the fine aggregate is only sand.

Table 4 - Relative compressive strength of mortars

Mixture	Relative compressive strength (%)		
	3 days	7 days	28 days
Ref	100	100	100
HGM-I-10	103	109	101
HGM-I-20	96	102	97
HGM-I-40	81	82	84
HGM-II-10	98	106	102
HGM-II-20	83	94	90
HGM-II-40	79	85	75

The flexural strength results are shown in Fig. 12. A similar trend as in compressive strength was observed in flexural strength results of mortars. The flexural strength reduced with the HGM substitution, the exception was HGM-I-10, which showed a slight increase (about 3%) at 10% substitution ratio. The reduction in the flexural strength was noted as 13% and 31% for HGM-I-20 and HGM-II-20 mixes, and as 38% and 50% for HGM-I-40 and HGM-II-40 mixes respectively, compared to the reference. The higher strength loss in flexure compared to compression may indicate the weak interfacial bonding between HGM and matrix. The flexural strength of HGM-I mixes was found to be higher than that of the HGM-II mixes as in compressive strength at all HGM substitution ratios, which again indicates that the strength

characteristics of individual HGM particles play an important role in the mechanical properties of the cement mortars.

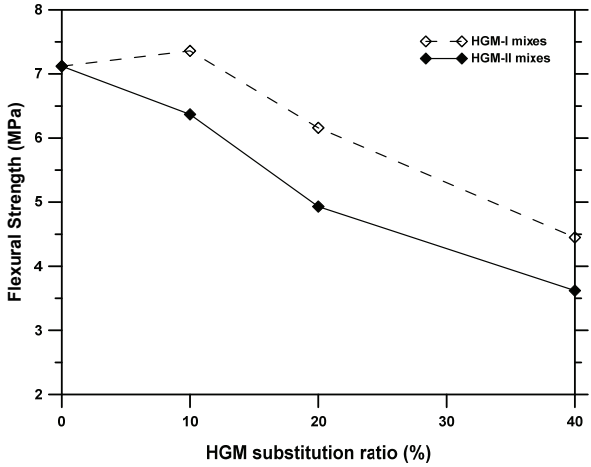

Fig. 12 - Flexural strength of mixes as a function of HGM substitution ratio

The most important function of incorporating LWA in the cementitious matrix is the reduction in the thermal conductivity coefficient with the reduced density. This beneficial reduction in the physical properties may unfortunately cause undesired reductions in mechanical properties, i.e. compressive strength, with the incorporation of LWA with weak strength properties. Table 5 summarizes previously researched different types of LWA in producing LWC for comparison with the HGMs used in this study. The general evaluation of the data presented in Table 5 shows that the compressive strength, density, and thermal conductivity reduces with an increase in the LWA content.

The strength reduction limits the use of these materials in structural applications where the compressive strength limit is set as 17-20 MPa in FIB and ACI codes [50]. Therefore the balance between strength, density, and thermal conductivity should be optimized with the aim of increasing strength and reducing density and thermal conductivity. This can be accomplished by carefully adjusting the amount of LWA and with a proper mix design to obtain reduced thermal conductivity and increased strength-to-density ratio (specific strength). It can be noticed from Table 5 that HGM incorporation in cementitious matrix leads to a reduced thermal conductivity coefficient comparable to the other LWA and an improved specific strength which is comparable to fly ash cenosphere (FAC) and significantly higher than the other LWAs, which makes it an ideal material for structural LWC applications. The information in Table 5 also shows that the compressive strength of LWC produced with natural aggregates such as pumice and perlite generally has lower compressive strength compared to those with artificial LWA (i.e. FAC and HGM) due to the fact that the latter have higher particle strength compared to the former. The use of expanded polystyrene (EPS) beads and polystyrene granules also results in significant reductions in compressive strength, which restricts the use of these materials where strength is also a major parameter.

Table 5 - A summary of LWC properties with various LWAs

Type of LWA	Reference	w/b	Dry Density (kg/m^3)	Thermal conductivity (W/mK)	Compressive strength, 28d (MPa)	Specific strength (kNm/kg)
HGM	Present study	0.50	1670 - 2033	0.75 - 1.38	42.7 - 57.7	25.6 - 27.9
	[2][1]	0.43	1434 - 2027	0.66 - 2.18	35.23 - 52.69	21.3 - 29.0[4]
EPS beads	[2] [1]	0.43	1300 - 2085	0.71 - 2.50	12.73 - 43.59	9.8 - 20.9[4]
Polystyrene granules	[51] [1]	0.55	1560 - 1980	0.27 - 0.61	19.0 - 37.0[3]	12.2 - 18.7[4]
Fly ash cenosphere (FAC)	[52] [1]	0.70	1098	0.41	23.54	21.4[4]
	[2] [1]	0.43	1396 - 2019	0.80 - 2.21	35.4 - 53.5	23.1 - 26.5[4]
Expanded perlite (EP)	[53] [2]	0.55	354 - 1833	0.13 - 0.60	0.1 - 28.8	0.3 - 15.7[4]
	[54] [2]	0.36	945 - 1540	0.30 - 0.67	15.6 - 29.1	16.1 - 18.9
Pumice	[55] [2]	0.64-1.23	1150 - 1271	0.345 - 0.455	14.63 - 26.09	12.7 - 20.5[4]
	[56] [2]	0.48	1370 – 2370[3]	0.41 - 2.0[3]	10.0 - 51.0[3]	7.3 - 21.5[4]
Expanded glass	[57] [2]	0.38 -0.59	1280 - 1490	0.485 - 0.847	23.3 - 30.2	18.2 - 20.3
Polyethylene beads (PEB) and Scoria+PEB	[58] [2]	0.45	1366 - 1744	0.338 - 0.510	16.93 - 26.53	11.9 - 15.2[4]

[1] Mortar mixes / [2] Concrete mixes / [3] Predicted values from the reference / [4] Calculated values

Table 6 presents the test results of selected LWC mixes from Table 5 incorporating different types of LWA with similar densities (1660 ± 40 kg/m^3) to compare their thermal insulation and strength properties.

Table 6 - Comparison of physical and mechanical properties of LWACs with similar density

Type of LWA	Reference	w/b	Dry Density (kg/m^3)	Thermal conductivity (W/mK)	Compressive strength, 28d (MPa)	Specific strength (kNm/kg)
HGM	Present study	0.50	1670	0.75	42.7	25.6
HGM	[2]	0.43	1670	0.98	48.4	29.0*
EPS beads	[2]	0.43	1705	1.42	26.1	15.3*
Scoria+polyethylene beads	[59]	0.45	1621	0.392	20.9	12.9*
FAC	[2]	0.43	1669	1.15	62.8	37.6*
EP	[53]	0.55	1677	0.57	17.3	10.3*

** Calculated values*

The present study shows that lightweight composite with an oven-dry density of 1670 kg/m^3, thermal conductivity coefficient of 0.75 W/mK, the compressive strength of 42.7 MPa, and specific strength of 25.6 kNm/kg can be manufactured by using HGM as LWA. With relatively low strength LWA, such as EPS beads [2] and expanded perlite [53], at similar density, the compressive strength and specific strength is 26 and 17 MPa and 15 and 10 kNm/kg, respectively. It can be seen from Table 6 that the higher specific strength could be obtained by using LWAs such as HGM and FAC, however, the lowest thermal conductivity values belong to mixes incorporating EPS beads, expanded perlite, and combination of scoria and polyethylene beads as LWAs. The results of the present study compared to the other studies in the literature confirm that strength reductions can be lowered by using HGM in LWC and also show its beneficial effects on the thermal conductivity, density, and specific strength.

3.4. Microstructure and Fracture Topography

The secondary scanning electron microscopic images of the fracture surface of paste mixes are shown in Figs. 13 and 14. As it is clearly seen in Fig. 13, HGMs are well distributed in the cement matrix as individuals without any agglomerations even at 40% incorporation ratio. In addition, it can be seen that the HGMs remained unreacted in the matrix. It can also be noticed that HGM-II mostly acts as weak points within the matrix which may promote the initiation and percolation of cracks (see Fig. 13 (c)). This phenomenon might have altered the physical and mechanical properties (Figs. 10-12) of mortar samples as the volume fraction of HGM increases, the mechanical properties decrease at higher dosages of HGM incorporation. The low mechanical strength of HGM-II particles could not resist the stresses within the matrix and the stress cracks mostly propagated through them, see Figs. 13 (d) and 14 (c). On the other hand, HGM-I particles mostly presented a different behaviour. The HGM-I particles are generally smaller in size (with an average particle size around 20 μm) and have higher crushing strength as compared to the HGM-II particles. Thus, the higher mechanical strength of HGM-I particles would alter the damage mode, where it can be observed that the crack growth was resisted by the HGM-I particles by hindering its path (Figs. 13 (a) and (b)). While some particles did break, many particles within the mortar have shown debonding instead of shell breakage, see Fig. 13 (a).

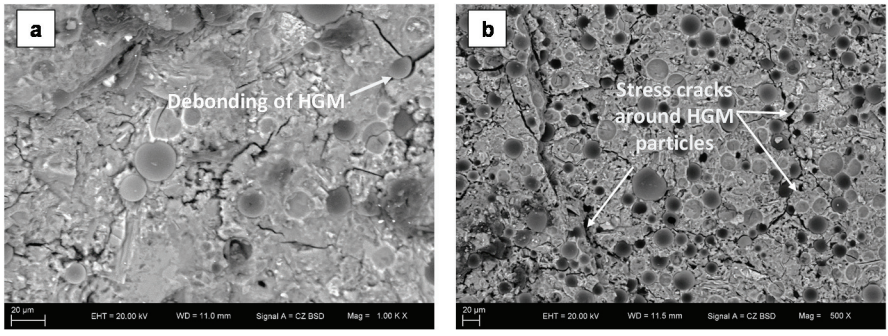

Fig. 13 - SEM micrographs of (a) HGM-I-10 (b) HGM-I-40 (c) HGM-II-10 (d) HGM-II-40 mixes

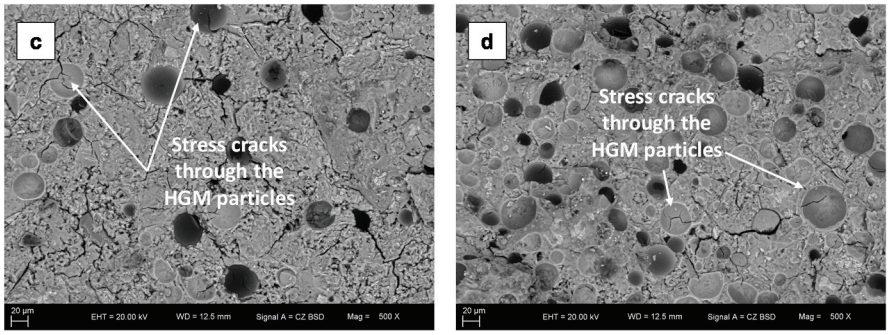

Fig. 13 - SEM micrographs of (a) HGM-I-10 (b) HGM-I-40 (c) HGM-II-10 (d) HGM-II-40 mixes (continue)

Fig.14 shows the interfacial transition zone characteristics of HGMs and the matrix. Generally, the dense cement hydration reaction products around the HGM particles are observed for both types of HGMs, which might also indicate that the distributed fine HGM in the cement matrix may act as nucleation sites for cement hydration products. However, large HGM-II particles allow stress cracks to propagate through their shell (Fig. 14 (c)) whereas the smaller HGM-I may act as barriers to hinder the propagation of stress crack (Fig. 14 (a)).

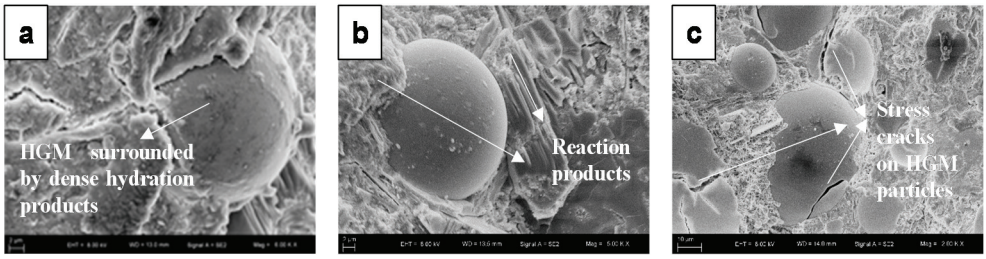

Fig. 14 - Microstructure of cement pastes incorporating HGMs: (a) HGM-I-10, (b) HGM-II-10, (c) HGM-II-40

3.5. Correlations between Physical and Mechanical Properties

It is well known that the physical and mechanical properties of concrete are correlated with each other and empirical relations have been developed between density, thermal conductivity, and compressive strength as shown in Tables 7 and 8. Since there is no available data in the literature which shows the relationship between density-thermal conductivity and density-compressive strength of HGM-modified cement composites, a regression analysis was performed to evaluate possible correlations between these parameters. Fig. 15 shows that the thermal conductivity and the compressive strength of HGM-modified composites can be predicted using the oven-dry density values with R-squared values of 0.9403 and 0.9116 respectively. The equation developed for thermal conductivity assessment was chosen in the

same format as the other works in the literature and presented comparable R^2 values as seen in Table 7. It should be noted here that for different LWA content and/or water to cement ratios, and for density values that fall outside the tested range of the present study, the equations proposed here should be used with care.

Table 7 - Empirical relations between density and thermal conductivity of lightweight concrete

Reference	Equation	R^2
Present study	$\lambda = 0.0718e^{0.0014\rho}$	0.9403
[56]	$\lambda = 0.0676e^{0.0015\rho}$	0.9498
[54]	$\lambda = 0.064e^{0.0015\rho}$	0.9476
[58]	$\lambda = 0.0625e^{0.0015\rho}$	0.8100
[60]	$\lambda = 0.000201\rho + 0.0776$	0.9440

Table 8 - Empirical relations between density and compressive strength of lightweight concrete

Reference	Equation	R^2
Present study	$f_c = 77.706\ln(\rho) - 532.31$	0.9116
[56]	$f_c = 4 \times 10^{-8}\rho^3 - 0.0002\rho^2 + 0.2734\rho - 128.64$	0.9100
[61]	$f_c = 0.1752\rho - 282.34$	0.8814
[62]	$f_c = 2 \times 10^{-17}\rho^{5.77}$	0.9710
[63]	$f_c = 10.3 \times \rho^{1.918} \times 10^{-6}$	0.9760

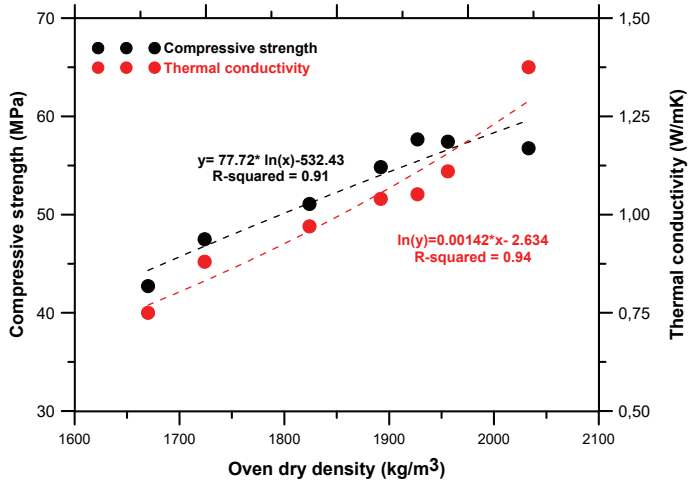

Fig. 15 - Correlations between compressive strength – oven dry density and thermal conductivity – oven dry density

4. CONCLUSIONS

Low thermal conductivity and density are the main characteristics of lightweight cement-based composites. Producing lightweight composites with improved thermal, physical, rheological, and mechanical properties is still a great concern for energy-efficient buildings. In this study, lightweight cementitious mortars were developed with improved thermal and physical characteristics by using HGMs. It was found that the composites comply with the ACI specifications of structural lightweight concrete which requires density between 1120 - 1920 kg/m^3 and a minimum compressive strength of 17 MPa at 28 days. To observe the effectiveness of the different types of HGMs on the rheological, physical, thermal, and mechanical characteristics, flow diameter, yield stress, thermal conductivity, along with the compressive and flexural strength tests were performed.

Based on the findings of this study, the following outcomes may be drawn:

- The particle size of the HGMs was found to be one of the most important parameters affecting the rheological properties and the flow diameter of the cement matrix. The finer the HGM resulted in higher yield stress and plastic viscosity and lower flow diameter. The HGM incorporation ratio also affected the rheological properties and flow diameter of cement paste and mortar, a consistent reduction in workability was noted with an increasing amount of both types of HGMs.

- The incorporation of HGM is found to be an effective method to obtain lower density and thermal conductivity. The type and amount of HGM play an important role in the reduction of thermal conductivity and density, HGM-II mixes possessed lower density and thermal conductivity values. Moreover, higher contents of HGM provided higher reductions. It was found that the density and the thermal conductivity of cement mortar may be reduced by up to 20% and 45%, respectively, by 40% HGM inclusion.

- The incorporation of HGM altered the mechanical properties of cement mortars. The compressive strength of cement mortar slightly increased with both HGMs at 10% ratio. The 20% HGM ratio was found to be critical for compressive strength where only minor reductions were observed compared to the reference, beyond this ratio (at 40%) the compressive strength reduced by 16% and 25% in HGM-I-40 and HGM-II-40 mixes, respectively. However, the compressive strength of mortars with 40% HGM inclusion may still satisfy the requirements of most civil engineering components in practice, since the compressive strength values appeared to be more than 43 MPa.

- The HGM-I mixes showed higher strength values than the HGM-II mixes, due to the higher mechanical strength characteristics compared to that of HGM-I. This also indicates that HGMs with higher mechanical strength should be chosen to achieve cement composites with higher mechanical properties.

- Comparison with other works revealed that at similar composite density, HGM as a LWA contributes to mechanical properties of cement composites more than the natural LWAs and EPS and polyethylene beads. Strong correlations were established between oven-dry density, thermal conductivity, and compressive

strength of HGM-modified composites, with correlation coefficients comparable to other studies.

- The SEM micrographs indicate homogeneous, well-distributed HGMs in the matrix and presence of dense cement hydration reaction products around the HGM particles. It was also noticed that HGM-I incorporated mixes presented a better performance in terms of resisting to stress cracks, which was the key parameter affecting the mechanical behavior.

It can be seen from the overall test results that the HGM-incorporation has a great influence on the thermal and physical performance of cement mortar mixes. The incorporation of HGM provides lower thermal conductivity and density. Moreover, desirable compressive strength values can be obtained by adjusting the amount of HGMs. It is thought that the results of the present study may contribute to the literature and also in the design and development of lightweight cementitious composites with enhanced thermal and physical properties by the incorporation of HGMs.

Acknowledgments

This work was supported by Research Fund of the Yildiz Technical University. Project Number: FBA-2017-3059.

References

[1] Yasar, E., Atis, C.D., Kilic, A., Gulsen, H. Strength properties of lightweight concrete made with basaltic pumice and fly ash. Mater. Lett. 57, 2267–2270, 2003. https://doi.org/10.1016/S0167-577X(03)00146-0

[2] Brooks, A.L., Zhou, H., Hanna, D., Comparative study of the mechanical and thermal properties of lightweight cementitious composites. Constr. Build. Mater., 159, 316–328, 2018 https://doi.org/10.1016/j.conbuildmat.2017.10.102

[3] Kabay, N., Aköz, F., Effect of prewetting methods on some fresh and hardened properties of concrete with pumice aggregate. Cem. Concr. Compos., 34, 503–507, 2012. https://doi.org/10.1016/j.cemconcomp.2011.11.022

[4] Kramar, D., Bindiganavile, V., Mechanical properties and size effects in lightweight mortars containing expanded perlite aggregate. Mater. Struct. Constr., 44, 735–748, 2011.
https://doi.org/10.1617/s11527-010-9662-0

[5] Lanzón, M., García-Ruiz, P.A., Lightweight cement mortars: Advantages and inconveniences of expanded perlite and its influence on fresh and hardened state and durability. Constr. Build. Mater., 22, 1798–1806, 2008. https://doi.org/10.1016/j.conbuildmat.2007.05.006

[6] Lu, Z., Xu, B., Zhang, J., Zhu, Y., Sun, G., Li, Z., Preparation and characterization of expanded perlite/paraffin composite as form-stable phase change material. Sol. Energy., 108, 460–466, 2014. https://doi.org/10.1016/j.solener.2014.08.008

[7] de Gennaro, R., Langella, A., D'Amore, M., Dondi, M., Colella, A., Cappelletti, P., de' Gennaro, M., Use of zeolite-rich rocks and waste materials for the production of structural lightweight concretes. Appl Clay. Sci. 41, 61–72, 2008. https://doi.org/10.1016/j.clay.2007.09.008

[8] Ke, Y., Beaucour, A.L., Ortola, S., Dumontet, H., Cabrillac, R., Influence of volume fraction and characteristics of lightweight aggregates on the mechanical properties of concrete. Constr. Build. Mater., 23, 2821-2828, 2009. https://doi.org/10.1016/j.conbuildmat.2009.02.038

[9] Lotfy, A., Hossain, K.M.A., Lachemi, M., Lightweight self-consolidating concrete with expanded shale aggregates: modelling and optimization. Int. J. Concr. Struct. Mater., 9, 185–206, 2015. https://doi.org/10.1007/s40069-015-0096-5

[10] Chandra, S., Berntsson, L., Lightweight aggregate concrete: science, technology, and applications, Elsevier, New York, USA, 2002.

[11] Ünal, O., Uygunoğlu, T., Diyatomitin hafif beton üretiminde kullanilmasi, Tek. Dergi/Technical J. Turkish Chamb. Civ. Eng., 18, 4025–4034, 2007. https://doi.org/10.18400/td.60606.

[12] Aglan, H., Shebl, S., Morsy, M., Calhoun, M., Harding, H., Ahmad, M., Strength and toughness improvement of cement binders using expandable thermoplastic microspheres. Constr. Build. Mater., 23, 2856–2861, 2009. https://doi.org/10.1016/j.conbuildmat.2009.02.031.

[13] Yun, T.S., Jeong, Y.J., Han, T.S., Youm, K.S., Evaluation of thermal conductivity for thermally insulated concretes. Energy. Build., 61:125–132, 2013. https://doi.org/10.1016/j.enbuild.2013.01.043.

[14] Zhang, Q., Li, V.C., Development of durable spray-applied fire-resistive Engineered Cementitious Composites (SFR-ECC). Cem. Concr. Compos., 60, 10–16, 2015. https://doi.org/10.1016/j.cemconcomp.2015.03.012.

[15] Oreshkin, D., Semenov, V., Rozovskaya, T., Properties of light-weight extruded concrete with hollow glass microspheres. Procedia Eng., 153, 638–643, 2016. https://doi.org/10.1016/j.proeng.2016.08.214.

[16] Huang, X., Ranade, R., Zhang, Q., Ni, W., Li, V.C., Mechanical and thermal properties of green lightweight engineered cementitious composites. Constr. Build. Mater., 48, 954–960, 2013. https://doi.org/10.1016/j.conbuildmat.2013.07.104.

[17] Xu, B., Ma, H., Hu, C., Yang, S., Li, Z., Influence of curing regimes on mechanical properties of magnesium oxychloride cement-based composites. Constr. Build. Mater., 102, 613–619, 2016. https://doi.org/10.1016/j.conbuildmat.2015.10.205.

[18] Hanif, A., Parthasarathy, P., Ma, H., Fan, T., Li, Z., Properties improvement of fly ash cenosphere modified cement pastes using nano silica, Cem. Concr. Compos., 81, 35–48, 2017. https://doi.org/10.1016/j.cemconcomp.2017.04.008.

[19] 3MGlass Bubbles, (n.d.). https://www.3m.com/3M/en_US/company-us/all-3m-products/~/All-3M-Products/Advanced-Materials/Glass-Bubbles/?N=5002385+8710783+8711017+8745513+3294857497&rt=r3 (accessed January 4, 2020).

[20] Al-Gemeel, A.N., Zhuge, Y., Youssf, O., Use of hollow glass microspheres and hybrid fibres to improve the mechanical properties of engineered cementitious composite. Constr. Build. Mater., 171, 858–870, 2018. https://doi.org/10.1016/j.conbuildmat.2018.03.172

[21] Li, H., Xu, H., Xu, B., Zhong, Z., Jiang, J., Li, Z., Wang, S., Zhang, H., Lightweight glass/carbon composite hollow microspheres with intact shell and good thermal stability. Ceram. Int., 43, 10581–10584, 2017. https://doi.org/10.1016/j.ceramint.2017.04.154.

[22] Ren, S., Li, X., Zhang, X., Xu, X., Dong, X., Liu, J., Du, H., Guo, A., Mechanical properties and high-temperature resistance of the hollow glass microspheres/borosilicate glass composite with different particle size. J. Alloys. Compd., 722, 321–329, 2017. https://doi.org/10.1016/j.jallcom.2017.06.092.

[23] Bubnov, A.S., Khorev, V.S., Boyko, I.A., The effect of lightweight agents on the density of cement slurry applied during oil and gas well drilling. IOP Conf. Ser. Earth Environ. Sci., 24, 2015. https://doi.org/10.1088/1755-1315/24/1/012008.

[24] Ichikawa, T., Miura, M., Modified model of alkali-silica reaction. Cem. Concr. Res., 37, 1291–1297, 2007. https://doi.org/10.1016/j.cemconres.2007.06.008

[25] Perfilov, V.A., Oreshkin, D.V., Semenov, V.S., Environmentally safe mortar and grouting solutions with hollow glass microspheres. Procedia Eng., 150, 1479–1484, 2016. https://doi.org/10.1016/j.proeng.2016.07.086

[26] Senff, L., Hotza, D., Labrincha, J.A., Effect of lightweight aggregates addition on the rheological properties and the hardened state of mortars, Appl. Rheol. 21, 1–8, 2011. https://doi.org/10.3933/ApplRheol-21-13668.

[27] Assaad, J.J., Rheology and stability of lightweight polymer-modified self-consolidating concrete, Appl. Rheol., 27, 1–11, 2017. https://doi.org/10.3933/APPLRHEOL-27-25807.

[28] Gogoi, R., Kumar, N., Mireja, S., Ravindranath, S.S., Manik, G., Sinha, S., Effect of Hollow Glass Microspheres on the Morphology, Rheology and Crystallinity of Short Bamboo Fiber-Reinforced Hybrid Polypropylene Composite, JOM, 71, 548–558, 2019. https://doi.org/10.1007/s11837-018-3268-3.

[29] Aguayo, M., Das, S., Maroli, A., Kabay, N., Mertens, J.C.E., Rajan, S.D., Sant, G., Chawla, N., Neithalath, N., The influence of microencapsulated phase change material (PCM) characteristics on the microstructure and strength of cementitious composites: Experiments and finite element simulations. Cem. Concr. Compos., 73, 29–41, 2016. https://doi.org/10.1016/j.cemconcomp.2016.06.018

[30] Li, L.G., Wang, Y.M., Tan, Y.P., Kwan, A.K.H., Filler technology of adding granite dust to reduce cement content and increase strength of mortar. Powder Technol., 342, 388–396, 2019. https://doi.org/10.1016/j.powtec.2018.09.084

[31] Bédérina, M., Khenfer, M.M., Dheilly, R.M., Quéneudec, M., Reuse of local sand: Effect of limestone filler proportion on the rheological and mechanical properties of different sand concretes. Cem. Concr. Res., 35, 1172–1179, 2005. https://doi.org/10.1016/j.cemconres.2004.07.006

[32] Yang, E.I., Yi, S.T., Leem, Y.M., Effect of oyster shell substituted for fine aggregate on concrete characteristics: Part I. Fundamental properties. Cem. Concr. Res., 35, 2175–2182, 2005. https://doi.org/10.1016/j.cemconres.2005.03.016

[33] Thomas, B.S., Damare, A., Gupta, R.C., Strength and durability characteristics of copper tailing concrete. Constr. Build. Mater., 48, 894–900, 2013. https://doi.org/10.1016/j.conbuildmat.2013.07.075

[34] Vance, K., Sant, G., Neithalath, N., The rheology of cementitious suspensions: A closer look at experimental parameters and property determination using common rheological models. Cem. Concr. Compos., 59, 38–48, 2015. https://doi.org/10.1016/j.cemconcomp.2015.03.001

[35] Erzengin, S.G., Kaya, K., Perçin Özkorucuklu, S., Özdemir, V., Yıldırım, G., The properties of cement systems superplasticized with methacrylic ester-based polycarboxylates. Constr. Build. Mater., 166, 96–109, 2018. https://doi.org/10.1016/j.conbuildmat.2018.01.088

[36] Arora, A., Aguayo, M., Hansen, H., Castro, C., Federspiel, E., Mobasher, B., Neithalath, N., Microstructural packing- and rheology-based binder selection and characterization for Ultra-high Performance Concrete (UHPC). Cem. Concr. Res., 103, 179–190, 2018. https://doi.org/10.1016/j.cemconres.2017.10.013

[37] Torres-Carrasco, M., Rodríguez-Puertas, C., Del Mar, A.M., Puertas, F., Alkali activated slag cements using waste glass as alternative activators. Rheological behaviour. Bol. La Soc. Esp. Ceram. y Vidr., 54, 45–57, 2015. https://doi.org/10.1016/j.bsecv.2015.03.004

[38] Nazário, S.F., Gomes de Sousa S.R., Bombard, A.J. F., Lopes, V.S., Rheological study of cement paste with metakaolin and/or limestone filler using Mixture Design of Experiments. Constr. Build. Mater., 143, 92–103, 2017. https://doi.org/10.1016/j.conbuildmat.2017.03.001

[39] Colombo, A., Geiker, M.R., Justnes, H., Lauten, K., De Weerdt, On the effect of calcium lignosulfonate on the rheology and setting time of cement paste. Cem. Concr. Res., 100, 435–444, 2017. https://doi.org/10.1016/j.cemconres.2017.06.009

[40] Tan, H., Zou, F., Ma, B., Guo, Y., Li, X., Mei, J., Effect of competitive adsorption between sodium gluconate and polycarboxylate superplasticizer on rheology of cement paste. Constr. Build. Mater., 144, 338–346, 2017. https://doi.org/10.1016/j.conbuildmat.2017.03.211

[41] Papo, A., Piani, L., Ricceri, R., Rheological properties of very high-strength portland cement pastes: influence of very effective superplasticizers. Int. J. Chem. Eng., 1–7, 2010. https://doi.org/10.1155/2010/682914.

[42] Bentz, D.P., Ferraris, C.F., Galler, M.A., Hansen, A.S., Guynn, J.M., Influence of particle size distributions on yield stress and viscosity of cement-fly ash pastes. Cem. Concr. Res., 42, 404–409, 2012. https://doi.org/10.1016/j.cemconres.2011.11.006

[43] Lee, S.H., Kim, H.J., Sakai, E., Daimon, M., Effect of particle size distribution of fly ash-cement system on the fluidity of cement pastes. Cem. Concr. Res., 33, 763–768, 2003. https://doi.org/10.1016/S0008-8846(02)01054-2

[44] Roussel, N., Stefani, C., Leroy, R., From mini-cone test to Abrams cone test: Measurement of cement-based materials yield stress using slump tests. Cem. Concr. Res., 35, 817–822, 2005. https://doi.org/10.1016/j.cemconres.2004.07.032

[45] Roussel, N., Coussot, P., Fifty-cent rheometer for yield stress measurements: From slump to spreading flow. J. Rheol., 49, 705–718, 2005. https://doi.org/10.1122/1.1879041

[46] Roussel, N., Correlation between yield stress and slump: Comparison between numerical simulations and concrete rheometers results. Mater. Struct. Constr., 39, 501–509, 2006. https://doi.org/10.1617/s11527-005-9035-2

[47] Choi, S.J., Choi, J.I., Song, J.K., Lee, B.Y., Rheological and mechanical properties of fiber-reinforced alkali-activated composite. Constr. Build. Mater., 96, 112–118, 2015. https://doi.org/10.1016/j.conbuildmat.2015.07.182

[48] Zhang, W., Yao, X., Yang, T., Liu, C., Zhang, Z., Increasing mechanical strength and acid resistance of geopolymers by incorporating different siliceous materials. Constr. Build. Mater., 175, 411–421, 2018. https://doi.org/10.1016/j.conbuildmat.2018.03.195

[49] Le Roy, R., Parant, E., Boulay, C., Taking into account the inclusions' size in lightweight concrete compressive strength prediction. Cem. Concr. Res., 35, 770–775, 2005. https://doi.org/10.1016/j.cemconres.2004.06.002

[50] Dixit, A., Pang, S.D., Kang, S.H., Moon, J., Lightweight structural cement composites with expanded polystyrene (EPS) for enhanced thermal insulation. Cem. Concr. Compos., 102, 185–197, 2019. https://doi.org/10.1016/j.cemconcomp.2019.04.023

[51] Wang, R., Meyer, C., Performance of cement mortar made with recycled high impact polystyrene. Cem. Concr. Compos., 34, 975–981, 2012. https://doi.org/10.1016/j.cemconcomp.2012.06.014

[52] Hanif, A., Diao, S., Lu, Z., Fan, T., Li, Z., Green lightweight cementitious composite incorporating aerogels and fly ash cenospheres-Mechanical and thermal insulating properties. Constr. Build. Mater., 116, 422–430, 2016. https://doi.org/1037//0033-2909.I26.1.78

[53] Sengul, O., Azizi, S., Karaosmanoglu, F., Tasdemir, M.A., Effect of expanded perlite on the mechanical properties and thermal conductivity of lightweight concrete. Energy Build. 43, 671–676, 2011. https://doi.org/10.1016/j.enbuild.2010.11.008

[54] Tajra, F., Abd Elrahman, M., Lehmann, C., Stephan D (2019) Properties of lightweight concrete made with core-shell structured lightweight aggregate. Constr Build Mater 205:39–51. https://doi.org/10.1016/j.conbuildmat.2019.01.194

[55] Gündüz, L., Uğur, I., The effects of different fine and coarse pumice aggregate/cement ratios on the structural concrete properties without using any admixtures. Cem. Concr. Res., 35, 1859–1864, 2005. https://doi.org/10.1016/j.cemconres.2004.08.003

[56] Oktay, H., Yumrutaş, R., Akpolat, A., Mechanical and thermophysical properties of lightweight aggregate concretes. Constr. Build. Mater., 96, 217–225, 2015. https://doi.org/10.1016/j.conbuildmat.2015.08.015

[57] Yu, Q.L., Spiesz, P., Brouwers, H.J.H., Development of cement-based lightweight composites – Part 1: Mix design methodology and hardened properties. Cem. Concr. Compos., 44, 17–29, 2013. https://doi.org/10.1016/j.cemconcomp.2013.03.030

[58] Iman, A., Payam, S., Fitri, A.H.Z., Binti, M.N., Thermal conductivity of concrete – A review. J, Build, Eng., 20, 81–93, 2018. https://doi.org/10.1016/j.jobe.2018.07.002

[59] Ali, M.R., Maslehuddin, M., Shameem, M., Barry, M.S., Thermal-resistant lightweight concrete with polyethylene beads as coarse aggregates. Constr. Build. Mater., 164, 739–749, 2018. https://doi.org/10.1016/j.conbuildmat.2018.01.012

[60] Demirboğa, R., Gül, R., The effects of expanded perlite aggregate, silica fume and fly ash on the thermal conductivity of lightweight concrete. Cem. Concr. Res., 33, 723–727, 2003. https://doi.org/10.1016/S0008-8846(02)01032-3

[61] Kockal, N.U., Ozturan, T., Strength and elastic properties of structural lightweight concretes. Mater. Des., 32, 2396–2403, 2011. https://doi.org/10.1016/j.matdes.2010.12.053

[62] Blanco, F., Garciéa, P., Mateos, P., Ayala, J., Characteristics and properties of lightweight concrete manufactured with cenospheres. Cem. Concr. Res., 30, 1715–1722, 2000. https://doi.org/10.1016/S0008-8846(00)00357-4

[63] Babu, D.S., Ganesh Babu, K., Tiong-Huan, W., Effect of polystyrene aggregate size on strength and moisture migration characteristics of lightweight concrete. Cem. Concr. Compos., 28, 520–527, 2006. https://doi.org/10.1016/j.cemconcomp.2006.02.018

Teknik Dergi, 2022 11569-11589, Paper 648

Fundamental Frequencies of Elliptical Plates using Static Deflections

Murat ALTEKIN[1]

ABSTRACT

Fundamental frequencies of solid and annular elliptical plates were approximated using the static deflections by means of finite element method (FEM) without computing the eigenvalues. The problem was formulated within the framework of the first order shear deformation theory (FSDT). The effects of (i) the inner and outer boundary conditions, (ii) the size of the perforation, (iii) the aspect ratio, and (iv) the thickness of the plate on the performance of the method were examined via a large number of numerical simulations. Convergence study was performed through h-refinement. Accuracy of the results was validated through comparison studies. The results reveal that the application of Morley's formula which does not require eigenvalue analysis approximates the fundamental frequency with finer mesh compared to the eigenvalue analysis. The method can be considered as a practical technique to approximate the fundamental frequency. However, the boundary conditions have dominant role on the accuracy of the solution particularly when the plate is perforated.

Keywords: Vibration, fundamental frequency, static deflection, plate, finite element.

1. INTRODUCTION

Plates are lightweight members which are extensively used as primary or secondary structures (e.g., slabs, wings of aircrafts, parts of machines, solar panels, power plants, aircrafts, electronic devices, etc.) in a broad variety of industrial fields by various engineering disciplines (e.g., civil, mechanical, aeronautical, ocean, and naval engineering) [1-6]. Due to architectural demands or design purposes such as reduction of weight, efficiency of materials, and ventilation cutouts of various shapes are frequently incorporated in plate-type structures which may be thin or thick [7-8]. Sensors, actuators [9], and mechanical power transmission components [10] are some of the typical applications of annular plates.

Their widespread use gives rise to the publications in which static or dynamic response of plates is studied (e.g. [1-59]). The majority of the investigations on plates involve the

Note:
- This paper was received on October 27, 2020 and accepted for publication by the Editorial Board on September 20, 2021.
- Discussions on this paper will be accepted by March 31, 2020.
- https://doi.org/10.18400/tekderg.817251

1 Department of Civil Engineering, Yildiz Technical University, Istanbul, Turkey
altekin@yildiz.edu.tr - https://orcid.org/0000-0003-3532-688X

classical plate theory (CPT) which is a valid model only for thin plates [50], or FSDT [51]. The superiority of FSDT over CPT is that the transverse shear deformation which should be considered for a reliable analysis of moderately thick plates [51], is included in FSDT. Although FSDT has been proved to be sufficiently effective and accurate [52], it requires a shear correction factor which is difficult to determine [50]. Various higher order shear deformation theories (HSDTs) have been developed to overcome this difficulty [50, 53]. Compared to the solution within the framework of FSDT, the accuracy of the analysis using HSDTs has been slightly improved [50], but the equations of motion in HSDTs are more complicated than those in FSDT [50]. The computational cost of HSDTs, and the simplicity of FSDT might have been the primary motivations for the rigorous use of FSDT [54] in the literature.

Vibration characteristics of structures have vital importance for engineers. Due to the increasing demand for the solutions of such problems [8], dynamic analysis has been an active research topic (e.g., [1-7, 9-35]). Since the boundary conditions and the geometry of the plate are two of the leading factors that affect the availability of closed form solutions (e.g., [36]), various numerical methods have frequently been used in the papers on plates with curvilinear boundaries (e.g., [5, 21-35]). Apart from the widely used numerical procedures which require the computation of the eigenvalues such as Ritz, FEM, finite difference method, discrete singular convolution (DSC), and differential quadrature method (e.g., [3, 20, 23-25, 37, 49, 55, 60]), there are several approximate techniques (e.g., Dunkerley's method, Southwell method, and Morley's formula) which are used to estimate the fundamental frequency of structures especially when an exact solution is not available [27], or the time cost of the eigenvalue analysis is not preferable or affordable. Weiss [28] calculated the fundamental frequency of thin solid circular plates by means of Dunkerley's formula. Jaroszewicz et al. [29] applied the Bernstein-Kieropian simplest lower estimators for calculation of basic natural vibration frequencies of variable-thickness circular plates. Recently, Jaroszewicz, and Radziszewski [30] investigated the approximate fundamental frequency of clamped circular plates using Dunkerley's formula. Altekin [31-32] reported the fundamental frequencies of solid and annular circular plates using Morley's formula.

The engineering motivation of the problem is to determine the fundamental frequencies of solid and annular elliptical plates using the static deflections by means of Morley's formula which is based on Rayleigh's method [40], rather than performing a typical eigenvalue analysis which is inherently non-linear [42]. However, since "the accuracy depends largely on how closely the static deflection shape approximates the fundamental mode" [40], the accuracy is improved with increasing number of elements in the solution domain. To the best of the author's knowledge, there have been no published papers on the dynamic analysis of shear deformable elliptical plates using static deflections. FSDT was adopted in the formulation in the current study. The influence of the boundary conditions, the aspect ratio, and the effect of the perforation on the results were discussed. The algorithm was coded by the author in Matlab. The classical FEM solution which was also presented in the paper to highlight the performance of Morley's method, was coded in Julia as well. The accuracy of the results was validated through comparison studies, and admissible accuracy was obtained.

2. FORMULATION

The family of concentric ellipses is defined by [23]

$$\left(x/a\right)^2+\left(y/b\right)^2=1-u, \qquad 0\le u\le u_i\le 1 \tag{1}$$

where a and b denote the semi-major, and the semi-minor axes, respectively (Fig. 1). u is the variable which is used to generate concentric ellipses with the same aspect ratio such that $c=a/b=a_i/b_i$. Here, a_i and b_i stand for the semi-major, and the semi-minor axes of the elliptical perforation, respectively. The size of the cutout is defined by the parameter α given by [23]

$$a/a_i=b/b_i=\alpha, \qquad \alpha=\sqrt{1-u_i}\ . \tag{2}$$

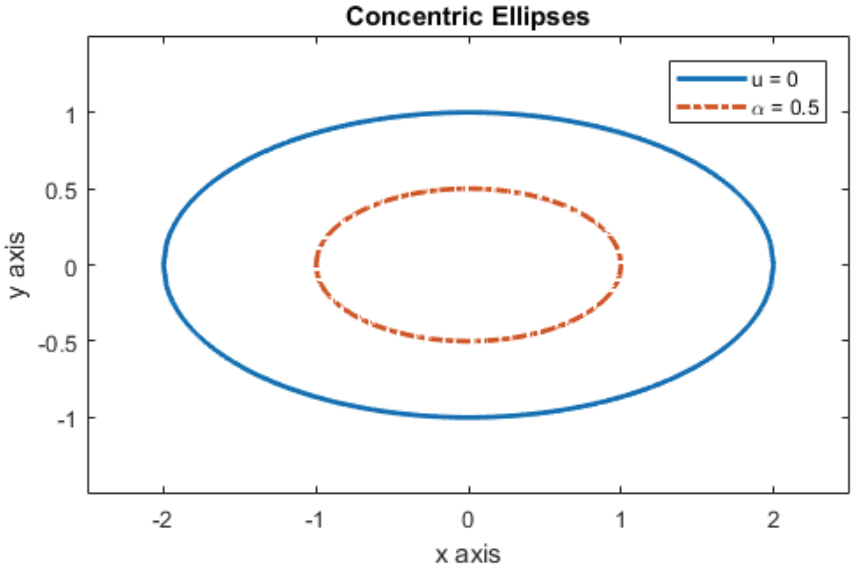

Fig. 1 - Concentric ellipses (c=2)

If $u=0$ and $u=u_i$ are substituted into Eq. (1) the outer periphery and the inner boundary of the plate are obtained. One-quarter of the plate is regarded as the computational domain in the solution, and the FEM procedure is applied. Four-noded isoparametric quadrilateral plate bending element with straight boundaries [38-39] is used for the discretization of the plate. Configuration of the finite elements for a perforated elliptical plate is shown in Figure 2. The number of elements, and the number of nodes are introduced by m, and n, respectively. Both m, and n are determined by the integer p which controls the number of partitions such

that *m*, and *n* increase with increasing *p*. The geometry of the element and the shape function are identified by [39]:

$$x = \sum_{j=1}^{4} N_j x_j, \qquad y = \sum_{j=1}^{4} N_j y_j, \qquad N_j = \frac{1}{4}\left(1 + r r_j\right)\left(1 + s s_j\right) \tag{3}$$

where r_j and s_j denote the local coordinates r and s of node j [39].

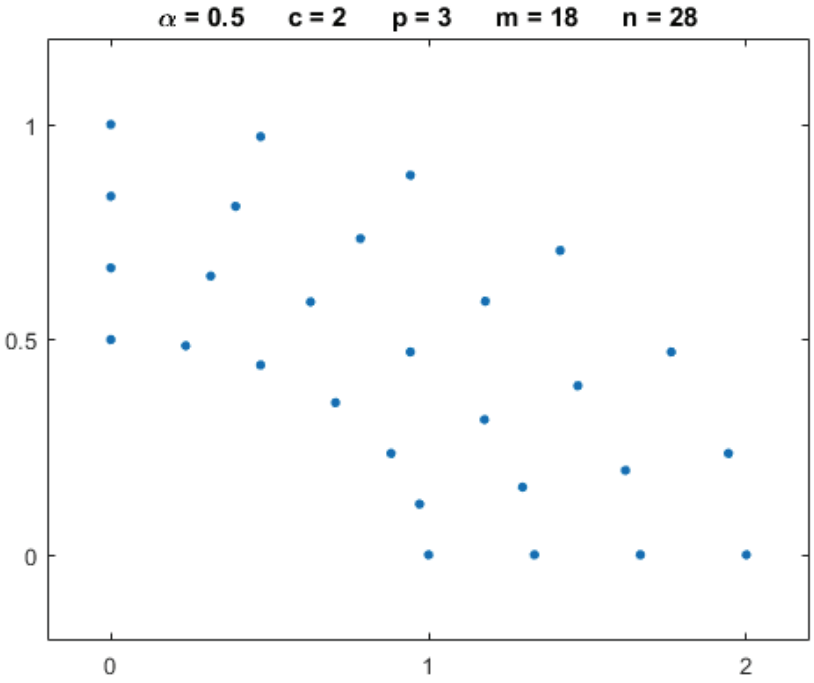

Fig. 2 - Location of the nodes in the first quadrant of a perforated elliptical plate (c=2)

Each element has three degrees of freedom per node defined by [39]

$$w = \sum_{j=1}^{4} N_j w_j, \qquad \theta_x = \sum_{j=1}^{4} N_j \theta_{xj}, \qquad \theta_y = \sum_{j=1}^{4} N_j \theta_{yj}\,. \tag{4}$$

Here, the normal deflection is indicated by *w*, and the rotations are denoted by θ_x and θ_y. The relation between the curvature and shear deformation vector ***{ε}*** and the nodal displacement vector ***{dⱼ}*** is given by [39]

$$\left\{d_j\right\}^T=\left\{w_j \quad \theta_{xj} \quad \theta_{yj}\right\}, \qquad \left\{\varepsilon\right\}=\sum_{j=1}^{4}\left[B_j\right]\left\{d_j\right\}, \tag{5}$$

$$\left\{\varepsilon\right\}=\begin{Bmatrix} k_x=\sum_{j=1}^{4}\theta_{yj}\frac{\partial N_j}{\partial x} \\ k_y=-\sum_{j=1}^{4}\theta_{xj}\frac{\partial N_j}{\partial y} \\ k_{xy}=\sum_{j=1}^{4}\theta_{yj}\frac{\partial N_j}{\partial y}-\sum_{j=1}^{4}\theta_{xj}\frac{\partial N_j}{\partial x} \\ \phi_x=\sum_{j=1}^{4}w_j\frac{\partial N_j}{\partial x}+\sum_{j=1}^{4}\theta_{yj}N_j \\ \phi_y=\sum_{j=1}^{4}w_j\frac{\partial N_j}{\partial y}-\sum_{j=1}^{4}\theta_{xj}N_j \end{Bmatrix}, \tag{6}$$

$$\left[B_j\right]=\begin{bmatrix} 0 & 0 & 0 & \frac{\partial N_j}{\partial x} & \frac{\partial N_j}{\partial y} \\ 0 & -\frac{\partial N_j}{\partial y} & -\frac{\partial N_j}{\partial x} & 0 & -N_j \\ \frac{\partial N_j}{\partial x} & 0 & \frac{\partial N_j}{\partial y} & N_j & 0 \end{bmatrix}^T. \tag{7}$$

The element stiffness matrix is given by

$$\left[k_e\right]=\iint_A\left[B\right]^T\left[C\right]\left[B\right]dxdy, \qquad \left[k_e\right]=\left[k_B\right]+\left[k_S\right] \tag{8}$$

where [39]

$$\left[C\right]=\begin{bmatrix}\left[C_B\right] & \left[0\right] \\ \left[0\right] & \left[C_S\right]\end{bmatrix}, \qquad \left[C_B\right]=D\begin{bmatrix} 1 & \nu & 0 \\ \nu & 1 & 0 \\ 0 & 0 & \frac{(1-\nu)}{2} \end{bmatrix}, \tag{9}$$

$$[B]=\left[[B_1]\ \ [B_2]\ \ [B_3]\ \ [B_4]\right],\qquad D=\frac{Eh^3}{12\left(1-\nu^2\right)},\qquad G=\frac{E}{2(1+\nu)} \tag{10}$$

$$\left[C_S\right]=D_S\begin{bmatrix}1 & 0\\ 0 & 1\end{bmatrix},\qquad D_s=Gh\kappa\,. \tag{11}$$

Here, h is the thickness of the plate, D denotes the bending rigidity, and κ is the shear correction factor. Selective integration is performed to prevent shear locking [38-39]. The nodal displacements are determined by

$$[K]\{U\}=\{F\}\,. \tag{12}$$

3. ANALYSIS

The plate is divided into m sections ("sections" refer to "elements"), and it is assumed that the mass of each section (element) is lumped at discrete points [40]. Morley's formula (or Rayleigh quotient) is given by

$$\omega^2=g\sum_{i=1}^{m}q_i w_i\Big/\sum_{i=1}^{m}q_i w_i^{\,2} \tag{13}$$

where q_i is the weight of the i^{th} element, and ω denotes the natural circular frequency [40]. In the current paper the thickness of the homogeneous and isotropic plate is uniform. It is assumed in the solution that the plate is subjected to uniformly distributed transverse pressure. Such an external load represents the weight of the plate. First, the nodal displacements of the plate are determined. Next, the area of each quadrilateral element is found. Then, the centroidal deflection of each quadrilateral region is computed via interpolation. Finally, Morley's formula is employed, and the fundamental frequency is obtained.

4. NUMERICAL SIMULATION

Due to symmetry the first quadrant of the plate is regarded as the computational domain, and it is divided into quadrilateral elements (Fig. 2). Numerical simulations were made to investigate the effects of several parameters on the fundamental frequency. Annular elliptical plates were identified by two letter symbols [41]. The first and the second letters relate to the inner edge and the outer edge, respectively [41]. For instance, F-C indicates an annular plate with a free (F) inner edge, and a clamped (C) outer edge [41]. Likewise, C-S denotes an annular plate with a clamped (C) inner edge, and a simply supported (S) outer edge [41]. Convergence study for h-refinement was presented for several values of p which controls the number of nodes in the quarter of the plate (Table 1). For convenience, the non-dimensional frequency parameter (λ), and the parameter of thickness (η) defined by

$$\lambda = \omega a^2 \sqrt{\frac{m_p}{D}}, \qquad \eta = \frac{h}{b} \tag{14}$$

were used. Here, m_p stands for the mass of the plate per unit area. Unless otherwise stated, $\nu=0.3$, and $\kappa=5/6$ were used in the solution.

5. NUMERICAL RESULTS

The classical FEM solution that involves the computation of the eigenvalues was also included in the study to test the performance of Morley's method. The accuracy of the results was validated through comparison studies presented for particular cases (Tables 1-3). Some of the solutions of annular elliptical plates for a large variety of plate categories ranging from thin to moderately thick were presented in Tables 4-9, and the other solutions were presented in Appendix A (Tables A1-A10). The ratio $\lambda_{66}/\lambda_{36}$ was used to examine the performance of Morley's formula where λ_{66} and λ_{36} denote the non-dimensional fundamental frequencies obtained using statics deflections (for $p=66$), and FEM (for $p=36$), respectively (Figs. 3-6).

- Compared to solid plates, annular plates require more refined meshes to obtain the same accuracy. This statement holds for both methods. Admissible accuracy can easily be achieved for solid plates.
- The performance of Morley's formula depends highly on the boundary conditions. Even for solid plates, the solution of (S) plates is more accurate than that of (C) plates. (Table 1).
- The accuracy of Morley's formula increases with decreasing size of the cutout (Tables 2-9). The performance of Morley's formula is very sensitive to the boundary conditions. The highest accuracy is achieved for F-S, and S-F plates.
- The performance of Morley's formula decreases with increasing aspect ratio (Figs. 3-6). The error is about only 1% for circular plates.
- Combined effects of the thickness and the size of the perforation on the results depend on the aspect ratio.
- Compared to FEM solution, the use of Morley's formula requires finer mesh, and consequently, it needs more computer storage requirement since larger matrix operations are performed. On the other hand, the execution time of the code spent for the computation of the eigenvalues is much longer. Therefore, FEM provides less memory storage with longer runtime, whereas Morley's formula requires more memory storage with shorter runtime of the code.
- The convergence study reveals that although fine mesh was used in the study, the rate of convergence of the solution obtained by means of Morley's formula is slow compared to eigenvalue analysis by means of FEM. Good agreement was obtained in the comparison studies for $p=36$, and $p=66$ for FEM, and Morley's method, respectively. The accuracy of the results can be improved with increasing p.

Table 1 - Convergence and comparison of λ for a solid elliptical plate ($\kappa = \pi^2/12$)*

		c=1	c=1	c=2	c=2
Reference	η	(C)	(S)	(C)	(S)
[35]	thin	10.216	4.9351	27.377	13.213
[5]	thin	10.216		27.377	
p=66	0.002	10.32856	4.947658	28.04912	13.30464
p=36 (FEM)	0.002	10.21788	4.935512	27.38297	13.21493
[22]	0.100	9.931			
p=66	0.100	10.09877	4.919172	27.55031	13.213
p=64	0.100	10.09881	4.919191	27.55042	13.21305
p=62	0.100	10.09886	4.919211	27.55053	13.2131
p=36 (FEM)	0.100	9.945924	4.895016	26.81448	13.10122
[34]*	0.100	9.941	4.894		
p=66*	0.100	10.0958	4.9188	27.5439	13.2120
p=36 (FEM)*	0.100	9.9428	4.8946	26.8078	13.1002

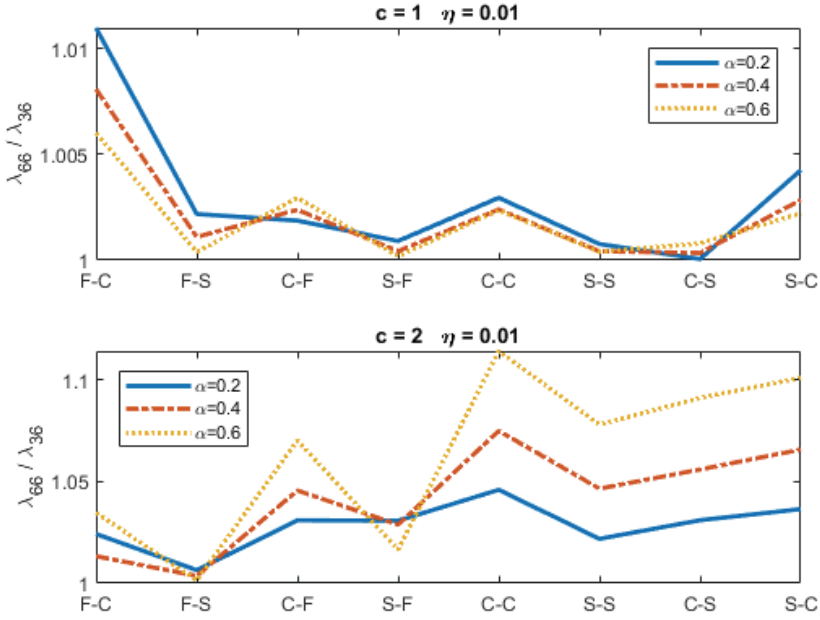

Fig. 3 - Performance of Morley's formula (η=0.01)

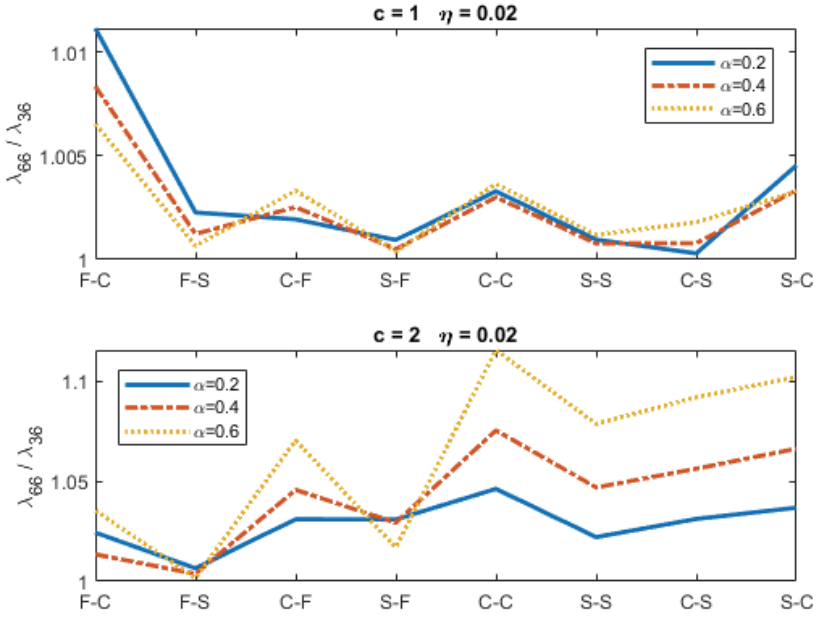

Fig. 4 - Performance of Morley's formula (η=0.02)

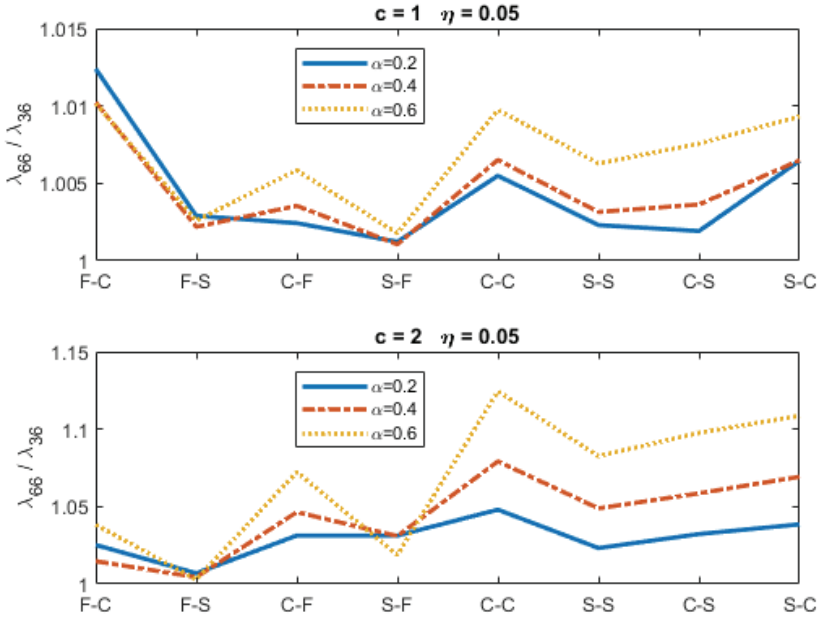

Fig. 5 - Performance of Morley's formula (η=0.05)

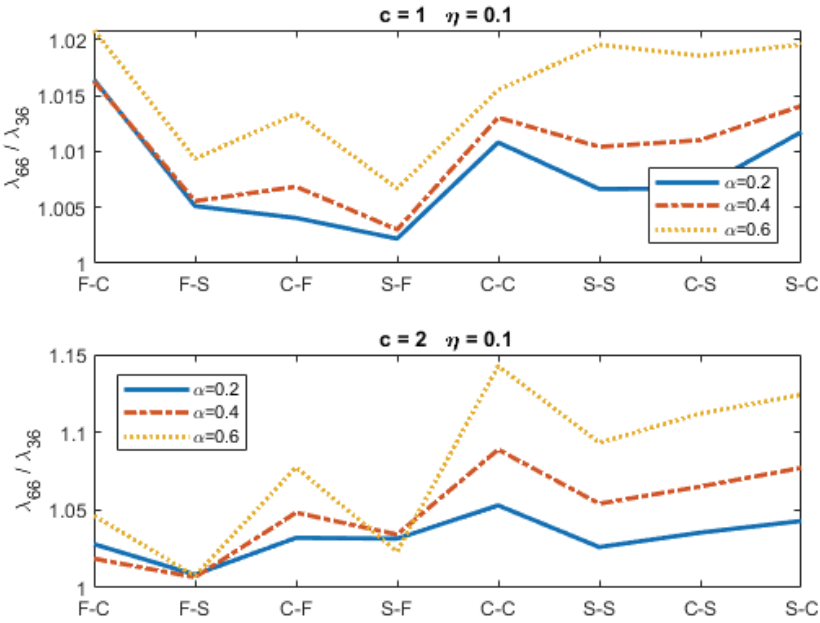

Fig. 6 - Performance of Morley's formula (η=0.10)

Table 2 - Comparison of λ for an annular circular plate
($\kappa = \pi^2/12,\ \nu = 0.3,\ \alpha = 0.5,\ c = 1$)

Reference	η	F-C	F-S	C-F	S-F	C-C	S-S	C-S	S-C
[2]	0.001	17.714	5.0769	13.024	4.1210	89.248	40.043	59.819	63.972
p=66	0.001	17.83635	5.08058	13.06239	4.122594	89.65655	40.09287	59.94969	64.21778
p=36 (FEM)	0.001	17.71669	5.077479	13.0289	4.12163	89.47581	40.08485	59.93064	64.07627
[20]	0.010					89.028			
p=66	0.010	17.83115	5.080441	13.05857	4.122462	89.40652	40.06908	59.85334	64.12041
p=36 (FEM)	0.010	17.7094	5.07709	13.0241	4.121309	89.20003	40.05427	59.8213	63.96385
[2]	0.050	17.533	5.0655	12.905	4.1135	83.051	39.297	57.250	61.327
p=66	0.050	17.70612	5.077075	12.96667	4.119285	83.88555	39.50478	57.64512	61.87609
p=36 (FEM)	0.050	17.53489	5.066203	12.90945	4.114152	83.23865	39.33776	57.34992	61.4204
[2]	0.100	17.024	5.0321	12.568	4.0915	70.277	37.326	51.219	55.090
[20]	0.100					73.192			
p=66	0.100	17.32577	5.066598	12.68914	4.1094	71.41084	37.88385	52.02557	56.06585
p=36 (FEM)	0.100	17.02585	5.032749	12.57189	4.092101	70.39852	37.36243	51.29502	55.16269

Table 3 - Comparison of λ for an annular thin elliptical plate ($\kappa = 5/6,\ \nu = 1/3,\ \eta = 0.010$)

Reference	c	α	F-C	F-S	C-F	S-F	C-C	S-S	C-S	S-C
[3]	1	0.2	10.46	4.851	5.384	3.466	35.12	16.86	23.34	26.68
p=66	1	0.2	10.46079	4.744199	5.225187	3.316449	34.7595	16.75183	22.79789	26.75026
p=36 (FEM)	1	0.2	10.34657	4.733602	5.215471	3.313606	34.65731	16.73882	22.79646	26.6368
[3]	1	0.4	13.50	4.748	9.082	3.634	61.88	28.08	41.27	44.93
p=66	1	0.4	13.60651	4.749357	9.094636	3.631488	62.04021	28.11009	41.29792	45.07354
p=36 (FEM)	1	0.4	13.49753	4.744096	9.073019	3.630024	61.89147	28.0981	41.28357	44.94572
[17]	1	0.5	17.51	5.04	13.05	4.06	89.30	40.01	59.91	64.06
[23]	1	0.5	17.6	5.051			89.25	40.01	59.91	63.85
p=66	1	0.5	17.71343	5.046765	13.12382	4.071506	89.39738	40.03639	59.92877	63.99972
p=36 (FEM)	1	0.5	17.59267	5.043425	13.08911	4.070423	89.19059	40.02144	59.89641	63.84337
[3]	1	0.6	25.24	5.663	20.60	4.809	139.6	62.12	94.26	98.79
p=66	1	0.6	25.68104	5.665307	20.66217	4.809878	139.6056	62.14223	94.23564	98.8963
p=36 (FEM)	1	0.6	25.52804	5.663133	20.60139	4.809027	139.276	62.11734	94.16034	98.67716
[3]	2	0.2	28.03	12.79	8.167	5.895	66.09	35.74	43.46	56.22
p=66	2	0.2	28.25411	12.40696	6.411882	5.281222	61.43884	33.41811	38.52188	54.84044
p=36 (FEM)	2	0.2	27.57337	12.32522	6.212873	5.117726	58.73469	32.71354	37.35849	52.92731
[3]	2	0.4	36.35	12.26	12.19	7.666	94.54	49.93	62.90	78.41
[56]	2	0.4	36.428							
p=66	2	0.4	36.71034	12.23611	11.57788	7.04996	97.51724	50.60931	62.75333	81.80067
p=36 (FEM)	2	0.4	36.22175	12.19083	11.0594	6.846701	90.71251	48.36802	59.41423	76.77172
[23]	2	0.5	45.76	13.06			128.9	66.21	87.84	102.6
p=66	2	0.5	46.1018	12.97565	16.79966	8.485305	133.2842	67.50973	86.78968	108.3289
p=36 (FEM)	2	0.5	45.42884	12.94443	15.8843	8.286729	121.9813	63.63252	80.9714	100.1394
[3]	2	0.6	59.75	14.56	25.38	10.84	181.7	91.78	122.5	142.7
p=66	2	0.6	61.67075	14.55428	26.41716	10.61525	198.614	97.87311	130.7351	156.0929
p=36 (FEM)	2	0.6	59.54442	14.533	24.64509	10.44007	178.2366	90.79605	119.776	141.798

Table 4 - Nondimensional frequency parameter λ for an annular circular plate ($m = 8712,\ \kappa = 5/6,\ \nu = 0.3$)

	η	c	α	F-C	F-S	C-F	S-F	C-C	S-S	C-S	S-C
p=66	0.01	1	0.1	10.27533	4.866091	4.246569	3.454977	27.42665	14.50681	17.81764	22.83659
p=66	0.01	1	0.2	10.52178	4.728858	5.19275	3.342947	34.76155	16.80173	22.74546	26.86897
p=66	0.01	1	0.3	11.53152	4.672342	6.676209	3.424803	45.51021	21.10243	30.01327	33.90118
p=66	0.01	1	0.4	13.70983	4.769607	9.043253	3.67466	62.04628	28.1477	41.2328	45.18836
p=66	0.01	1	0.5	17.83122	5.080443	13.05862	4.122464	89.4098	40.06939	59.85461	64.12169
p=66	0.01	1	0.6	25.8166	5.713021	20.57742	4.871151	139.6356	62.17265	94.15094	99.03704

Table 5 - Nondimensional frequency parameter λ for an annular circular plate
(m = 8712, κ = 5/6, ν = 0.3)

	η	c	α	F-C	F-S	C-F	S-F	C-C	S-S	C-S	S-C
p=66	0.02	1	0.1	10.26871	4.8653	4.244113	3.453594	27.34163	14.48966	17.78078	22.79219
p=66	0.02	1	0.2	10.51551	4.728204	5.190017	3.342171	34.63947	16.78556	22.69566	26.81612
p=66	0.02	1	0.3	11.52458	4.671804	6.672452	3.424258	45.31072	21.08042	29.93423	33.81993
p=66	0.02	1	0.4	13.70047	4.769148	9.037208	3.67422	61.68519	28.11128	41.09183	45.04503
p=66	0.02	1	0.5	17.81571	5.080028	13.0472	4.122072	88.67334	39.99846	59.56906	63.83279
p=66	0.02	1	0.6	25.78418	5.712617	20.55115	4.870768	137.8675	62.00594	93.46592	98.34604

Table 6 - Nondimensional frequency parameter λ for an annular circular plate
(m = 8712, κ = 5/6, ν = 0.3)

	η	c	α	F-C	F-S	C-F	S-F	C-C	S-S	C-S	S-C
p=66	0.05	1	0.1	10.22261	4.859776	4.227019	3.443957	26.76735	14.3714	17.52907	22.4881
p=66	0.05	1	0.2	10.4718	4.723629	5.170982	3.336756	33.81776	16.67371	22.35586	26.45389
p=66	0.05	1	0.3	11.47614	4.668049	6.646296	3.420449	43.97994	20.92828	29.39734	33.26545
p=66	0.05	1	0.4	13.63523	4.76594	8.995159	3.671147	59.31244	27.86023	40.14239	44.07494
p=66	0.05	1	0.5	17.70781	5.077121	12.9679	4.119328	83.9542	39.51228	57.67356	61.90514
p=66	0.05	1	0.6	25.55933	5.709787	20.36939	4.868088	127.0362	60.87526	89.03812	93.85425

Table 7 - Nondimensional frequency parameter λ for an annular circular plate
(m = 8712, κ = 5/6, ν = 0.3)

	η	c	α	F-C	F-S	C-F	S-F	C-C	S-S	C-S	S-C
p=66	0.1	1	0.1	10.06173	4.840197	4.167365	3.41014	24.97495	13.97325	16.71164	21.48976
p=66	0.1	1	0.2	10.31862	4.707396	5.10441	3.317617	31.28547	16.29225	21.25577	25.26151
p=66	0.1	1	0.3	11.3062	4.654707	6.554914	3.406945	40.0056	20.41088	27.68858	31.47084
p=66	0.1	1	0.4	13.40679	4.754535	8.848778	3.660232	52.57634	27.01571	37.21098	41.02994
p=66	0.1	1	0.5	17.33224	5.066779	12.69384	4.109572	71.58349	37.91035	52.10979	56.1539
p=66	0.1	1	0.6	24.78697	5.699714	19.75	4.858548	102.0849	57.28992	77.12697	81.57558

Table 8 - Nondimensional frequency parameter λ for an annular elliptical plate
(m = 8712, κ = 5/6, ν = 0.3)

	η	c	α	F-C	F-S	C-F	S-F	C-C	S-S	C-S	S-C
p=66	0.01	2	0.1	27.76433	12.97897	5.195505	4.838216	51.60946	29.15151	31.82645	48.07377
p=66	0.01	2	0.2	28.38664	12.44127	6.429249	5.318576	61.44063	33.4344	38.39179	54.99793
p=66	0.01	2	0.3	31.21666	12.16949	8.434909	6.070422	75.73697	40.22054	47.95923	65.68264
p=66	0.01	2	0.4	36.87373	12.35509	11.57985	7.116293	97.52059	50.62572	62.54868	82.03108
p=66	0.01	2	0.5	46.30899	13.12671	16.79345	8.575032	133.2898	67.52182	86.52295	108.6167
p=66	0.01	2	0.6	62.00036	14.74158	26.39735	10.73895	198.6252	97.87762	130.3741	156.4694

Table 9 - Nondimensional frequency parameter λ of an annular elliptical plate ($m = 8712,\ \kappa = 5/6,\ \nu = 0.3$)

	η	c	α	F-C	F-S	C-F	S-F	C-C	S-S	C-S	S-C
p=66	0.02	2	0.1	27.74381	12.97043	5.190193	4.823988	51.52595	29.0839	31.7808	47.95688
p=66	0.02	2	0.2	28.36601	12.43045	6.423655	5.30274	61.34398	33.37031	38.33973	54.88079
p=66	0.02	2	0.3	31.19722	12.15688	8.428647	6.055412	75.60862	40.14524	47.89198	65.54309
p=66	0.02	2	0.4	36.85242	12.34013	11.57174	7.10352	97.32946	50.52876	62.45162	81.84741
p=66	0.02	2	0.5	46.27514	13.10799	16.78094	8.564884	132.9654	67.38578	86.36362	108.3474
p=66	0.02	2	0.6	61.93203	14.71623	26.3741	10.73086	197.9662	97.6612	130.0627	156.0095

6. CONCLUSIONS

The fundamental frequencies of solid and perforated elliptical plates were computed using static deflections by means of Morley's formula. FEM was implemented to determine the static deflections of the plate. FSDT was adopted in the formulation of the problem. The solution was validated through comparison studies.

The computational results reveal that the main advantage of Morley's formula is that it is a straightforward and simple solution technique for approximating the natural frequencies without performing eigenvalue analysis. However, the deformed form of the plate should be as close as possible to the fundamental mode shape in order to obtain results with admissible accuracy. Owing to this condition, inevitably, fine mesh is required in the analysis. The rate of convergence depends closely on the boundary conditions. It can be concluded that Morley's formula can be used to predict the approximate fundamental frequencies of solid and annular elliptical plates.

Nomenclature

g, h, p : gravitational acceleration, thickness of the plate, number of partitions in the quarter of the plate

r, q, w : radial coordinate, uniform transverse pressure, deflection

D, E, G : flexural rigidity, Young's modulus, shear modulus

k_x , k_y, k_{xy} : curvatures, twist

r_j, s_j : local coordinates of the node j (j=1, 2, 3, 4)

D_s, N_j : shear rigidity, shape function (j=1, 2, 3, 4)

m_p, q_i : mass of the plate per unit area, weight of the i^{th} element

$[k_e]$, [K] : element, and global stiffness matrices

[B], [C] : strain-displacement matrix, constitutive matrix

{F}, {U} : global nodal load vector, global displacement vector

$[k_B]$, $[k_S]$: bending, and shear stiffness part of $[k_e]$

$[C_B]$, $[C_S]$: bending, and shear deformation part of [C]

λ, θ : nondimensional frequency parameter, transverse coordinate

ω : natural circular frequency

κ, η, ν : shear correction factor, parameter of thickness, Poisson's ratio

θ_x, θ_y : rotations

ϕ_x, ϕ_y : average shear deformations

$\{\varepsilon\}$, $\{d_j\}$: curvature and shear deformation vector, nodal displacement vector

References

[1] Liew, K.M., Kitipornchai, S., Lim, C.W., Free Vibration Analysis of Thick Superelliptical Plates, Journal of Engineering Mechanics, 124(2), 137-145, 1998. https://doi.org/10.1061/(ASCE)0733-9399(1998)124:2(137)

[2] Han, J.-B., Liew, K.M., Axisymmetric Free Vibration of Thick Annular Plates, International Journal of Mechanical Sciences, 41(9), 1089–1109, 1999. https://doi.org/10.1016/S0020-7403(98)00057-5

[3] Chakraverty, S., Bhat, R. B., Stiharu, I., Free Vibration of Annular Elliptic Plates Using Boundary Characteristic Orthogonal Polynomials as Shape Functions in the Rayleigh-Ritz Method, Journal of Sound and Vibration 241(3), 524-539, 2001. https://doi.org/10.1006/jsvi.2000.3243

[4] Zhong, S., Jin, G., Ye, T., Zhang, J., Xue, Y., Chen, M., Isogeometric Vibration Analysis of Multi-directional Functionally Gradient Circular, Elliptical and Sector Plates with Variable Thickness, Composite Structures, 250, 112470, 2020. https://doi.org/10.1016/j.compstruct.2020.112470

[5] Yuan, Y., Li, H., Parker, R.G., Guo, Y., Wang, D., Li, W., A Unified Semi-Analytical Method for Free In-plane and Out-of-plane Vibrations of Arbitrarily Shaped Plates with Clamped Edges, Journal of Sound and Vibration, 485, 115573, 2020. https://doi.org/10.1016/j.jsv.2020.115573

[6] Suganthi, G., Karthikeyan, S., Linear Modal Analysis of Ring Shaped - Elliptical Plate Using Finite Element Method, International Conference on New Trends in Mathematical Modelling with Applications, Uthangarai, India, July 29-30 2019. https://doi.org/10.1088/1742-6596/1597/1/012041

[7] Lim, C.W., Liew, K.M., Vibrations of Perforated Plates with Rounded Corners, Journal of Engineering Mechanics, 121(2), 203-213, 1995. https://doi.org/10.1061/(ASCE)0733-9399(1995)121:2(203)

[8] Karapınar, I.S., Determination of Buckling Temperatures for Elliptical FGM Plates with Variable Thicknesses, Uludağ University Journal of the Faculty of Engineering, 24(1), 75-88, 2019. https://doi.org/10.17482/uumfd.480661

[9] Okada, K., Maruyama, S., Nagai, K., Yamaguchi T., Analysis on Nonlinear Static Deflection and Natural Frequencies of a Thin Annular Plate with Initial Deformation, Proceedings of International Conference on Mechanical, Electrical and Medical Intelligent System 2017

[10] Sharma, P., Singh, R., Investigation on Modal Behaviour of FGM Annular Plate Under Hygrothermal Effect, IOP Conference Series: Materials Science and Engineering, 624, 012001

[11] Lin, C.-C., Tseng, C.-S., Free Vibration of Polar Orthotropic Laminated Circular and Annular Plates, Journal of Sound and Vibration, 209(5), 797-810, 1998. https://doi.org/10.1006/jsvi.1997.1293

[12] Zietlow, D.W., Griffin, D.C., Moorea, T.R., The Limitations on Applying Classical Thin Plate Theory to Thin Annular Plates Clamped on the Inner Boundary, AIP Advances 2, 042103, 2012. http://dx.doi.org/10.1063/1.4757928

[13] Bao, R.H., Chen, W.Q., Xu, R.Q., Free Vibration of Transversely Isotropic Circular Plates, AIAA Journal, 44(10), 2415-2418, 2006. https://doi.org/10.2514/1.18093

[14] Varghese, V., Dhakate, T., Khalsa, L., Thermoelastic Vibrations in a Thin Elliptic Annulus Plate with Elastic Supports, Theoretical and Applied Mechanics Letters, 8(1), 32-42, 2018. https://doi.org/10.1016/j.taml.2018.01.009

[15] Kang, S., Improved Non-dimensional Dynamic Influence Function Method for Vibration Analysis of Arbitrarily Shaped Plates with Simply Supported Edges, Advances in Mechanical Engineering, 10(2), 1-12, 2018. https://doi.org/10.1177/1687814018760082

[16] Liew, K.M., Wang, C.M., Xiang, Y., Kitipornchai, S., Vibration of Mindlin Plates, Elsevier Science Ltd., Oxford, UK, 1998, 131-132. https://doi.org/10.1016/B978-0-08-043341-7.X5000-6

[17] Leissa, A.W. Vibration of Plates, Columbus, Acoustical Society of America, 1993.

[18] Guenanou, A., Houmat, A., Hachemi, M., Chebout, R., Bachari, K., Free Vibration of Shear Deformable Symmetric VSCL Elliptical Plates by a Curved Rectangular P-element, Mechanics of Advanced Materials and Structures, 2020. https://doi.org/10.1080/15376494.2020.1770382

[19] Hasheminejad, S.M., Ghaheri, A., Exact Solution for Free Vibration Analysis of an Eccentric Elliptical Plate, Archive of Applied Mechanics, 84, 543–552, 2014. https://doi.org/10.1007/s00419-013-0816-8

[20] Powmya, A., Narasimhan, M.C., Free Vibration Analysis of Axisymmetric Laminated Composite Circular and Annular Plates Using Chebyshev Collocation, International Journal of Advanced Structural Engineering, 7, 129–141, 2015. https://doi.org/10.1007/s40091-015-0087-4

[21] Singh, A.V., A Numerical Free Vibration Analysis of Annular Elliptic Plates, Multidiscipline Modeling in Materials and Structures, 1(1), 53-62, 2005. https://doi.org/10.1163/1573611054455166

[22] Liew, K.M., Wang, J., Ng, T.Y., Tan, M.J., Free Vibration and Buckling Analysis of Shear-deformable Plates Based on FSDT Meshfree Method, Journal of Sound and Vibration, 276(3-5), 997-1017, 2004. https://doi.org/10.1016/j.jsv.2003.08.026

[23] Singh, B., Chakraverty, S., Transverse Vibration of Annular Circular and Elliptic Plates Using the Characteristic Orthogonal Polynomials in Two Dimensions, Journal of Sound and Vibration, 162(3), 537-546, 1993. https://doi.org/10.1006/jsvi.1993.1138

[24] Civalek, O., Gürses, M., Free Vibration of Annular Mindlin Plates with Free Inner Edge via Discrete Singular Convolution Method, The Arabian Journal for Science and Engineering, 34(1B), 81-90, 2009.

[25] Altekin, M., Free Transverse Vibration of Shear Deformable Super-Elliptical Plates, Wind and Structures, 24(4), 307-331, 2017. https://doi.org/10.12989/was.2017.24.4.307

[26] Merneedi, A., Nalluri, M.R., Vissakodeti, V.S.R., Free Vibration Analysis of an Elliptical Plate with Cut-out, Journal of Vibroengineering, 19(4), 2341-2353, 2017. https://doi.org/10.21595/jve.2016.17575

[27] Blevins, R.D. Formulas for Dynamics, Acoustics and Vibration, Wiley, United Kingdom, 2016. https://doi.org/10.1002/9781119038122

[28] Weiss, G., Approximated Fundamental Frequency for Thin Circular Plates Clamped or Pinned at the Edge, ASME International Mechanical Engineering Congress and Exposition (IMECE2007), Seattle, USA, November 11-15, 2007. https://doi.org/10.1115/IMECE2007-41018

[29] Jaroszewicz, J., Misiukiewicz, M., Puchalski, W., Limitations in Application of Basic Frequency Simplest Lower Estimators in Investigation of Natural Vibrations of Circular Plates with Variable Thickness and Clamped Edges, Journal of Theoretical and Applied Mechanics, 46(1), 109-121, 2008. [online] Available at: https://citeseerx.ist.psu.edu/viewdoc/download?doi=10.1.1.608.4235&rep=rep1&type=pdf

[30] Jaroszewicz, J., Radziszewski, L., The General Formula for Calculation of Fundamental Frequency of Axisymmetric Vibrations of Circular Plates with Linearly Variable Thickness, Technical Sciences, 19(4), 401—410, 2016.[online] Available at: http://www.uwm.edu.pl/wnt/technicalsc/tech_19_4/jaroszew.pdf

[31] Altekin, M., Approximate Fundamental Frequency of a Circular Mindlin Plate by Morley's Formula, International Conference on Numerical Analysis and Applied Mathematics (ICNAAM), Rhodes, Greece, Sept. 13-18, 2018. https://doi.org/10.1063/1.5114529

[32] Altekin, M., Approximate Fundamental Frequency of an Annular Plate by Using Static Deflections, Ulusal Mekanik Kongresi, Niğde, Turkey, September 02-06, 2019.

[33] Dhakate, T., Varghese, V., Khalsa, L., Integral Transform Approach for Solving Dynamic Thermal Vibrations in the Elliptical Disk, Journal of Thermal Stresses, 40(9), 1093-1110, 2017. https://doi.org/10.1080/01495739.2017.1285215

[34] Irie, T., Yamada, G., Aomura, S., Natural Frequencies of Mindlin Circular Plates, Journal of Applied Mechanics 47(3),652-655, 1980. https://doi.org/10.1115/1.3153748

[35] Chakraverty, S. Vibration of Plates, CRC Press, Boca Raton, USA, 2009.

[36] Demirhan, P.A., Taskin, V., Static Analysis of Simply Supported Functionally Graded Sandwich Plates by Using Four Variable Plate Theory, Teknik Dergi, 30(2), 8987-9007, 2019. https://dx.doi.org/10.18400/tekderg.396672

[37] Altunsaray, E., Bayer, I., Buckling Analysis of Symmetrically Laminated Rectangular Thin Plates under Biaxial Compression, Teknik Dergi, https://doi.org/10.18400/tekderg.606620

[38] Hughes, T.J.R., Taylor, R.L., Kanoknukulchai, W. A Simple and Efficient Finite Element for Plate Bending, International Journal for Numerical Methods in Engineering, 11(10), 1529–1543, 1977. https://doi.org/10.1002/nme.1620111005

[39] Krishnamoorthy, C.S. Finite Element Analysis: Theory and Programming (Second Edition), Tata McGraw-Hill Publishing Company Limited, 1994.

[40] Szilard, R. Theories and Applications of Plate Analysis, John Wiley & Sons Inc., Hoboken, USA, 2004.

[41] Han, J.-B., Liew, K.M., Analysis of Annular Reissner/Mindlin Plates Using Differential Quadrature Method, International Journal of Mechanical Sciences. 40(7), 651–661, 1998. https://doi.org/10.1016/S0020-7403(97)00087-8

[42] Golub, G.H., Van der Vorst, H.A., Eigenvalue Computation in the 20th Century, Journal of Computational and Applied Mathematics. 123, 35–65, 2000. https://doi.org/10.1016/S0377-0427(00)00413-1

[43] Civalek, Ö., Baltacıoglu, A.K., Free Vibration Analysis of Laminated and FGM Composite Annular Sector Plates, Composites Part B, 157, 182–194, 2019. https://doi.org/10.1016/j.compositesb.2018.08.101

[44] Thai, H.-T., Kim, S.-E., Levy-Type Solution for Free Vibration Analysis of Orthotropic Plates Based on Two Variable Refined Plate Theory, Applied Mathematical Modelling, 36, 3870–3882, 2012. https://doi.org/10.1016/j.apm.2011.11.003

[45] Liu, W.H., Yeh, F.H., Non-linear Vibrations of Initially Imperfect, Orthotropic, Moderately Thick Plates with Edge Restraints, Journal of Sound and Vibration. 165(1), 101–122, 1993. https://doi.org/10.1006/jsvi.1993.1245

[46] Kolakowski, Z., Jankowski, J., Some Inconsistencies in the Nonlinear Buckling Plate Theories—FSDT, S-FSDT, HSDT, Materials, 14, 2154, 2021, 2154. https://doi.org/10.3390/ma14092154

[47] Thai, H.-T., Vo, T.P., A New Sinusoidal Shear Deformation Theory for Bending, Buckling, and Vibration of Functionally Graded Plates, Applied Mathematical Modelling, 37, 3269–3281, 2013. http://dx.doi.org/10.1016/j.apm.2012.08.008

[48] Szekrenyes, A., Analysis of Classical and First-Order Shear Deformable Cracked Orthotropic Plates, Journal of Composite Materials, 48(12), 1441–1457, 2014. https://doi.org/10.1177/0021998313487756

[49] Aksoylar, C., Omurtag, M.H., Mixed Finite Element Analysis of Composite Plates Under Blast Loading (Turkish), Teknik Dergi, 22(109), 5689-5711, 2011.

[50] Park, M., Choi, D.-H., A Simplified First-Order Shear Deformation Theory for Bending, Buckling and Free Vibration Analyses of Isotropic Plates on Elastic Foundations, KSCE Journal of Civil Engineering 22(4), 1235-1249, 2018. https://doi.org/10.1007/s12205-017-1517-6

[51] Oktem, A.S., Chaudhuri, R.A., Levy Type Analysis of Cross-Ply Plates Based on Higher-Order Theory, Composite Structures, 78, 243–253, 2007. https://doi.org/10.1016/j.compstruct.2005.09.012

[52] Zuo, H., Yang, Z., Chen, X., Xie, Y., Miao, H., Analysis of Laminated Composite Plates Using Wavelet Finite Element Method and Higher-Order Plate Theory, Composite Structures, 131, 248–258, 2015. http://dx.doi.org/10.1016/j.compstruct.2015.04.064

[53] Singh, S.K., Singh, I.V., Mishra, B.K., Bhardwaj, G., Singh, S.K., Analysis of Cracked Plate Using Higher-Order Shear Deformation Theory: Asymptotic Crack-tip Fields and XIGA Implementation, Computer Methods in Applied Mechanics and Engineering, 336, 594–639, 2018. https://doi.org/10.1016/j.cma.2018.03.009

[54] A. Bhar, A., Phoenix, S.S., Satsangi, S.K., Finite Element Analysis of Laminated Composite Stiffened Plates Using FSDT and HSDT: A Comparative Perspective, Composite Structures, 92, 312–321, 2010. https://doi.org/10.1016/j.compstruct.2009.08.002

[55] Zhou, D., Lo, S.H., Cheung, Y.K., Au, F.T.K., 3-D Vibration Analysis of Generalized Super Elliptical Plates Using Chebyshev-Ritz Method, International Journal of Solids Structures, 41(16-17), 4697-4712, 2004. https://doi.org/10.1016/j.ijsolstr.2004.02.045

[56] Nallim, L.G., Grossi, R.O., Natural Frequencies of Symmetrically Laminated Elliptical and Circular Plates, International Journal of Mechanical Sciences 50(7), 1153–1167, 2008. https://doi.org/10.1016/j.ijmecsci.2008.04.005

[57] Wang, Y., Ding, H., Xu, R., Three-Dimensional Analytical Solutions for the Axisymmetric Bending of Functionally Graded Annular Plates, Applied Mathematical Modelling, 40, 5393–5420, 2016. http://dx.doi.org/10.1016/j.apm.2015.11.051

[58] Yükseler, R.F., Exact Nonlocal Solutions of Circular Nanoplates Subjected to Uniformly Distributed Loads and Nonlocal Concentrated Forces, Journal of the Brazilian Society of Mechanical Sciences and Engineering, 42(1), 61, 2020. https://doi.org/10.1007/s40430-019-2144-6

[59] Altekin, M., Bending of Super-Elliptical Mindlin Plates by Finite Element Method, Teknik Dergi, 29(4), 8469-8496, 2018. https://doi.org/10.18400/tekderg.332384

[60] Civalek, Ö., Kiracioglu, O., Free Vibration Analysis of Timoshenko Beams by DSC Method, International Journal for Numerical Methods in Biomedical Engineering, 26(12), 1890-1898, 2010. https://doi.org/10.1002/cnm.1279

Appendix A Fundamental frequencies of elliptical plates

Table A1 - Nondimensional frequency parameter λ of an annular elliptical plate $(\kappa = 5/6,\ \nu = 0.3)$

	η	c	α	F-C	F-S	C-F	S-F	C-C	S-S	C-S	S-C
p=66	0.05	2	0.1	27.62733	12.9389	5.163452	4.772515	51.00799	28.79606	31.53625	47.39444
p=66	0.05	2	0.2	28.25236	12.39328	6.391149	5.240666	60.70895	33.09019	38.04565	54.28566
p=66	0.05	2	0.3	31.08028	12.11513	8.390859	5.995446	74.7496	39.8203	47.50148	64.82146
p=66	0.05	2	0.4	36.7095	12.29159	11.52259	7.051332	96.03922	50.10879	61.87333	80.87554
p=66	0.05	2	0.5	46.0534	13.04783	16.70599	8.521915	130.7639	66.78147	85.38971	106.8744
p=66	0.05	2	0.6	61.52715	14.63499	26.23721	10.69514	193.4737	96.65242	128.1097	153.3746

Table A2 - Nondimensional frequency parameter λ of an annular elliptical plate $(\kappa = 5/6,\ \nu = 0.3)$

	η	c	α	F-C	F-S	C-F	S-F	C-C	S-S	C-S	S-C
p=66	0.1	2	0.1	27.25841	12.86729	5.107701	4.689845	49.47486	28.18328	30.88405	45.99706
p=66	0.1	2	0.2	27.89727	12.31621	6.304909	5.117169	58.71751	32.42768	37.1991	52.66475
p=66	0.1	2	0.3	30.69696	12.03293	8.281958	5.864725	71.99508	39.02555	46.33504	62.78054
p=66	0.1	2	0.4	36.21748	12.1989	11.37634	6.930247	91.8612	49.05637	60.10567	78.05461
p=66	0.1	2	0.5	45.30089	12.93473	16.48031	8.416539	123.6177	65.22066	82.36526	102.4925
p=66	0.1	2	0.6	60.2246	14.4827	25.82327	10.6032	179.0274	93.9424	121.993	145.3354

Table A3 - Nondimensional frequency parameter λ of an annular circular plate (FEM solution, $\kappa = 5/6,\ \nu = 0.3$*)*

FEM	η	c	α	F-C	F-S	C-F	S-F	C-C	S-S	C-S	S-C
p=36	0.01	1	0.1	10.16095	4.854815	4.239875	3.450487	27.33339	14.49218	17.82	22.71585
p=36	0.01	1	0.2	10.40764	4.718579	5.183075	3.339924	34.65944	16.78894	22.74426	26.75526
p=36	0.01	1	0.3	11.42226	4.664591	6.662063	3.422662	45.39191	21.09087	30.00767	33.78549
p=36	0.01	1	0.4	13.60002	4.764384	9.021792	3.673099	61.89774	28.13587	41.21872	45.06032
p=36	0.01	1	0.5	17.70948	5.077093	13.02415	4.12131	89.20341	40.05458	59.82259	63.96517
p=36	0.01	1	0.6	25.66254	5.710824	20.51702	4.870248	139.3069	62.14791	94.07616	98.81788

Table A4 - Nondimensional frequency parameter λ of an annular circular plate (FEM solution, $\kappa = 5/6,\ \nu = 0.3$*)*

FEM	η	c	α	F-C	F-S	C-F	S-F	C-C	S-S	C-S	S-C
p=36	0.02	1	0.1	10.15282	4.853632	4.237204	3.448992	27.24102	14.47278	17.77977	22.66629
p=36	0.02	1	0.2	10.39956	4.717498	5.179976	3.339014	34.52571	16.76948	22.68892	26.69485
p=36	0.02	1	0.3	11.41289	4.663549	6.657637	3.421929	45.1727	21.06343	29.91894	33.69194
p=36	0.02	1	0.4	13.587	4.763271	9.014418	3.672367	61.50055	28.08955	41.05951	44.89502
p=36	0.02	1	0.5	17.68755	5.075732	13.00979	4.120418	88.39363	39.96336	59.49884	63.63227
p=36	0.02	1	0.6	25.6165	5.708846	20.48311	4.868893	137.3667	61.93224	93.29816	98.02369

Table A5 - Nondimensional frequency parameter λ of an annular circular plate (FEM solution, $\kappa = 5/6,\ \nu = 0.3$)

FEM	η	c	α	F-C	F-S	C-F	S-F	C-C	S-S	C-S	S-C
p=36	0.05	1	0.1	10.09647	4.845381	4.218652	3.438585	26.6209	14.33938	17.50587	22.32891
p=36	0.05	1	0.2	10.3436	4.709959	5.158445	3.332665	33.63307	16.63539	22.31302	26.28409
p=36	0.05	1	0.3	11.34805	4.656282	6.626918	3.416807	43.72638	20.87481	29.32022	33.05996
p=36	0.05	1	0.4	13.49705	4.75551	8.963356	3.66726	58.92849	27.77279	39.99698	43.79075
p=36	0.05	1	0.5	17.53672	5.06625	12.91073	4.114196	83.30723	39.34522	57.37823	61.44953
p=36	0.05	1	0.6	25.30217	5.695071	20.251	4.859451	125.8104	60.49522	88.36972	92.98754

Table A6 - Nondimensional frequency parameter λ of an annular circular plate (FEM solution, $\kappa = 5/6,\ \nu = 0.3$)

FEM	η	c	α	F-C	F-S	C-F	S-F	C-C	S-S	C-S	S-C
p=36	0.1	1	0.1	9.903308	4.81635	4.154329	3.402203	24.72229	13.89426	16.62559	21.24375
p=36	0.1	1	0.2	10.15168	4.683416	5.083779	3.310321	30.95082	16.18475	21.11429	24.96806
p=36	0.1	1	0.3	11.12634	4.630692	6.520838	3.398744	39.54025	20.24643	27.45337	31.08072
p=36	0.1	1	0.4	13.19183	4.728196	8.788512	3.649243	51.89957	26.73705	36.80524	40.46014
p=36	0.1	1	0.5	17.03251	5.032932	12.57659	4.092272	70.56465	37.38758	51.37575	55.24679
p=36	0.1	1	0.6	24.28046	5.646847	19.48954	4.826287	100.5254	56.19086	75.72119	80.00907

Table A7 - Nondimensional frequency parameter λ of an annular elliptical plate (FEM solution, $\kappa = 5/6,\ \nu = 0.3$)

FEM	η	c	α	F-C	F-S	C-F	S-F	C-C	S-S	C-S	S-C
p=36	0.01	2	0.1	27.07475	12.89165	5.061909	4.705916	49.9703	28.74601	31.19623	46.89436
p=36	0.01	2	0.2	27.71352	12.36115	6.2358	5.159577	58.73685	32.71842	37.23537	53.0603
p=36	0.01	2	0.3	30.62607	12.10697	8.130193	5.885239	71.46238	38.92184	45.98906	62.5087
p=36	0.01	2	0.4	36.38827	12.31036	11.07393	6.916658	90.71647	48.37151	59.22958	76.964
p=36	0.01	2	0.5	45.64588	13.09593	15.89885	8.378603	121.9879	63.63077	80.73704	100.3753
p=36	0.01	2	0.6	59.91472	14.72081	24.66326	10.56417	178.25	90.78511	119.468	142.1002

Table A8 - Nondimensional frequency parameter λ of an annular elliptical plate (FEM solution, $\kappa = 5/6,\ \nu = 0.3$)

FEM	η	c	α	F-C	F-S	C-F	S-F	C-C	S-S	C-S	S-C
p=36	0.02	2	0.1	27.05248	12.8827	5.056732	4.692196	49.88217	28.6755	31.14844	46.77119
p=36	0.02	2	0.2	27.69017	12.34974	6.230057	5.143487	58.62993	32.64789	37.17866	52.92971
p=36	0.02	2	0.3	30.60245	12.09353	8.123538	5.86876	71.31582	38.83712	45.91398	62.35069
p=36	0.02	2	0.4	36.36089	12.29423	11.06497	6.901032	90.49134	48.26135	59.11815	76.75303
p=36	0.02	2	0.5	45.59931	13.07545	15.8844	8.364583	121.5942	63.4735	80.5481	100.0575
p=36	0.02	2	0.6	59.81491	14.69253	24.63489	10.55184	177.4297	90.52549	119.0857	141.5359

Table A9 - Nondimensional frequency parameter λ of an annular elliptical plate (FEM solution, $\kappa = 5/6,\ \nu = 0.3$)

FEM	η	c	α	F-C	F-S	C-F	S-F	C-C	S-S	C-S	S-C
p=36	0.05	2	0.1	26.92087	12.84704	5.030552	4.643395	49.33088	28.3771	30.89008	46.18035
p=36	0.05	2	0.2	27.55669	12.30781	6.197077	5.081753	57.92898	32.33943	36.85662	52.27125
p=36	0.05	2	0.3	30.45735	12.04584	8.083991	5.804767	70.3419	38.4682	45.47485	61.53595
p=36	0.05	2	0.4	36.17673	12.23775	11.01151	6.839482	88.99195	47.77492	58.45026	75.63519
p=36	0.05	2	0.5	45.30272	13.00367	15.79882	8.307599	118.9842	62.75531	79.39263	98.32019
p=36	0.05	2	0.6	59.25524	14.59195	24.46842	10.49861	172.0657	89.27894	116.7155	138.342

Table A10 - Nondimensional frequency parameter λ of an annular elliptical plate (FEM solution, $\kappa = 5/6,\ \nu = 0.3$)

FEM	η	c	α	F-C	F-S	C-F	S-F	C-C	S-S	C-S	S-C
p=36	0.1	2	0.1	26.50014	12.75995	4.973981	4.564428	47.69939	27.72737	30.1902	44.69753
p=36	0.1	2	0.2	27.13612	12.21358	6.108853	4.96051	55.76555	31.60222	35.92572	50.49555
p=36	0.1	2	0.3	29.98335	11.94283	7.969649	5.668513	67.3097	37.55621	44.16602	59.26773
p=36	0.1	2	0.4	35.55259	12.11762	10.85214	6.700999	84.36307	46.53941	56.43275	72.46566
p=36	0.1	2	0.5	44.32941	12.85067	15.54084	8.171946	111.121	60.87652	75.90456	93.35418
p=36	0.1	2	0.6	57.55466	14.37337	23.96595	10.36267	156.6773	85.92528	109.7005	129.2727

Teknik Dergi, 2022 11591-11615, Paper 649

Estimation of Intensity-Duration-Frequency (IDF) Curves from Large Scale Atmospheric Dataset by Statistical Downscaling

Khaled ALRAMLAWI[1]
Okan FISTIKOĞLU[2]

ABSTRACT

The study proposes a new approach that combined statistical downscaling, bias correction, and disaggregation of rainfall techniques to derive the IDF curve from large scale atmospheric reanalysis data. The applied methodology details the NCEP/NCAR reanalysis dataset being downscaled by an ANN-based approach to estimate the daily rainfall of Izmir. The annual maximum rainfall series of the study area were sampled from the daily downscaled rainfall series. The sampled daily maximum rainfalls were then bias-corrected by the quantile mapping method and disaggregated into the annual maximum standard-duration rainfall heights regarding the rainfalls' scale-invariant properties. Finally, the IDF curves of the study area were determined by using the disaggregated rainfall heights. The results confirmed that the IDF curves dependent on short-duration extreme rainfall heights could be reasonably estimated from the large-scale atmospheric variables using the statistical downscaling approach.

Keywords: Statistical downscaling, bias correction, quantile mapping, rainfall disaggregation, IDF curve.

1. INTRODUCTION

Local weather conditions of a region highly depend on the synoptic patterns evolving in three-dimensional large-scale atmospheric coverage over the region. The existing global large-scale atmospheric datasets, assimilated to better understand climate change, constructs a worldwide historical base for this large-scale coverage. The National Center for Environmental Prediction and National Center for Atmospheric Research (NCEP/NCAR) distribute reanalysis data of the global atmosphere from 1948 to the present day at 2.5° X

Note:
- This paper was received on February 3, 2021 and accepted for publication by the Editorial Board on August 13, 2021.
- Discussions on this paper will be accepted by March 31, 2022.
- https://doi.org/10.18400/tekderg.874035

1 Dokuz Eylul University, The Graduate School of Natural And Applied Sciences, Civil Engineering Department, Izmir, Turkey - khaled.alramlawi@ogr.deu.edu.tr - https://orcid.org/0000-0002-3432-2660

2 Dokuz Eylul University, The Graduate School of Natural And Applied Sciences, Civil Engineering Department, Izmir, Turkey - okan.fistikoglu@deu.edu.tr - https://orcid.org/0000-0002-9483-1563

2.5° resolution [1], while the European Centre for Medium-Range Weather Forecasts (ECMWF) produce ERA-Interim Reanalysis dataset from 1979 to today at 1.5° X 1.5° resolution [2]. Both datasets have been used as observed data for explanatory data analyses in historical and/or future climate studies. Both datasets were also compared in the context of representation of regional climatic variables, such as precipitation and temperature from Asia [3] to Australia [4] and from Europe [5] to Africa [6]. The studies concluded that, in general, although each dataset performed almost similar results, the ERA-Interim dataset often reproduced slightly better observed climate relative to the NCEP/NCAR datasets due to the difference in their distinctive spatial resolutions that coarser-resolution smoothens the inter-variability of the observed climatological variables. Also, in terms of the temporal coverage, a longer period is generally preferred in most statistical analyses, and NCEP/NCAR contains 30 years more data, makes itself the preferred dataset.

Studies using reanalysis data such as NCEP/NCAR are mainly categorized into two different groups. One group regards the dataset as a benchmark relative to the estimations of the historical climate patterns of the Global Circulation Models (GCMs) [7–10], while the other group regards the dataset as independent atmospheric variables explaining the dependent local weather variables such as precipitation or temperature via quantitative estimation approaches such as linear or non-linear regression models [11–14]. The reanalysis datasets can also be used to estimate the response of a hydrological system to changing climates [15,16].

The estimation of local weather variables (i.e., precipitation and temperature) from large-scale atmospheric data is called downscaling. The focal point of downscaling is to transfer large-scale patterns of atmospheric variables (predictors) of either reanalysis datasets or GCMs output to local weather variables (predictands) [12,17]. Several downscaling methodologies have been developed, such as dynamical downscaling and statistical downscaling. The dynamical downscaling is associated with the physically based Regional Climate Models (RCMs), where the GCM results constitute the model domain's boundary conditions. It is computationally intensive, complex, and requires substantial computational resources [18,19]. Statistical downscaling utilizes statistical relationships to predict local climate variables from large-scale variables. It was developed to establish quantitative relationships between large-scale atmospheric variables and local surface variables [12]. Some of its main categories include transfer functions, weather classification methods, and weather generators [19,20], with transfer functions being the most commonly used category [21]. Some examples of statistical downscaling include linear and non-linear regression, principal component analysis (PCA), canonical correlation, redundancy analysis, and Artificial Neural Networks (ANN) [12,22].

Downscaling hydro-meteorological variables result in biases inherent in the downscaling methods themselves [23] and the spatial resolution of the predictors [24–26]. These inherent biases can be removed by applying bias correction procedures on the downscaled predictands, which increases the accuracy of the results [27,28].

The statistical downscaling of hourly rainfall, required for frequency analysis of severe weather conditions, is rarely conducted because the large-scale datasets have rough temporal resolutions such as 6 hours. The majority of statistical downscaling studies focus on the estimation of monthly, daily, or annual maximum rainfall due to the temporal deficiencies of the predictor datasets [12,29–31].

Studies focusing on estimating sub-daily rainfall generally utilize RCMs [32] that are not practical for individual research endeavors due to their inaccessibility to the results of regional models. This impediment requires practical and functional statistical downscaling methods for the researchers dealing with the sub-daily rainfall analysis like the estimation of Intensity-Duration-Frequency (IDF) curves.

There are some reported examples in the literature of IDF curve estimation using large-scale atmospheric datasets. However, most of these reported works utilize RCMs for downscaling due to the abovementioned limitations. Mailhot et al. (2007) compared regional estimates in control and future climates on a grid box scale and reported that return periods of 2-h and 6-h events would approximately be halved in future climates. The same study reported that return periods of 12-h and 24-h events would decrease by a third in Quebec, Canada[32]. Mirhosseini et al. (2013) reported future IDF curves of 3-hourly precipitation simulated by combining six GCMs and RCM results temporally downscaled using a stochastic method. The study evaluated the performance of downscaling methods and develop IDF curves using the RCM results for the state of Alabama, USA [33].

This paper details an approach for establishing local IDF curves using large-scale atmospheric variables. The NCEP/NCAR Reanalysis dataset over Izmir, Turkey, was used to estimate the daily rainfall values using the Artificial Neural Network (ANN)-based statistical downscaling approach. The annual maximum daily rainfall values were estimated after the bias-correction of the sampled annuals from the daily rainfall series. The annual maximum rainfall values were disaggregated based on a simple scale-invariant approach, and the maximum rainfall heights at standard durations were estimated to construct the IDF curves of the study area.

2. STUDY AREA AND DATASETS

Izmir, located on the Aegean coast of Turkey (see Fig. 1), was selected as the study area. It is the third-largest city in Turkey with a typical Mediterranean climate. According to the Turkish State Meteorological Service, the average annual precipitation in the area is 610 mm/year, and 80% of the total annual rainfall is observed in November – March period.

There are many weather stations in the study area, but only the Izmir station contains the annual maximum standard duration rainfall records. The other stations have different operation periods within the region, so their datasets were only used to validate the results of the downscaling networks of the Izmir station. The spatial locations of the stations and available datasets in the study area are summarized in Table 1 and Figure 1. The observed daily rainfall series of the Izmir stations was the predictand (output) of the downscaling networks.

The NCEP/NCAR Reanalysis dataset, as a large-scale atmospheric parameter set, is available in sub-daily, daily, and monthly time resolution for 1948 - present at a spatial resolution of 2.5°x 2.5° [34]. The daily atmospheric dataset of the NCEP/NCAR re-analysis grid, located between latitudes from 36.25° N to 38.75° N, and the longitudes from 26.25° E to 28.75° E (see Figure 1), were used as predictors (inputs) of the downscaling networks. In order to validate the model, the period from 1948–1990 was used for the training period and 1991-2018 as the testing period.

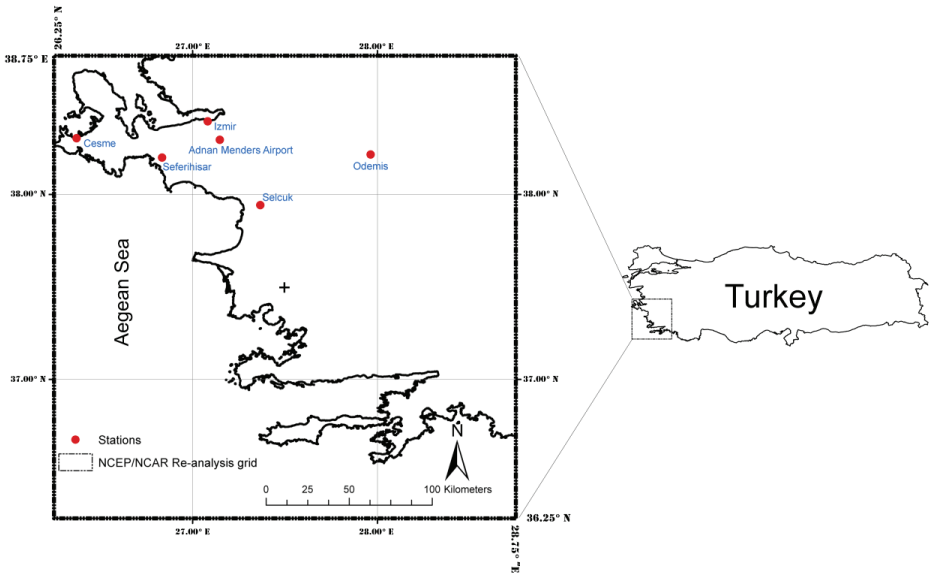

Figure 1 - Locations of the study area and selected stations

Table 1 - Meteorological stations in the study area

Station Number	Station Name	Latitude (°) N	Longitude (°) E	Altitude (m)	Data Availability
17220	Izmir	38.3949	27.0819	29	1938 - 2018
17219	Adnan Mend.	38.2950	27.1479	119	2009 - 2018
17820	Seferihisar	38.1990	26.8350	22	1980 - 2011
17221	Cesme	38.3036	26.3724	5	1965 - 2018
17822	Odemis	38.2157	27.9642	111	1960 - 2011
17854	Selcuk	37.9423	27.3669	18	1965 - 2011

The first step in statistical downscaling involves selecting the appropriate predictors. Any predictor can be used for downscaling as long as it has an acceptable correlation with the predictands [35,36]. However, using many predictors may not result in a better relationship relative to using a parsimonious predictor set. Therefore, stepwise regression and correlation analysis, combining the inputs and outputs, can be used to select the main explanatory predictors [11,37–39].

In literature, there is not a general agreement on the selection of the most appropriate predictor variables. Generally, the selection procedure depends on the region's unique characteristics, such as its large-scale atmospheric circulation, seasonality, topography, and the predictand to be downscaled [40]. Table 2 summarizes several studies on selecting various predictors for downscaling precipitation in different regions across the world.

Table 2 - Predictor selection in various studies

		This study	Fistikoglu, 2011 [12]	Wetterhall, 2009 [41]	Dayon,2015 [42]	Vu, 2016 [43]	Hu, 2013 [44]	Tatli, 2004 [45]	Tareghian, 2013 [46]
Levels	Predictor variables	Turkey	Turkey	Sweden	France	Bangkok	China	Turkey	Canada
200 hPa	Air temperature		X						
	Geopotential height	X	X	X				X	
	Meridional and zonal winds							X	
500 hPa	Air temperature	X	X				X		X
	Geopotential height	X	X	X		X		X	X
	Relative humidity	X	X			X			X
	Specific humidity			X		X	X		
	Meridional and zonal winds			X			X		X
	Vertical pressure velocities							X	
850 hPa	Air temperature	X	X						X
	Geopotential height	X	X	X		X		X	X
	Relative humidity	X	X			X			X
	Specific humidity			X	X	X			
	Module of moisture flux			X	X				
	Meridional and zonal winds			X			X		X
Surface	Air temperature	X	X		X	X	X		
	Pressure		X						
	Precipitation	X	X	X	X				
	Relative humidity	X	X			X			
	Specific humidity					X			X
	Sea-level pressure	X	X	X	X	X	X	X	X
	Mean daily v-wind	X			X				

The correlation analyses depicted that the geopotential height, air temperature, relative humidity, v-wind, and mean sea level pressure play significant roles in daily rainfall events in the studied area. The predictors were then selected based on the i) acceptable correlation with the predictand and ii) the preference in the previous downscaling studies in the region. Several ANN models were constructed between the selected predictors and the daily rainfall series to determine which predictors are better suited for downscaling networks. As a result, 12 atmospheric variables from the NCEP/NCAR Reanalysis dataset listed in Table 3 were selected as predictors for the study area.

Table 3 - Selected atmospheric predictors from NCEP/NCAR Reanalysis dataset

Atmospheric level	Selected variables	Unit	Abbreviation
200 hPa	Mean daily geopotential height	m	Hgt200
500 hPa	Mean daily air temperature	K	Air500
	Mean daily geopotential height	m	Hgt500
	Mean daily relative humidity	%	Rhum500
850 hPa	Mean daily air temperature	K	Air850
	Mean daily geopotential height	m	Hgt850
	Mean daily relative humidity	%	Rhum850
Surface	Mean daily air temperature	K	Air
	Mean daily sea-level pressure	Pascal	Slp
	Mean daily relative humidity	%	Rhum
	Mean daily v-wind at 10 m	m/s	V-wind
	Mean daily precipitation rate	kg/m^2	Prate

3. METHODOLOGY

The methodology of this study is summarized in Figure 2. The first step involves constructing three downscaled ANN models of the large-scale NCEP/NCAR Reanalysis data into station-based daily rainfall series within the study area. The best ANN structure is then determined based on the performance yield from statistical analysis (e.g., R^2, RMSE). The second step entails correcting the biases of the estimated annual maximum daily rainfall values sampled from the daily rainfall series downscaled by the best ANN model. This step is followed by estimating the annual 24-hour maximum rainfall values from the annual maximum daily values using the observed ratio. The final step is to disaggregate the annual 24-hour maximum rainfall into the standard-duration rainfall depths according to the scale-invariant properties of the short-duration rainfall, then estimate the IDF curves of the studied area using the probability distribution functions fitted to the standard-duration rainfall heights. Details for each step are outlined in the following sections.

3.1. Estimation of Daily Rainfall Series Using Ann-Based Downscaling Approach

ANN was used as a well-known machine learning technique to estimate the observed daily rainfall from the large-scale atmospheric reanalysis variables [36]. The ANN is utilized as a practical black-box tool for developing a non-linear regression between the atmospheric dataset (predictors) and observed daily rainfall (predictands) [20,47]. The earlier studies [36,47] concluded that ANN is not the best statistical approach due to its exclusion of the atmospheric variables of the antecedent days as inputs and the lack of bias correction of the downscaled estimations. However, ANN proved to be one of the best alternatives in the statistical downscaling approaches when bias correction is applied to the statistically downscaled atmospheric variables [43,48]. Details of the ANN-based downscaling method are reported by Fistikoglu and Okkan (2011), and its applications in hydrological science are reviewed in the report of ASCE [49]. ANNs were used effectively for the daily rainfall and monthly rainfall estimations [16,43,50].

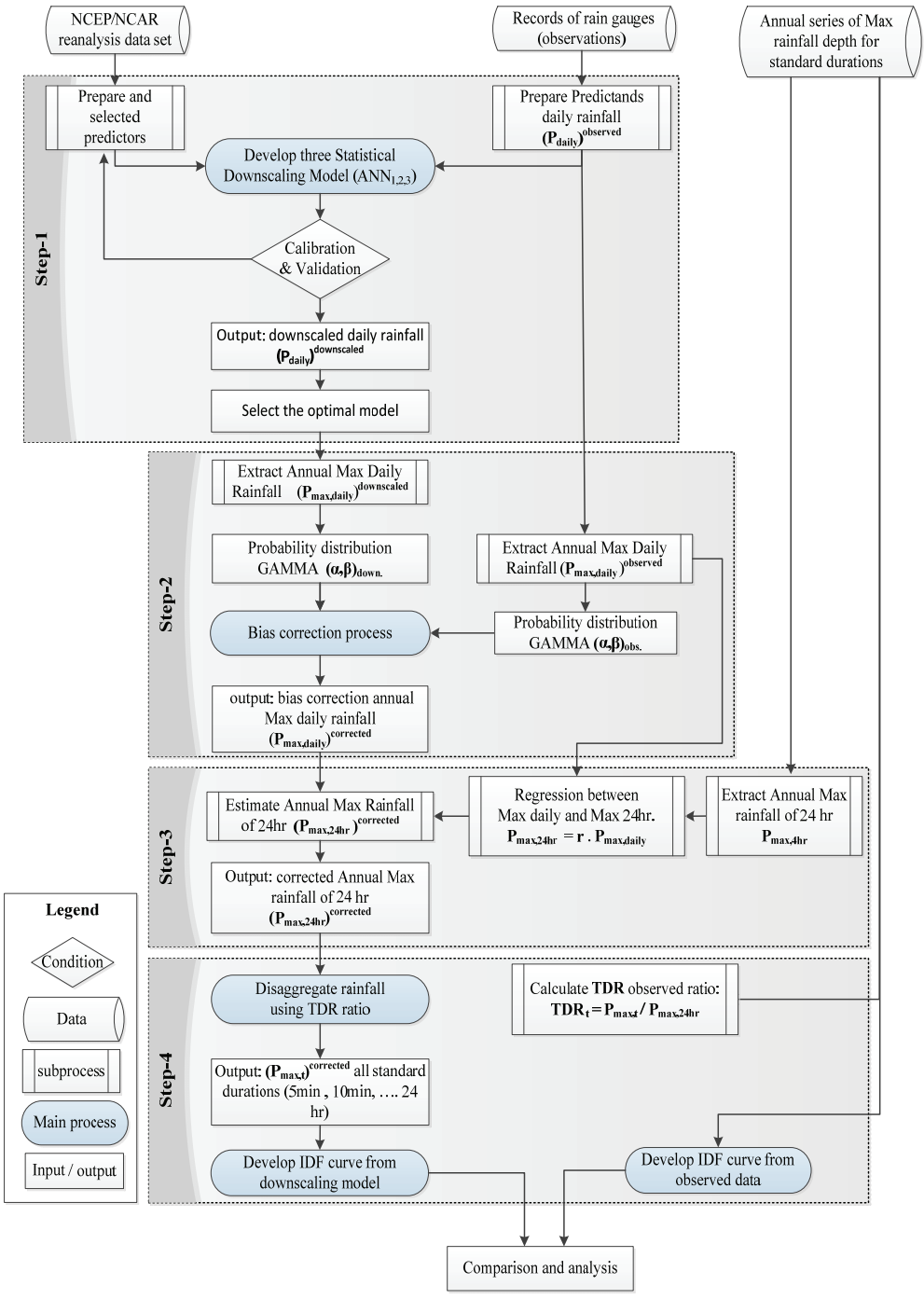

Figure 2 - The flow chart of the methodology

As past and present large-scale atmospheric conditions significantly influence the current local weather conditions, the present and antecedent large-scale atmospheric variables were considered as inputs of the daily downscaling networks [51]. Three statistical downscaling models were tested regarding the antecedent atmospheric conditions in this study, as shown in Fig. 3.

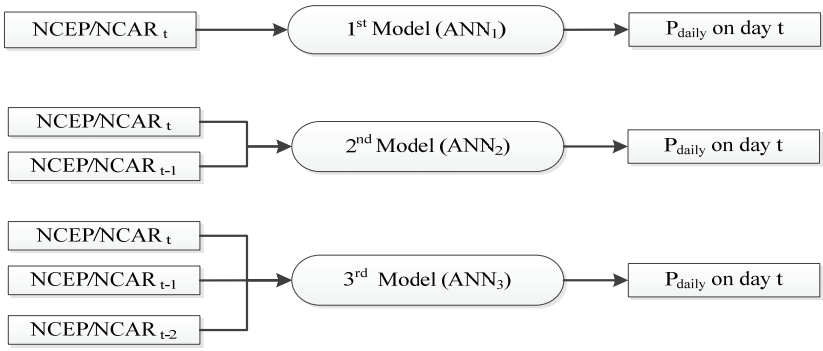

Figure 3 - Three alternative ANN-based downscaling models tested in the study

In the first model (ANN_1), the daily atmospheric variables on the day (t) are used as input (predictors) for estimating the daily rainfall on the day (t). In the second model (ANN_2), the atmospheric variables of the previous (t-1) and current (t) day are used as predictors, while the variables of the two antecedent days (t-2) are added in the final model (ANN_3). Figure 3 shows the three downscaling models based on the input variables of NCEP/NCAR dataset.

The coefficient of determination (R^2) and the root mean squared errors (RMSE) were utilized to evaluate the performance of the downscaling models and to select the optimal model structure to be used for estimating the daily rainfall in the study area.

3.2. Bias Correction of the Annual Maximum Daily Rainfall

The annual maximum daily rainfall is a sub-sample of the daily rainfall series. The maximum value of each year was sampled among the downscaled daily rainfall series to construct the annual maximum daily rainfall estimations. Biases emerge from the input dataset of the downscaling networks that do not represent the existing atmospheric conditions due to the spatial and temporal discrepancies, or they are caused by systematic errors depending on the structure of the downscaling networks. Therefore, the outputs of the downscaling network were evaluated based on whether their respective biases were apparent, and if they are significant, they must be removed from the downscaled series. Teutschbein and Seibert [28] evaluated bias correction methods and reported that the distribution mapping is the best method, where its core concept involves correcting the downscaled outputs based on the observed probability distribution function, which can be realized by shifting the downscaled model's outputs to the observed records with the same probability of non-exceedance [52]. The distribution mapping approach is also called quantile mapping in other studies [53–55].

Eqs. 1 and 2 summarize the distribution mapping method for bias correction used in this study. Figure 4 also illustrates this method with respect to the distribution functions.

$$F_{downscaled} = CDF_{downscaled}\left(P_{max.daily,downscaled}|\alpha_{downscaled}\right) \quad (1)$$

$$P_{max,daily,corrected} = CDF^{-1}_{observed}(F_{downscaled}|\alpha_{observed}) \quad (2)$$

where;

$F_{downscaled}$, *is n*on-exceedance probability of the downscaled annual maximum daily rainfall, $CDF_{downscaled}(.|\alpha_{downscaled})$ is cumulative distribution function with the parameter $\alpha_{downscaled}$ fitted to the downscaled annual maximum daily rainfall, $P_{max.daily,downscaled}$ is downscaled annual maximum daily rainfall, $CDF^{-1}_{observed}(.|\alpha_{observed})$is inverse cumulative distribution function with the parameters $\alpha_{observed}$ fitted to the observed annual maximum daily rainfall and $P_{max.daily,corrected}$ is bias-corrected annual maximum daily rainfall.

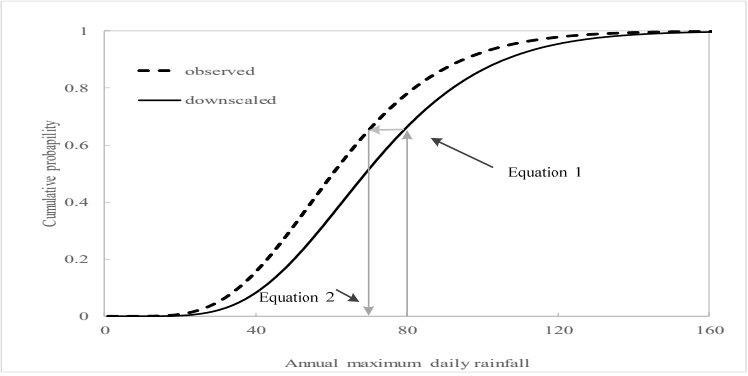

Figure 4 - Distribution mapping method for bias correction

3.3. Estimation of the Annual Maximum 24-hour Rainfall

The annual maximum daily rainfall ($P_{max,daily}$) is slightly different from the annual 24-hour maximum rainfall ($P_{max,24}$). The $P_{max,daily}$ is the annual maximum rainfall height observed in a calendar day, while the $P_{max,24}$ the rainfall height observed in 24-hour durations that might not overlap with the calendar day duration. Although they might be different rain events, most heavy rain heights are observed in 24 hours also occur on a calendar day as it starts and ends on a calendar day. In some rare cases, it starts on a calendar day and extends to the next calendar day. Thus, the empirical ratio between $P_{max.24}$ and $P_{max.daily}$ is slightly bigger than 1.0 and given in Eq. 3.

$$r = P_{max.24}/P_{max.daily} \qquad r \geq 1.0 \quad (3)$$

The empirical ratio (r) between $P_{max.24}$ and $P_{max.daily}$ can be estimated from the local pluviograph records. For example, r is reported as 1.13 for the USA by National Weather Service, and this ratio is nearly similar within a large spatial coverage in the USA [56]. Therefore, using the empirical relationship given in Eq. 3 for the study area facilitates predicting the annual maximum 24-hour rainfall from the annual maximum daily rainfall $P_{max,daily}$. The ratio r can be obtained from any stations with the pluviograph observations in the study area. If the observations do not exist for a particular area, they can be transferred from the nearest station where the observations are available in the region, as it does not change dramatically over the region [56].

3.4. Disaggregation of $P_{max.24}$ to Shorter Standard Duration Rainfall $P_{max.d}$ and IDF Curve Estimation

The establishment of IDF curves requires rainfall heights with durations shorter than 24 hours. Short duration rainfalls, called standard duration rainfalls, are the observed annual maximum rainfall heights for each standard duration, such as 5 mins, 10 mins, 15 mins, 30 mins, 1 hour,.., 24 hours. Determining the maximum rainfall heights at standard duration *d* requires calculating the maximum slope ($\Delta P/d$) on each year's pluviograph records. If the pluviograph records do not exist, empirical ratios between standard duration rainfall and 24-hour rainfall can be used to estimate the standard duration maximum rainfall. Those ratios can be formulated using the median values of the observed ratios, which are based on the scale-invariant rainfall models in literature [57–59].

The shorter duration annual maximum rainfalls are non-linearly proportional to the annual maximum 24-hour rainfall's height [60]. The Indian Meteorological Department (IMD) uses an empirical formula (Equation 4) to estimate the empirical ratios of short-duration rainfalls to 24-hour rainfall if the observations do not exist [61]. Chowdhury et al. [62] and Jahnvi et al. [63] used Eq. 4 to estimate the shorter rainfall intensity of any return period in their studies.

$$P_{max.d} = P_{max.24}\left(\frac{d}{24}\right)^{(1/3)} \tag{4}$$

Huff and Angel analyzed records of 34 rain gauges in Illinois, USA, then propose the empirical ratio for every duration to estimate short duration rainfall from daily rainfall [56]. The proposed ratios in their study are quite like the ratios estimated from Eq. 4.

In this study, the mean values of the observed ratios of each year, which we refer to Temporal Distribution of Maximum Rainfall (TDR), are used to disaggregate the $P_{\max.24}$ to shorter standard-duration rainfall heights $P_{max.d}$ (i.e., 5-min, 10-min, 15-min, 30-min, 1-hr, 2-hr, 4-hr, 6-hr, 12-hr, 18-hr). The TDR given in Eq. 5 is also compared to test the validity of both the IMP method (Eq. 4) and the empirical ratios proposed by Huff and Angel [56].

$$TDR_{\,d} = \frac{(\sum_1^n P_{max,d})/n}{(\sum_1^n P_{max,24})/n} \tag{5}$$

where $TDR_{\,d}$ is the observed mean ratio of the annual maximum rainfall with duration (*d*) $P_{max,d}$ to annual maximum 24-hour rainfall $P_{max,24}$, n is the number of observations. If the

observed ratios are not available in a particular area due to the lack of standard duration rainfall observations, the ratios of the nearest station in the region can be used like the case of the ratio of the daily and 24-hour maximum rainfall.

The Intensity-Duration-Frequency (IDF) curves represent the relationship between intensity, duration, and return period of the maximum rainfall height within an area [62]. The curves make it easier to compute the rainfall intensity of maximum rainfall event with different duration and the probability of exceedance, which are significant input to design urban drainage systems. The IDF curve establishment requires fitting a theoretical probability distribution to the annual maximum rainfall heights for each standard duration to calculate the return periods of them. Then, the estimated annual maximum rainfall intensities with different durations but the same return period are plotted as curves [63].

4. RESULTS

4.1. Downscaling of the Daily Rainfall

Using the large-scale atmospheric variables of the study area given in Table 3, three alternative ANN-based downscaling models were established considering the time lag configuration of the inputs as described in the section 3.1. The coefficient of determination (R^2) and the root mean squared error (RMSE) were utilized to evaluate three downscaling models. Table 4 summarizes the results of three alternative downscaling ANN structures of the Izmir station and gives the R^2 between downscaled daily rainfall values and observations of the neighbor stations. Fig. 5 shows the overall performances of three downscaling models for the Izmir station as scatter diagrams. Table 4 and Fig. 5 clearly show that the second model (ANN_2), where the inputs are the atmospheric variables of the previous and current day, has better performance than the other models. It is also evident that the performance of the first model (ANN_1) produced the worst results, while the third model (ANN_3) shows no significant difference relative to the optimal model (ANN_2). Table 4 also highlights the performance of the models as R^2 regarding the observations of each neighbor station. The high R^2 indicates that the ANN_2 based downscaled daily rainfall of the Izmir station is also spatially consistent with the observations of near stations in the region.

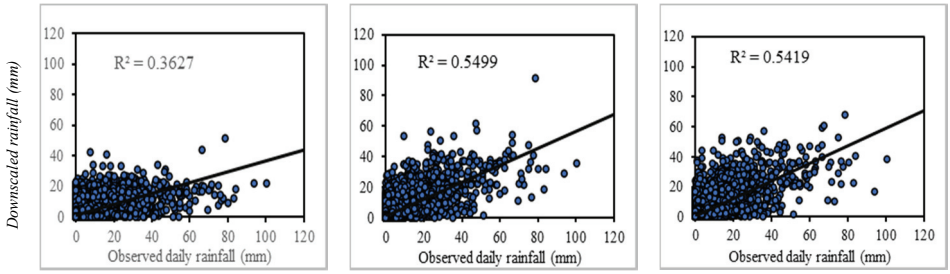

ANN_1 *ANN_2* *ANN_3*

Figure 5 - Comparison of the observed and the downscaled daily rainfall series resulted from three alternative models for the Izmir station at all training and testing period

Table 4 - Results of the three downscaling models for the training and testing periods for each meteorological station

Station	Period	Indicators	ANN_1	ANN_2	ANN_3
Izmir	Train 1948-1990	R^2	0.363	0.550	0.542
		RMSE	5.256	4.410	4.460
Izmir	Test 1991-2018	R^2	0.331	0.462	0.451
		RMSE	5.91	5.250	5.330
A. Menderes	Test 2009-2018	R^2	0.372	0.507	0.487
Seferihisar	Test 1980-2011	R^2	0.257	0.351	0.348
Cesme	Test 1965-2018	R^2	0.267	0.327	0.322
Odemis	Test 1960-2011	R^2	0.278	0.408	0.366
Selcuk	Test 1965-2011	R^2	0.329	0.442	0.427

4.2. Estimation of Annual Maximum Daily Rainfall and Bias Correction

After daily rainfall values were downscaled by ANN_2 model, the maximum rainfall value in each year was sampled to construct the annual maximum daily rainfall series. As the output of the downscaling model contains biases caused by the discrepancy between the real and representative NCEP/NCAR atmospheric conditions and the inadequate model structure of the downscaling network, the biases must be removed from the annual maximum daily rainfall values. The annual maximums sampled from the daily rainfall series are as accurate as the daily estimations. Fig. 6(a) shows the observed and estimated annual maximum daily rainfall values as well as the large-scale precipitation variable of the NCEP/NCAR reanalysis dataset. Although the observed and estimated values show similar fluctuations, the biases are apparent in the estimations. Figure 6(a) also shows that both observed and downscaled annual maximum daily rainfall have approximately the same increasing trend pattern over time. This result indicates that despite the biases in the large-scale atmospheric variables, the ANN_2 model structure preserves the trend mechanism in the observed rainfall series.

For bias correction, the distribution mapping method which proposed by Teutschbein and Seibert [28] was used. The cumulative distribution function of the observed and estimated annual maximum daily rainfall was considered as Gamma after the distribution analyses. The bias corrections of the annual maximum rainfall values were realized by Eq. 6.

$$P_{max,daily}^{corrected} = F_{\Upsilon}^{-1}\left\{F_{\Upsilon}\left(P_{max,daily}^{downscaled}\middle|\alpha_{downscaled},\beta_{downscaled}\right)\middle|\alpha_{observed},\beta_{observed}\right\} \quad (6)$$

where; $P_{max,daily}^{corrected}$ is bias-corrected annual maximum daily rainfall, $P_{max,daily}^{downscaled}$ is downscaled annual maximum daily rainfall sampled from the daily series, α and β are the shape and scale parameters of the Gamma distribution, respectively. The values of the α and β are 7.16, 8.84 for the observed, and 6.82, 9.29 for the downscaled values, respectively.

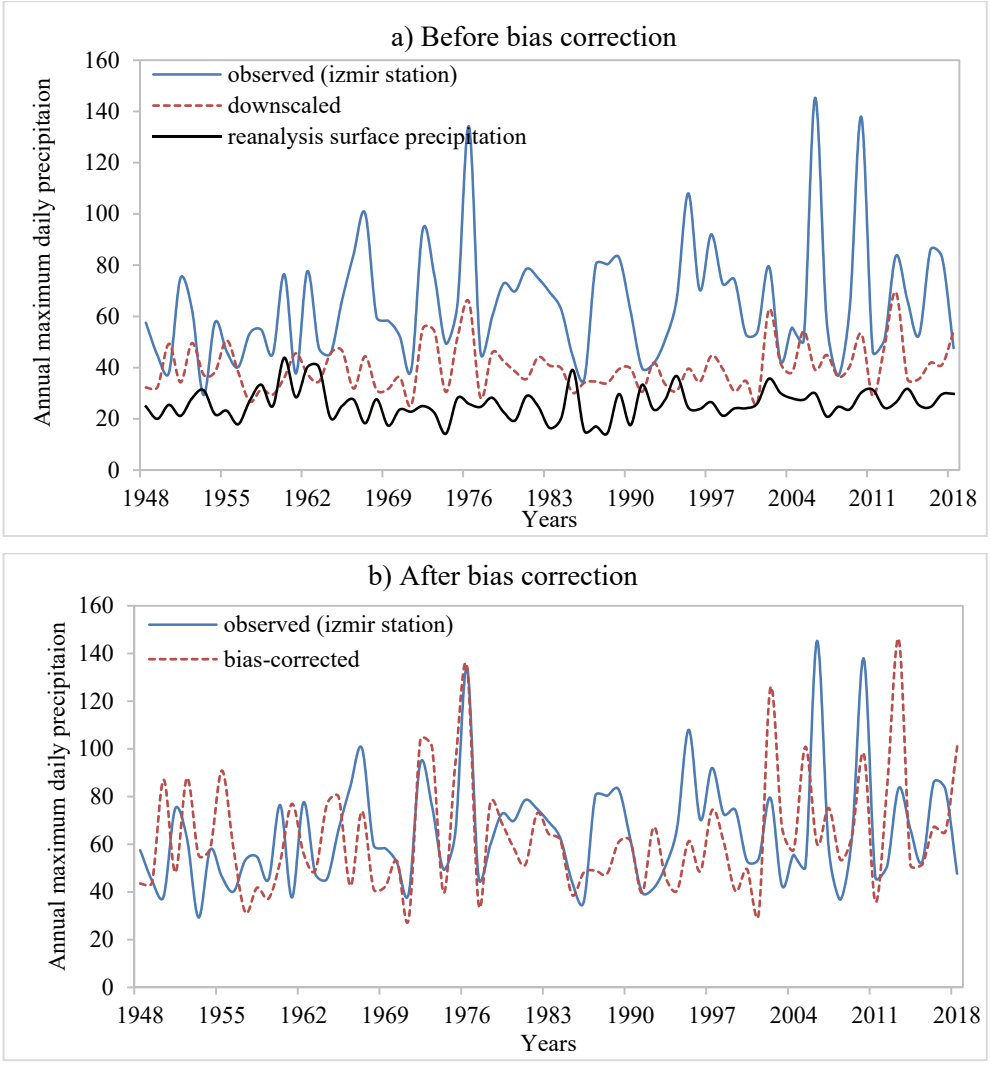

Figure 6 - a) The observed and downscaled annual maximum daily rainfall (before bias correction) and reanalysis daily precipitation at surface level b) the observed and bias-corrected annual maximum daily rainfall

Figure 6(b) exhibits the observed and bias corrected annual maximum daily rainfall values of the Izmir station. Figure indicates that bias correction stretches and shifts the downscaled annuals regarding the mean value and the distribution of the observations properly. In Figure 6(b), it is apparent that bias correction still preserves the trend mechanism in the maximum daily rainfall series. Table 5 also gives the statistics of the observed, downscaled (uncorrected), and bias corrected annual maximum daily rainfall values of the Izmir station. In addition to Table 5, Figure 7 also shows the box plot diagrams of the observed, downscaled, and bias corrected annual maximum daily rainfall $P_{\text{max,daily}}$ of the study area. Table 5 and Fig. 7 indicate that the bias correction applies a decent correction to the downscaled maximums and the corrected maximums fairly fit to the observations.

Table 5 - Statistical parameters of annual maximum daily rainfall ($P_{max,daily}$) of observed, downscaled and bias-corrected

	$P_{max,daily}$ Observed	$P_{max,daily}$ Downscaled	$P_{max,daily}$ Bias corrected
N	71	71	71
Mean	63.35	41.44	63.30
Median	59.70	40.70	61.11
St. Dev	23.67	11.62	23.94
RMSE		31.76	28.39

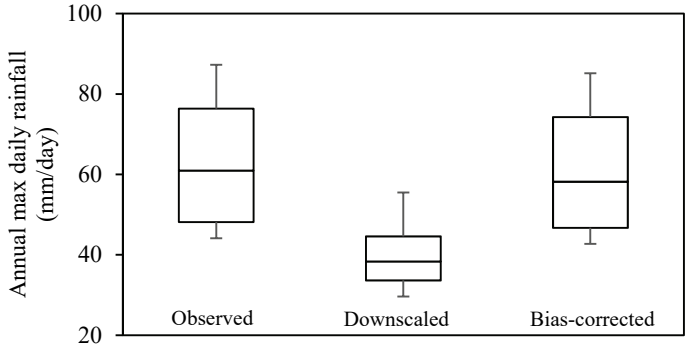

Figure 7 - The box plot of the observed, downscaled, and the bias-corrected annual maximum daily rainfall $P_{max,daily}$ in the Izmir station

4.3. Estimation Annual Maximum 24-hour Rainfall

The observed annual maximum daily rainfall values were compared with observed annual maximum 24-hour rainfall obtained from the station pluviograph records during 1948-2018. The scatter diagram (Fig. 8) of the maximum daily and 24-hour rainfall demonstrates that most of the 24-hour rainfall event occurs in a calendar day and the 24-hour maximum

precipitation is slightly higher than the maximum daily rainfall. The regression equation between the observed daily and 24-hour rainfall observations given in Fig. 8 is used to estimate 24-hour maximum precipitation after bias corrected daily maximum rainfall is estimated.

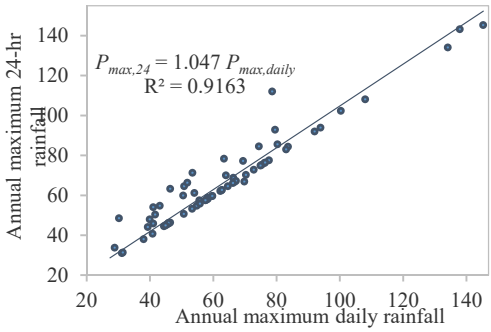

Figure 8 - The relation between $P_{max,24}$ and $P_{max,daily}$

The regression equation $P_{max,24} = 1.047\ P_{max,daily}$ for the study area is consistent with the results of the Huff and Angel [56] in USA, which show that the ratio between $P_{max,24}$ and $P_{max,daily}$ vary in 1.01 - 1.13. The reason of these rates are so close to each other is that the 24-hour maximum rainfall usually occurs within a calendar day. Therefore, the empirical ratio (1.047) between the annual maximum 24-hour and daily rainfall, which is slightly higher than 1.0, can be used to estimate the $P_{max,24}$ by using the daily maximum rainfall in the study area.

4.4. Disaggregate Maximum 24-hour Rainfall into Standard Durations

The maximum rainfall intensities at standard durations generally occur during the maximum 24-hour rainfall event. Several studies [61,64,65] used this assumption to formulate a correlation between the standard duration rainfall and 24-hour rainfall heights.

Fig. 9 compares the disaggregation methods of the annual maximum 24-hour rainfall, IMD empirical method, observed TDR ratios in the study area, and Huff and Angel's empirical ratios. It can be seen that the observed ratios (TDR), which is used in this study, is almost similar to the IMD empirical formula [61] and also Huff and Angel's empirical ratios in the USA [56].

The observed mean of TDR values was used to disaggregate the maximum 24-hour rainfall into the values at standard duration (5, 10, 15, and 30 mins, and 1, 2, 3, 4, 5, 6, 8, 12, 18 hr) rainfall heights. The disaggregated values were also tested for their median and distribution properties using the Mann Whitney-U test. The basic statistics and the Mann-Whitney test of the observed and disaggregated standard duration rainfall are tabulated in Table 6. The p-values of the Mann Whitney-U tests reveal that the differences between the median value of the observed and disaggregated standard duration rainfall heights are statistically insignificant at risk of 0.05 (see Table 6). Fig. 10 also shows the comparison between the median and distribution of the standard duration rainfall heights in the form of box plots.

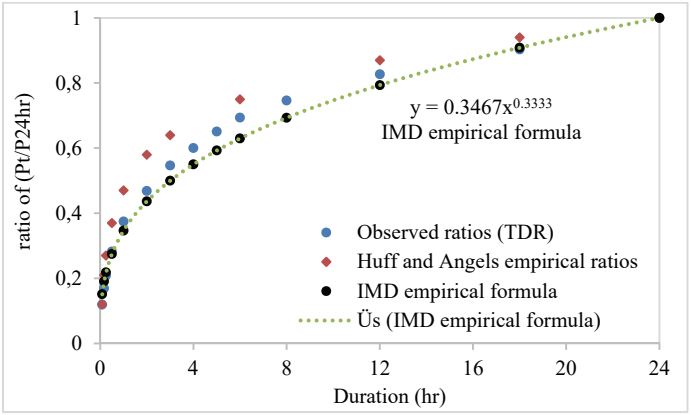

Figure 9 - Comparison of the three disaggregation methods

Table 6 - The basic statistics of the observed and disaggregated standard duration rainfall series and results of Mann-Whitney U tests

Standard Duration		Mean	Max	Min	St.dev	Skewness	Mann-Whitney (P-value) *
5 min	obs.	8.26	22.57	2.50	3.09	1.48	0.0601
	dis.	7.70	19.60	3.74	3.06	1.77	
10 min	obs.	11.59	31.66	3.10	4.33	1.48	0.0864
	dis.	10.90	29.70	5.24	4.35	1.87	
15 min	obs.	14.25	38.93	4.30	5.32	1.48	0.0816
	dis.	13.50	37.40	6.45	5.43	1.80	
30 min	obs.	19.02	51.96	6.00	7.11	1.48	0.0732
	dis.	18.20	52.30	8.61	7.81	1.85	
1 hr	obs.	24.94	68.13	9.10	9.32	1.48	0.0983
	dis.	24.20	60.80	11.29	10.99	1.56	
2 hr	obs.	30.90	84.40	11.20	11.54	1.48	0.1278
	dis.	30.20	76.50	13.98	13.57	1.45	
3 hr	obs.	35.54	97.07	14.80	13.27	1.48	0.1327
	dis.	35.30	83.50	16.08	15.23	1.58	
4 hr	obs.	39.09	106.77	16.70	14.60	1.48	0.146
	dis.	38.70	92.60	17.69	15.52	1.53	
5 hr	obs.	42.23	115.35	17.50	15.77	1.48	0.1097
	dis.	42.00	115.70	19.11	17.51	1.93	
6 hr	obs.	44.87	122.55	18.50	16.76	1.48	0.1259
	dis.	44.80	132.90	20.30	18.67	2.30	
8 hr	obs.	48.02	131.17	18.50	17.94	1.48	0.2127
	dis.	48.20	144.90	21.73	19.63	2.37	
12 hr	obs.	52.84	144.34	18.50	19.74	1.48	0.2043
	dis.	53.40	145.10	23.91	21.30	1.91	
18 hr	obs.	57.32	156.56	18.50	21.41	1.48	0.3097
	dis.	58.30	145.30	25.94	22.47	1.58	
24 hr	obs.	63.65	173.85	31.10	23.77	1.48	0.638
	dis.	64.50	145.30	28.80	22.76	1.47	

*If the p-value is greater than the significance level (0.05), the decision fails to reject the null hypothesis that the median of the observations equals the median of the estimated values.

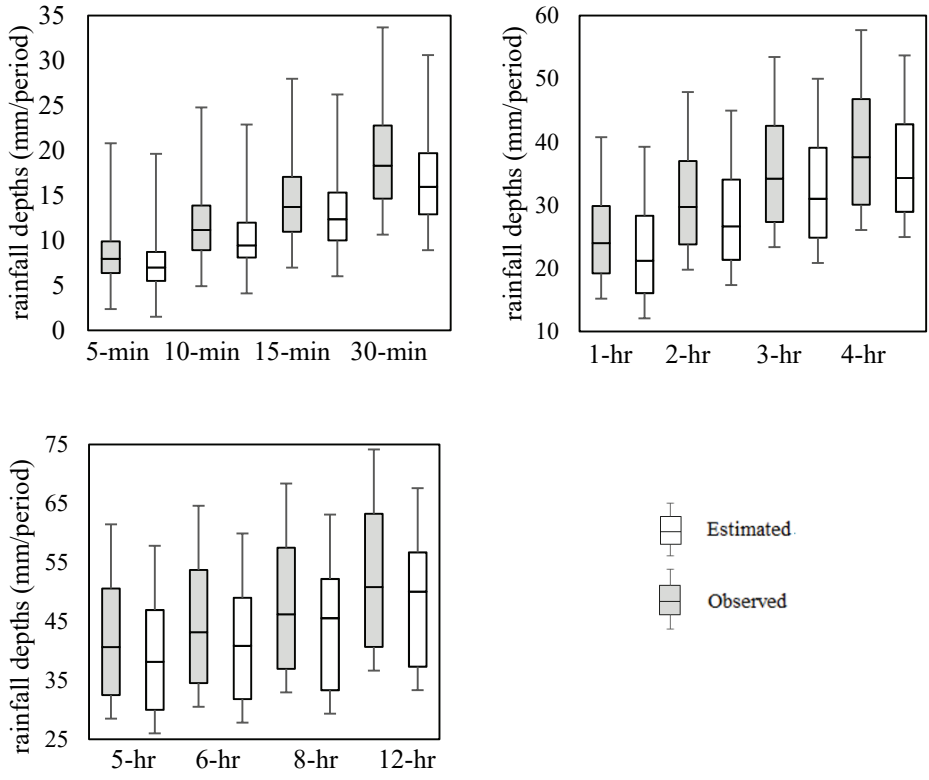

Figure 10 - Box plots of the observed and disaggregated standard duration rainfall heights

4.5. Observed and Estimated IDF Curves

The observed annual maximum rainfalls for the standard durations (5, 10, 15, 30 min, 1, 2, 3, 4, 5, 6, 8, 12, and 24 hr) were analyzed to develop the IDF curves, and the 2-, 5-, 10-, 25-50- and 100-years rainfall intensities were calculated using the probability distribution function of the observed standard duration rainfalls as log-normal.

Fig. 11(a) shows the IDF curves obtained from the observed rainfall records of the Izmir station. The IDF curves can be expressed as an equation, assuming logarithmic relationships between intensities, durations, and frequencies [66]. The equation is also shown in Fig. 11(a).

Similarly, the disaggregated estimations for standard duration rainfalls were also used to construct the estimated IDF curves using the same durations and occurrences. The log-normal distribution was again selected as an appropriate probability distribution function for the estimated standard duration rainfall intensities. The estimated IDF curves and their equation form of the Izmir station are also shown in Figure 11(b). It was noticed that the observed and estimated IDF curves and their simple forms of equations are not significantly different.

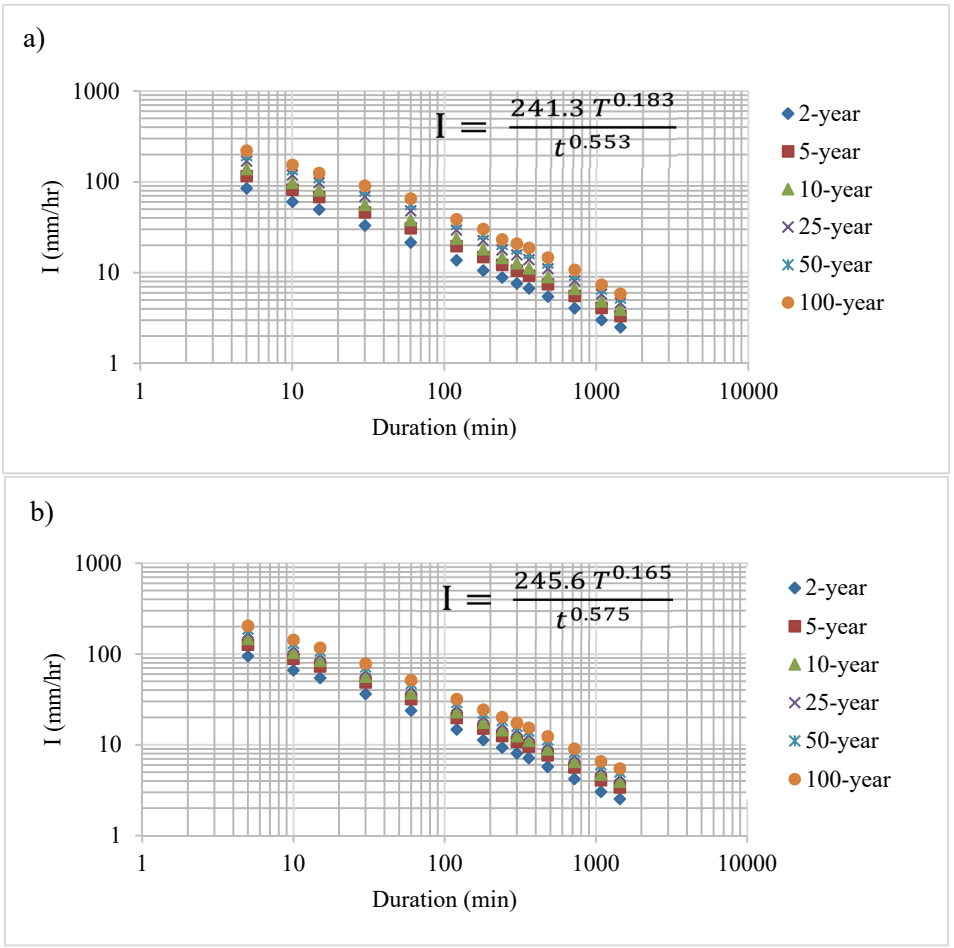

Figure 11 - IDF curves for the Izmir station (a) obtained from observed values (b) estimated from large scale atmospheric variables

5. CONCLUSIONS

The ANN technique was used to establish a statistical downscaling model for estimating the station-based daily rainfall values from large-scale NCEP/NCAR atmospheric variables for the city of Izmir in the Aegean region. The best downscaling model structure was achieved by using atmospheric variables of the current and previous day as predictors. The results of the model were compared with observations of the neighbor stations for spatial validation. The atmospheric variables selected as predictors such as air temperature, relative humidity, and geopotential height at different atmospheric levels and sea level pressure, v-wind, and areal precipitation rate at the surface on the current and previous day were the most explanatory variables for the daily rainfall estimations in the study area. The atmospheric conditions of the previous day were crucial as they increase the accuracy of the estimations.

The annual maximum daily values were sampled from the downscaled daily rainfall series. The biases in the annual maximum daily values were removed using the distribution mapping approach. The results showed that the estimated annual maximum daily rainfall values were consistent with the observations in the study area, which led to the conclusion that the bias correction is a crucial step in a statistical downscaling approach. The method presented here requires the daily rainfall observations to construct a downscaling model and bias corrections. If the observations do not exist at all, it is not possible to find the relationship between large scale atmospheric variables and daily rainfall values. On the other hand, the method presented here can be used to extend the inadequate rainfall observations to estimate long term values.

The bias corrected annual maximum daily rainfall values sampled from the daily rainfall series (1948-2018) were transformed to the annual maximum 24-hour values using the observed empirical ratio. The observed empirical ratio in the study area was revealed that the 24-hour rainfall values were slightly higher than the daily maximum rainfall values. If the 24-hour rainfall values are not available in the study area, 24-hour rainfall values can be assumed as equal to the daily maximum rainfall values since the ratio is very close to one.

The estimated annual maximum 24-hour rainfall values were disaggregated into the shorter standard duration rainfall values using the mean values of the observed ratios (TDR) between 24-hour rainfall and standard duration rainfall. The Mann-Whitney U statistics revealed that the disaggregated estimations have similar medians and distributions with the observed standard duration rainfalls. The results of the disaggregation phase of the study revealed that the observed empirical ratios between the standard duration rainfall and 24-hour rainfall could be used to estimate the sub-daily rates of the maximum rainfall. The observed ratios are very close to the IMD equation, which only consider the power function of durations. If the observed standard duration rainfall records do not exist in the study area, the IMD equation can be used conveniently.

Finally, the estimated standard duration rainfall values were used to generate IDF curves, and a simple form of the IDF equation was fitted to both observed and estimated rainfall intensities. The concordance between estimated and observed IDF curves and equations indicate that the large-scale atmospheric variables can be used to estimate IDF curves reasonably if the daily rainfall values were downscaled and bias-corrected appropriately.

As the number of annual maximum values are essential for statistical analysis of the extreme rainfall events, the approach detailed here could extend the annual maximum dataset of a region where the observation period is inadequate for proper statistical data analyses. Although the methodology applied in this study estimates the IDF curves from historical atmospheric variables, it can be also used to predict future IDF curves using the atmospheric variables of the GCMs running under different climate scenarios. The bias correction of the daily rainfall predictions for the future must be realized by using the historical and future atmospheric predictions of the GCMs.

Symbols

ANN	: Artificial neural networks
CDF	: Cumulative distribution function

CDF^{-1}	: Inverse cumulative distribution function
GCMs	: Global Circulation Models
IDF	: Intensity-Duration-Frequency
IMD	: Indian Meteorological Department
NCEP/NCAR	: National Center for Environmental Prediction and National Center for Atmospheric Research
Obs.	: Observed
Dow.	: Downscaled
$P_{max,24hr}$	: Annual maximum rainfall in 24 hours
$P_{max,d}$	: Annual maximum rainfall in duration d
$P_{max,daily}$	: Annual maximum daily rainfall
RCMs	: Regional climate models
TDR	: Temporal distribution of rainfall
α, β	: Shape and scale parameters of Gamma distribution
γ	: Gamma distribution

References

[1] Kalnay, E. et al., The NCEP/NCAR 40-Year Reanalysis Project, *Bull. Am. Meteorol. Soc.*, vol. 77, no. 3, pp. 437–471, 1996.

[2] Dee, D. P. et al., The ERA-Interim Reanalysis: Configuration and Performance of the Data Assimilation System, *Q. J. R. Meteorol. Soc.*, vol. 137, no. 656, pp. 553–597, 2011.

[3] Wang, A. and Zeng, X., Evaluation of Multireanalysis Products with in Situ Observations over the Tibetan Plateau, *J. Geophys. Res. Atmos.*, vol. 117, no. 5, 2012.

[4] Fu, G., Charles, S. P., Timbal, B., Jovanovic, B., and Ouyang, F., Comparison of NCEP-NCAR and ERA-Interim over Australia, *Int. J. Climatol.*, vol. 36, no. 5, pp. 2345–2367, 2016.

[5] Mooney, P. A., Mulligan, F. J., and Fealy, R., Comparison of ERA-40, ERA-Interim and NCEP/NCAR Reanalysis Data with Observed Surface Air Temperatures over Ireland, *Int. J. Climatol.*, vol. 31, no. 4, pp. 545–557, 2011.

[6] Druyan, L. and Fulakeza, M., Downscaling Reanalysis over Continental Africa with a Regional Model: NCEP versus ERA Interim Forcing, *Clim. Res.*, vol. 56, no. 3, pp. 181–196, 2013.

[7] Tolika, K., Maheras, P., Flocas, H. A., and Arseni-Papadimitriou, A., An Evaluation of a General Circulation Model (GCM) and the NCEP–NCAR Reanalysis Data for Winter Precipitation in Greece, *Int. J. Climatol.*, vol. 26, no. 7, pp. 935–955, 2006.

[8] Plummer, D. A., Caya, D., Frigon, A., Côté, H., Giguère, M., Paquin, D., Biner, S., Harvey, R., and De Elia, R., Climate and Climate Change over North America as Simulated by the Canadian RCM, *J. Clim.*, vol. 19, no. 13, pp. 3112–3132, 2006.

[9] Fu, G., Liu, Z., Charles, S. P., Xu, Z., and Yao, Z., A Score-Based Method for Assessing the Performance of GCMs: A Case Study of Southeastern Australia, *J. Geophys. Res. Atmos.*, vol. 118, no. 10, pp. 4154–4167, 2013.

[10] Jiang, D., Tian, Z., and Lang, X., Reliability of Climate Models for China through the IPCC Third to Fifth Assessment Reports, *Int. J. Climatol.*, vol. 36, no. 3, pp. 1114–1133, 2016.

[11] Wilby, R. L., Hay, L. E., and Leavesley, G. H., A Comparison of Downscaled and Raw GCM Output: Implications for Climate Change Scenarios in the San Juan River Basin, Colorado, *J. Hydrol.*, vol. 225, no. 1–2, pp. 67–91, 1999.

[12] Fistikoglu, O. and Okkan, U., Statistical Downscaling of Monthly Precipitation Using NCEP/NCAR Reanalysis Data for Tahtali River Basin in Turkey, *J. Hydrol. Eng.*, vol. 16, no. 2, pp. 157–164, 2011.

[13] Brands, S., Gutiérrez, J. M., Herrera, S., and Cofiño, A. S., On the Use of Reanalysis Data for Downscaling, *J. Clim.*, vol. 25, no. 7, pp. 2517–2526, 2012.

[14] Sachindra, D. A. and Perera, B. J. C., Statistical Downscaling of General Circulation Model Outputs to Precipitation Accounting for Non-Stationarities in Predictor-Predictand Relationships, *PLoS One*, vol. 11, no. 12, p. e0168701, 2016.

[15] Chen, H., Xu, C. Y., and Guo, S., Comparison and Evaluation of Multiple GCMs, Statistical Downscaling and Hydrological Models in the Study of Climate Change Impacts on Runoff, *J. Hydrol.*, vol. 434–435, pp. 36–45, 2012.

[16] Okkan, U. and Fistikoglu, O., Evaluating Climate Change Effects on Runoff by Statistical Downscaling and Hydrological Model GR2M, *Theor. Appl. Climatol.*, vol. 117, no. 1, pp. 343–361, 2014.

[17] Liu, J., Yuan, D., Zhang, L., Zou, X., and Song, X., Comparison of Three Statistical Downscaling Methods and Ensemble Downscaling Method Based on Bayesian Model Averaging in Upper Hanjiang River Basin, *Adv. Meteorol.*, pp. 1–12, 2016.

[18] Murphy, J., An Evaluation of Statistical and Dynamical Techniques for Downscaling Local Climate, *J. Clim.*, vol. 12, no. 8, pp. 2256–2284, 1999.

[19] Trzaska, Y. and Schnarr, E., A Review of Downscaling Methods for Climate Change Projections (USAID, 2014), 2014.

[20] Khan, M. S., Coulibaly, P., and Dibike, Y., Uncertainty Analysis of Statistical Downscaling Methods, *J. Hydrol.*, vol. 319, no. 1–4, pp. 357–382, 2006.

[21] Schoof, J. T., Pryor, S. C., and Robeson, S. M., Downscaling Daily Maximum and Minimum Temperatures in the Midwestern USA: A Hybrid Empirical Approach, *Int. J. Climatol.*, vol. 27, no. 4, pp. 439–454, 2007.

[22] Benestad, R. E., Hanssen-Bauer, I., and Førland, E. J., An Evaluation of Statistical Models for Downscaling Precipitation and Their Ability to Capture Long-Term Trends, *Int. J. Climatol.*, vol. 27, no. 5, pp. 649–665, 2007.

[23] Cannon, A. J., Sobie, S. R., and Murdock, T. Q., Bias Correction of GCM Precipitation by Quantile Mapping: How Well Do Methods Preserve Changes in Quantiles and Extremes?, *J. Clim.*, vol. 28, no. 17, pp. 6938–6959, 2015.

[24] Mendoza, P. A., Mizukami, N., Ikeda, K., Clark, M. P., Gutmann, E. D., Arnold, J. R., Brekke, L. D., and Rajagopalan, B., Effects of Different Regional Climate Model Resolution and Forcing Scales on Projected Hydrologic Changes, *J. Hydrol.*, vol. 541, pp. 1003–1019, 2016.

[25] Karmacharya, J., Jones, R., Moufouma-Okia, W., and New, M., Evaluation of the Added Value of a High-Resolution Regional Climate Model Simulation of the South Asian Summer Monsoon Climatology, *Int. J. Climatol.*, vol. 37, no. 9, pp. 3630–3643, 2017.

[26] Sun, Y., Wendi, D., Kim, D. E., and Liong, S. Y., Deriving Intensity–Duration–Frequency (IDF) Curves Using Downscaled in Situ Rainfall Assimilated with Remote Sensing Data, *Geosci. Lett.*, vol. 6, no. 1, p. 17, 2019.

[27] Christensen, J. H., Boberg, F., Christensen, O. B., and Lucas-Picher, P., On the Need for Bias Correction of Regional Climate Change Projections of Temperature and Precipitation, *Geophys. Res. Lett.*, vol. 35, no. 20, 2008.

[28] Teutschbein, C. and Seibert, J., Bias Correction of Regional Climate Model Simulations for Hydrological Climate-Change Impact Studies: Review and Evaluation of Different Methods, *J. Hydrol.*, vol. 456–457, pp. 12–29, 2012.

[29] Singh, V. K. and Kumar, D., Downscaling Daily Precipitation over the Upper Shivnath Basin: A Comparison of Three Statistical Downscaling Techniques, *Int. J. Curr. Microbiol. Appl. Sci.*, vol. 9, no. 1, pp. 1676–1688, 2020.

[30] Goly, A., Teegavarapu, R. S. V., and Mondal, A., Development and Evaluation of Statistical Downscaling Models for Monthly Precipitation, *Earth Interact.*, vol. 18, no. 18, pp. 1–28, 2014.

[31] Hung, N. Q., Babel, M. S., Weesakul, S., and Tripathi, N. K., An Artificial Neural Network Model for Rainfall Forecasting in Bangkok, Thailand, *Hydrol. Earth Syst. Sci.*, vol. 13, no. 8, pp. 1413–1425, 2009.

[32] Mailhot, A., Duchesne, S., Caya, D., and Talbot, G., Assessment of Future Change in Intensity-Duration-Frequency (IDF) Curves for Southern Quebec Using the Canadian Regional Climate Model (CRCM), *J. Hydrol.*, vol. 347, no. 1–2, pp. 197–210, 2007.

[33] Mirhosseini, G., Srivastava, P., and Stefanova, L., The Impact of Climate Change on Rainfall Intensity-Duration-Frequency (IDF) Curves in Alabama, *Reg. Environ. Chang.*, vol. 13, no. SUPPL.1, pp. 25–33, 2013.

[34] Hofer, M., Mölg, T., Marzeion, B., and Kaser, G., Empirical-Statistical Downscaling of Reanalysis Data to High-Resolution Air Temperature and Specific Humidity above a Glacier Surface (Cordillera Blanca, Peru), *J. Geophys. Res. Atmos.*, vol. 115, no. 12, 2010.

[35] Giorgi, F., Hewitson, B., Arritt, R., Gutowski, W., Knutson, T., and Landsea, C., Regional Climate Information—Evaluation and Projections, *Clim. Chang. 2001 Sci. bases*, 2001.

[36] Wilby, R. L., Wigley, T. M. L., Conway, D., Jones, P. D., Hewitson, B. C., Main, J., and Wilks, D. S., Statistical Downscaling of General Circulation Model Output: A Comparison of Methods, *Water Resour. Res.*, vol. 34, no. 11, pp. 2995–3008, 1998.

[37] Karl, T. R., Wang, W.-C., Schlesinger, M. E., Knight, R. W., and Portman, D., A Method of Relating General Circulation Model Simulated Climate to the Observed Local Climate. Part I: Seasonal Statistics, *J. Clim.*, vol. 3, no. 10, pp. 1053–1079, 1990.

[38] Kidson, J. W. and Thompson, C. S., A Comparison of Statistical and Model-Based Downscaling Techniques for Estimating Local Climate Variations, *J. Clim.*, vol. 11, no. 4, pp. 735–753, 1998.

[39] Chen, H., Guo, J., Xiong, W., Guo, S., and Xu, C.-Y., Downscaling GCMs Using the Smooth Support Vector Machine Method to Predict Daily Precipitation in the Hanjiang Basin, *Adv. Atmos. Sci.*, vol. 27, no. 2, pp. 274–284, 2010.

[40] Anandhi, A., Srinivas, V. V., Kumar, D. N., and Nanjundiah, R. S., Role of Predictors in Downscaling Surface Temperature to River Basin in India for IPCC SRES Scenarios Using Support Vector Machine, *Int. J. Climatol.*, vol. 29, no. 4, pp. 583–603, 2009.

[41] Wetterhall, F., Bárdossy, A., Chen, D., Halldin, S., and Xu, C. Y., Statistical Downscaling of Daily Precipitation over Sweden Using GCM Output, in *Theoretical and Applied Climatology*, May 2009, vol. 96, no. 1–2, pp. 95–103.

[42] Dayon, G., Boé, J., and Martin, E., Transferability in the Future Climate of a Statistical Downscaling Method for Precipitation in France, *J. Geophys. Res. Atmos.*, vol. 120, no. 3, pp. 1023–1043, 2015.

[43] Vu, M. T., Aribarg, T., Supratid, S., Raghavan, S. V., and Liong, S. Y., Statistical Downscaling Rainfall Using Artificial Neural Network: Significantly Wetter Bangkok?, *Theor. Appl. Climatol.*, vol. 126, no. 3–4, pp. 453–467, 2016.

[44] Hu, Y., Maskey, S., and Uhlenbrook, S., Downscaling Daily Precipitation over the Yellow River Source Region in China: A Comparison of Three Statistical Downscaling Methods, *Theor. Appl. Climatol.*, vol. 112, no. 3–4, pp. 447–460, 2013.

[45] Tatli, H., Nüzhet Dalfes, H., and Sibel Menteş, A Statistical Downscaling Method for Monthly Total Precipitation over Turkey, *Int. J. Climatol.*, vol. 24, no. 2, pp. 161–180, 2004.

[46] Tareghian, R. and Rasmussen, P. F., Statistical Downscaling of Precipitation Using Quantile Regression, *J. Hydrol.*, vol. 487, pp. 122–135, 2013.

[47] Harpham, C. and Wilby, R. L., Multi-Site Downscaling of Heavy Daily Precipitation Occurrence and Amounts, *J. Hydrol.*, vol. 312, no. 1–4, pp. 235–255, 2005.

[48] Mendes, D. and Marengo, J. A., Temporal Downscaling: A Comparison between Artificial Neural Network and Autocorrelation Techniques over the Amazon Basin in Present and Future Climate Change Scenarios, *Theor. Appl. Climatol.*, vol. 100, no. 3, pp. 413–421, 2010.

[49] ASCE, Artificial Neural Networks in Hydrology. II: Hydrologic Applications, *J. Hydrol. Eng.*, vol. 5, no. 2, pp. 124–137, 2000.

[50] Nourani, V., Razzaghzadeh, Z., Baghanam, A. H., and Molajou, A., ANN-Based Statistical Downscaling of Climatic Parameters Using Decision Tree Predictor Screening Method, *Theor. Appl. Climatol.*, vol. 137, no. 3–4, pp. 1729–1746, 2019.

[51] Coulibaly, P., Dibike, Y. B., and Anctil, F., Downscaling Precipitation and Temperature with Temporal Neural Networks, *J. Hydrometeorol.*, vol. 6, no. 4, pp. 483–496, 2005.

[52] Sennikovs, J. and Bethers, U., Statistical Downscaling Method of Regional Climate Model Results for Hydrological Modelling, 2009.

[53] Ines, A. V. M. and Hansen, J. W., Bias Correction of Daily GCM Rainfall for Crop Simulation Studies, *Agric. For. Meteorol.*, pp. 44–53, 2006.

[54] Piani, C., Haerter, J. O., and Coppola, E., Statistical Bias Correction for Daily Precipitation in Regional Climate Models over Europe, *Theor. Appl. Climatol.*, vol. 99, no. 1–2, pp. 187–192, 2010.

[55] Johnson, F. and Sharma, A., Accounting for Interannual Variability: A Comparison of Options for Water Resources Climate Change Impact Assessments, *Water Resour. Res.*, vol. 47, no. 4, 2011.

[56] Huff, F. A. and Angel, J. R., Rainfall Frequency Atlas of the Midwest. Bulletin (Illinois State Water Survey) No. 71, 1992.

[57] Nguyen, V. T. V., Nguyen, T. D., and Wang, H., Regional Estimation of Short Duration Rainfall Extremes, *Water Sci. Technol.*, vol. 37, no. 11, pp. 15–19, 1998.

[58] Borga, M., Vezzani, C., and Dall Fontana, G., Regional Rainfall Depth-Duration-Frequency Equations for an Alpine Region, *Nat. Hazards*, vol. 36, no. 1–2, pp. 221–235, 2005.

[59] Bonaccorso, B., Brigandì, G., and Aronica, G. T., Regional Sub-Hourly Extreme Rainfall Estimates in Sicily under a Scale Invariance Framework, *Water Resour. Manag.*, vol. 34, no. 14, pp. 4363–4380, 2020.

[60] Huff, F. A., Time Distribution of Rainfall in Heavy Storms, *Water Resour. Res.*, vol. 3, no. 4, pp. 1007–1019, 1967.

[61] Al Mamun, A., bin Salleh, M. N., and Noor, H. M., Estimation of Short-Duration Rainfall Intensity from Daily Rainfall Values in Klang Valley, Malaysia, *Appl. Water Sci.*, vol. 8, no. 7, p. 203, 2018.

[62] Anilan, T., Yüksek, Ö., Saka, F., and Orgun, E., Rainfall Intensity-Duration-Frequency Analysis in Turkey, with the Emphasis of Eastern Black Sea Basin, *Tek. Dergi*, vol. 33, no. 4, 2022.

[63] Chow, T. V., Maidment, D. R., and Larry, W. M., *"Applied hydrology." Water Resources Handbook; McGraw-Hill*. New York, NY, USA, 1988.

[64] Chowdhury, R., Alam, M. J., Das, P., and Alam, M. A., Short Duration Rainfall Estimation of Sylhet: IMD and USWB Method, *J. Indian Water Work. Assoc.*, vol. 39, no. 4, pp. 285–292, 2007.

[65] Jahnvi, M., Bhatt, P., Gandhi, H. M., and Gohil, K. B., Generation of Intensity Duration Frequency Curve Using Daily, *J. Int. Acad. Res. Multidiscip.*, vol. 2, no. 2, pp. 717–722, 2014.

[66] AlHassoun, S. A., Developing an Empirical Formulae to Estimate Rainfall Intensity in Riyadh Region, *J. King Saud Univ. - Eng. Sci.*, vol. 23, no. 2, pp. 81–88, 2011.

TECHNICAL NOTE

Teknik Dergi, 2022 11617-11623, Paper 650, ***Technical Note***

Large Scale Direct Shear Box Tests on Gravels

Ali Anıl YUNATCI[1]
Kemal Önder ÇETİN[2]

ABSTRACT

Within the confines of this study, the results of direct shear box tests performed on poorly- (GP) and well-graded (GW) gravel samples are presented. Samples are tested under effective normal stresses ranging from 77 to 205 kPa, and with initial void ratio ranging from 0.42 to 0.53. The estimated peak secant-angles of shearing resistances vary in the range of 49 to 61 degrees. On the basis of the ratio of vertical to horizontal deformation rates, the peak angles of dilation are estimated as 10-16 degrees. These estimated values are concluded to be in coherency with available literature, other than the recommendations of Navfac DM 7.01.

Keywords: Murat River gravel, direct shear box test, peak angle of shearing resistance, dilation angle, void ratio.

1. INTRODUCTION

Owing to difficulties in testing gravels or coarser materials in conventional triaxial, simple shear or direct shear devices due to scale and/or membrane compliance effects, there exists relatively a limited number of studies regarding their engineering properties and straining responses. Liu (2009) summarizes the results of direct shear tests performed by using 122.5 cm x 122.5 cm testing frames on rockfill materials with various compacted densities and D_{max} values ranging from 200 mm to 300 mm, which were tested under effective normal stresses reaching 260 kPa (Matsuoka et. al., 2001; Liu et. al., 2004). Tests on rockfill materials of sandstone origin by using 80 cm x 80 cm sized frames are similarly presented in Wang et. al. (2016), along with case studies on soil – rock mixtures, which were tested in 50 cm x 50 cm shear frames at a maximum effective normal stress of 250 kPa (Li et. al., 2014). A different approach towards utilizing the conventional laboratory triaxial testing apparatus is summarized in Vasistha et. al. (2012), in which samples from river beds and blasted sources having maximum particle sizes ranging from 200 mm to 600 mm were used to create a downscaled gradation curve using parallel gradation techniques. In addition to large scale

Note:
- This paper was received on September 18, 2019 and accepted for publication by the Editorial Board on August 17, 2020.
- Discussions on this paper will be accepted by March 31, 2020.
- https://doi.org/10.18400/tekderg.606816

1 Geodestek Engineering and Consulting Co. Ltd., Ankara, Turkey - ayunatci@geodestek.com https://orcid.org/0000-0003-4279-0007

2 Middle East Technical University, Civil Engineering Department, Ankara, Turkey - kemalondercetin@gmail.com xx - https://orcid.org/0000-0003-0540-2247

direct shear testing, several attempts to characterize gravel and rock fill materials through large scale laboratory triaxial testing exist (Xiao et. al., 2014). A comprehensive review and discussion of large scale triaxial testing on rockfill materials has been presented by Xiao et. al. (2016) with special emphasis on dilatancy behaviour and grain crushing. Scaling, along with grain crushing effects are also discussed in Frossard et. al. (2012), Asadzadeh and Soroush (2009).

Within the confines of this manuscript, after the introduction of the custom-designed and -made large scale direct shear box apparatus, the discussion of test results performed on poorly and well graded Murat River, Muş gravels will be discussed, followed by comparative discussions with available literature. The scope of this technical note is defined as not to assess a new problem, but to present high quality test data regarding a problem, where i) laboratory data is limited and ii) a consensus has not been reached yet.

2. DIRECT SHEAR BOX FRAME AND APPARATUS

A custom-designed and made direct shear box frame with 600 mm x 600 mm plan dimensions and height of 800 mm has been designed for the purpose. Figure 1 shows the direct shear box testing system used in this study.

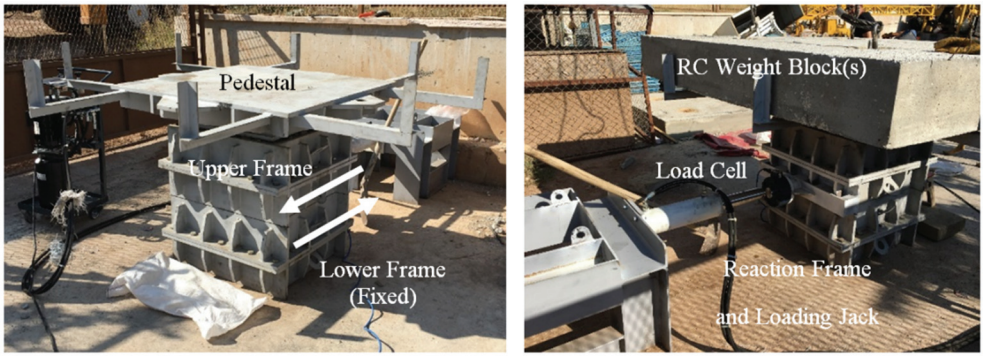

Figure 1 - Direct Shear Box testing system used in this study

Thickness of each frame element was selected as 200 mm, to enable specimen preparations using different compaction procedures (layer thickness, equipment use, etc.). A total number of 4 frame pieces; two lower and upper pieces internally bound were used. The interface between lower and upper frame elements constituted the shearing plane. The plan dimensions of the top cap were selected as 580 mm x 580 mm in order to enable proper placement with minimum disturbance. The platform was then expanded with the addition of steel frame elements and to reach to 1100 mm x 1100 mm to plan dimensions. It is instrumented via a single foil strain gauge type load cell having 200 kN measurement capacity, 2 symmetrically-placed vertical displacement transducers of 50 mm capacity and again 2 symmetrically-placed horizontal displacement transducers of 150 mm capacity. A sampling interval of 8 Hz was preferred during the tests.

3. SAMPLE CHARACTERISTICS AND SPECIMEN PREPARATION

On the samples prepared, a series of soil classification tests including sieve analyses and specific gravity tests, was performed. Soil samples are classified as "GW" or "GP" (well graded gravels or poorly graded gravels) in conformity with Unified Soil Classification System (USCS), with D_{10}, D_{30} and D_{60} values varying in the ranges of 8.29 – 12.49 mm, 17.48 – 24.24 mm and 34.94 – 40.26 mm, respectively. C_u (coefficient of uniformity) and C_c (coefficient of curvature) values are estimated to fall in the range of 3.22 – 4.21 and 1.06 – 1.17, respectively. The average specific gravity value was calculated as G_s= 2.72. A number of representative samples with varying degrees of roundness was randomly selected. Their Roundness Index (RI) (Wadell, 1932) and corresponding classification in accordance with (Powers, 1953) are estimated as 0.18 (very angular – angular with low sphericity), 0.24 (angular – sub angular with low sphericity), 0.30 (sub angular with low sphericity) and 0.76 (well-rounded with low sphericity) respectively, addressing the presence of particles with wide range of roundness in the granular mix. For the purpose of producing homogeneous specimens at the target dry density, the sample preparation process was controlled via vibratory equipment capable of providing constant energy / duration. The thicknesses of compacted layers and the duration of compaction was controlled to achieve four different target densities. A total number of twelve tests (four different densities x 3 different normal stresses) were performed. The last (fourth) set of the large scale shear box tests was conducted under "wet" conditions. The calculated dry unit weights for the Sets 1 through 4 are estimated as 17.44 kN/m^3, 18.77 kN/m^3, 18.49 kN/m^3 and 17.99 kN/m^3 respectively. Initial void ratios (e_0) before the application of normal stresses are estimated as 0.53, 0.42, 0.44 and 0.48, accordingly. Minimum dry unit weight and maximum void ratio values were estimated as 16.09 kN/m^3 and 0.66. Similarly, the maximum dry unit weight and minimum void ratio values were estimated as 19.29 kN/m^3 and 0.41. On the basis of these, relative densities (D_R) of samples were estimated to vary in the range of 48 to 96 %, covering the density range extending from relatively loose to dense.

4. TEST RESULTS AND THEIR INTERPRETATIONS

Test results are presented in the form of three way plots, as shown in Figure 2. Three-way plots enable to consistently follow the shear stress - normal stress – shear displacements throughout the test. Peak tangent angle of shear resistance was simply estimated by fitting a linear failure line on the basis of Mohr-Coulomb failure criterion, with regression forced to a cohesion intercept value of c=0, which is judged to be an acceptable assumption for clean gravels. Similarly, peak secant angle of shearing resistance was also estimated by fitting linear failure envelope to failure Mohr circle of each test, again with c=0. Additionally, maximum dilation angles were estimated from the ratio of shear (lateral) displacement to volumetric (vertical) displacement rates, consistent with the principles of dilation and plasticity theorems (e.g.: Bolton 1986, Vermeer and de Borst 1984). A summary of test results is presented in Table 1. During Test Set 1-1, the vertical displacement transducers were observed to be dislocated; hence corresponding vertical displacement data was excluded in Figure 2. The stress values shown in Figure 2 are estimated after the application of area corrections. Calculation of the dilation angle is based on the assumption that the horizontal plane of the shear box is a zero extension line (Roscoe, 1970). Due to suppression of dilatancy

with increasing stresses, secant friction angles are mostly observed to be reduced with increasing normal stresses.

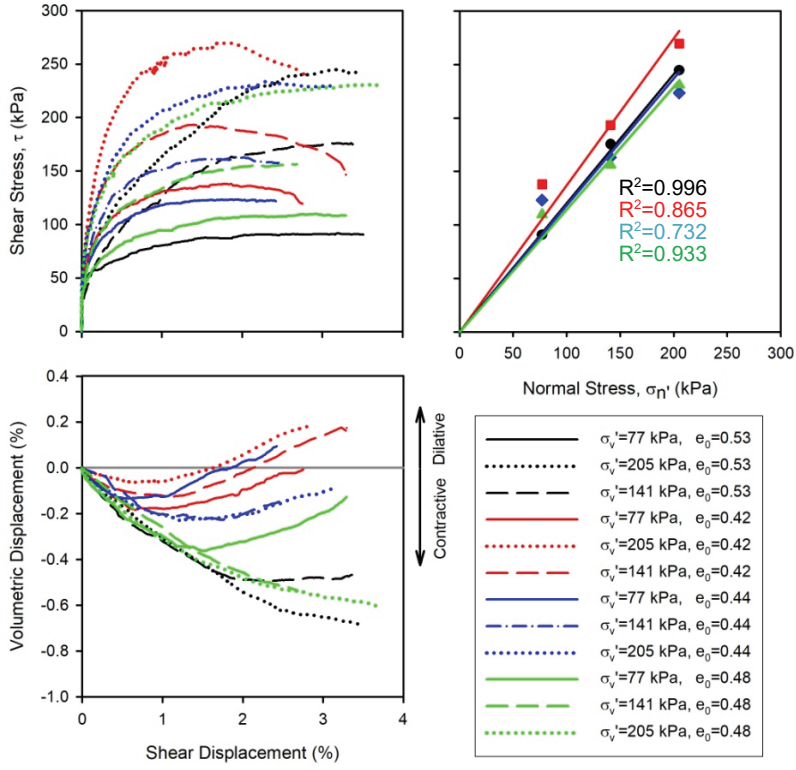

Figure 2 - Three way plots summarizing shear and volumetric deformation responses for the samples with initial void ratios of 0.53, 0.42, 0.44 and 0.48 (Sets 1-4)

5. COMPARISONS WITH AVAILABLE LITERATURE AND CONCLUSIONS

The estimated peak secant angles of shearing resistance are comparatively shown in Figure 3 with the typical ranges given for rockfills, gravels and sands by Terzaghi, Peck and Mesri (1996). Estimated peak secant angles of shearing resistance and initial porosity (n_0), of samples, which vary in the range of 49-61 degrees, and 0.30-0.35, respectively, compare well with the values recommended for sandy gravels and rockfills. They are also found to be in agreement with other studies available in the literature (Simoni and Houlsby, 2006); but, significantly larger than the values recommended by Navfac DM 7.01 for well graded gravels. Significantly lower angles of shearing resistances by Navfac DM 7.01 can be judged to be reasonable, if these values are i) recommended as tangent but not secant angles of shearing resistances, ii) applicable to larger stress ranges, iii) already penalized by partial material factors, widely preferred to be used in design. Unfortunately, due to lack of clear documentation and definitions provided by Navfac DM 7.01, discussions attempting to resolve these differences cannot go beyond crude speculations; hence skipped herein.

Table 1 - Summary of results for large scale direct shear box tests on unsorted fill material

Test No	Normal Stress (kPa)	Shear Strength (kPa)	Shear (Lateral) Displ. at Failure (%)	Volumetric (Vertical) Displ. at Failure (%)**	Peak Secant Angle of Shearing Resist.,ϕ_s (^{0})	Peak Tangent Angle of Shearing Resist.,ϕ_t (^{0})	Peak Angle of Dilation ψ_{max} (^{0})
Test 1-1	77.1	90.7	3.51	-	49.6		-
Test 1-2	141.1	175.6	3.45	-0.47	51.2	50.3	-
Test 1-3	205.2	244.5	3.47	-0.68	50.0		-
Test 2-1	77.1	138.0	1.76	-0.13	60.8		10.0
Test 2-2	141.1	193.3	1.40	-0.11	53.9	53.9	10.5
Test 2-3	205.2	269.4	1.77	0.02	52.7		11.2
Test 3-1	77.1	123.4	1.86	0.00	58.0		16.0
Test 3-2	141.1	163.2	1.91	-0.22	49.2	49.8	13.7
Test 3-3	205.2	233.5	2.29	-0.18	48.7		13.2
Test 4-1*	77.1	109.7	2.93	-0.21	54.9		16.8
Test 4-2*	141.1	156.2	2.63	-0.53	47.9	48.9	-
Test 4-3*	205.2	230.8	3.55	-0.59	48.4		-

*: Performed under wet conditions, **: Negative values indicate contractive behaviour

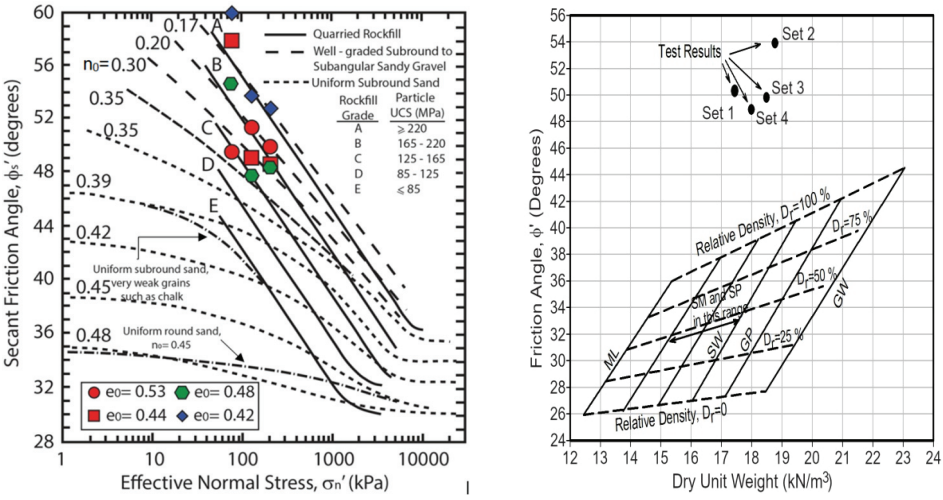

(a) (b)

Figure 3 - The estimated peak secant angles of shearing resistance compared with typical ranges of friction angle for rockfills, gravels and sands as suggested by (a) Terzaghi, Peck and Mesri (1996) and (b) NavFac DM 7.01

The peak angles of dilation values at failure are estimated to vary in the range of 10 to 16 degrees, which are observed to be consistent with available literature (Simoni and Houlsby, 2006). Similarly, the minimum void ratio values reported herein from large scale direct shear tests (approximately in the range of 0.35 – 0.40) are judged to be also consistent with the e_{min} dataset presented by Simoni and Houlsby (2006). Last but not least, similar conclusions can be made for peak secant angles of shearing resistance and relative density relations; although the nature of coarse grained soil characteristics slightly differ in this study. As the concluding remark, the test results are concluded to be in coherency with available literature, other than the "friction angle" recommendations of Navfac DM 7.01 for well graded gravels.

References

[1] Asadzadeh, M., Soroush, A., Direct Shear Testing on a Rockfill Material. Arabian Journal for Science and Engineering, Vol. 34, No. 2B, 379-396, 2009.

[2] Bolton, M. D., The strength and dilatancy of sands. Geotechnique, Vol. 36, No. 1, 65-78, 1986.

[3] Frossard, E., Hu, W., Dano, C., Hicher, P. Y., Rockfill shear strength evaluation: a rational method based on size effects. Géotechnique, Thomas Telford, 62 (5), pp.415-427, 2012.

[4] Li, X. Z, Li, J. L., Deng, H. F., In-Situ Direct Shear Test Research of Rock and Soil of Typical Bank Slope in Three Gorges Reservoir Area. Electronic Journal of Geotechnical Engineering, Vol. 19, Bundle K, 2523-2534, 2014.

[5] Liu, S. H., Application of in situ direct shear device to shear strength measurement of rockfill materials. Water Science and Engineering, 2 (3): 48-57, 2009.

[6] Liu, S. H., Xiao, G. Y., Yang, J. Z., and Wu, G. Y, New in-situ direct shear tests on rockfill materials at Yixing Pumped Storage Power Station Project. Chinese Journal of Geotechnical Engineering, 26(6), 772-776, 2004, (in Chinese).

[7] Matsuoka, H., Liu, S. H., Sun, D., and Nishikata, U., Development of a new in-situ direct shear test. Geotechnical Testing Journal, 24(1), 92-102, 2001. [doi:10.1520/GTJ11285J]

[8] NAVFAC, Soil Mechanics Design Manual 7.01. Naval Facilities Engineering Command, 1986.

[9] Powers, M.C., A new roundness scale for sedimentary particles. Journal of Sedimentary Petrology, 23:117-119, 1953.

[10] Roscoe, K.H., The Influence of Strains in Soil Mechanics, Tenth Rankine Lecture, Geotechnique, Vol. 20, No. 2, pp. 129-170.

[11] Simoni, A., Houlsby, G.T., The Direct Shear Strength and Dilatancy of Sand-gravel Mixtures. Geological and Geotechnical Engineering, Vol. 24, pp. 523-549, 2006.

[12] Terzaghi, K., Peck, R. B., Mesri, G., Soil Mechanics in Engineering Practice, 3rd Edition, 1996, John Wiley & Sons Inc.

[13] Vasistha, Y., Gupta, A. K., Kanwar, V., Prediction of Shear Strength Parameters of Two Rockfill Materials. Electronic Journal of Geotechnical Engineering, Vol. 17, Bundle W, 3221 – 3232, 2012.

[14] Vermeer, P. A., de Borst, R., Non-associated plasticity for soils, concrete and rock. Heron, Delft University of Technology, Vol. 29, No.3, 1984.

[15] Wadell, H., Volume, shape and roundness of rock particles. Journal of Geology, 40:443-451, 1932.

[16] Wang, J. J., Yang, Y., Chai, H.J., Strength of a Roller Compacted Rockfill Sandstone from In-Situ Direct Shear Test. Soil Mechanics and Foundation Engineering, Vol. 53, No.1, March 2016.

[17] Xiao, Y., Liu, H., Chen, Y., Jiang, J., Strength and Deformation of Rockfill Material Based on Large-Scale Triaxial Compression Tests. I: Influences of Density and Pressure. ASCE Journal of Geotechnical and Geoenvironmental Engineering, Vol. 140, No:12, December 2014.

[18] Xiao, Y., Liu, H., Zhang, W., Liu, H., Yin, F., Wang, Y., Testing and modeling of rockfill materials: A review. Journal of Rock Mechanics and Geotechnical Engineering, Vol. 8., 415-422, 2016.

TEKNİK DERGİ MANUSCRIPT DRAFTING RULES

1. The whole manuscript (text, charts, equations, drawings etc.) should be arranged in Word and submitted in ready to print format. The article should be typed on A4 (210 x 297 mm) size paper using 10 pt (main title 15 pt) Times New Roman font, single spacing. Margins should be 40 mm on the left and right sides and 52.5 mm at the top and bottom of the page.
2. Including drawings and tables, articles should not exceed 25 pages, technical notes 10 pages.
3. Your contributed manuscript must be sent over the DergiPark system. (http://dergipark.gov.tr/tekderg)
4. The text must be written in a clear and understandable language, conform to the grammar rules. Third singular person and passive tense must be used, and no inverted sentences should be contained.
5. Title must be short (10 words maximum) and clear, and reflect the content of the paper.
6. Sections should be arranged as: (i) abstract and keywords, (ii) title, abstract and keywords in the other language, (iii) main text, (iv) symbols, (v) acknowledgements (if required) and (vi) references.
7. Both abstracts should briefly describe the object, scope, method and conclusions of the work and should not exceed 100 words. If necessary, abstracts may be re-written without consulting the author. At least three keywords must be given. Titles, abstracts and keywords must be fitted in the first page leaving ten line space at the bottom of the first page and the main text must start in the second page.
8. Section and sub-section titles must be numbered complying with the standard TS1212.
9. Symbols must conform to the international rules; each symbol must be defined where it appears first, additionally, a list of symbols must be given in alphabetic order (first Latin, then Greek alphabets) at the end of the text (before References).
10. Equations must be numbered and these numbers must be shown in brackets at the end of the line.
11. Tables, drawings and photographs must be placed inside the text, each one should have a number and title and titles should be written above the tables and below the drawings and photographs.
12. Only SI units must be used in the manuscripts.
13. Quotes must be given in inverted commas and the source must be indicated with a reference number.
14. Acknowledgement must be short and mention the people/ institutions contributed or assisted the study.
15. References must be numbered (in brackets) in the text referring to the reference list arranged in the order of appearance in the text. References must include the following information:

    If the reference is an article: Author's surname, his/her initials, other authors, full title of the article, name of the journal, volume, issue, starting and ending pages, year of publication.

    Example : Naghdi, P. M., Kalnins, A., On Vibrations of Elastic Spherical Shells. J. Appl. Mech., 29, 65-72, 1962.

    If the reference is a book: Author's surname, his/her initials, other authors, title of the book, volume number, editor if available, place of publication, year of publication.

    Example : Kraus. H., Thin Elastic Shells, New York. Wiley, 1967.

    If the reference is a conference paper: Author's surname, his/her initials, other authors, title of the paper, title of the conference, location and year.

    If the source is a thesis: Author's surname, his/her initials, thesis title, level, university, year.

    If the source is a report: Author's surname, his/her initials, other authors, title of the report, type, number, institution it is submitted to, publication place, year.
16. Discussions to an article published in Teknik Dergi should not exceed two pages, must briefly express the addressed points, must criticize the content, not the author and must be written in a polite language. Authors' closing remarks must also follow the above rules.
17. A separate note should accompany the manuscript. The note should include, (i) authors' names, business and home addresses and phone numbers, (ii) brief resumes of the authors and (iii) a statement "I declare in honesty that this article is the product of a genuinely original study and that a similar version of the article has not been previously published anywhere else" signed by all authors.
18. Copyright has to be transferred to UCTEA Turkish Chamber of Civil Engineers. The standard copyright form signed by the authorised author should therefore be submitted together with the manuscript.

CONTENTS

A New Minimum Delay Model for Multi-Lane Traffic Circles 11429
Serhan TANYEL, Süheyla Pelin ÇALIŞKANELLİ, Mustafa ÖZUYSAL

Application of the Dynamic Compaction Method for Ground Improvement of Collapsible Loess in Qinhai 11455
Jun CAI, Jingtao ZHANG, Guangyin DU, Han XIA

Sediment Incipient Motion in Sewer with a Bed Deposit 11473
Wan Hanna Melini WAN MOHTAR, Charles HIN JOO BONG, Aminuddin AB. GHANI, Mir Jafar Sadegh SAFARI, Aizat Mohd TAIB, Haitham Abdulmohsin AFAN, Ahmed EL-SHAFIE

Teaching-Learning Based Optimization of Nonlinear Isolation Systems under Far Fault Earthquakes 11487
Seda ÖNCÜ-DAVAS, Rasim TEMÜR, Cenk ALHAN

The Strain Sensitivity of Coal Reinforced Smart Concrete by Piezoresistive Effect 11507
Özkan Ayberk KOLATAR, Egemen TEOMETE, Serap KAHRAMAN

Analysis of a Prefabricated Vertical Drain (PVD) Soil Improvement Project 11521
Ahmet Can MERT, Akın ÖNALP, Ersin AREL

Lightweight Cement-Based Composites Incorporating Hollow Glass Microspheres: Fresh and Hardened State Properties 11543
Nihat KABAY, Ahmet B. KIZILKANAT, Büşra AKTÜRK, Yusuf KAHRAMAN

Fundamental Frequencies of Elliptical Plates using Static Deflections 11569
Murat ALTEKIN

Estimation of Intensity-Duration-Frequency (IDF) Curves from Large Scale Atmospheric Dataset by Statistical Downscaling 11591
Khaled ALRAMLAWI, Okan FISTIKOĞLU

TECHNICAL NOTE
Large Scale Direct Shear Box Tests on Gravels 11617
Ali Anıl YUNATCI, Kemal Önder ÇETİN

ISSN: 1300-3453